Modular Design Principles and Biomedical Application of DNA Nanostructures

Johann Moritz Weck

München 2025

Modular Design Principles and Biomedical Application of DNA Nanostructures

Johann Moritz Weck

Dissertation
Fakultät für Physik
Ludwig-Maximilians-Universität München

vorgelegt von
Johann Moritz Weck
aus Frankfurt am Main

München, den 18.03.2025

Erstgutachter: Prof. Dr. Ralf Jungmann
Zweitgutachter: Prof. Dr. Amelie Heuer-Jungemann
Tag der mündlichen Prüfung: 24.06.2025

FORM ~~FOLLOWS~~ ***is*** FUNCTION

Zusammenfassung

Diese Dissertation präsentiert zwei neuartige Methoden zur Assemblierung von DNA-Origami-Superstrukturen und nutzt DNA-Origami, um Ligand-Rezeptor-Zusammenlagerungs-Interaktionen, insbesondere die eines Todesrezeptors, zu untersuchen.

Im ersten Teil werden zwei Methoden für den modularen Aufbau von DNA-Origami und DNA-Origami-Superstrukturen entwickelt. Beide Methoden senken die Kosten für den Bau von Superstrukturen, während sie gleichzeitig die strukturelle Vielfalt und vollständige Adressierbarkeit jeder Komponente innerhalb der Superstruktur gewährleisten. Zudem wird in diesem Teil die (kontrollierte) Assemblierung und Disassemblierung der Strukturen untersucht sowie deren Kinetik im Detail analysiert.

Der zweite Teil befasst sich mit der Ligand-Rezeptor-Zusammenlagerungs-Interaktion zwischen Fas-Ligand (FasL) und Fas-Rezeptor (FasR). Durch nanometer-genaue Positionierung auf DNA-Origami werden FasL in unterschiedlichen Valenzen, Abständen und Geometrien zu DNA-Origami-FasL Nanoagenten angeordnet. Diese Nanoagenten wurden Krebszellen präsentiert, die je nach Muster stark unterschiedliche Apoptose-Reaktionen zeigten, der Effektivste davon eine >100-fachen Erhöhung der Apoptoseinduktion im Vergleich zu freiem FasL.

Zuletzt wird das therapeutische Potenzial der DNA-Origami-FasL-Nanoagenten an großen 3D-Sphäroiden untersucht. Die Sphäroid-Penetration von DNA-Origami von unterschiedlicher Größe und struktureller Flexibilität wurde untersucht, und eine hauptsächliche Abhängigkeit von der Origamigröße gefunden. Die Wirksamkeit der Nanoagenten jedoch wurde eher durch die Art der FasL-Anbindung als durch die Origami-Struktur beeinflusst. Insbesondere eine starke Anbindung von FasL mit Neutravidin rief robuste Apoptoseinduktion hervor und führte zu Apoptose aller Zellen im Sphäroiden.

Diese Dissertation trägt zur DNA-Nanotechnologie durch die Entwicklung zweier Methoden der Modularität bei, sowie zum biologischen Verständnis der FasL-FasR-Zusammenlagerung und eröffnet neue Möglichkeiten für die Konstruktion innovativer Nanotherapeutika.

Abstract

This dissertation presents two novel methods for DNA origami superstructure assembly, and employs DNA origami to probe ligand-receptor clustering interactions, specifically of a death receptor.

In the first part, two methods are developed for the modular construction of DNA origami and DNA origami superstructures. Both methods lower construction costs for superstructures while maintaining the high structural diversity and full addressability of each part of the superstructure. Further, this part examines the (controlled) assembly and disassembly of the structures and also analyses their kinetics in detail.

The second part examines the ligand-receptor clustering interaction between Fas ligand (FasL) and Fas receptor (FasR). By leveraging the nanometer-precise addressability of DNA origami, FasL are positioned in different valencies, distances, and geometries constructing DNA origami-FasL nanoagents. These DNA origami-FasL nanoagents were then presented to cancer cells, which exhibit strongly different apoptosis responses depending on the FasL pattern, with the most potent pattern showing a more than 100-fold increase in apoptosis induction efficiency compared to unpatterned FasL.

Finally, the therapeutic potential of the DNA origami-FasL nanoagents were examined on large 3D spheroids. The spheroid penetration of DNA origami with different sizes and structural flexibilities was evaluated, showing penetration mainly depending on origami size. However, the DNA origami-FasL nanoagent showed effects on the spheroid, which were barely dependent on origami structure, but highly dependent on the attachment strategy of FasL to DNA origami. Specifically, a strong FasL attachment via neutravidin induced robust apoptosis induction, killing all cells throughout the whole spheroid.

This dissertation contributes to the field of structural DNA nanotechnology through the invention of two methods of modularity, as well as to the biological understanding of FasL-FasR clustering, with implications towards the construction of novel nanotherapeutics.

Contents

List of Figures

List of Tables

Abbreviations

aa	amino acid(s)
Ab	antibody
AFM	atomic force microscopy
Ag	antigen
APC	antigen presenting cell
Au NP	gold nanoparticle
BID	BH3 interacting domain death agonist
bp	basepair(s)
CAD	caspase-activated DNase
CAD	computer-aided design
casp	caspase
DC	dendritic cell
DED	death effector domain
DISC	death-inducing signalling complex
DMEM	Dulbecco's modified eagle medium
DMSO	dimethylsulfoxide
DNA	deoxyribonucleic acid
dsDNA	double-stranded DNA
ssDNA	single-stranded DNA
DNA-PAINT	DNA points accumulation for imaging in nanoscale topography
DR4/5	death receptor 4/5
EDTA	ethylenediaminetetraacetic acid
ER	endoplasmatic reticulum
FACS	fluorescence-activated cell sorting
FADD	Fas-associated protein with death domain
FBS	fetal bovine serum (also: fetal calf serum, FCS)
FRET	Förster resonance energy transfer
h	hour(s)
hc	honeycomb (lattice)
HD	Hamming distance
HH	hinge helix
HPLC	high-pressure liquid chromatography
ILD	inter-ligand-distance

IZ	isoleucine zipper
MD	molecular dynamics
min	minute(s)
MHC	major histocompatibility complex
moDON	modular DNA origami nanostructure
MOMP	mitochondrial outer membrane permeabilization
mQ	milliQ (deionized water)
NA	neutravidin
NK (cell)	natural killer (cell)
nt	nucleotide(s)
OF	origami-FasL (nanoagent)
ONF	origami-neutravidin-FasL (nanoagent)
ORF	open reading frame
PBS	phosphate-buffered saline
PFA	paraformaldehyde
ph	packed hexagonal (lattice)
RMSF	root mean squared fluctuation
RNA	ribonucleic acid
rro	Rothemund rectangle origami
RT	room temperature
sq	square (lattice)
(m)SA	(monovalent) streptavidin
SST	single stranded tile(s)
TCEP	tris(2-chloroethyl)phosphate
TAE	tris, acetic acid, EDTA (buffer)
TBE	tris, boric acid, EDTA (buffer)
TEM	transmission electron microscopy
TE	trypsin EDTA (buffer)
TIRF(M)	total internal reflection fluorescence (microscopy)
TNF	tumor necrosis factor
TNF(R)SF	tumor necrosis factor (receptor) superfamily
TRADD	TNF receptor-associated protein with death domain
TRIS	tris(hydroxymethyl)aminomethane
UFO	uranylformate
wf	wireframe
wt	wild -type
1D/ 2D/ 3D	1-/ 2-/ 3-dimensional

Chapter 1

Introduction

1.1 Miniaturization, Down to Atoms

Miniaturization is the key to scientific advance in many fields. The construction of incrementally smaller semiconductor circuits drove the development of computer science in the latter half of the 20th century. The discovery, investigation, and utilization of biomolecules has achieved a high understanding of biological processes, as well as drug development in medicine. The ability to analyze and create materials on an atomic level has also led to advances in physics and material science. And *nanotechnology* is the pinnacle of miniaturization.

Two approaches to nanotechnology exist: top-down and bottom-up. Top-down technologies, like photolithography, or e-beam lithography can create precise patterns of 100 nanometer (nm), or a few nm resolutions, respectively. The latter is employed, *e.g.*, to etch nanoscale transistors for computer chips, a process that drove the miniaturization of semiconductor technology. Bottom-up technologies harness the chemical properties of molecules for nanoscale assembly, allowing them to form highly specific connections and thus self-assemble into pre-defined higher-order structures. The molecular precision of these higher-order assemblies can be down to single Angström, atomistic precision.

1.2 DNA Nanotechnology

DNA nanotechnology is a type of bottom-up nanotechnology. The addressability of the DNA bases facilitates the assembly of many DNA strands to higher-order structures. In principle, DNA nanotechnology is based on the connections of several DNA strands, where the sequence of the first is partially complementary to a second, which is partially complementary to a third strand, *etc.*. Those DNA strands connect through *hybridization*, the formation of complementary base pairs between the individual strands, and form higher-order structures, most notably *DNA origami* structures. As the specificity of DNA is very high, this approach

allows the formation of structures with tens of thousands of bases. The size and shape of these structures are almost arbitrary, with each DNA strand having a unique position in the structure, owed to their unique sequence. DNA nanostructure assembly also happens in a highly parallel fashion, synthesizing trillions of identical structures at the same time. Further, since most DNA strand are synthesized chemically, modifications can be attached during synthesis, which are later positioned precisely in the structure.

1.3 Probing Nanoscale Systems

The ability to address each part on DNA nanostructures precisely predisposes them as frameworks to study nanoscale systems. This feature of DNA nanotechnology has been widely employed to probe nanoscale forces, plasmonic system, or systems of fluorophores, and most importantly, biological systems. Biological processes are governed by the interaction of proteins. Since proteins themselves are usually only of a few nm in size, the interactions between them also take place on the nanoscale. DNA origami cover this scale, and can be functionalised arbitrarily with different protein conformations. These DNA origami-protein constructs are then presented to biological systems and their response allows to draw conclusions on the nanoscale interactions.

1.4 Contributions in this Dissertation

This Dissertation has two parts. The first part describes the extension of DNA nanotechnological methods itself. Here, two approaches to modularity are introduced to the design of DNA origami, with which larger, but still fully addressable structures can be created at low cost.

Modularity is an often employed design principle in various engineering disciplines, such as hardware manufacturing, civil engineering, or software design. It is based upon the construction of reusable, normed components, lowering the monetary cost and speeding up the production process. This principle was adapted for DNA nanotechnology in this dissertation. With this principle applied in two ways to the design of DNA origami, tens of thousands of unique monomers, and from them large superstructures with full addressability, or superstructures reaching micrometer (μm) size and Gigadalton (GDa) weight were constructed.

The second part utilizes the addressability of DNA origami to probe one specific nanoscale system: the interaction of Fas ligands (FasL) and receptors, which induces apoptosis. With FasL, site-specifically attached to DNA origami, the apoptosis induction in 2D and 3D cell culture was tested.

Apoptosis is a central process in the immune system. It is a form of programmed cell death, which allows for the clearance of malignant cells from the organism without causing further harm. Apoptosis can be induced by outer cues,

extrinsically, but the overarching structure of ligand-receptor interaction clusters, inducing the apoptosis signal, is unknown. Here, DNA origami are used as a molecular pegboard to position FasL, a death ligand, in different patterns, distances and valencies. Cells were found to respond very differently, depending on the ligand pattern, both in 2D and 3D cell culture. A most potent ligand pattern was found, able to induce apoptosis more than 100 times more effectively than soluble FasL in adherent cells and even eradicate the whole cancer cell population in a large 3D cancer spheroid model.

In this dissertation DNA origami are not only employed to probe a biological process at different scales and with different setups, elucidating the biological processes, while paving the way for biomedical applications, the work in this dissertation also simplifies the construction of large DNA nanostructures in general, lowering the price and effort for their construction, and thus decreasing hurdles for the application of DNA origami in future works and on grander scales.

Chapter 2

Biology & Technology

This chapter introduces the scientific background of this dissertation. It serves as contextualization within the greater scientific problems and as motivation for the experiments performed in this thesis. The inner mechanisms of life, especially in eukaryotic cells, are introduced, alongside the background to apoptosis within the context of immune response. Lastly, the biological, chemical, structural, physical, and informational aspects of DNA are discussed in detail.

2.1 Biology

2.1.1 A Physicists Perspective

Physical problems are typically of abstract nature, but well-defined and thus result in very simple, reduced experimental setups. This is different for biological systems, whose sheer complexity renders simplistic approaches inept at correctly grasping the underlying rules. These complex biological systems are a "black box", the whole of their inner mechanics hidden from the onlooker. It follows, that the experimental design always is a trade-off between biological scale and phenomenological accuracy: One can either describe a subsystem accurately or know the response of the complex biological system. In this doctoral thesis, one of those complex biological systems is examined in chapter 4; Apoptosis induction. This is done by looking at only the response of a complex machinery. But before, the biological objects need to be defined:

2.1.2 Life

What is Life? Is one of the most fundamental questions in Philosophy. The answer [1] is given by a phenomenological approach: Entities are declared alive axiomatically, their traits are observed, and the overlap in an imaginary Venn

[1] another honorable mention is Erwin Schrödingers *Negative Entropy* definition

diagram is defined as the core traits of life. Depending on the respective interpreter life is characterized by having (1) a metabolism, (2) an internal structure, (3) being able to respond to the environment, (4) having the ability to store and use information, and (5) undergo an evolution[1], or subsets of those. Life is also (6) compartmentalized in cells, a feature, which is implicit in some of the aforementioned characteristics. This holds true across all kingdoms of life, but for this dissertation, the most relevant of those is the kingdom of *animalia*, animals, of which the human is one.

Mariscal, 2021

2.1.3 The Human, an Animal

The human is an animal. The human shares a vast amount of features with other animals, the most fundamental one being its cells, which are of eukaryotic nature. These eukaryotic cells have several organelles, analogously to the human organs, which fulfill a wide variety of roles (see Figure 2.1a): The (i) cell membrane encloses the cell, establishing an outer-inner distinction, maintaining the metabolism and transducing cues of the environment. Inside the cell membrane, embedded in the cytosol, the (ii) nucleus sits, which engulfs the DNA, storing the genetic information of the cell, discussed in more detail in section 2.2.2. The genetic information is read from DNA and transcribed to mRNA, which translocates through nuclear pore complexes and is translated into proteins by ribosomes. Optionally, membrane-associated proteins will attach to the lipid layers of the Endoplasmatic Reticulum (ER), and fold properly in the ER lumen. The fully folded proteins then undergo post-translational modification in the Golgi Apparatus [2]. Eukaryotic cells also possess a cytoskeleton, namely microtubules and actin filaments, which fulfill organizational roles in transportation through the cell, or are responsible for cell adhesion and cell movement, respectively [3].

Alberts, 2002

Fletcher/Mullins, 2010

The human as a complex eukaryotic organism possesses several subsystems responsible for the maintenance of somatic processes (see Figure 2.1b). These systems are interdependent and closely coordinated with each other. The movement apparatus consists of bones, muscles, and tendons. It is coordinated by the nervous system, namely the brain and nerve cords, running through the body. Another part of it is the sensory apparatus, signaling cues of the environment. To the sensory apparatus belongs the visual sense, the olfactoric, sensual, hearing, tasting sense, and also the sense of balance. All this serves to feed a metabolic system, it is simultaneously powered by. The metabolic system consumes organic matter, food, and molecular oxygen to create usable energy. Food is processed in the digestive system, of mouth, gullet, stomach, and intestines, while oxygen follows the trachea into the lungs. Both, nutrients extracted in the digestive system, and oxygen from the lungs are transported by blood through the veins and distributed in the whole organism. The blood also transports waste products to the liver and kidney, which dispose of them. The veins are one part of the vascular system, the other part is the lymph fluid, which again is a main constituent of the immune system [4].

Standring, 2015

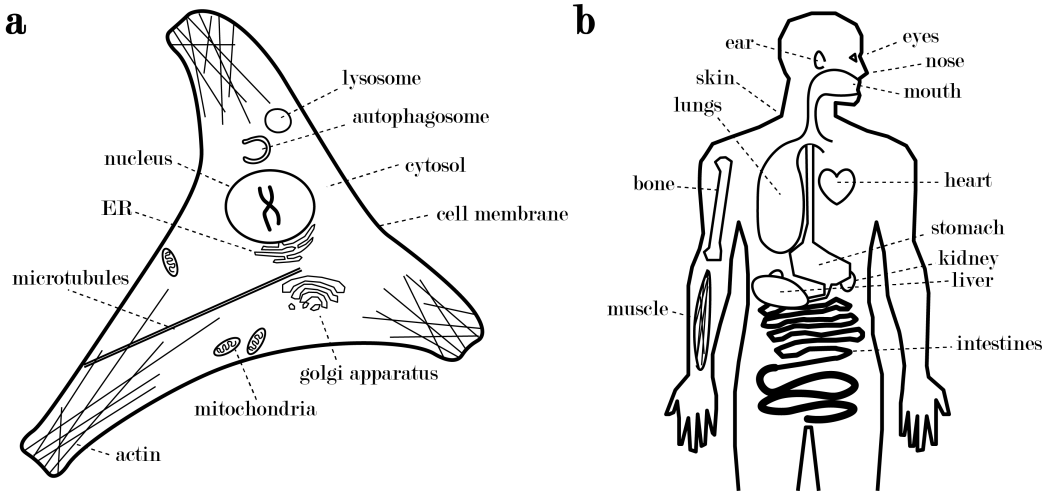

Figure 2.1: Organelles & Organs

(**a**) Organelles in eukaryotic cells and (**b**) organs in a human body fulfill conceptually similar functions on different scales. (**a**) The eukaryotic cell has cell membrane, a movement apparatus (actin filaments and microtubules), it possesses an apparatus that generates energy (via mitochondria) and can respond to environmental cues through transcription, translation of genetic information to functional proteins (nucleus, ER, Golgi). Further, the eucaryotic cell regulates itself and its waste products (autophagosome, lysosome). The (**b**) organs in the body of the human, as it is a eukaryotic organism fulfill similar roles. It possesses skin, a movement apparatus (muscles and bones), organs for the recognition of outer cues (eyes, nose, mouth, ears, skin), a digestive tract (stomach, intestines), and regulatory organs (liver, kidney).

The immune system protects the organism from harm caused by pathogens, such as bacteria, viruses or parasites, but also from self-harm through malignant cells. The immune system can be divided into an innate immune system and an adaptive immune system. The latter is an intricate system, which can form an individual and precise immune answer to new pathogens the body encounters. In short, dendritic cells (DC) lay dormant in tissue, testing their surrounding fluid by continuous ingestion, and upon ingestion of a pathogen, the DC *matures*; it travels through the lymph to the lymph nodes, digests the surface proteins of the pathogens and presents those peptides as *antigens* (Ag) to the lymphoid cells. The DC is now an antigen-presenting cell (APC), presenting the peptide on an MHC (major histocompatibility complex) to naive T cells (T lymphocytes). There are different types of T cells, most importantly helper T cells and cytotoxic T cells, which both mature to fulfill different functions. Helper T cells aid the activation of cytotoxic T cells and B cells (B lymphocytes). Cytotoxic T cells can differentiate between somatic peptides and peptides from pathogens presented to them by the MHC I complex on most somatic cells. Upon being presented a peptide from a pathogen, the cytotoxic T cell prevents further harm by clearing the APC from the organism, through induction of apoptosis, a programmed cell death[5]. B cells then present a plethora of antibodies (Ab) against the Ag, which are generated by a (re-)combinatory process, called VDJ (variable, diversity, joining) recombination, in combination with the introduction of point mutations (*somatic hypermutation*), and the use of different Ab types in the first place[2]. Upon successfully binding Ab to the antigen, the B cells become plasma cells, which produce and secrete the Ab *en masse*, or they become memory B cells, storing the information about the correct Ab for the next infection.

Bonilla, 2010

The innate immune system is non-specific towards pathogens, not requiring prior exposure to them, but instead, it is many-layered: The outermost layer being the skin, but also the mucus, saliva, and sweat produced by the body, all constitute physical barriers towards pathogens, hindering their entry or actively sweeping them out of the organism. The secretions also contain enzymes (lysozymes, RNAses, *etc.*) which constitute a (bio-)chemical barrier against pathogens. Additionally, specialized cells participate in the innate immune defense: Leukocytes plug injuries, phagocytes recognize preserved motifs on pathogens and then digest them, and natural killer (NK) cells recognize malignant somatic cells and induce apoptosis, just like the T lymphocytes of the adaptive immune system [7].

Janeway, 2002

In this dissertation one mode of apoptosis induction is examined: Fas ligand (FasL) - Fas receptor (FasR) interaction. An introduction to the biological topic is given in section 2.1.4 and the problems examined in this doctoral thesis are laid out in sections4.1, and 4.2.

[2]the total amount of different Ab that can be generated is estimated from 10^{12} [2] to 10^{18} [6]

2.1.4 Apoptosis, a Programmed Cell Death

Programmed cell death (PCD) is involved in many regulatory somatic functions. The ability to have specific cells undergo controlled *suicide* allows for clearing potentially malignant cells, or cells that hinder the organism's development.

Functions of Apoptosis

As already mentioned in section 2.1.3, the immune system can actively induce apoptosis[3] in cells, which are either infected by pathogens or dysfunctional, meaning potentially harmful for the whole organism: Cytotoxic T cells induce apoptosis to cells presenting pathogen peptides on their MHC I complex. Similarly, NK cells induce apoptosis to virally infected, stressed, or tumor cells [8]. Neutrophils commit apoptosis after ingestion of pathogens [9]. But already in the maturing of B cells or T cells, the subpopulation of autoreactive cells is cleared out via apoptosis [10][11]. This regulatory mechanism of negative selection ensures the immune system does not harm normal, somatic cells. As an additional safety mechanism, which preventing cells from turning malignant, they can undergo apoptosis without outer cues but as a response to damage to their DNA. Further, during embryogenesis, apoptosis helps to sculpt the limbs, tissue, and organs, *e.g.* the recession of the interdigital web between fingers is caused by apoptosis [12].

Wolf, 2022
Kennedy, 2009
Palmer, 2003
Nemazee, 2017
Jacobsen, 1997

Apoptosis is distinct from other types of cell death[13]. This is apparent in the causes, the activated signaling pathways, the morphogenesis of the cell death [14] , and the effects on other somatic processes. Apoptosis can be induced by a set of extracellular or intracellular cues, some of which are specific for apoptosis, while autophagy can be activated by stress or nutrient deprivation, and necrosis is a result of unspecific cell damage. Necrosis also does not have a main pathway that is activated in the cell, whereas autophagy is an excessive case of intracellular recycling mechanism, and apoptosis a directed cellular suicide, whose pathways will be examined *in extenso* in the following. A distinct morphological sign of apoptosis is the membrane *blebbing* during cell death, where the cell becomes granular and packs it contents inside vesicles, see Figure 2.2a. During necrosis, the necrotic cells swell and their membranes burst, and during autophagy, the autophagosomes are formed excessively. As a result of the compartmentalization of the cell debris, apoptosis is non-immunogenic, which is crucial as it does not alert immune cells and thus does not activate the immune system further, unlike the other kinds of cell death[4].

D'Arcy, 2019
Häcker, 2000

[3] *apoptosis* comes from the old greek $\alpha\pi o\pi\tau\omega\sigma\iota\varsigma$, meaning *falling off*

[4] *N.B.:* several other kinds of genetically and biochemically distinct cell deaths were omitted, as the mentioned three are commonly considered the main mechanisms

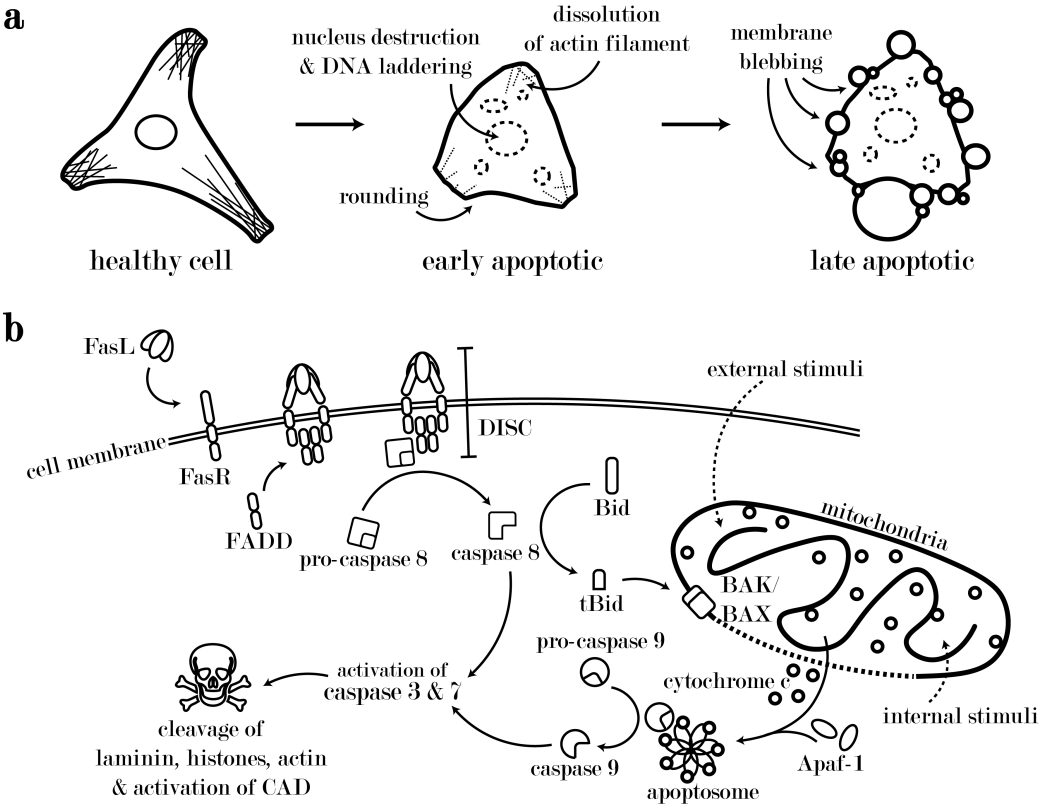

Figure 2.2: Morphology & Pathways of Apoptosis

(**a**) Morphological changes & intracellular processes during apoptosis. Upon activation of apoptosis, in its early stadium, the nucleus is fragmented, the cytoskeleton degraded, and the cell rounds up. This leads to the characteristic membrane blebbing in the late apoptosis. (**b**) Signal pathways of apoptosis: The extrinsic and intrinsic pathway of apoptosis only differ in their beginning: The extrinsic pathway is activated by the binding of a ligand (here: FasL) to a death receptor, followed by recruitment of FADD, cleavage of pro-caspase 8 to caspase 8, and activation of the effector caspase 3 & 7. The extrinsic pathway can also activate parts of the intrinsic pathway by caspase 8 cleaving Bid to tBid, which results in poration of mitochondrial walls via BAK/BAX. From the inside of the mitochondria, cytochrome c is released which recruits Apaf-1 to form the apoptosome, which cleaves pro-caspase 9 to caspase 9, that also activates the effector caspases 3 & 7, which proteolytically fragment the nucleus and degrade the cytoskeleton.

Apoptosis Pathways

Apoptosis can be induced via an intrinsic or an extrinsic pathway. Different causes activate different pathways of apoptosis, but eventually lead to the same mechanism of cell death. A graphical summary of the pathways is shown in Figure 2.2b.

The intrinsic pathway, or mitochondrial pathway, is activated by DNA damage in the cell, ER stress, as well as chemical cues from outside the cell (chemokines, irradiation, deprivation from growth factors[15] , or lack of attachment points[16]). Collins, 1994
All these lead to a process called mitochondrial outer membrane permeabilization Frisch, 1994
(MOMP). Crucial for this process is the activation of BAX and BAK, which are suspected to form a pore in the outer mitochondrial membrane, allowing pro-apoptotic factors to leave the mitochondria [17]. The pro-apoptotic factor cy- McArthur, 2018
tochrome c then binds to the protein Apaf-1 and forms a heptamer (of dimers, or 14-mer, respectively), which is called the *apoptosome*. The apoptosome itself cleaves procaspase 9 into the initiator caspase 9 (casp9), which activates the executioner caspases 3 and 7 (casp3/7), ultimately leading to apoptosis.

The extrinsic apoptosis pathway is activated by death factors binding to death receptors on the cell. These death factors are released or presented by effector cells, which recognize the target cell as malignant due to pathogen infection or cellular dysfunction. The death factors are mainly produced and presented by NK cells and cytotoxic T cells, fulfilling immunoregulatory roles, already touched upon in section 2.1.3. The most important death factors are FasL, TRAIL, and TNFα. Upon binding of those to the respective receptor (FasR, DR4/DR5, and TNFR1/TNFR2) the extrinsic apoptosis pathway is activated: In the cytoplasm, FADD (Fas-associated protein with death domain) or TRADD (TNF receptor-associated protein with death domain) can attach to the intracellular part of the receptor, thereby presenting their death effector domain (DED). To the DED, procaspase 8 attaches, which undergoes proteolysis and becomes the initiator caspase 8 (casp8). The complex of the ligand, receptor, FADD (or TRADD), and procaspase 8 is called the death-inducing signaling complex (DISC). The cleaved casp8 is released and diffuses further to cleave and therefore activates the executioner casp3/7. This direct activation of the executioner casp3/7 is the extrinsic pathway, but casp8 can also truncate BID (BH3 interacting domain death agonist) into tBID, which then activates the intrinsic apoptosis pathway [18]. Li, 1998

Both pathways lead ultimately to the activation of executioner caspases 3/7. The executioner caspases then proteolytically cleave a multitude of proteins inside the cell, effectively stopping cellular processes: The executioner caspases cleave actin and tubulin, which make up the actin filaments and the microtubules, destroying the cytoskeleton. Further, lamin protein is cleaved, fragmenting the nucleus. Histones are also cleaved and the DNA is fragmented and *laddered* by the activation of CAD (caspase-activated DNase). In total these lead to *blebbing* of the cell membrane, the formation of small and large membrane buds, which engulf the cellular remnants and can be non-immunogenically dismantled.

2.2 Molecules of Life

The doors for molecular biology were opened wide, by a set of experiments in the middle of the 20th century: Salvador Luria and Max Delbrück found that subpopulations of bacteria developed resistance towards bacteriophages, in the absence of bacteriophages [19]. This indicated that (at least in bacteria) mutations occurred spontaneously, not in defense against the bacteriophages. Shortly after, inheritance of a trait in pneumococcal bacteria was found to be connected with the presence of DNA [20]. And almost a decade later, the proof was found that the information of life is stored in DNA [21]. One year afterwards, the structure of DNA was determined from X-ray crystallography data and published, the authors already suggesting DNA as a storage molecule for the information and a translation mechanism of the information into proteins [22]. Francis Crick went on to state the *Central Dogma of Molecular Biology*, about information transfer in life [23]

Luria & Delbrück, 1943

Avery, 1944

Chase & Hershey, 1952

Watson & Crick, 1953

Crick, 1958

> *[...] the transfer of information from nucleic acid to nucleic acid, or from nucleic acid to protein may be possible, but transfer from protein to protein, or from protein to nucleic acid is impossible.*

which holds true until today. Nowadays it is known that deoxyribonucleic acid (DNA) stores the genetic information and can reproduce itself, and the information of DNA is transcribed into ribonucleic acids (RNA), and then translated to proteins, this information direction is depicted with solid black lines in Figure 2.3. Later it was found, that information has a few additional routes it can follow, which are indicated in Figure 2.3 as dotted lines: DNA can be used directly to produce proteins, as found in a cell-free system [24]. RNA was found to be able to be produced from RNA, independent of DNA [25]. Additionally, RNA can also be reversely transcribed into DNA, a mechanism used by retroviruses [26] like the HI virus [27]. Even though RNA can fulfill functional roles and also a role as information storage, DNA is the main information storage in all life forms, owing to its unreactive chemical and physical properties, which are explored in the following.

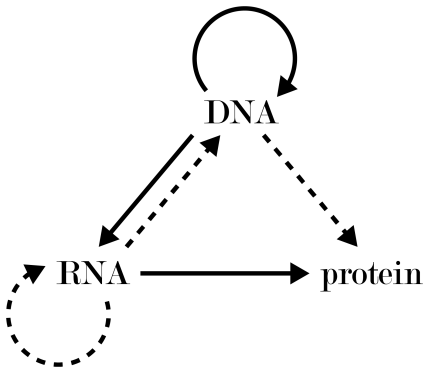

Figure 2.3: The Central Dogma of Molecular Biology

McCarthy, 1965

Baltimore, 1963

Temin, 1970

Poiesz, 1980

2.2.1 Perspectives on DNA

While DNA is usually bespoken in a biological context, it more generally is a macromolecule with a chemical structure and physical properties and can also be viewed abstractly as just a sequence of four letters. In the following section,

several aspects of DNA are discussed: Their role in biological processes, followed by a detailed section on their structural, chemical, and physical properties, needed for understanding DNA nanotechnology. Finally, an abstract, informational view on DNA is given.

2.2.2 Biological Perspective on DNA

The molecule DNA is the primary information storage in all life. The genetic information is written in genetic code, consisting of the four nucleobases Adenine (A), Thymine (T), Cytosine (C) and Guanine (G). The information is transcribed into RNA, and written in the same sequence of nucleobases, except that Thymine is replaced with Uracil (U). RNA is then translated into a sequence of amino acids, making up functional proteins that fulfill most cellular tasks.

The genetic information in eukaryotic cells is stored in the cell nucleus[5]. As seen in Figure 2.4a the DNA is spatially organized around histone proteins, forming protective nucleosome complexes, which again curl up to form the chromatin strands, of which the chromosomes are made. During cell division, *mitosis*, the DNA is unwrapped from the histones and replicated by DNA polymerase, forming two identical copies of the same DNA sequence. Those copies are then pulled by microtubules into the daughter cells, again wrapped around histones and compartmentalized in chromatin filaments. The histone state of DNA (*i.e.* wrapped or unwrapped), is directly influencing whether the genetic information can be transcribed, as wrapped DNA cannot be accessed by RNA polymerases. The wrapping is controlled by chemical modifications to the DNA (methylation at CpG sites) and post-translational modification on the histones. These modifications can be inherited non-genetically and are therefore called *epigenetics*.

DNA functions as information storage not only in eukaryotic cells but also in prokaryotic cells. Even though prokaryotes do not possess a nucleus, histones or chromatin to organize their genetic information, prokaryotes organize their DNA in a *nucleoid*. The nucleoid lacks a nuclear membrane, but the DNA is also condensated and bent by a number of proteins [28]. In condensating and bending the DNA, they also control the reading of the genetic information, similar to histones [29]. Further, prokaryotes are able to transfer genetic information *horizontally*[6] by transfer of small, circular DNA snippets, called plasmids. Many viruses also store their genetic information in DNA (while others use RNA), which is compacted and contained within an outer shell.

Wang, 2013

Dame, 2019

[5] approximately 16 kb DNA is also stored in the mitochondria

[6] between unrelated bacteria; as opposed to vertically, meaning through cell division from mother to daughter cell

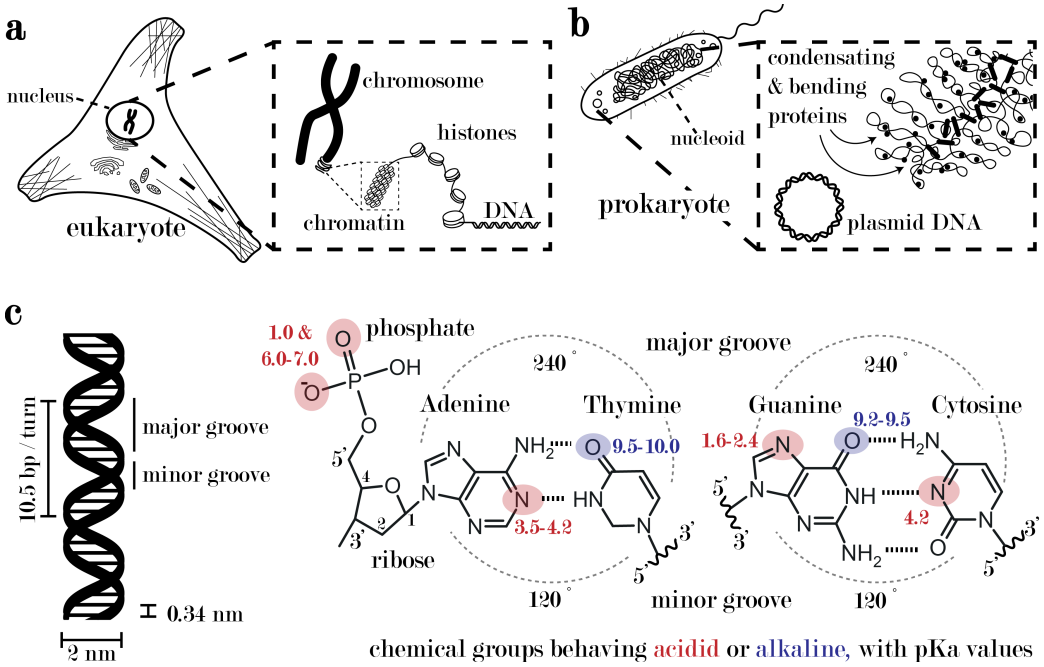

Figure 2.4: Biological & Structural Properties of DNA

DNA acts as the main information storage in Life. The implementation of DNA in the cell, however, is different for different forms of life, even though parallels exist. (**a**) Eukaryotic cells compartmentalized their DNA in a nucleus. The DNA is wrapped around histone proteins, which themselves condense to chromatin fibres making up the chromosomes. (**b**) Prokaryotic cells possess a nucleoid, where the DNA is loosely organized by proteins which condensate and bend the DNA. Independent from the genomic information, the plasmids harbor short snippets of information. (**c**) DNA usually exists as dsDNA double helix, made from two ssDNA strands, which wind around another, creating a major and a minor groove. The ssDNA strands are held together covalently by a sugar-phosphate backbone, and connect to other strands via hydrogen bonds by specific pairing of bases; Adenine (A(with Thymine (T) and Guanine (G) with Cytosine (C). Colors indicate the parts on the chemical structure, behaving acidic (red) or alkaline (blue), with pK_a values annotated. Wiggled lines abbreviate the DNA backbone, and dotted lines indicate hydrogen bonds.

2.2.3 Structural, Chemical, and Physical Properties

DNA Structure

In nature, DNA primarily exists as a double helix (or double-stranded DNA, dsDNA). It consists of two single-stranded DNA (ssDNA) strands, running in opposite directions concerning their 5' and 3' ends. The strands are connected through complementary base pairing on each strand. A connects to T, and G connects to C on the respective other strand, through hydrogen bonding on the bases. The double helix can occur in several structures, the most common in nature being the B-form. The B-form is helical with a right-handed twist and it fully rotates every 10.5 base pairs (bp). B-form DNA is extending 0.34 nm/bp in the helical direction and has a diameter of ≈ 2 nm. In the dsDNA helix the two backbones of the ssDNA strands wind around each other, creating a major and a minor groove, displayed in Figure 2.4c. The respective grooves take up approximately 240° and 120° of the 360° of the helix.

The single ssDNA strands are made up of a sugar-phosphate backbone and the nucleobases. The sugar-phosphate backbone is a repetitive polymer, as seen in Figure 2.4c. The phosphate linker is between the third and the fifth carbon atom on the deoxyribose sugar. This gives the DNA molecule a directionality and defines the nomenclatural 5' and 3' ends of ssDNA. The nucleobases are attached to the first carbon atom on the ribose sugar and are divided into purines (A and G) and pyrimidines (T and C). The overall isoelectric point of DNA is slightly acidic (6.0 - 6.5) which is the average of the rather alkaline nucleobases and the acidic backbone. In Figure 2.4c the pKa values of the respective subparts on the DNA are shown.

DNA and pH

The pKa values of bases and backbone have a direct impact on the behavior of DNA. If the pH of a solution is higher than the pKa values of parts on T and G, it changes the hydrogen bonding interface of the molecule such that it cannot form hydrogen bonds with its counterpart anymore and the dsDNA undergoes alkaline denaturation into its ssDNA parts [30]. Conversely, lower pH values change the structure of C, G, or A in such a way that an additional hydrogen bonding interface is created, which can lead to a triplex structure (Hoogsteen base pairs) or a quadruplex structure (i-motif or G-quadruplex). Very low pH values can favor depurination of the DNA strands, and as a result, denature the dsDNA. Lindahl, 1993

Optical Properties

DNA also has unique optical properties. The delocalized π electrons of the nucleobases absorb light at 260 nm and the backbone absorbs light at 190 nm. The contributions from both absorbances appear as broad, overlapping peaks in the absorbance graph, Figure 2.5a. The absorption in the 260 nm range is decreased

by the π-π stacking in dsDNA, compared to ssDNA. This shift of the absorbance is called hyperchromic effect (dsDNA to ssDNA) or hypochromic effect (ssDNA to dsDNA), and it allows for distinction between dsDNA and ssDNA, when comparing the ratios of 260 nm absorption to 190 nm or 230 nm absorption. These unique absorption properties make DNA easily distinguishable from other biomolecules, for example proteins, which have absorption maxima at 230 and 280 nm, as shown in Figure 2.5a. The concentration of DNA can be determined by use of the Lambert-Beer law

$$A = c\epsilon L \tag{2.1}$$

with c [M] being the concentration of the analyte, ϵ [$M^{-1}cm^{-1}$] the molar absorption coefficient and L [cm] the beam path length through the sample. A is the absorbance, which can easily be determined experimentally, as the common logarithm of the ratio between incident light intensity I_0 and transmitted light I_{trans}

$$A = \log_{10}\left(\frac{I_0}{I_{trans}}\right) \tag{2.2}$$

solved for c, equations 2.1 and 2.2 become

$$c = \frac{\log_{10}\left(\frac{I_0}{I_{trans}}\right)}{\epsilon L} \tag{2.3}$$

with ϵ depending on its double- or single-stranded nature, and the wavelength of incident light. Generally, the extinction coefficient at 260 nm for ssDNA is 1/33 [L $mol^{-1}cm^{-1}$] and for dsDNA 1/50 [L $mol^{-1}cm^{-1}$]. To obtain the molar concentration of DNA with a certain size, this is then multiplied by the weight of the DNA, which can be averaged for large enough molecules at $\approx$ 660 Dalton (Da := g mol^{-1}) for dsDNA and 330 Da of ssDNA.

Binding Energies

Several forces are contributing to the stability of DNA. As seen in Figure 2.5b the connection between A and T involves two hydrogen bonds, whereas the connection between G and C involves three hydrogen bonds, making it slightly stronger. However, the largest contribution to the stability of DNA stems from stacking π-orbitals of the nucleobases, which also depend on the base sequence. Additionally, the Van-der-Waals forces, resulting from interactions between molecular dipoles, contribute to the stability of the DNA duplex. The negatively charged, polar backbone and the unpolar bases, lead to hydrophilic and hydrophobic interactions, which further stabilize the duplex structure of the DNA by exposing the backbone to the solution and hiding the bases in the middle. Counteracting the stability to a small degree is the repulsive force of the negatively charged backbones of both ssDNA strands. Additionally, DNA in its rigid double-stranded form is of

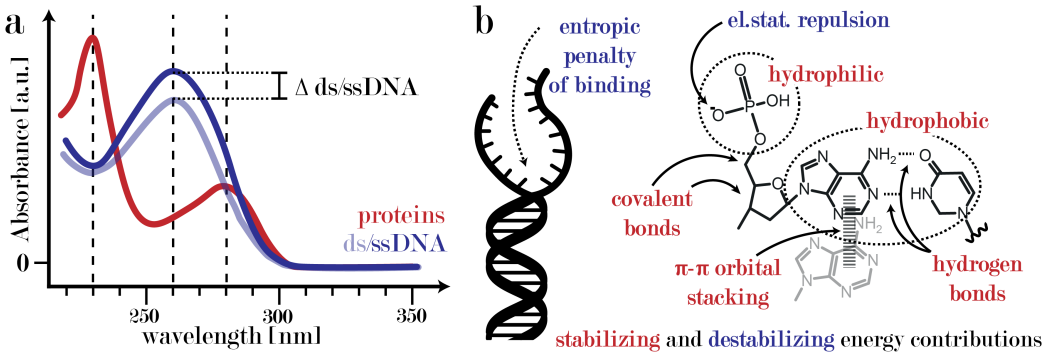

Figure 2.5: Optical Properties and Stability of DNA

(**a**) The absorption depends on the wavelength of the light. DNA has a local maximum of absorbance at 260 nm and a local minimum at 230 nm, whereas proteins have local maxima at 230 nm and 280 nm, and a local minimum at 250 nm. dsDNA also has lower absorbance intensities at 260 nm than ssDNA, owing to the reduced base absorbance in the stacked form. (**b**) There are several stabilizing and destabilizing factors in dsDNA stability. The dsDNA helix is stabilized by overlapping π-π orbitals and the hydrogen bonds between the bases. The bases are uncharged, which makes them hydrophobic in comparison the charged backbone and stabilizes the positions of bases inside and backbone outside of the helix. The backbone itself is held together by covalent bonds, but it is also negatively charged, which leads to an electrostatic repulsive force destabilizing the duplex. Further, for the transition from ssDNA to dsDNA an entropic penalty needs to be paid.

lower entropy than the more freely moving ssDNA form, also reducing the stability of the dsDNA. Minor contributions to the stability of DNA are further given by the displaced water molecules from the ssDNAs hydration shell, which slightly increase the entropy. Further, the ion shell around the DNA has a stabilizing effect, which will be discussed later.

All of those values are implicit in the heuristic model of SantaLucia Jr. [31][32]. It provides nearest neighbor values for free enthalpy contributions ΔG, SantaLucia, 1998 SantaLucia, 2004

$$\Delta G_{total} = \Delta H - T\Delta S \tag{2.4}$$

which is necessary, since the contributions from π-π stacking and hydrogen bonds are sequence-specific, contrary to the other contributions. The other contributions, listed above, are implicit in this model. The respective values are listed in Table 2.1:

Additionally, there are corrections for initial and terminal *end* base pairs, as those only form π-π interactions on one side, and a symmetry correction, accounting for the increased hybridization probability of self-complementary sequences.

parameter	ΔG [kcal/mol]
AA/TT	-1.00
AT/TA	-0.88
TA/AT	-0.58
CA/GT	-1.45
GT/CA	-1.44
CT/GA	-1.28
GA/CT	-1.30
CG/GC	-2.17
GC/CG	-2.24
GG/GC	-1.84
GC end	+1.03
AT end	+0.98
symmetry correction	+0.43

Table 2.1: Gibbs Free Energy Paramters in DNA Hybridization

The stability of a complementary DNA duplex is then a simple sum over all nearest neighbor values ΔG_i, the initial and terminal base pairs, ΔG_{init} and ΔG_{term}, as well as a potential symmetry correction, ΔG_{sym}:

$$\Delta G_{total} = \left[\sum_i \Delta G_i\right] + \Delta G_{init} + \Delta G_{term} + \Delta G_{sym} \tag{2.5}$$

Together with Van't Hoffs equation 2.6, an expression for the equilibrium of chemical reactions

$$K = e^{\frac{-\Delta G_{total}}{k_B T}} \tag{2.6}$$

The respective stability of a DNA duplex can be determined. Here described is the relation between free enthalpy and reaction and the equilibrium constant K

$$K = \frac{k_{on}}{k_{off}} \tag{2.7}$$

with k_{on} [$s^{-1}M^{-1}$] and k_{off} [s^{-1}] being the reaction rates of association and dissociation of the ssDNA (S and S*) into and from their hybridized dsDNA (D = S:S*) form

$$S + S^* \underset{k_{off}}{\overset{k_{on}}{\rightleftharpoons}} D \tag{2.8}$$

the respective stability of a DNA duplex can be determined. Exemplarily, the stability of the DNA sequence S with the sequence GGCGAATA, and its com-

plementary sequence TATTCGCC (both noted 5' to 3') is calculated following equation 2.5 in kcal/mol:

$$\Delta G_i = -1.84 - 2.24 - 2.17 - 1.30 - 1.00 - 0.88 - 0.58 \tag{2.9}$$

$$\Delta G_{init} + \Delta G_{term} = +0.98 + 1.03 \tag{2.10}$$

$$\Delta G_{total} = -8.00 \tag{2.11}$$

Which is approximately -0.35 eV, or -16.6 k_BT.

DNA in Solution

DNA in solution is surrounded by counter ions, which organize in different layers around the molecule. Those layers are described by the Stern-Gouy-Chapman theory. Directly neighboring the negatively charged surface of the molecule is a layer of directly adsorbed positively charged counter ions, static in its behavior, which is called the Stern layer. As seen in Figure 2.6 the border of the Stern layer is called the Stern plane, after which a diffusive layer with associated, but not adsorbed cations and anions follows. The diffusive layer is bordered by the slipping plane at the distance of the Debye length from the molecule's surface. The presence of the ion shell around the molecule gives rise to an electrochemical potential, influencing its surroundings (see Figure 2.6).

In addition to the electrostatic interactions, the Van-der Waals (VdW) forces of the molecule enact an attractive force, coming into play at approximately 5 nm around the molecule, and the electrons of the atoms themselves enact a Born repulsion at too close distance, approximately 0.2 to 0.3 nm. Taken together, these three potentials form an energy landscape around the DNA, as well as any other charged molecule in solution, that would act on a similar particle. The electrostatic potential, and with it, the structure of the whole energy landscape depends on the concentration of ions in the solution. In any case, the global maximum is determined by the Born repulsion of the atoms. Further distant from the molecule a minimum appears, caused by VdW forces. Again, further from the molecule, a local maximum appears, due to the electrostatic potential superimposing the VdW forces. For solutions of higher ionic strength, *i.e.* higher ion concentrations, the thickness of the diffusive layer is smaller, and as a result, the electric potential diminished. In this case, an additional local minimum appears, acting attractive. Some differentiate between connections in the first, deeper, and the second, shallower potential wells as aggregates and agglomerates, the latter being more loosely bound.

An estimate of the number of counterions around the DNA is given by the Manning-Oosawa theory. Here, the initial thought is that if several charges of the

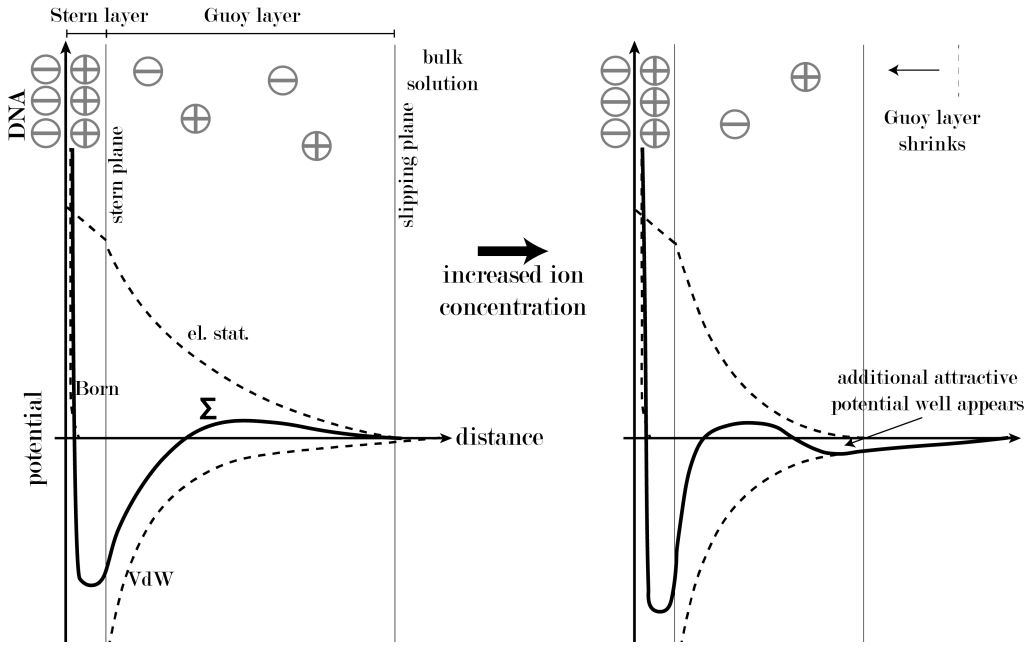

Figure 2.6: Electrochemical Potential Around DNA

The total potential around a DNA duplex (indicated with a Σ and the thick line) in ionic solution is a sum over several different potentials, each enacting an attractive or a repelling force. Most importantly, the electrostatic force, generated by the charge on the DNA and the condensed ions, the Van-der-Waals forces, acting attractively, and the Born repulsion, coming to play only close to the molecule. The qualitative course of the total potential depends on the ion concentration in solution: For increased ion concentration, the onset of the electrostatic potential changes and an additional attractive minimum is created.

same kind are close together, a cloud of counterions starts forming around it. As a rough criterion whether this is applicable, the Manning parameter γ

$$\gamma = \frac{\lambda_B}{l_{charge}} \tag{2.12}$$

is introduced, with l_{charge} being the distance between charges on the DNA and λ_B the Bjerrum length given as the distance of two charged particles where the thermal energy equals the energy from the mutually enacted electric field,

$$\lambda_B = r = \frac{e^2}{4\pi\epsilon_0\epsilon_r k_B T} \tag{2.13}$$

with e being the charge of the respective ions, ϵ_0 is the permittivity, ϵ_r the relative permittivity of the medium, and r is the distance between the two charged ions. If $\gamma > 1$, then the percentage of ions in the cloud around the DNA is $1/\gamma$ and the percentage of ions directly condensed to the DNA

$$1 - \frac{1}{\gamma} = 1 - \frac{l_{charge}}{\lambda_B} = 1 - \frac{\pi\epsilon_0\epsilon_r k_B T l_{charge}}{e^2} \tag{2.14}$$

With $l_{charge} \approx 0.20$ nm/e, simplifying DNA as a one-dimensional rod, and the Bjerrum length $\lambda_B \approx 0.7$, the amount of counterions condensed to the DNA is 28.6 %, and the amount in the diffusive cloud 71.4 %, respectively.

2.2.4 DNA from an Information Perspective

Information Density

DNA stores the genetic information of Life. The one-dimensional DNA chain encodes this information in a sequence of four bases. Abstractly viewed, this four-letter code is much more efficient than the two-letter code used in digital data storage: Instead of a bit made of the binary 0 and 1, a DNA base has the four states 0, 1, 2, and 3, doubling the amount of information in this biological quasi-bit[7]. A byte equivalent consists of four bio-bits, instead of eight digital bits. Thus the information density in DNA is very high: For the dsDNA, one bp only takes 0.34 nm along the 1D chain (1.36 nm/byte), or in the 2D projection 0.68 nm^2 (2.72 nm^2/byte), results in an information density of almost 40 GB/cm^2. DNA can also store information in 3D, which conventional data storage can not. This results in a theoretical data density of

$$\frac{1byte}{4V_{cylinder}} = \frac{1byte}{4\pi r^2 h} \approx 0.25\frac{bytes}{nm^3} = 250\frac{GB}{\mu m^3} \tag{2.15}$$

where the DNA is assumed to be a cylinder with a diameter of 2 nm and height of 0.34 nm/bp.

[7] ssDNA and dsDNA hold the same amount of information

IHGSC, 2001

Yang, 2021

Erlich, 2007

This model falls short of describing DNA data storage density in biology: The human genome has approximately 3 billion bp [33] , which amounts to 0.75 GB, packed in the cell nucleus, with a diameter of 6μm, thus a volume of 113μm^3, and a density of 6.6 GB/μm^3. Also, most of the human genome does not encode useful information and is nonsensical[8]. Additionally, there is the additional bottleneck of data reading, namely sequencing the DNA. Even though there has been significant progress with nanopore sequencing, the reading limit is currently at 450 bp/s [34]. However, DNA storage promises cost-effective long-time storage of large quantities of information, already reaching 2.1 Petabytes per gram of DNA [35]. DNA data storage will be further discussed in section 2.3.5. Besides the slow data reading through DNA sequencing, there are even more problems to consider when using DNA as information storage:

On Sequence Uniqueness

Gout, 2013

Boutabout, 2001

Johnson, 2000

Lang & Murray, 2008

Wang, 2021

Albertson, 2006

Another limiting factor for information storage in DNA, both for biological and artificial systems is *misreading*. Two types of misreading can occur, misreading the DNA sequence and misreading the positional information. Sequence misreading occurs in both biological and synthetic systems. The biological transcription apparatus has certain rates of misreading, resulting in a wrongly constructed product, *e.g.*: it is estimated that RNA polymerase misreads every 100,000 bp [36], reverse transcriptase misreads once per $\approx 10^4$ bp [37], while DNA polymerase misreads once per 100 [38] to 10^9 bp [39]. The highest accuracy for (commerically available) nanopores is 95%, corresponding to one misread per 20 bp [34]. The underwhelming performance of the DNA polymerase is compensated by post-replication mismatch repair and exonucleic proofreading, decreasing what would mathematically have been 30,000-300,000 erroneous bases to just ≈ 100 per replication cycle [40]. In the synthetic system of the nanopore, many copies of the same strand are sequenced, decreasing the error rate tremendously. But this multi-copy approach is suboptimal for high-efficiency data storage, as the copy-number proportionally increases the storage used. The readout for portions of information in the storage needs to be unambiguous, which directly leads to two problems: Is the sequence unique? What is the error tolerance of encoding? While the latter depends on the respective encoding method, the former can be approximated more easily:

The problem of sequence uniqueness can be interpreted as variation of the *Birthday Paradox*, with the single probability and the sequence length disentangled: 365 days in one year becomes positions in the DNA strand, and the probability for a birthday becomes the probability of strand match. The number of possible sequences n in the strand L is $L - n + 1$.

Given a DNA strand of length L, the probability $P^{sequence}_{reoccurrence}$ that a sequence of length n does appear (again) in the strand, is given as

[8] also true for digital data

$$P^{sequence}_{reoccurrence} = (L-n)(\frac{1}{4})^n \tag{2.16}$$

as there are $L-n$ possiblities with the probability of $\frac{1}{4}$ for each of the n bases at the correct position in the sequence. And the probability that the sequence does not reoccur, $P^{sequence}_{no\ reoccurrence}$ is then the counter probability[9]

$$P^{sequence}_{no\ reoccurrence} = 1 - P^{sequence}_{reoccurrence} \tag{2.17}$$

Now there are $L-n$ individual sequences of length n in the strand L. The probability that none of these sequences reoccurs in the strand L is given by the product of the probabilities for reoccurrence of each individual sequence n_i.

$$P^{strand}_{no\ reoccurence} = \left(1-(L-n)\left(\frac{1}{4}\right)^n\right)\left(1-(L-n-1)\left(\frac{1}{4}\right)^n\right)... \tag{2.18}$$

$$= \prod_{i=0}^{L-n}\left(1-(L-n-i)\left(\frac{1}{4}\right)^n\right) \tag{2.19}$$

$$= \prod_{i=0}^{L-n}\left(1-\frac{(L-n-i)}{4^n}\right) \tag{2.20}$$

$$= \prod_{i=0}^{L-n}\left(1-\frac{i}{4^n}\right) \tag{2.21}$$

and the probability $P^{strand}_{reoccurrence}$ that a sequence reoccurs in the whole strand is again the counter probability:

$$P^{strand}_{reoccurrence} = 1 - P^{strand}_{no\ reoccurrence} \tag{2.22}$$

The probabilities $P^{strand}_{reoccurrence}$ of equation 2.22 for different n are plotted on the strand lengths L in Figure 2.7: The probabilities for sequences of length n to reoccur is very different, depending on the sequence length L: For a specific dimer to reoccur in a strand of length $L = 20$ is already 1, while the probability of a sequence of length $n = 32$ to reoccur in a sequence of lengths exceeding 1 million nt is $<< 1\%$. The probabilities for sequences with a length of four, eight, or sixteen nt (corresponding to eight, 16, or 32 bit) follow a sigmoidal curve at the logarithmic abscissa. While for $n = 4$ a probability of reoccurrence of ≈ 0.5 is reached already for $L = 20$, for $n = 8$ this is only reached at $L = 320$, and for $n = 16$ at $L = 81920$.

It is to be pointed out that the strand lengths for these numbers are much smaller than intuitively guessed, owing to the fact that this is a variation of the *Birthday Paradox*: while 100 % certainty of repeat for $n = 4$ is reached at $L = 160$,

[9] here we are implicitly discarding all combinations of correct and incorrect bases, as each mismatch is disqualifying

the length of all $256 = 4^4$ different sequence together would be 1024 nt. Similarly, 100 % certainty for $n = 8$ is reached at $L = 2560$ for 100% certainty, while the pure sequence length of all permutations would be $\approx 262 * 10^3$, or for $n = 16$, 100 % certainty is reached at $L = 655,360$, with a pure sequence length of $\approx 17 * 10^9$. This is due to the fact that we are comparing any sequence in the strand with every other sequence.

These calculations allow us to draw two conclusions: The high probability of sequence reoccurrence already at low strand length for a short sequence, illustrates the difficulties of setting reliable "start" and "end" markers to a string of coded information. Wrongly interpreted positions could lead to shifts in the open reading frame (ORF) and render the information unusable. And thus, mere 8 or 16 bit encoding in DNA (corresponding to 4nt and 8nt sequences) might not to be sufficient enough for encoding larger snippets of information.

This calculation also has implications for the construction of DNA origami: The 7 nt or 8 nt snippets with which each staple connects to different scaffold parts are likely to have some reoccurrence somewhere else in the scaffold strand. The erroneous connection of these parts could potentially facilitate the folding into a wrong conformation. The fact that this is not the case illustrates the highly cooperative nature of the folding process, which will be discussed further below in section 2.3.3.

Hamming Distance & Mismatches

Hamming, 1950

The measure for the difference between two sequences is called the *Hamming Distance* (HD)[41]. The HD is a natural number, counting the differences between strand A and strand B. The difference can either be a switch of one base, its deletion, or its addition to or from the sequence. A switch of one base from A to B would thus amount to a HD of 1. As a more practical example, which was already discussed above, the HD of a human cell after one replication step is approximately 100. In this case, the use of Hamming Distance is almost identical to mutations.

The Hamming Distance also has implications for base pairing. Simply put, a dsDNA becomes more unstable the larger the HD between its two ssDNA becomes, or rather: the larger the HD between one ssDNA and the complement of the other ssDNA becomes. For short DNA sequences (of less than approximately 20 nt) a HD of one, can fully destabilize the dsDNA, especially if the mismatch is in the middle of the dsDNA. A mismatch in bases leads to unmatched bases, and thus, figuratively, to another end of the sequence, from which the DNA can unzip. If the mismatch is at the dsDNA's ends, the number of helix ends stays the same, just the sequence length is decreased by the amount of mismatches.

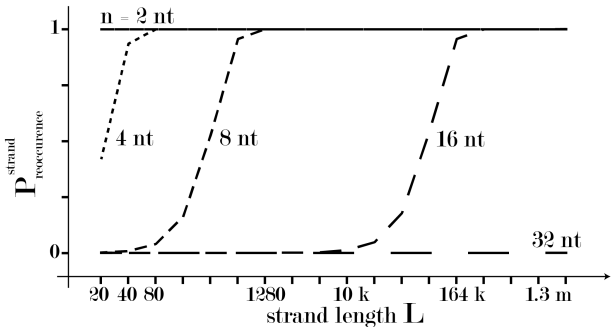

Figure 2.7: Probabilities for Sequence Reoccurrence

The probability that a sequence of length n reoccurs in a strand of length L is shown for different n on a logarithmic scale of L, given four possible letters in n and L. The probability for $n = 2$ is already 1 for $L = 20$. The probabilies for the other sequence lengths ($n = 4$, $n = 8$, and $n = 16$) only becomes 1 for longer strand lengths of $L = 160$, $L = 2560$, and $L = 655,360$. For the calculated L, the probability of a sequence of length $n = 32$ to reoccur stays ≈ 0. All curves follow the same sigmoidal trend.

2.3 DNA Nanotechnology

Several properties of DNA predestine it as a building material on the nanoscale. (1) The hybridization of DNA is very target-specific, depending on its sequence. (2) The experimenter can choose the DNA sequence at will, as the (bio)chemical synthesis of DNA is a well-established and cheap process, and (3) a plethora of modifications are easily implemented into the DNA during that process. Finally, (4) DNA is inherently biocompatible, as it is a biomolecule itself. Taken together, they make DNA a very attractive building material, the use of which had first been suggested over 40 years ago.

2.3.1 Structural DNA Nanotechnology

The utilization of these unique properties was first proposed by Nadrian "Ned" Seeman [10]. Inspired by M.C. Escher's woodcut "Depth" (Figure 2.8a), he sought to construct regular lattices from DNA, which would be able to host guest molecules, such as proteins, and with which one could perform crystallography. His theoretical paper, suggesting immobile DNA junctions to connect several DNA strands was published in 1982 in the journal "theoretical biology"[43], and laid the very foundation for the field of DNA nanotechnology [11].

Seeman, 1982

The immobilization of DNA junctions was fundamental for the development of structural DNA nanotechnology. DNA junctions are well known in biology: The replication fork (Figure 2.8b) is a three-armed junction, and the Holliday junction (Figure 2.8c), found in processes of genetic recombination and repair [44], is a four-armed junction. Both have in common that they occur in dynamic biological processes, with reoccurring sequences, in case of the replication fork, two identical DNAs are replicated from an identical template, and in case of the Holliday junction, two homologous dsDNAs recombine. Ned Seeman proposed the use of mutually exclusive DNA sequences for each arm of the junction, rendering the junction immobile, then further use it as a building block to create higher order constructions, see Figure 2.8d.

Holliday, 1964

In the following years, Ned Seeman published several papers on immobile DNA junctions, from the first immobile branched junction [45] up to 12-armed junctions [46], followed the construction of a small DNA cuboid [47], intricate catenanes [48], and infinite 2D crystals [49], see Figure 2.8d-e.

Kallenbach, 1983
Wang, 2007
Chen, 1991
Mao, 1997
Winfree, 1998

2.3.2 Dynamic DNA Nanotechnology

Parallel to the first works on structural DNA nanotechnology, the field of dynamic DNA nanotechnology developed. In the year 2000 toehold-mediated strand dis-

[10] *nota bene:* FISH was invented in the very same year by Langer-Safer *et al.* [42]

[11] or "sematomorphic science", as Ned Seeman phrased it. *semanto* describing the programmability of nucleic acids and *morphic*, describing the assembly process

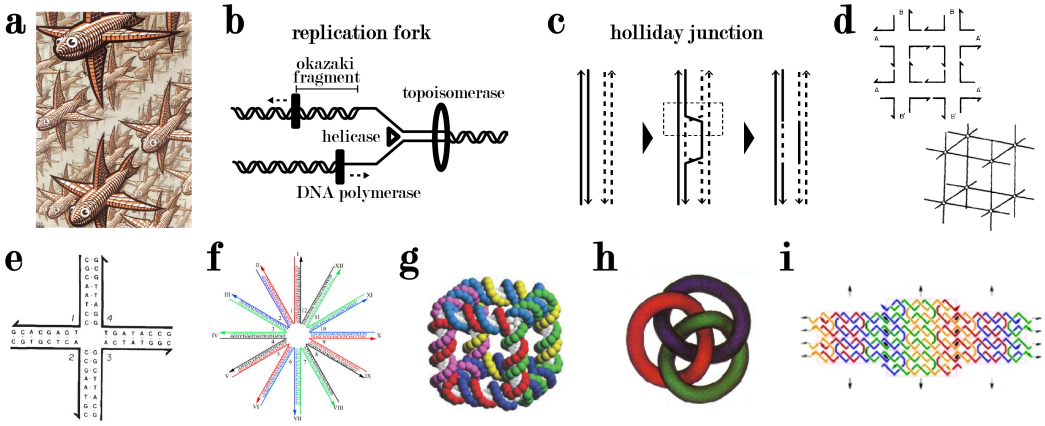

Figure 2.8: The Beginning of DNA Nanotechnology

(**a**) M.C. Eschers Woodcut *depth* (All M.C. Escher works © 2025 The M.C. Escher Company - the Netherlands. All rights reserved. Used by permission. www.mcescher.com) inspired Nadrian Seeman, who knew two distinct multi-armed DNA junctions from nature: (**b**) the replication fork and (**c**) the holliday junction. The replication fork is a DNA motif, which occurs during replication: A helicase splits the dsDNA strand into ssDNA, whose respective complement is then synthesized by a DNA polymerase. The DNA polymerase synthesizes from 5' to 3' ends, which leads to a continuous DNA polymerisation on the lower arm, but a fragmented (*Okazaki fragments*) polymerisation on the upper arm. The nicks in the backbone between Okazaki fragments are then closed by a ligase. (**c**) The Holliday junction[44] is a gene repair mechanism in case a DNA break occurs: Two homologous ssDNA strands partially switch their ssDNA partner, to recombine into two intact dsDNA strands. The Holliday junction in the schematic is indicated with a dotted box. Analogously to these mobile 3- and 4-armed junctions Nadrian Seeman proposed immobile Holliday junctions, which could be used to construct (**d**) larger lattices[43]. (**e**) The first immobile Holliday junction was then synthesized one year later [45], followed (in non-chronological order) by (**f**) a 12-armed junction[46], (**g**) a DNA cuboid[50], (**h**) topologically entangled DNA catenanes[48], and (**i**) 2D DNA crystals[49]. Panel (**d**) and (**e**) are adapted and reprinted with permission from ref [43], copyright 1982 Elsevier. Panel (**f**) is adapted and reprinted with permission from ref [46], copyright 2007 American Chemical Society. Panel (**g**) is adapted and reprinted with permission from [50], copyright 2003 Springer Nature Ltd. Panel (**h**) is adapted and reprinted with permission from ref [48], copyright 1997 Springer Nature Ltd. Panel (**i**) is adapted and reprinted with permission from ref [49], copyright 1998 Springer Nature Ltd.

Yurke, 2000 placement was developed [51], which sparked the use of DNA for logical operations on the nanoscale. Also in this period, hybridization chain reactions were developed Dirks, 2004 [52], used for amplification of signal in the fluorescence in situ hybridization (FISH) Langer-Safer, 1982 method [42]. In the following years, fueled by these structural and dynamic DNA nanotechnology developments, logically operating DNA devices [53] and walkers Douglas, 2012 [54] were constructed.

Sherman, 2004 Dynamic DNA nanotechnology is based on strand displacement. Strand displacement describes a process, where one single strand S of a dsDNA S:S* is displaced by a third strand, also complementary to S*. This process is already found in nature. For example, the above-discussed Holliday junctions invade and Holliday, 1964 displace another dsDNA as an intermediate step during recombination [44]. Another example is the invasion and displacement of dsDNA by the gRNA of the Jerkin, 2012 CRISPR-Cas9 complex [55]. The naturally occurring displacement reactions are taking place in the genome, for dynamic DNA nanotechnology, these principles can be applied to minimal systems made from oligomers.

The synthetic system is shown in Figure 2.9a: As an anchoring point for the incoming strand a so-called toehold region was added in the synthetic system: The incoming strand, consisting of the toehold t and the strand sequence S would first bind to the single-stranded complementary toehold t* on the duplex S:S*t* (ii.) and then start to displace the strand S (iii.). Next, the incoming strand St is replacing the bound strand S, which is not a driven process, but rather a stochastic zipping and unzipping process of both strands, where the strand St, has an advantage through its toehold and its lower free enthalpy value in the bound Srinivas, 2013 state [56]. When the strand displacement is completed, a duplex St:S*t* is formed (Figure 2.9 a, iv.), and the initially bound strand S is present as a single strand. In Figure 2.9b, the free energy landscape of this reaction is depicted: The initial binding of the strand St to the toehold, fixes the spatial position of the strand, which reduces the entropy in the system, and raises the free energy of the system. This presents an energy barrier for the start of the strand displacement reaction. The surrounding media provides the energy needed for the toehold binding.

2.3.3 DNA Origami

The field of DNA nanotechnology was revolutionized when Paul Rothemund in- Rothemund, 2006 troduced DNA Origami in 2006 [57] . Rothemund developed a new approach of constructing DNA nanoparticles, by designing a manyfold of short ssDNA *staple* strands, complementary to a long ssDNA *scaffold* strand. Each staple had multiple regions of 8-16 nt on the scaffold it is complementary to, bringing these scaffold parts in proximity as it binds to them, as depicted in Figure 2.10a. A whole set of staple strands would bind to every part of the scaffold and fold it into a fixed 2D or 3D structure. Rothemund demonstrated the versatility of this approach by showcasing several, almost arbitrary DNA origami structures, most famously the smiley face (Figure 2.10b).

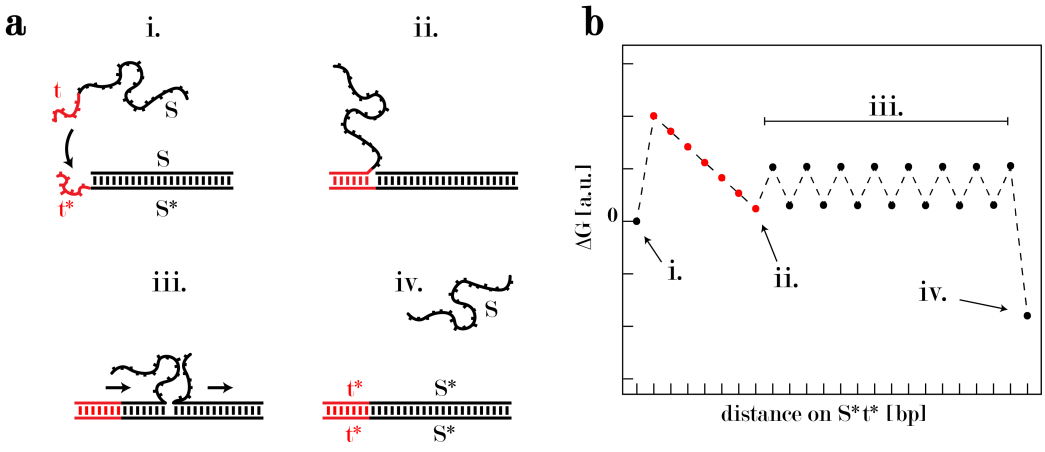

Figure 2.9: Toehold-Mediated Strand Displacement

(**a**) The principle of toehold-mediated strand displacement is shown: (i) A strand St is approaching a duplex made from strands S and strand S*t*, which are bound everywhere but at the toehold region t* of strand S*t*. (ii.) The strand St is binding with its toehold t to the ssDNA t* part of the duplex S:S*t* and (iii.) begins to displace the strand S. Finally (iv.), the strands St and S*t* form a full duplex and strand S is fully displaced. (**b**) The free energy landscape of a toehold-mediated strand displacement reaction: The relative free energy is shown on the ordinate and the position on the strand S*t* is given on the abscissa. The indicated steps i.-iv. correspond to the depicted states of the strand displacement in (**a**). The initial configuration (i.) is given as 0, from which the system needs to pay an entropic cost when strand St binds to the toehold. The binding to the toehold in sum lowers the free energy of the system (ii.) and the gradual displacement of strand S begins (iii.). The free energy is minimized when the amount of DNA bonds is maximized and strand S is fully displaced (iv.).

Until then, the construction of DNA nanoparticles was limited to small structures made from only a few DNA strands (see Figure 2.8), infinite structures, or
Shih, 2004 tailor-made dsDNA structures [58]. The DNA origami technique brought several improvements: it allowed for (1.) constructing arbitrary shapes with (2.) high yields and (3.) full addressability. Importantly, Rothemund provided a set of (4.) universal design rules, which essentially stayed the same until today. Further, using different-sized scaffold strands, the size of DNA origami promised to be scalable, while the use of scaffold strands reduced the amount of chemically synthesized DNA, thus also the monetary cost, by half.

In the following years, the laboratory of William Shih developed the DNA origami method further: They introduced multilayered origami structures in square
Ke, 2009 lattice [62] , packed hexagonal (ph) [63], and honeycomb (hc) lattice, as well as
Ke, 2012 wireframe (wf) structures [59], extending the construction possibilities into the
Douglas, 2009 third dimension (Figure 2.10c). And to those 3D structures curves and twists were
Dietz, 2009 introduced[60], see Figure 2.10d. This was made possible with the introduction
Douglas, 2009 of *caDNAno* [64], a computer-aided design software for DNA origami design. Another design approach for DNA origami, wireframe structures with dsDNA edges between vertices, with its specialized design software *vHelix* was created in the
Benson, 2015 Lab of Björn Högberg [61], such a wf structure is shown in Figure 2.10e.

DNA Origami Design

The construction of DNA origami follows several rules: Given the helicity of the DNA double helix, one strand in a DNA helix can only cross over to another DNA helix, when the backbones are in proximity. Thus, the positions of the crossovers are dictated by the angle of the backbone in the dsDNA helix, which in turn dictates the form of the lattice (see Figure 2.11). For the hc lattice, crossovers are positioned every 0.66 turns, after 7 bp, or 240° (one turn every 10.5 bp, or two turns after 21 bp, as discussed in 2.2.3). Similarly, the ph lattice introduces crossovers each 5/6 or 7/6 turns, each 9 bp or 13 bp. For the sq lattice, one full turn of the helix is approximated with 10.66 bp, resulting in 1.5 turns after 16 bp, or 0.75 after 8 bp [12]. The staples are designed in such a way that one subpart, complementary
Ke, 2012 to one part on the scaffold, is larger than the other subparts [65] . This means an increased stability of the larger part, resulting in a stability advantage over the same staples, bound to shorter parts, thus decreasing the chance of incorporating two staples and misfolding the origami.

The design of wireframe structures faces slightly different challenges. Wireframe structures are based on a triangular motif, as a stable and minimal motif. The resulting wireframe structures are formed by meshes of triangles. The edges of this mesh merge in vertices, with the number of edges converging in one vertex depending on the overall origami design, usually six edges. Translated to the wf

[12] this slight inaccuracy inadvertently leads to a global right-handed twist of the DNA origami structure

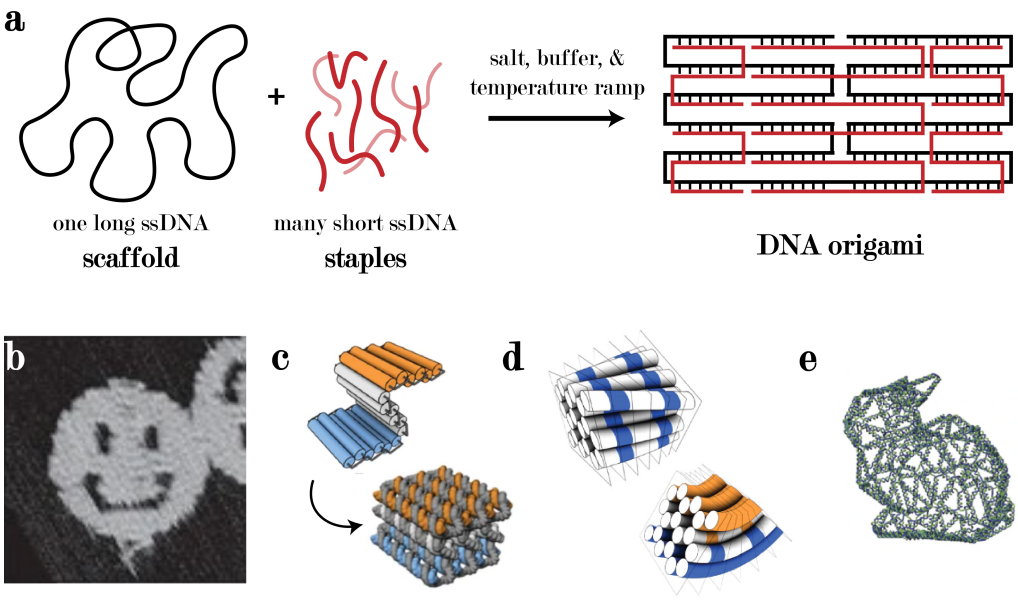

Figure 2.10: DNA Origami

(**a**) The DNA origami folding process: DNA origami are folded by the combination of a long ssDNA scaffold strand with a manifold of short ssDNA staple strands. To the DNA, salt and a buffer are added and the mixture is heated, then cooled over a long period of time. During this, the staples attach to their complementary parts on the scaffold, but since the staples are complementary to several, mutually distant parts on the scaffold, the binding process brings these scaffold parts into proximity and the 3D structure is *folded*. The final DNA origami product has the pre-programmed form, given by the staple sequences. (**b**) The famous smiley face DNA origami, one of the very first structures, taken from [57]. (**c**) A sketch of a 3D DNA origami in hc lattice, taken from [59]. (**d**) Curved and twisted DNA origami from [60], and (**e**) a DNA origami wireframe structure in form of a bunny [61]. Panel (**b**) is adapted and reprinted with permission from [57], copyright 2006 Springer Nature Ltd. Panel (**c**) is adapted and reprinted with permission from [59], copyright 2009 Springer Nature Ltd. Panel (**d**) is adapted and reprinted with permission from [60], copyright 2009 The American Association for the Advancement of Science. Panel (**e**) is adapted and reprinted with permission from [61], copyright 2015 Springer Nature Ltd.

origami structure, the edges are dsDNA strands and the vertices are multi-armed junctions (similar to Figure 2.11e). The junctions serve as cross-overs between the dsDNA edges, connecting different scaffold parts, similar to lattice-based DNA origami (with sq, hc, or ph lattices). But unlike in lattice-based DNA origami, these crossovers are much more flexible regarding their position in the structure, as well as their structural integrity. However, the largest design problem seems to be the layering of the scaffold, in a path through the wireframe mesh, in such a way that the edges only consist of one dsDNA. The software provided by Benson et al. [61] solves this *Eulerian Path* problem from a given mesh structure, routes the ssDNA scaffold through the structure, and fits the mesh to the physical structure of DNA. The finished wireframe structure is a direct output by the software, with near to no manual design process. Interestingly, the construction of wireframe structures from only oligomers required the insertion of four Thymine linkers for each edge on each vertex [66]. However, this does not seem to be a requirement for scaffolded wireframe origami [13].

Benson, 2015

Matthies, 2019

2.3.4 Simulation of DNA Nanostructures

To aid the construction of DNA nanostructures and model the behavior of DNA sequences, computer-based simulation programs are commonly used. The computational assessment of a designed DNA nanostructure or an ensemble of DNA strands before its experimental implementation is an important filter for erroneous systems. An ensemble of DNA strands can form a variety of hybridization connections, depending on the respective sequences [14]. Interestingly, already short complementary sequence parts form short-lived, hybridized states, which can impede their function in some experimental setups [15].

One of the most widely used computational suites, also employed in this dissertation, is *NUPACK*[68][69] . In principle, *NUPACK* calculates the ΔG for each pairing of the bases and from that the most probable pairing of the DNA strands in an ensemble. It incorporates several corrections for loops, bulges, or stacking effects to the algorithm, whose impact has been determined experimentally.

Zadeh, 2011

Fornace, 2022

Simulating ensembles of DNA strands gets more complex with the number of strands, their length, and the molecular detail of the simulation. Common atomistic simulation programs like NAMD (VMD) [70] are only able to simulate small DNA strands with reasonable computing power and expenditure of time. To still be able to simulate larger structures, their properties are simplified, reducing the computational effort tremendously. For example, *mrDNA* [71] works directly in combination with the NAMD program, as a coarse-grained simulation.

Phillips, 2020

Maffeo, 2020

The laboratory of Petr Šulc developed *oxDNA*, a suite for coarse-grained simulation of DNA and RNA structures [72] . Ease of implementation, handling [73]

Šulc, 2012

[13] Björn Högberg told me at the DNA29 conference

[14] which is an even larger issue in RNA structure determination, *cf.* Weck, 2020 [67]

[15] *e.g.* fluorescent imager probes for DNA-PAINT

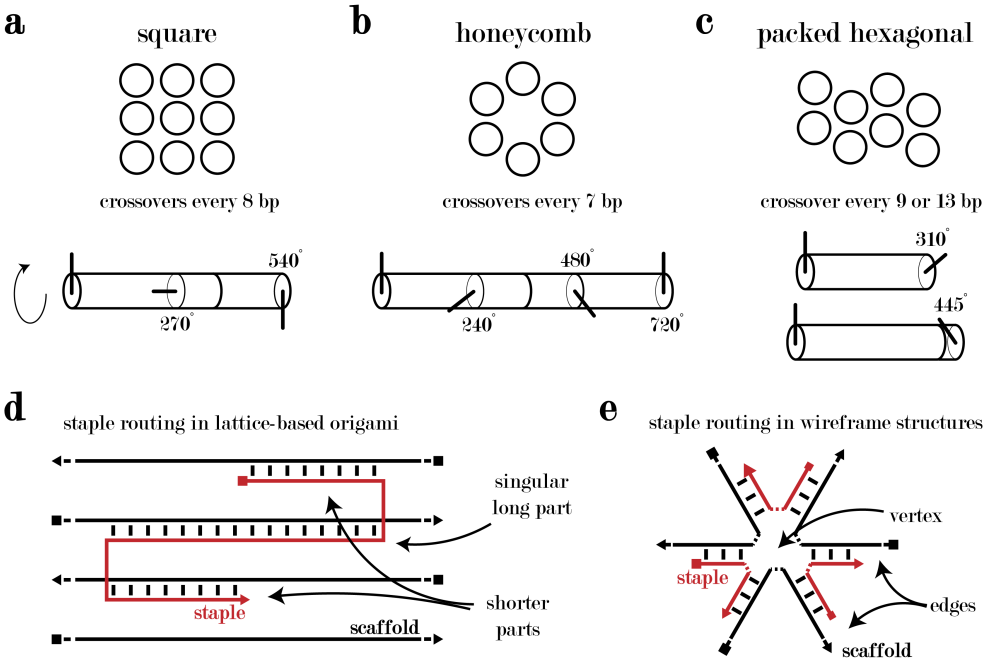

Figure 2.11: Design Principles for DNA Origami

The three lattice types of DNA origami are (**a**) square (sq) lattice, (**b**) honeycomb (hc) lattice, and (**c**) packed hexagonal (ph) lattice. For (**a**) the sq lattice, the B-DNA is assumed to perform one full turn every 10.66 bp, leading to possible crossovers every 8 bp, corresponding to 270° turns around the helix. (**b**) The honeycomb lattice assumes the literature value of 10.5 bp per turn, leading to crossovers every 7 bp, corresponding to 240° turns around the helix. The literature value of 10.5 bp is also assumed for the (**c**) packed hexagon lattice, which has crossovers either every 9 or every 13 bp, corresponding to 310° or 445° turns. (**d**) The staples (red) in lattice-based DNA origami are optimally designed to have a singular long part on the scaffold (black) and several shorter parts on other scaffold regions, giving the long part an advantage during the folding process. (**e**) The staple design in wireframe structures is centered around stabilizing the scaffold at the vertices, securing the mesh structure in place. Optional, unpaired linker regions [66] are indicated as dotted lines.

Poppleton, 2021

and the browser-based software oxView make it the most widely used platform for DNA origami design. It simplifies each DNA base with a few physical parameters (covalent backbone connection, steric hindrance, stacking, and hydrogen bonding), but simulate each strand in the DNA origami. This does not only give intel on the (variable) structure of the DNA origami, its fluctuations, potentially defective strands, or the effects of forces on the structure, but can also simulate strand-displacement interactions.

Kim, 2012
Lee, 2021
Truong-Quoc

Beside the already mentioned programs, the very first simulation program for DNA origami was *CanDo*[74] , developed by Do-Nyun Kim, who later went on to develop *SNUPI*[75] and *DEEP-SNUPI*[76] . DEEP-SNUPI is a machine-learning based approach, while CaDNAno and SNUPI are working with physical/mechanical models to simplify the properties of the whole DNA origami. Due to their short computation time, these can be used to iteratively design DNA origami structures.

2.3.5 Applications of DNA Nanotechnology

In the more than 40 years since DNA nanotechnology was conceived, it has been applied in several fields. The possibilities to adjust DNA nanostructures with nanometer precision, to modify them with chemical groups, and yields in the pmol range easily obtainable make it very appealing in disciplines relying on nanoscale control.

Park, 2008
Nykypanchuk, 2008
Kuzyk, 2012
Acuna, 2012
Jungmann, 2010
Dirks, 2004
Langer, 1982
Wang, 2023
Qian, 2011
Franco, 2011
Green, 2014

DNA nanotechnology was applied to probe systems of plasmonic particles and/or fluorophores. Plasmonic particles have been arranged, by utilizing the programmability of the DNA:DNA hybridization to form regular microscale crystal structures [77][78] . The addressability of DNA nanostructures was used to position nanometer-sized, and plasmonically active gold nanoparticles in a left- or right-handed chirality, which controlled the optical properties of the structures [79], see Figure 2.12a. DNA origami were also used to position two plasmonic nanoparticles with a 20 nm gap, creating a plasmonic hotspot in between, and enhancing the signal of a fluorophore in that hotspot more than 100 fold [80], see Figure 2.12b. The tunability of DNA has been used to construct short imager probes with tailored on- and off-blinking binding characteristics, enabling the super-resolution technique DNA-PAINT[81], shown in Figure 2.12c. As already mentioned in section 2.3.2, the hybridization chain reaction [52] was used to increase fluorescence signal in FISH probes [42], by concentrating the fluorescence signal This method was later also expanded to visualize DNA origami in tissue [82]. Ensembles of strand-displacement cascades were used to construct neural networks[83]. Dynamic DNA circuits can also regulate the production of downstream molecules, as RNA [84], or proteins [85].

DNA nanotechnology was also employed to probe forces in nanoscale systems. For this purpose three different effects have been exploited: The 3D arrangement of polymers at the nanoscale is statistical, and distributed over a multitude of spatial

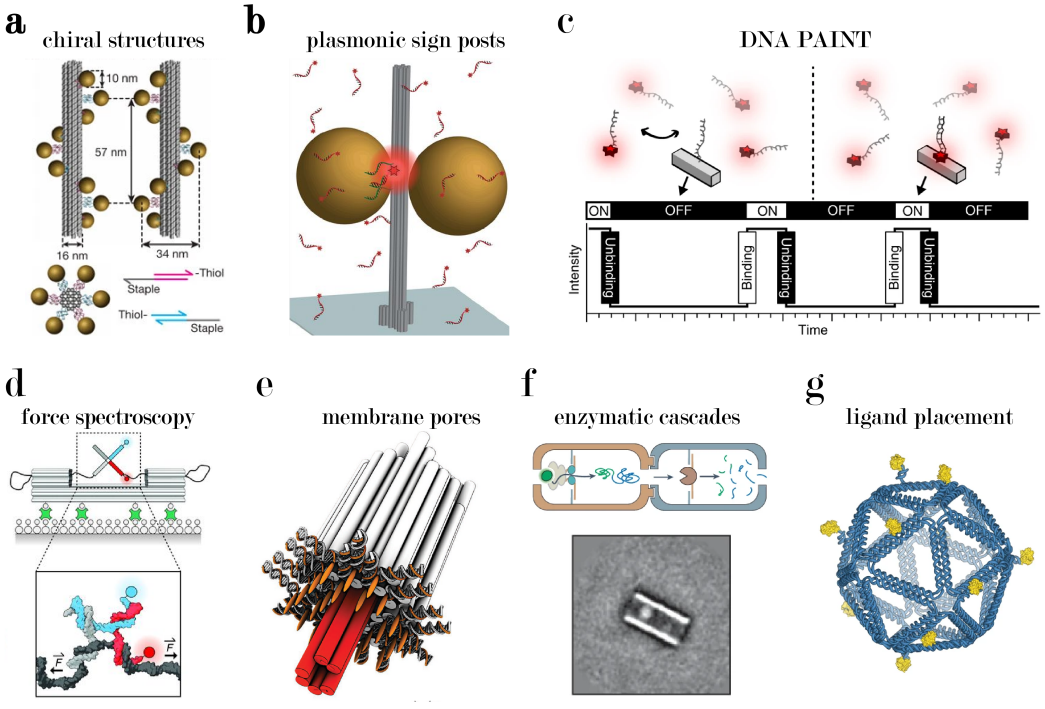

Figure 2.12: Applications of DNA Origami

Many applications for DNA origami developed over the past years, some of them are shown in this collage: (**a**) Plasmonic nanostructures, exhibiting chirality dependent optical dichroism[79]. (**b**) DNA origami antennas, increasing the fluorescence of target fluorophores in the plasmonic hotspot[80]. (**c**) The super-resolution microscopy method DNA PAINT [81][86]. (**d**) Multiplexed single-molecule force spectroscopy [87]. (**e**) Synthetic DNA origami membrane pores [88]. (**f**) DNA origami channels for proteins from unfoldase to protease in enzymatic cascades [89]. (**g**) Ligand placement for the probing of biological systems, here: B-cell activation [90]. Panel (**a**) is adapted and reprinted with permission from [79], copyright 2012 Springer Nature Ltd. Panel (**b**) is adapted and reprinted with permission from [80], copyright 2012 The American Association for the Advancement of Science. Panel (**c**) is adapted and reprinted with permission from [81], copyright 2010 Springer Nature Ltd. Panel (**d**) is adapted and reprinted with permission from [87], copyright 2016 The American Association for the Advancement of Science. Panel (**e**) is adapted and reprinted with permission from [88], copyright 2012 The American Association for the Advancement of Science. Panel (**f**) is adapted and reprinted with permission from [89], copyright 2024 Springer Nature Ltd. Panel (**g**) is adapted and reprinted with permission from [90], copyright 2020 Springer Nature Ltd.

conformations, underlying entropic principles. A displacement from statistically probable conformations results in a restoring force, acting against the displacement, which is purely driven by entropy, and thus this effect is called an *entropic spring*. This effect was harnessed by fixing a ssDNA to two points on a rigid DNA origami frame, which then was enacting (up to $\sim$ 12 pN) force on a protein, as *entropic spring* [87], see Figure 2.12d. In a different nanostructure, made from two arms, joined together with a hinge, torque was generated in a hinge region, in combination with a repulsive force from the two negatively charged arms, and thus was able to enact soft forces of $\sim$ 1.2 pN to elucidate histone stacking [91] A different way of generating forces on the nanoscale is with DNA hybridization. The hybridization of two ssDNA to one dsDNA leads to a straightening of the polymer, an extension in one dimension and thus enacts a force between its two ends[92][93]. Further, a plethora of functional molecules can be incorporated in a DNA origami structure, which change configuration, thus DNA origami structure, and ultimately are able to enact a force. This has been done with light-sensitive molecules[94] , pH-responsive components [95] , or salt concentration-dependent mechanisms [96] .

Nickels, 2016
Funke, 2016
Mills, 2022
Chung, 2024
Kuzyk, 2016
Karna, 2021

Besides the already discussed uses, DNA origami has also been used as a framework for a plethora of synthetic systems. Their comparably large size (almost 100 nm x 100 nm for 2D structures, or several hundred nm for 1D structures) in connection with their arbitrary shape and addressability allow DNA origami to assemble guest molecules with unparalleled precision. In this way, DNA origami were used as molds in which gold nanoparticles (AuNP) were grown, controlling size and shape of the nanoparticle ingot[97][98] . Further, DNA origami were used to position a variety of other guest molecules, such as polymers [99] , liposomes [100], protein capsules [101], or to graft DNA oligomers precisely onto the surface of gold nanoparticles [102].

Gerling, 2015
Helmi, 2014
Sun, 2014
Knudsen, 2015
Yang, 2016

The combination of DNA nanotechnology and lipid vesicles was further explored by the construction of artificial lipid membrane channels [88] in lipid vesicles, shown in Figure 2.12e. Lipid vesicles were found to be sculptured by DNA devices attached to their surface [103] and on the surface of planar 2D lipids DNA origami can diffuse and assemble into higher-order structures[104], even driven by motor-molecules[105].

Seitz, 2023
Edwardson, 2016
Langecker, 2012
Franquellim, 2018
Suzuki, 2015

DNA has a high information density, predisposing it as an information storage medium. As already discussed in section 2.2.4, the information density in the DNA is double the number of bits per unit as in silicon-based data storage. This allowed researchers to store 2.1 petabytes per gram of DNA [35] or 5.5 gram per mm^3[106]. The amount of data can also be increased by additional techniques like simultaneously encoding in DNA methylation patterns [107].

Ramm, 2021
Erlich, 2007
Church, 2012
Zhang, 2024

Interactions between proteins occur on the nanoscale, and DNA nanotechnology has been employed to probe biological systems. DNA nanostructures were used to assemble enzymes in a proximal arrangement, increasing the efficiency of the enzymatic cascade of horseradish peroxidase and glucose oxidase [108] . Sim-

Wilner, 2009

ilarly, DNA origami compartments were arranged to channel the functions of the p97 unfoldase and the protease α-chymotrypsin to increase the efficiency of protein degradation [89] , see Figure 2.12f. The influence of protein positioning on biological systems was also probed with DNA nanotechnology. The strength of motor proteins in a *tug-of-war* was accessed by their positioning on DNA origami [109]. Already in 2014, ligands were precisely positioned on DNA origami "calipers" and their interactions with their respective receptors were analyzed as functions of the nanoscale positioning[110]. With DNA origami platforms, several ligand-receptor interactions were examined for their dependencies on valency and distances: The avidity of Antibodies was examined depending on the distance of two Antigens on a DNA origami[111], the activation of B-cells with HIV antigens [90] (Figure 2.12g), or SARS-Cov-2 [112], and the activation of T-cells[113] was examined, to name a few.

Huang, 2024
Derr, 2012
Shaw, 2014
Shaw, 2019
Veneziano, 2020
Wamhoff, 2024
Hellmeier, 2021

Chapter 3

Modular Design of DNA Origami Nanostructures

In this chapter, modular design of DNA nanostructures is described. To decrease the cost and increase the versatility of DNA origami assemblies, two methods of modularity are incorporated into a single DNA origami, dubbed moDON (modular DNA origami nanostructure). These methods adapt and expand existing connection methods for the formation of multimeric assemblies from DNA origami monomers. Each method of modularity is introduced separately, used to construct precise and large DNA origami assemblies, and their assembly kinetics are analyzed. Finally, both methods are combined to construct even larger assemblies, as well as activate assembly processes parallelly or selectively.
The work in this chapter was also published in the journal *Nature Communication* in 2025, here as reference [114]:

J.M. Weck*, *A. Heuer-Jungemann** *Fully Addressable Designer Superstructures Assembled from One Single Modular DNA Origami, Nature Communications, 16, 1556, 2025*

3.1 Introduction: Size Limitations

DNA origami is arguably the most powerful tool to create precise nanoscale objects. The synthesis itself is comparably quick and easy and results in billions of identical structures. Each of the structures has the same, basepair-precise 3D structure with exactly positioned modifications. The extent of control over shape and modifications on the nanoscale is also unparalleled with the DNA origami method, but it is limited. Single DNA origami can only reach a certain size, which limits the area on which the nanoscale control can be enacted. A central aim in the field of DNA nanotechnology is to expand the area of nanometer precise control by expanding the size of DNA origami.

While DNA origami is unparalleled in its versatility of constructing nanoscale shapes, the size of DNA origami themselves is limited by the size of the scaffold. The scaffold is a long, circular ssDNA, extracted from the phage M13mp18 [1] and has a length of 7249nt, as already described in section 2.3.3. Consequently, a DNA origami structure made with this scaffold is limited to just below 5 MDa (7249 bp, times 650 kDa/bp), or approximately 5,000 nm^2 (2 nm DNA diameter, times 7249 bp, times 0.34 nm/bp). Effectively, these structures are larger: Often, additional ssDNA sequences are implemented to passivate a structure against unwanted interactions, or short strands for attachment of further components, increasing the number of bases in the DNA origami. Also, caused by the repulsive electrostatic forces between the backbone, the DNA strands in DNA origami are not seamlessly tight close to another, but rather have some space inbetween, resulting in effectively larger structures[2].

DSMZ

The 7249 nt long scaffold is already an extension of the wt genome of 6407 nt [115]. Later, inserts were incorporated into the M13mp18 sequence to increase the genome length, with the largest scaffold being that from the p8634 phage (see also section A.1.1). Further enlargement of the phage genome increases the chances of the full elimination of the insert. Thus, the enlargement strategy for the scaffold breaks down at approximately 20 % additional DNA. This necessitates other ways of increasing the size of DNA origami, and extending the control over the nanosphere.

3.1.1 Prior Methods

In the past, there were several approaches to increase the scope of nanoscale control. Alternative DNA assembly methods were conceived, scaffolds were modulated with much more resourceful approaches, and DNA origami multimer assemblies were constructed with several different approaches.

Wei, 2012

An alternative to DNA origami assembly, even slightly more controllable, are single-stranded tiles (SST)[116]. Here, several short ssDNA strands come together without a scaffold to form large, pre-defined structures which are easily variable through omission and modification of single strands and sets of strands. The extension into 3D [117] allowed for the construction of very large structures, reaching GDa sizes [118].

Ke, 2012

Ong, 2017

While being the most variable approach to design at the nanoscale, SST have other downsides. Firstly, they need a large number of single strands, which all need to be of a high purity, resulting in a high monetary price. Even more since no scaffold strand is used, which doubles the oligomers needed for a structure of the

[1] coincidentally, M13mp18 was constructed and expressed first in the laboratory of Peter Hans Hofschneider, director *emeritus* at the very institute this doctoral thesis was written

[2] *cf.* in chapter 4 the size of the rro origami is determined to be 87x64 nm, resulting in more than 5,000 nm^2, while not even using the whole scaffold. More so, wireframe structures are designed with especially large gaps between their helices

same size as a DNA origami. For example, the largest structure in reference [118] was composed of 30,000 single strands, amounting to 150,000 USD in purchase. Additionally, the yield for these structures is comparably low, not reaching 30 %, with most structures' yields below 20 %, or single-digit[117]. Ong, 2017 Ke, 2012

Scaffold Size Increase

A different approach for increasing the size of DNA origami is increasing the size of the scaffold. As already described above, the phage M13 itself can only handle minute enlargements of its genome. Therefore, other methods were used to increase the (effective) scaffold length.

For the creation of longer scaffolds, PCR of random sequences can be used. PCR is a well-established and easy-to-use method [119] to multiply the number of DNA strands and also edit and mutate the sequences in the process[120][121]. The scaffold length can be increased and a custom sequence can be designed with this[122] method, reaching 26 kb[123], but with two downsides: The process results in dsDNA, not the ssDNA needed for the synthesis of DNA origami, and secondly, the amount of scaffold synthesized in the process is very low. While the issue can be handled with tricks during the purification process, the second remains a limiting factor. Saiki, 1985 Higuchi, 1988 Ho, 1989 Pound, 2009 Zhang, 2012

To create custom scaffolds, microbiological systems with helper plasmids[124], or helper phages[125] were employed. Here, the information for the proteins and the packing signal, usually encoded in the same circular phage genome, are split. The helper carries the information for protein synthesis, but the packing signal is on a second strand, only that strand is then packed into the phage hull and secreted. Besides the packing signal, the second strand can have any sequence possible. Dente, 1983 Messing, 1983

The helper approach allowed the production of a plethora of different scaffolds on a large scale. While the lab or Shawn Douglas was able to create high-quality scaffolds up to the size of 10,000 nt[126], others expanded the reach of this approach to create ssDNA scaffolds larger than 30,000 nt[127]. Similarly, Engelhardt *et al.*[128] created a set of orthogonal scaffolds, *i.e.* scaffolds with highly unique sequences, with which different origami, or compounds of them can be folded at the same time. Recently, this system was again simplified by incorporating the helper strand directly into the bacterial genome, constructing a helper *strain*[129]. Nafisi, 2018 Chen, 2018 Engelhardt, 2019 Shen, 2024

LaBean and coworkers on the other hand, constructed a λ-M13 hybrid scaffold, the largest to date[130]. The constructed scaffold had over 50,000 nt and folded together with more than 1,600 staples into a 33 MDa-sized DNA origami. Marchi, 2014

Increasing scaffold size resulted in increased DNA origami size. However, the yields achieved with the enlarged scaffolds were rather underwhelming. While Nafisi *et al.*[126] was able to achieve overall good yields with just a marginally enlarged scaffold, the 30,000 nt scaffold of Chen *et al.*[127] showed many byproducts in AGE analysis, which would result in reduced yield. This was the same when producing the scaffold via PCR[123]. Similarly, the yield of compound structures Nafisi, 2018 Chen, 2018 Zhang, 2012

constructed with orthogonal scaffolds, decreased dramatically beginning with the third, ≈ 7,500 nt long scaffold in the reaction mixture, as the products started to aggregate[131]. As discussed in section 2.2.4, the approach of scaffold elongation is partially limited by sequence reoccurrence in the ssDNA scaffold.

Engelhardt, 2019

Multimeric Assemblies

A different approach is multimeric *assembly*. Here, several monomeric DNA origami get connected to form large, multimeric superstructures. The connections between DNA origami can be constructed in several ways. Usually, these connections are based on the base-pairing behavior of DNA. The base-pairing of DNA has already been used for a long time to join single DNA snippets and, for example, create composite plasmids. However, DNA origami is much more complex than single DNA strands, which results in a plethora of different methods for the implementation of DNA origami connections.

For the connection of DNA origami, different approaches have to be differentiated. There are *two-strand* systems, where two ssDNA strands with complementary sequences on different origami can be used to join them. For example, Tigges *et al.* created a simple DNA origami block with ssDNA overhangs protruding at opposing ends of the structure[132]. Upon re-annealing of these structures, the complementary ssDNA overhangs hybridized and the blocks polymerized into long filaments. For small tiles and if the helical pacing is carefully taken care of, this approach can yield vary large superstructures[49][133][134].

Tigges, 2016

Winfree, 1998

Then there are *pseudo-scaffold* approaches to DNA origami connections. For those connections, the pacing of the staple and scaffold between structures is kept and small staples are added that form pseudo-scaffolds between them. This approach can easily be applied to structures in 2D[135] or structures in 3D[136]. Similarly, frames made from long scaffolds have also been used to assemble DNA origami into larger structures[137]. This method creates positionally accurate and strong connections between different DNA origami. On the other hand, it requires a large number of unique DNA strands, to ensure accurate connectivity.

Rothemund, 2004
Zheng, 2009
Jungmann, 2011
Zhou, 2022
Zhao, 2011

Lastly, there are *three-strand* systems, where ssDNA strands on two different DNA origami are connected via a third, partially complementary strand. This was done in several systems with a variety of DNA origami[138][139][140][141]. This method suffers from similar problems as the pseudo-scaffold approach: To accurately connect the DNA origami, each connection point needs to be unique, which requires unique DNA strands. This results in an extensive use of unique DNA strands for each unique connection.

Zhou, 2018
Wickham, 2020
Kim, 2023
Luu, 2024

The advantage of three-strand systems (and to some degree of two-strand systems) is their reconfigurability. The third strand, the connector, with an added toehold region can easily be displaced by an invader strand, following the principle of toehold-mediated strand displacement introduced in section 2.3.2. Then again, the connection can be replenished, by adding additional connector strands. This can also be coupled to additional, dynamic networks[142][143]. But the larger

Jahnke, 2023
Stenke, 2024

the number of unique DNA strands in the system, the more numerous the unique invader strands, the higher the chance of unwanted, off-target interactions.

This illustrates the need for an approach to connectivity, that has the advantages of the sticky-end connections, while removing their downsides. Such a connection would need to be: rigid, dynamically alterable, stoichometrically correct, and constructed with as few unique DNA sequences, and as few DNA strands possible, to keep both cost and undesired interactions low, and a high dynamic fidelity. In section 3.3 such a connection, fulfilling these requirements, was constructed.

Connections via Third Molecules

Also, DNA origami can be jointed by other, third molecules. In the past, the stable interactions of peptide coiled-coil dimers were used to polymerize DNA origami, they are connected to[144][145]. Another approach was the use of photosensitive molecules to link otherwise inert polyA tails[146]. A major downside of these kinds of connections is the extremely low control over them.

Jin, 2019
Buchberger, 2020
Berg, 2023

Additional Shape-Complementarity

An additional layer of specificity can be added to nanoscale assemblies by the shape complementarity of monomers. Analogously to the shape-complementarity of the Watson-Crick base-pairing in dsDNA, the DNA origami building blocks can be designed to be shape-complementary, too. This was already done in 2012 for 2D assemblies[147], where larger multimers were constructed, using *jigsaw* structures. This was then further extended to 3D by Gerling *et al.* in 2015 [96]. The authors designed shape-complementary 2D connection sites one DNA-layer deep in a 3D DNA origami. These carvings into the structure are called *protrusions* and *indentations*.

Rajendran, 2012
Gerling, 2015

With this additional layer of shape complementarity, the specificity of each connection increases significantly. This specificity was already enough for Gerling *et al.* to construct multimeric structures, without Watson-Crick basepairing, just by blunt-end interactions[3]. Later, this method was used to construct GDa-sized structures by Wagenbauer *et al.*[148] or Sigl *et al.*[149], the latter in combination with base-pairing.

Wagenbauer, 2017
Sigl, 2021

The DNA origami are joint very tightly with these connections, which allows the construction of seamless, multimeric structures. These tight assemblies are most attractive for structures that require controlled porosity, to use, for example, for creating controlled enzymatic cascades[89], or the molding of inorganic particles[150]. Similarly, these connections are attractive for other nanoscale systems, which rely on the exact positioning of modifications over larger areas, such

Huang, 2024
Ye, 2021

[3] which also had been employed before as a method for connecting DNA strands in molecular biology

Zeng, 2024
Song, 2024

as CpG sites[151] for immune modulation or plasmonic assemblies with many components[152].

Wagenbauer, 2017

However, the structures used in these shape-complementary assemblies only have one shape and thus only one set of connections. Multimeric structures need to be constructed either by using periodic motifs[148] or with a large number of different DNA origami. This either reduces the control over the structure and addressability of the assemblies, or increases both monetary and time costs for this approach, as each DNA origami An approach to decrease the cost for these assemblies, while maintaining the tight, highly specific connections, is needed. In section 3.2 such a method is developed.

3.1.2 Modularity

Modularity describes a universal construction approach. Modularity breaks down larger structures or processes into smaller *modules*, which can be interchanged and individually altered, without affecting the other modules. The concept of modularity finds itself employed in many fields of engineering and science.

Standardized parts are an early form of modular design. This became increasingly important with more complex supply chains, starting with the Industrial Revolution. Standardized machine parts, starting with screws and nuts helped to expedite the development of machines and manufacturing processes. Further, shipping containers are standardized and can be used modularly on ships, trains, or trucks.

Civil Engineering uses modules to construct buildings at low cost. Most famously the *Plattenbau* (German for *slab construction*) buildings, consist of a multitude of smaller modules. Those modules are constructed in a central facility and then shipped to and erected on site. This allows for the quick and inexpensive construction[4].

Computer code is also often written in modular parts, called object-oriented programming. Similarly, the hardware for computer systems and electronics is modular; CPU, GPU, and storage being freely combinable and thus upgradeable.

Genes are also constructed modularly. The content in the open reading frame in eukaryotes or the operon in prokaryotes are modules that can be changed independently from the surrounding genes. Similarly, the regulatory parts (enhancers, repressors, silencers, promoters, operators) can be changed independently, by changing the respective DNA sequence. Larger genetic constructs, such as plasmids, are also modular because they can be read in the prokaryote, or transferred between cells, without affecting the chromosomal DNA.

[4] at the expense of questionable aesthetics

Modularity on the Nanoscale

Modularity on the nanoscale can only be achieved with high programmability. Therefore, methods of nanoscale construction that rely on the unstructured, bulk addition of atoms or molecules to form larger assemblies, such as gold nanoparticle (AuNP) or silica bead synthesis, are fully inept for modular approaches.

DNA nanotechnology, on the other hand, is highly programmable. The modular composition of genes was already mentioned above. It relies on the highly programmable nature of DNA and the already existing biomolecular tools in organisms, to manipulate it. Since DNA nanostructures rely on the same base-pairing, they are similarly programmable and can thus be designed modularly.

The simplest approach to modular design of DNA nanostructures is the use of different DNA sequences for different positions in the structure and connections of structures. An good example for this is the work of Zhou *et al.*[138]: The connections between the DNA origami monomers are simply made from different sets of DNA oligomers, of different sequences, and thus modules that can be interchanged freely. This approach is very straightforward, but, as already mentioned above, the difficulty lies in the minimization of the involved DNA strands, while keeping the connections rigid. Section 3.3 deals with exactly this problem. Zhou, 2018

The modular design of shape complementarities is facing different problems. The shape complementarities are designed into the DNA origami structure and are therefore scaffolded. The scaffold is routed through the DNA origami and alteration of its path would change the attachment position of the staples, and thus destroy the 3D structure. Thus, an approach that allows for modular scaffold routing is needed. Such an approach is developed in section 3.2.

3.2 Method I: Modular Scaffold Routing

To construct protrusions and indentations with exchangeable profiles, the challenge of the unalterable scaffold routing had to be overcome For this, a re-routable scaffold design was devised resulting in modular connection sites. In the following section, the design of the modular protrusion and indentation sites is described, then an analysis of the assembly and disassembly kinetics is given and finally a plethora of superstructures are constructed in simple and quick one-pot connections.

3.2.1 Design and Construction

The modular scaffold routing is based on the split between a stable *core* and a variable *shell* structure. In Figure B.1, the core structure is depicted in black, and the alterable scaffold loops are shown in green. At first, the core structure is layered evenly through the DNA origami, then it follows a different path, to accommodate for the re-routable scaffold loops: The two parts of the scaffold

split, one further follows the even layering, and the other forms the modular shell (shown as green loops). Finally, both scaffold parts join together at the end of the structure layout. The short (116 nt) scaffold loop is hidden inside the 6HB-sized cavity in the middle of the moDON.

The modular shell consists of six scaffold loops of a fixed size. For clarity, the loops will be named after the number of the helix in the core structure they attach to: These helices were dubbed *hinge helix* (HH) and since they are in the outermost layer of the DNA origami, with four structural helices between them, they have the numbers 50, 55, 60, 65, 70, and 75, as depicted in Figure B.1.

For those loops, sprouting from the HH, different scaffold (and thus also staple) routings were created, making the structure modular. Each protrusion-indentation connection site of the origami is composed of two parts, and *vice versa* each variable loop is part in two connection sites. This is depicted in Figure 3.1b and c. The reconfiguration of the respective connections site is then done by reconfiguring one or two scaffold loops for each structure: This approach leads to an asymmetry at the distribution of reconfigurations across the connections sites[5]. Thus HH 65 has only one configuration, while HH 50 has four. In total, 13 different configurations for the modular xy-connections were constructed, which can morph the 12 different connection sites of the moDON, shown in Figure 3.1c.

Gerling, 2015

The protrusion and indentations were designed to be orthogonal to all other potential connection sites. Firstly, the rules laid out in reference[96] were adapted, *i.e.* minimal size of 21 nt per helix and no scaffold cross-overs directly at the helix's ends. Secondly, special attention was paid to avoid point symmetries in the connection sites, which would lead to self-complementarity but at 180° changed connection angle. Thirdly, all permutations of connection sites were checked for undesired matching and iteratively optimized.

To increase the strength and the specificity of the connections, staple intrusions were designed for each site. The staple intrusions consist of elongated staples of one connection site, that would connect into staple omissions on the scaffold of the complementary site. Four variations of this were constructed; a blunt end connector, 2 nt staple intrusions, as well as 4 nt and 6 nt staple intrusions. The connection sites could also be passivated by the elongation of the staple with five single-stranded thymines. These would then constitute a barrier, both through their sequence *un*specificity and steric hindrance.

The full scaffold and staple outlines are found as images of the caDNAno software in Figures B.2 and B.3[6].

[5] A clarifying example: If connection site α is reconfigured into δ, its left part (from HH 50) is changed, and the right part (HH 55) is not. The complementary connection site α^* then also needs to change the left part (HH 70), and keep the right part (HH 65) constant. Since this is a mirror-symmetric constraint and the structure is point-symmetric, an asymmetry arises in the connection sites.

[6] and as JSON files on nanobase.org/structure/263

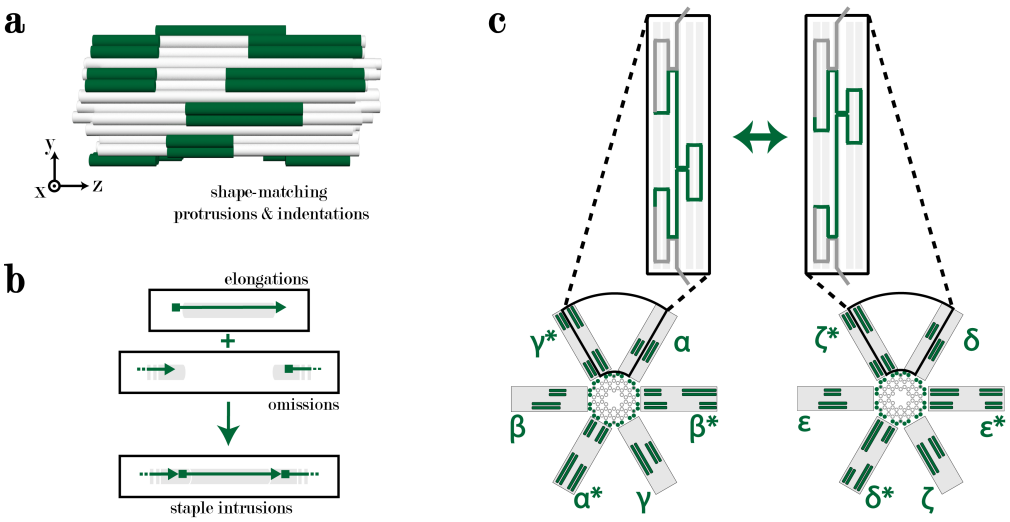

Figure 3.1: Design of the Modular Protrusions & Indentations

(**a**) Side-view of the moDON with the connection sites as protrusion and indentations colored in green. (**b**) Staple elongations and omissions of protrusions and indentations come together to create strong and specific connections. (**c**) Conformations one ($\alpha\beta\gamma$) and two ($\delta\epsilon\zeta$) and the reconfiguration of the scaffold at the shell. Panels were partially adapted and reprinted with permission from [114], copyright 2025 Springer Nature Ltd.

Structure Analysis & Folding

To access the structural stability, the moDON was simulated with the oxDNA software. Both configurations were simulated separately as described in A.1.17. Both configurations showed great structural stability and no errors or defects (such as dissociating staples or misaligned parts), as seen in Figures B.4 and B.5. RMSF analysis showed low thermal fluctuations, which is a positive trait for the connection sites depending on rigid sites.

The moDON structure folded exceptionally well. The DNA origami folded with quantitative yield over a vast array of $MgCl_2$ (see Figure B.6) and also NaCl conditions (the latter are not presented here). This again is even more surprising, when considering that it was folded with an in-house produced and only rudimentary quality-controlled p8634 scaffold[7]. The structure folded with as low as 2-fold staple excess, and the folding time could be reduced to approximately 3 hours (h) through isothermal folding[8].

The dimensions of the moDON were analyzed to assess the folding quality. The length and width dimensions of more than one hundred structures were extracted from TEM micrographs (Figure B.7). The average length was found to be approximately 43 nm, and the average width 24.5 nm. This is very close, but somewhat larger than the theoretical values, of 42.5 nm and 24.0 nm, where the length is calculated from the number of bp along the origami's side (125 bp), and the width is calculated from the distances in the honeycomb lattice. This can be an effect of measurement errors or rather explained by the increased helix distance in DNA origami, as already observed before[153].

Fischer, 2016

3.2.2 Assembly & Disassembly Characteristics

Next, the kinetics behind the moDONs xy-connections were examined. The dependence of the dimerization rate on several parameters was tested: $MgCl_2$ concentration, staple insertion length, and temperature.

Assembly Kinetics

Firstly, a parameter tensor of time, $MgCl_2$ concentration, and intrusion length were tested. The dimerization status was analyzed by AGE, as normalized ratio between the intensity values of monomer and dimer bands. As seen in Figure 3.2a, the $MgCl_2$ concentrations played a major role in the assembly of the protrusion-indentation connections of the moDON. This was seen already after 30 minutes (min) of incubation: The dimerization of the -relatively low- 20 mM $MgCl_2$, was

[7] from which it is known that a few point-mutations have snuck into the sequence, increasing the *Hamming Distance*. But, as I found out for a different project, which is not discussed within the scope of this dissertation, DNA origami can fold beautifully with ≈ 30 sequence mismatches, and maybe even more

[8] this was not further optimized: potentially, the folding can be even quicker

only around 10 %, while double the amount of $MgCl_2$ more than doubled the dimer fraction, and again doubling the amount of $MgCl_2$ yielded more than 60 % dimers in the first 30 min of the experiment. Longer incubation times increased the amount of dimers for all $MgCl_2$ concentrations. However, there were no qualitative differences in the kinetics between samples supplemented with 80 mM and those with double the amount, 160 mM $MgCl_2$. 80 and 160 mM $MgCl_2$ samples reached full dimerization already after 8 h, while samples with 40 mM $MgCl_2$ were only fully dimerized after in the tests that ran for 24 h. The samples with only 20 mM $MgCl_2$ only dimerized slowly and reached only $\approx$ 70 % dimerization even after 24 h of incubation.

When comparing the kinetics for different staple intrusion lengths, there was no qualitative difference: The dimerization increased with increasing $MgCl_2$ concentration and over time, but without major differences, between 80 and 160 mM of $MgCl_2$.

Separately, the blunt end connections were tested. As depicted in Figure B.8, the dimerization after 24 h with blunt ends was even more dependent on the $MgCl_2$ concentration, as for connections with staple intrusions. 40 mM $MgCl_2$, which was sufficient to fully dimerize all structures with staple intrusions, was not enough for the blunt end connections. 80 or 160 mM $MgCl_2$ did only yield some, but far from full dimerization in the samples after 24 h. Even though we found the blunt-end connections unfit for our aims in this work, an increased number of helices in the indentations and protrusions, also by an additional helix layer for the connection, can apparently increase the binding stability significantly.

Next, the temperature dependence of the xy-assembly was analyzed. Exemplarily, this was done for origami with 2 nt staple intrusions at 40 mM $MgCl_2$, since for these paramters a large range of dimerization states were observed in the prior experiments. The DNA origami were incubated for different time intervals at either 4 °C, 20 °C (RT), or 37 °C. As depicted in Figure 3.2c, we did not observe qualitative differences in the dimerization kinetics. The dimerization curves for all temperatures were approximately the same, following an almost linear trend.

Disassembly Kinetics

After testing the assembly kinetics, we pivoted to analyze the disassembly of our connections. Already in prior work[96], $MgCl_2$ reduction was used to disassemble the multimers again. Gerling, 2015

Different from Gerling *et al.* though, we varied the binding strength of the connections with the intrusion lengths. Analogously to the parameter tensor of time, $MgCl_2$ concentration, and intrusion length above, we tested these parameters for the disassembly of the xy-connections, too.

As depicted in Figure 3.2b, the disassembly process was even more governed by the intrusion lengths, than the $MgCl_2$ concentration: While for 2 nt staple intrusion, a reduction from 40 mM to 20 mM did not dissolve the connections over the observed time course of 8 h, a reduction to 10 mM slowly decreased the

amount of dimers to approximately 80 % after 8 h. When the $MgCl_2$ concentration was reduced to 5 mM, on the other hand, the dimers dissociated almost instantly. Already at the very first measuring point, after 30 min, there were no dimers left in the sample.

When the number of nucleotides of the staple intrusions was varied, the kinetics changed. A reduction to 20 or 10 mM $MgCl_2$ did not disassemble dimers connected with 4 nt intrusions, at least not in the 8 h of the experiment. When the $MgCl_2$ concentration was reduced to 5 mM, the connections held by 4 nt staple intrusions broke and the amount of dimers decreased linearly, to a total of 60-70 % after 8 h. This decrease in the dimer fraction (at 5 mM $MgCl_2$) was also observed for staple intrusions of 6 nt length, but the connections broke much slower, and after 8 h there were still approximately 90 % dimers. The amount of dimers for 20 and 10 nM $MgCl_2$ and 6 nt remained stable at 100 % for the whole length of the experiment, just as for 4 nt intrusion lengths. Further, the temperature played a role in the disassembly, as depicted in Figure 3.5d. Low and moderate temperatures of 4 °C or 20 °C lead to slower disassembly of the moDON, than the elevated temperature of 37 °C.

Summarizing, the kinetics of the xy-connections were found to be mainly dependent on the $MgCl_2$ concentration in assembly, and also on staple intrusion length in disassembly. Having analyzed the kinetics behind the xy-assemblies, these were then used to construct large, multimeric assemblies.

3.2.3 Multimeric Assemblies

The modular xy-connections allowed the folding of a plethora of monomers with different connection sites and combinations thereof. These monomers were folded, purified, and then combined to assemble into superstructures with each monomer at a designated position, defined by their connection sites.

To access the moDON capability of assembling into superstructures in one-pot reactions, successively larger structures were constructed and analyzed. Firstly, xy dimers were analyzed. Just as intended in the design, TEM micrographs revealed seamless and tight connections, connecting two monomers as if they were constructed with the same scaffold (see Figure 3.3b. The yield, as determined by AGE was 94.8 %, and 74.1 % as determined by counting out structures on TEM micrographs. This difference in yield from TEM and AGE was attributed to the additional strain on the connections during blotting. The assembly yields of dimers were similar for all connection sites (data not shown due to repetition).

Next, two kinds of trimers were constructed, shown in Figure 3.3c,d. The yields for the trimers differed a little. The first trimer (c), with a wide angle between its subparts and only two connections in total, showed a yield of 91.7 % in AGE and 50.0 % in TEM analysis. The second trimer (d), which had a closer angle and three connection sites, showed 87.6 % yield in AGE, and 80.1 % in TEM. We suspect the additional binding site of trimer (d) to stabilize the superstructure,

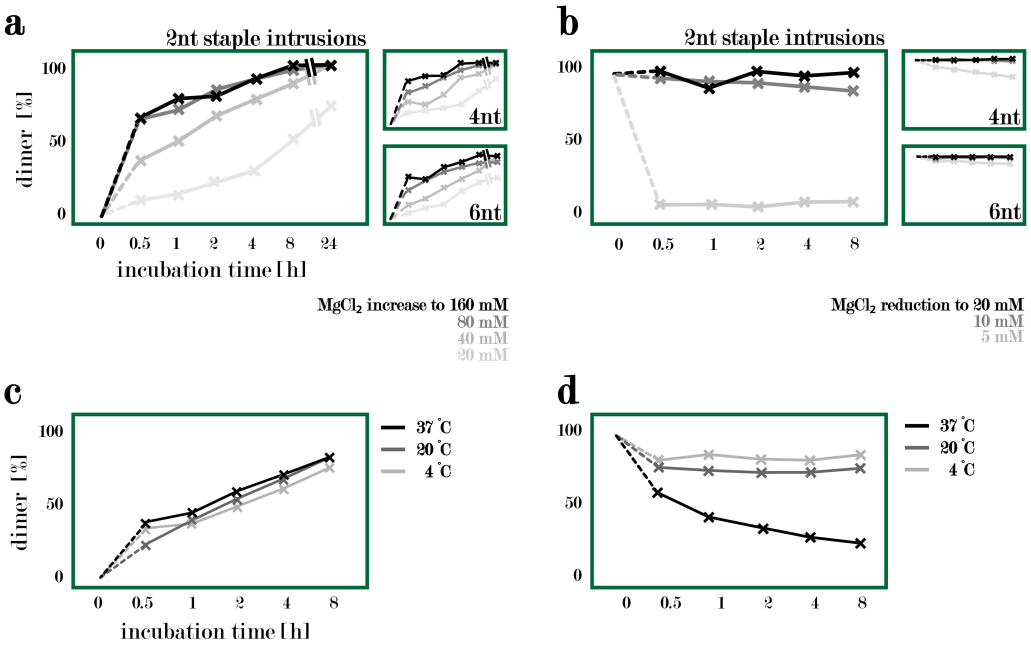

Figure 3.2: Analysis of xy-Connection Kinetics

(**a**) assembly and (**b**) disassembly kinetics, keeping the temperature at 37 °C. (**b**) assembly and (**d**) disassembly kinetics, keeping the intrusion length at 2 nt and the $MgCl_2$ concentration at 40 (or 7.5, respectively) mM. Panels were partially adapted and reprinted with permission from [114], copyright 2025 Springer Nature Ltd.

and therefore increase the yield.

Two different tetrameric superstructures were constructed, depicted in Figure 3.3e,f. The first tetramer showed a yield of 76.8 % in AGE, and 38.8 % in TEM. The second, diamond-shaped tetramer had an AGE yield of 66.1 % and a TEM yield of 49.6 %. Similar to the trimers the lower yield loss from AGE to TEM for the second tetramer can be explained through the stabilizing effect of the additional binding site.

Then two different hexamers were constructed, one in ring form (Figure 3.3g) and the other in triangle form (Figure 3.3h). The ring hexamer had a yield of 91.7 % in AGE, and 30.1 % in TEM. The triangle hexamer showed similar AGE (80.8 %) and TEM yields (19.2 %). Both structures had the same amount of connections.

Lastly, heptameric structures were built, the largest possible one-pot assemblies with the moDON (Figure 3.3i-l). This is because the number of possible, orthogonal xy-connections is six in total (12 connection sites, half complementary to the other half). However, for these largest, heptameric structures the yield decreased significantly. The AGE yield was not able to be determined confidently, and the TEM yields were low: 8.7 % for the first heptamer (i), 1.4 % for (j), 3.3 % for (k), and 7.9 % for heptamer (l). It can be assumed that the larger the structures, the larger the shearing forces, which makes the connections much more susceptible to breakage. Additionally, there were no double connections of monomers in the heptameric assemblies, that could have stabilized the superstructure.

In summary, the moDONs xy-connections showed functionality and orthogonality, as designed. Simple, one-pot reactions of folded and purified[9] monomers constructed the desired multimeric superstructures.

The yield of the superstructures was roughly dependent on the superstructure size and the number of connection sites. High yield was thus also achieved for large, hexameric structures as every monomer was attached at two sites. The yield determined from TEM micrographs was always lower compared to the yield extracted from AGE blots. It was reasoned that this is probably due to the increased stress on the structures during blotting[10].

3.3 Method II: Three-Strand-System

The second connection strategy incorporated in the moDON is a three-strand system. Three-strand systems are inherently modular and the difficulty lies in the incorporation of other traits: directionality, rigidity, dynamic alterability, stoichiometry, orthogonality, while avoiding self-passivation and with the minimal

[9] the xy-connections also work with unpurified monomers

[10] Some experiments with longer staple intrusions were conducted to test to which degree this can be counteracted. A rough scan of the results showed only minute differences. But at the same time, the longer intrusions make the ensemble more prone to unwanted off-target interactions

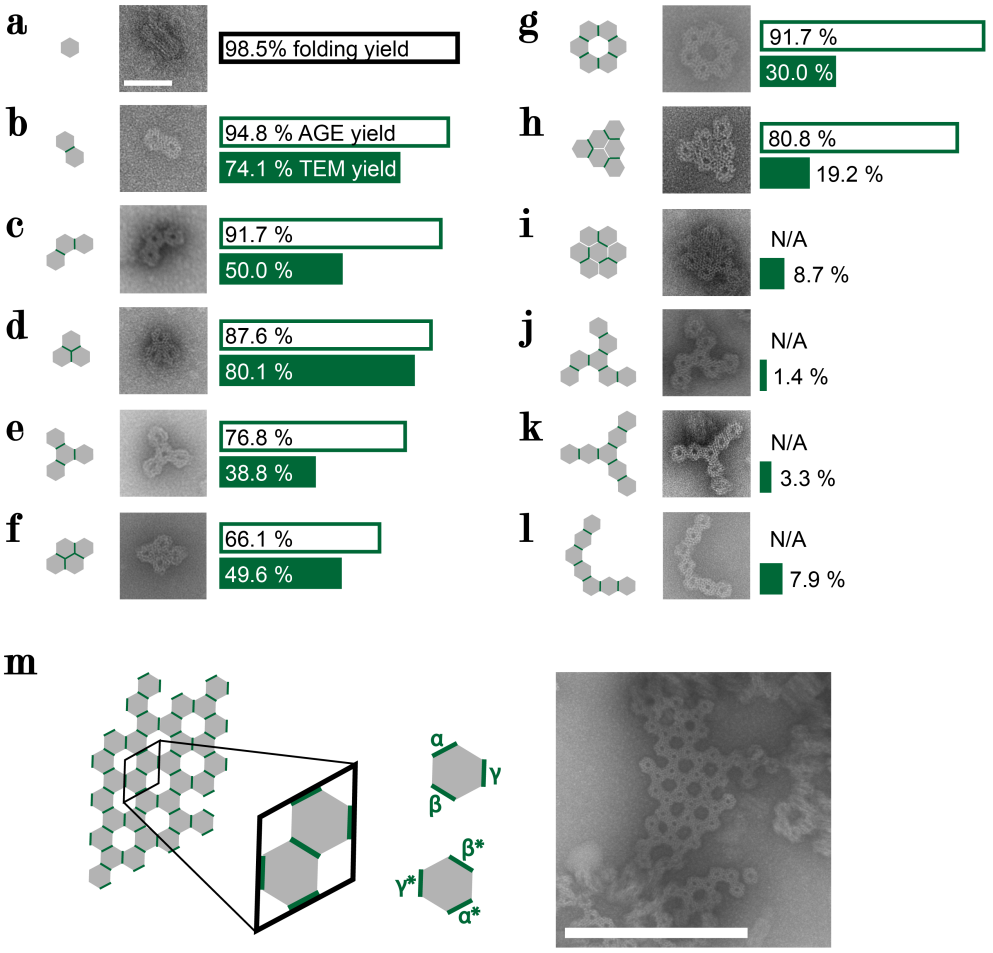

Figure 3.3: Multimeric Assemblies in xy-Direction

Superstructures in xy-direction assembled from one modular DNA origami: (**a**) monomer, (**b**)-(**l**) dimer, trimer 1, trimer 2, tetramer 1, tetramer 2, hexamer 1, hexamer 2, heptamers 1-4. (**m**) Periodic assembly with a two-moDON unit cell. The depicted infinite 2D structure spans approximately 39,000 nm^2. The scale bar in (**a**) is 50 nm and holds until (**l**), the scale bar in (**m**) is 250 nm. Panels were partially adapted and reprinted with permission from [114], copyright 2025 Springer Nature Ltd.

number of strands and sequences per connection. In the following, the design of the three-strands system is described, the connection kinetics analyzed and a multitude of different structures is constructed.

3.3.1 Design and Construction

For the three-strand system, staples at the helical ends of the structures were extended to create handles. The helices from which these handles extrude were extended a few bp to the respective direction to increase the accessibility (see Figures B.2 and B.3). The positions of the helices were evenly spaced, but not centered, to increase the stability and rigidity of the connections, in a wireframe-like manner. The directions of connections were named left and right, after the sides in the caDNAno outline.

Directionality was created by extending only one DNA end direction at the respective side, depicted in Figure 3.4b,c. Six staples on the one side were extended only at their 3' end for 11 nt. Conversely, six staples on the other side were extended on their 5' end for 10 nt. The 5' and 3' positions could be on the left and right side of the moDON, later allowing for symmetric assemblies. The extension length of 21 nt was chosen to keep the helical pacing between the monomers and thus increase the stability of the connections. A third strand, the *connector* strand, would bind to the two handles and create the connection. Since all six handles of each side share the same DNA sequence, the probability of attachment is increased, and as a result, the required amount of connector (excess) is lower. And since the handles only have a length of 10 or 11 nt, the connections are not self-passivating; The short handles allow connector strands to be released again, except when they are bound by both handles and contribute to a connection. Thus the full and stable occupation of handles on both connection sites is avoided.

Additionally, an option to remove the z-connections was implemented. This was done by the elongation of the connector strands by a toehold region, for an *invader* strand to bind to, then bind to the rest of the connector, and thus release the connections. Following the mechanisms described in section 2.3.2 and the guidance given by Zhang & Winfree[154] and Simmel *et al.*[155], a 7 nt long toehold was incorporated at the end of the connector, and a complementary part on the invader strand. The -comparably large- length of the toehold would ensure reliable binding and quick displacement with minimized dissociation after binding.

Zhang & Winfree, 2009

Simmel, 2019

The sequences of handles, connectors, and invader strands were analyzed regarding their orthogonality. To create the sequences in the first place, a three-letter alphabet was used, minimizing potential off-target interactions. To analyze the structures, the software NUPACK[68][69] was employed, already introduced in section 2.3.4.

Zadeh, 2011

Fornace, 2022

Four pairs of handles and connectors (and invaders) were designed and simulated. Firstly, the very basic ensemble of all handles and connectors was simulated: As shown in Figure B.9 as color-coded dots in the Nussinov-like matrix, the prob-

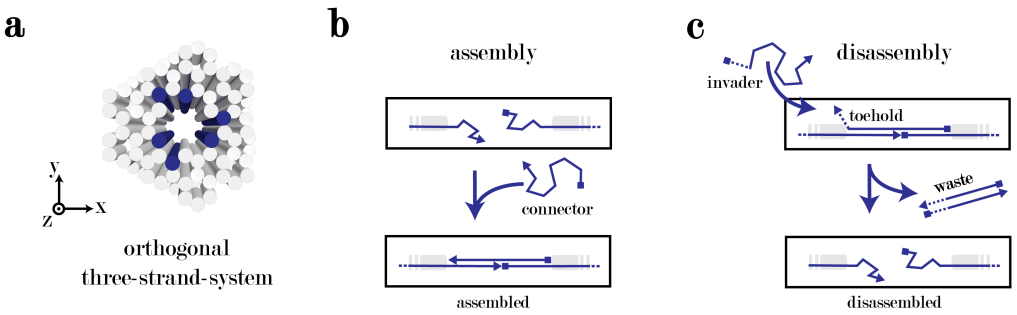

Figure 3.4: Design of the Modular Three-Strand System

(**a**) Positions of the extended helices in the DNA origami. (**b**) The assembly method of the three-strand system: A connector strand directionally connects the monomers by hybridizing to both handles. (**c**) The disassembly is analogously done by releasing the connector, which would have a short toehold extension, by hybridizing a fully complementary invader strand to it. Panels were partially adapted and reprinted with permission from [114], copyright 2025 Springer Nature Ltd.

ability of interaction was almost 100 % for the designed connections. This proved -at least *in silico*- the high specificity of the designed connectors, thus their orthogonality. Then, the impact of the addition of the toehold to the sequences was checked. The behavior of the extended connectors, shown in Figure B.10, revealed nearly no change in hybridization probabilities when compared to the basic ensemble in Figure B.9. Lastly, the effectiveness of the invader strands was checked. To the ensemble of simulated strands in Figure B.10 the invaders were added and the change in hybridization probability was checked. Shown in Figure B.11, the probabilities shifted fully to hybridization with the invader strands, instead of the handles. Even though this analysis (*cf.* Figures B.10 and B.11) does not reveal the dynamics behind the strand-displacement process, it does indicate a strong difference in the free energy levels of binding states, which is the ultimate prerequisite for successful strand-displacement interactions. However, the simulated interactions had to be verified experimentally.

3.3.2 Assembly & Disassembly Characteristics

Having engineered a three-strand system with a minimized number of connectors and sequences, the functionality of this approach needed to be verified experimentally. For this, the orthogonality, the rigidity, as well as the underlying kinetics, were analyzed.

Orthogonality & Rigidity

Firstly, the orthogonality of the connectors, tested *in silico*, was verified *in vitro*. To complementary moDON monomers, the different connectors were added to test for unwanted interactions. The formed structures were then analyzed by AGE, shown in Figure B.12a: Only if the correct connector was added, was the electrophoretic mobility shifted and a dimer band became visible. This indicated high orthogonality of the z-connections.

Another test of the orthogonality of the three-strand connections was done by successively adding the different connectors to an ensemble of moDON monomers. As seen in Figure B.12b, the electrophoretic mobility shifted, depending on the size of the superstructure, thus indicating connection. This again showed a high degree of orthogonality in the three-strand system. Further, both tests showed clear bands with near to no smear, off-target bands or aggregates, which further demonstrates the clean and orthogonal interactions.

Also, the rigidity of the molecular connections had to be verified so that higher-order structures could be constructed. For this, dimer connections with different connector excesses were constructed and then analyzed by TEM. It was found that for low excess of connectors the connections between the monomers were indeed established, but kinked. Figure B.13 shows these kinked connections, for an equimolar ratio of connectors and handles. If the ratio was increased to -at least- 4 connectors over handles, the connections in the z-direction indeed seemed rigid and directional, shown later in Figure 3.6.

Assembly Kinetics

To analyze the assembly kinetics of the z-connections, the parameters of connector excess, $MgCl_2$ concentration, and temperature were examined.

Firstly, the connector excess was varied, from 2-fold to 4- and 8-fold over the amount of handles. As seen in Figure 3.5a, the speed of DNA origami dimerization in the z-direction was independent of connector excess. The DNA origami reached more than 60 % dimerization already after 30 min and approached 100 % dimerization after 2-4 h. We hypothesize this is due to a very high *effective excess* of connectors over handles, since the connectors are of the same sequence, the actual excess multiplies. This results in an *effective excess* (*e.g.* for "2-fold" excess) actually somewhere between 12 and 7 depending on the number of already established connections. Since we discovered in the section above, that around 4-fold excess of connectors are needed to create stable z-connections, we did not reduce the excess further, where possibly other dynamics rule.

The impact of the temperature, as seen in Figure 3.5c, was not large: increased temperature sped up the assembly process, such that samples incubated at 37 °C were fully dimerized already after 2-4 h, but those samples incubated at RT only after 8 h. moDON ensembles incubated at 4 °C showed only $\approx$ 60 % dimerization after 8 h. We assume this is due to the diffusion speed of the connectors being pro-

portional to the temperature and/or the increased fidelity of strand-displacement reactions at elevated temperatures.

The $MgCl_2$ concentration had a mediocre impact on the dimerization rate: displayed in Figure 3.5e, the dimerization for 10, 20, and 40 mM $MgCl_2$ was complete after 8 h. However, increased $MgCl_2$ levels also increased the dimerization speed, such that samples with 40 mM $MgCl_2$, for example, were fully dimerized after 1 h already. Only the samples with 5 mM $MgCl_2$ were not fully dimerized at the end of the experiment, merely showing 50 % dimerization after 8 h. This minimal dependency on $MgCl_2$ was probably due to the repulsion effects of ion layers around the DNA origami, as discussed in section 2.2.3. Finally, the impact of the temperature was tested with samples incubated at 4 °C (fridge), 20 °C (room temperature), or 37 °C.

Disassembly Kinetics

As parameters for the disassembly process, again, the invader excess, the $MgCl_2$ concentration and the temperature were examined.

The invader excess proved to be irrelevant for the disassembly speed, as 2-, 4-, and 8-fold excess did not yield a different disassembly kinetic (Figure 3.5b). Already after 30 min, most of the connections were disassembled, with full disassembly in all samples achieved after 4-8 h. Similarly to the explanation for the connector strands, we assume that the uniqueness of the staple strands is increasing an *effective excess*, that in turn shifts the underlying dynamics into an area of diminishing returns.

We next examined the temperature dependence, as shown in Figure 3.5d. Here, just as with assembly, an increased temperature yielded faster kinetics. While the difference of 4 °C and 20 °C was minute, and yielded 50-60 % dimerization after 8 h, the increase to 37 °C starkly quickened the disassembly speed, reaching approximately 40 % after the first 30 min and full disassembly after 4 h.

Finally, we tested, whether a decrease in $MgCl_2$ alone can break the z-connections. For this, z-dimers were formed over night and then the $MgCl_2$ concentration in the samples was reduced to 20, 10, or 5 mM. The AGE analysis revealed no breakage of the connections, except a very small fraction for 5 mM $MgCl_2$ after 8 h of incubation, as can be seen in Figure 3.5f. This showed full orthogonality in assembly and disassembly trigger of xy- and z-connections since the xy-connections were exclusively $MgCl_2$ concentration dependent.

3.3.3 Multimeric Assemblies

Multimeric moDON structures in z-direction were assembled. The above characterized rigid, directional, and orthogonal z-connections were used to assemble several superstructures of various sizes and analyze them regarding their structural characteristics and yield.

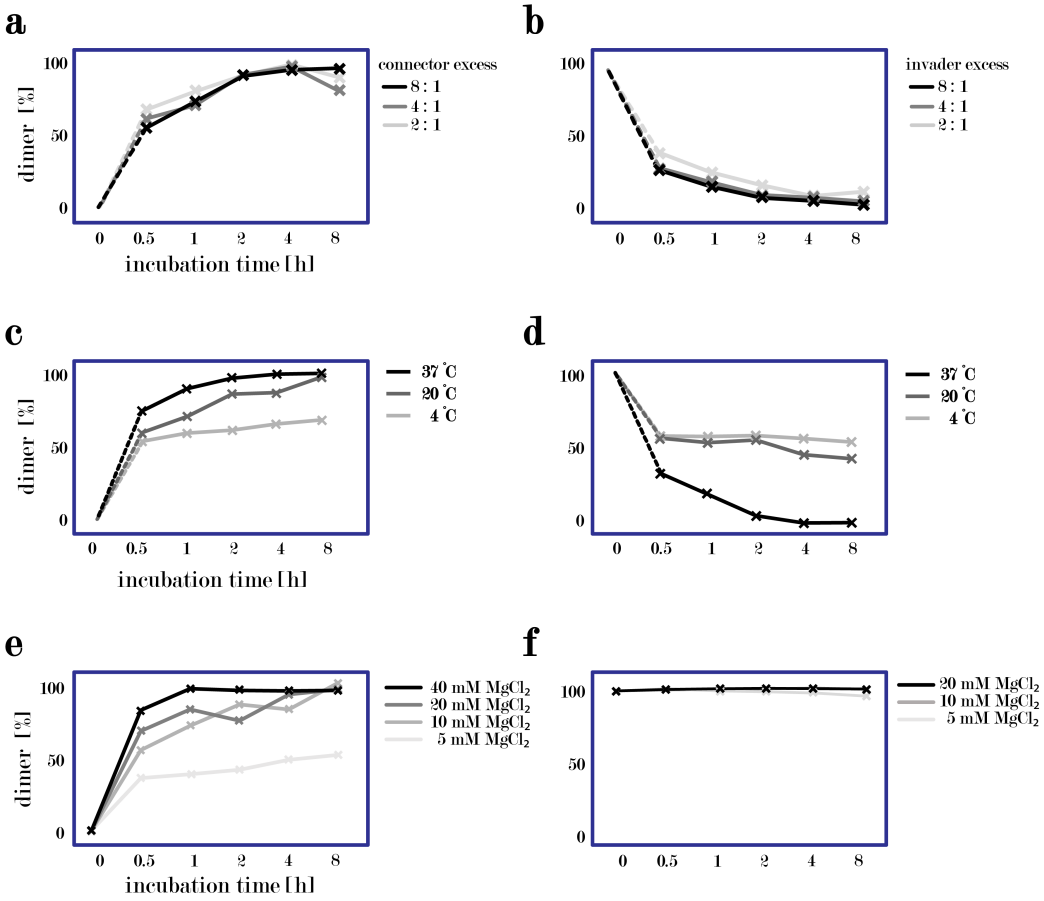

Figure 3.5: Analysis of z-Connection Kinetics

Analysis of reaction kinetics of the z-connections: (**a**) assembly and (**a**) disassembly, holding the temperature at 37 °C and $MgCl_2$ concentration at 20 mM. (**a**) assembly and (**a**) disassembly, holding the connector excess at 5x and the $MgCl_2$ concentration at 20 mM. (**e**) assembly and (**f**) disassembly, holding connector excess at 5x and temperature at 37 °C. Panels were partially adapted and reprinted with permission from [114], copyright 2025 Springer Nature Ltd.

Firstly, the four connectors were used to construct unidirectional assemblies. moDON monomers with the respective binding sites were connected to dimers, trimers, tetramers, and pentamers. As the AGE image in Figure B.14 and the TEM micrographs in Figure 3.6 reveal, the superstructures folded with excellent yield and in the designed structural shape. The dimers folded with a yield of 93.2 %, as judged by AGE, and 97.7 % as judged by TEM. Similarly, the yield for the trimers was 93.2 % (AGE) and 82.4 % (TEM), and for the tetramers it was 87.5 % (AGE) and 78.3 % (TEM), and for the pentamers 87.3 % (AGE) and 65.9 % as judged by TEM. The TEM yield for z-connections is again (almost always) lower than the AGE yield, and larger structures show reduced yield, compared to smaller structures. This again is a confirmation of the explanation, that the blotting process exerts additional stress on the structures. Further, we again observed that the increased number of breaking points, induced by more monomers in the superstructure increases the probability of breakage.

Secondly, symmetric assemblies were constructed. Conceptually, a central dimer or monomer was made, carrying two sets of the same handles at their left and right sides, pointing out with the same strand direction. To that central part double the amount of complementary moDONs would attach effectively creating larger symmetric structures, as shown in Figure 3.6f-i. With this approach, a hexamer, a heptamer, an octamer, and a nonamer were constructed. The yield for the hexamer was 70.4 % (AGE) and 50.4 % (TEM), for the heptamers it was 61.0 % (AGE) and 48.7 % (TEM). Octamers were constructed with a yield of 56.8 % (AGE) and 31.2 % (TEM), and nonamers with an AGE yield of 60.9 % and a TEM yield of 34.2 %. The observed yields align again with the observations of increased chance for structure breakage when increasing the size or blotting for TEM.

Lastly, infinite z-assemblies were made. For this, a self-complementary moDON was used and connected to form periodic, tubular structures. One of those is depicted in Figure 3.6j, and consists of 88 monomers with a contour length of more than 4 μm and a calculated weight of approximately 0.5 GDa. In section 3.4.2 these structures will be analyzed further.

However, the z-connections generally showed a larger yield than the xy- connections. We assume this is due to the increased binding strength of the z-connections: summing up the number of involved bp, the xy-connections were constructed with 4 helices, 2 nt, thus 8 bp in total, but the z-connections include six connections of 21 bp each, thus 126 bp, outweighing possible destabilizing effects due to the slightly increased structure radius of z-assemblies, compared to xy-assemblies.

3.4 Combination of Modularity Approaches

Since section 3.2 and 3.3 showed orthogonality of both connection approaches, combining both seemed possible. In the following, these combinations are tested: xyz-superstructures are constructed, as well as large periodic assemblies, structures

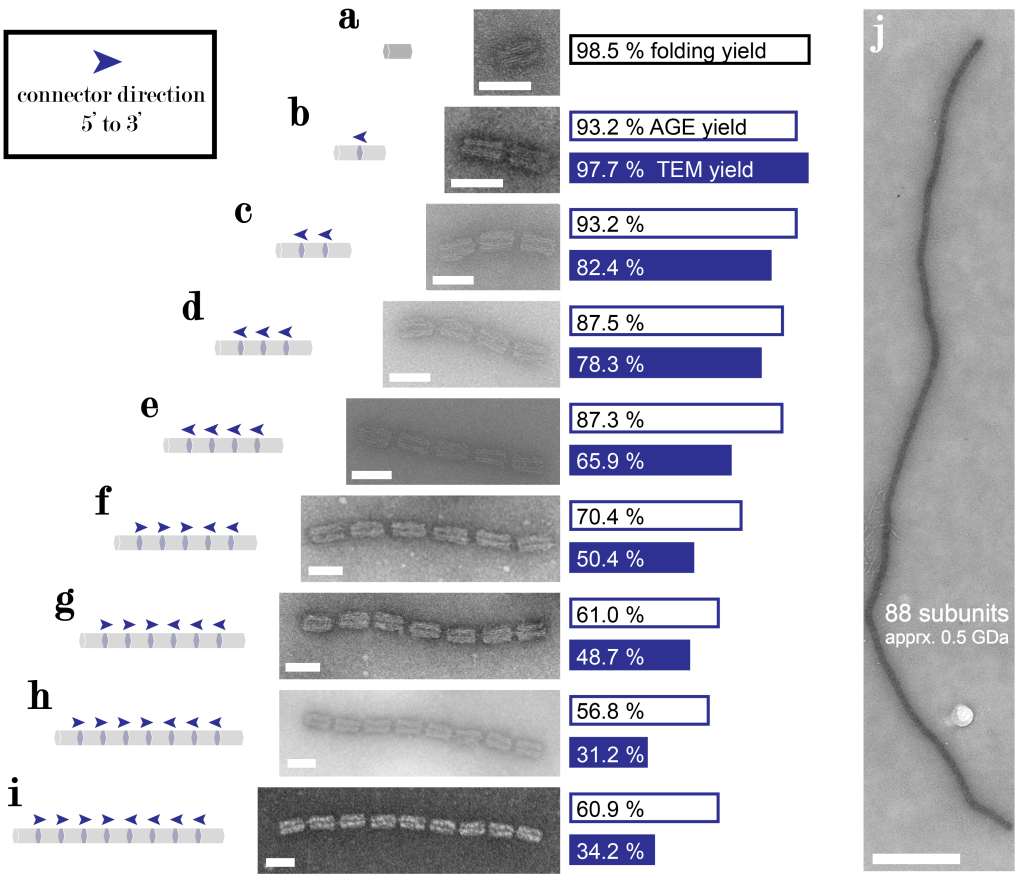

Figure 3.6: Multimeric Assemblies in z-Direction

Different multimeric z-Assemblies. The connector direction is indicated with a blue arrow from 5' to 3' ends of the connectors. (**a**) shows a moDON monomer, as in Figure 3.7a, (**b**)- (**e**) show dimers, trimers, tetramers, and pentamers. (**f**)(**i**) show hexamers to nonamers, assembled with the symmetric assembly method, as indicated by the direction arrows. (**j**) shows a periodic tubular assembly with 88 subunits, measuring almost 5 μm and almost 0.5 GDa. Scale bare in (**a**)-(**j**) are 50 nm, and in (**j**) 500 nm. Panels were partially adapted and reprinted with permission from [114], copyright 2025 Springer Nature Ltd.

are assembled parallelly and selectively, and also disassembled in the same way. In the last part, the retained addressability of the structures is demonstrated.

3.4.1 Combining xy- and z-Connections

Given the orthogonality in triggers for xy- and z-assembly and disassembly, we next thought to build larger finite superstructures with a combination of both approaches.

We constructed six different xyz-superstructures, from a pentamer to a 14-mer. As depicted in Figure 3.7a, the first structure, the pentamer had two xy- and two z-connections forming a structure, resembling a cross. The AGE yield of this structure was 68.7 %, and the TEM yield 39.5 %. Further, a heptamer in the form of an "H" was constructed (yield in AGE: 52.1 %, TEM: 35.1 %) and an octamer resembling an "O" (yield in AGE: 69.4 %, TEM: 16.1 %), see Figure 3.7b,c. Then a z-pentamer was modified in such a way that it would carry tetrameric subunits at two or three of its subunits, with which an undecamer (yield in AGE: 44.2 %, TEM: 17.4 %) and a 14-mer (yield in AGE: 17.31 %, TEM: 10.1 %) were constructed (Figure 3.7d,e).

Finally, we constructed a twisted trimeric trimer, a nonamer, by hierarchical assembly (Figure 3.7f). Three xy-trimers were constructed separately, then assembled them without purification in the z-direction through the addition of connectors (yield in AGE: 68.5 %, TEM: 43.5 %).

3.4.2 Periodic Assemblies

Besides combining xy- and z-connections to create finite structures, we then also created periodic superstructures with varying subunits. Starting with the periodic z-tubes shown in section 3.3, we constructed similar structures with trimeric and tetrameric subunits, similar to the xy-structure depicted in Figure 3.3d,e. The resulting periodic structures are depicted in Figure 3.7g-i. The monomeric tube is a duplicate from Figure 3.6j. The trimeric and tetrameric tubes had a somewhat reduced length, but still in the µm regime. The subunits were mostly fully assembled, but the tubes with the trimeric subunit showed much fewer defects than the one with a tetrameric subunit. Some of the larger structures constructed here had GDa weight, *e.g.* the tube in 3.6c, which, with 57 tetrameric subunits, has a calculated weight of 1.28 GDa.

We further analyzed the persistence length L_p of the tubes. For this, we fitted data of contour length l and end-to-end R distance of N > 50 tubes each with formula 3.1, taken from reference[156] Rivetti, 1996

$$< R >^2_{2D} = 4lL_p \left(1 - \frac{2L_p}{l}\left(1 - exp(-\frac{1}{2L_p})\right)\right) \tag{3.1}$$

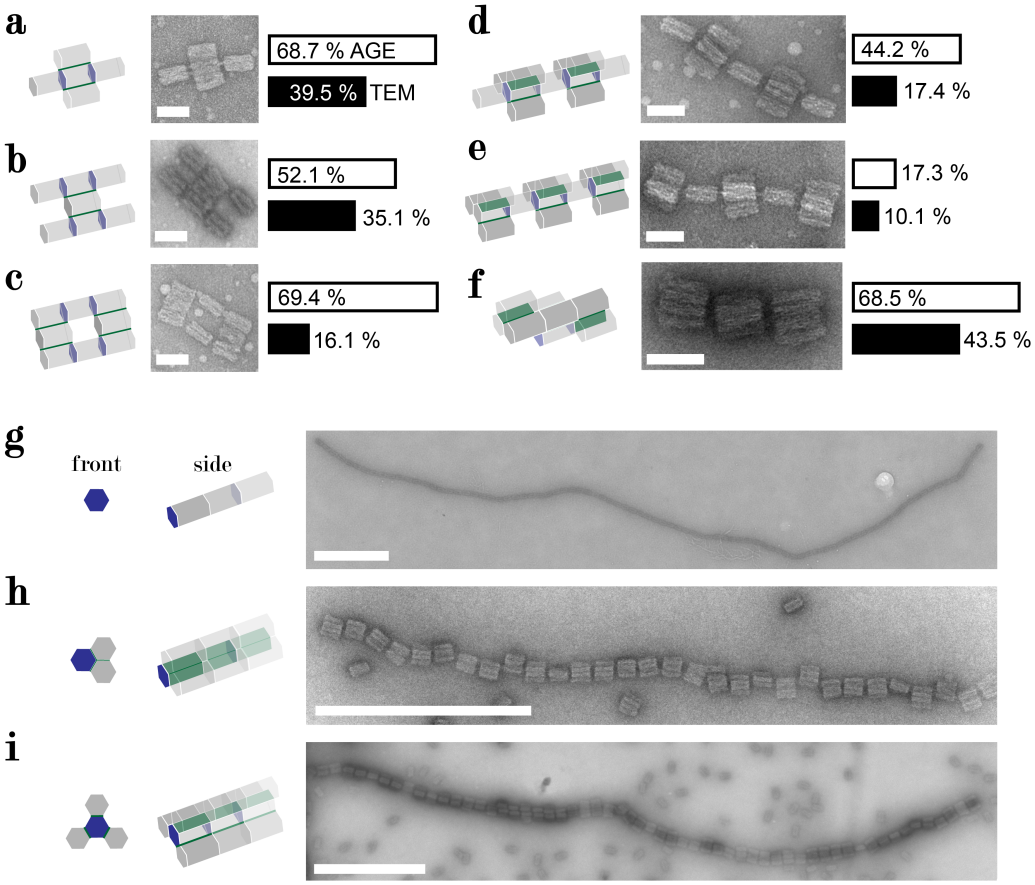

Figure 3.7: xyz-Assemblies

Different xyz-assemblies, combining both connection methods. Constructing (**a**) a pentamer in the form of a cross, (**b**) a heptamer in form of an "H", (**c**) an octamer in the form of an "O", and further (**d**) an undecamer, (**e**) a 14-mer, and (**f**) a nonamer in form of a twisted trimeric trimer. Further, different periodic structures were constructed with differently sized subunits: (**g**) monomeric subunit (duplicate from Figure 3.6j), (**h**) trimeric subunit, and (**i**) tetrameric subunit. Scale bars in (**a**)-(**f**) are 50 nm and in (**h**)-(**i**) 500 nm. Panels were partially adapted and reprinted with permission from [114], copyright 2025 Springer Nature Ltd.

and found high rigidity of the periodic tubes: As also displayed in Figure B.15 the persistence length of the monomeric subunit assembly was $L_p = 0.93 \pm 0.16$ μm, the L_p of the trimeric subunit structures was 1.10 ± 0.16 μm, and the L_p of tubular structures with tetrameric subunits was 1.76 ± 0.25 μm. The persistence length of the periodic structures got larger with the number of monomers in the subunit. We assume that this is due to the larger subunits enacting a straightening effect through steric hindrance.

3.4.3 Parallel and Selective Assembly

Since all connection sites constructed here are orthogonal to one another, we assumed that different superstructures could be assembled in *parallel* in the same tube. To test this hypothesis, we mixed twelve moDON monomers and assembled three different structures in the same tube at the same time. For easy differentiability, we chose a tight trimeric xy-structure, a wide tetrameric xy-structure, and a z-pentamer. For the assembly, the $MgCl_2$ concentration was raised and the respective connector strands added, then the yield was analyzed by TEM: As can be seen in Figure 3.8a, the structures assembled in parallel with near to no cross talk. The yields of the respective structures as extracted from the TEM micrographs was determined to be 20.6 % for the xy-trimer, 20.4 % for the xy-tetramer, and 18.8 % for the z-pentamer. This revealed first and foremost that the structures did not inhibit the assembly of another, since the yield of each structure was around 20 % of all structures. In total the yield is approximately 60 %, which corresponds on average with the TEM yields of the single structures: 80.1 % (xy-trimer), 38.8 % (xy-tetramer), and 65.9 % (z-pentamer).

Since the two connection methods are also fully orthogonal to another with respect to their assembly triggers, we suspected that a *selective* assembly of structures from the same monomer pool would be possible.

To test this second hypothesis, we constructed five moDON monomers all with xy- and z- connection sites. Only xy-connections would form a xy-pentamer, similar to a truncated version of the superstructure seen in Figure 3.3l. And only z-connections would lead to a z-pentamer as seen in Figure 3.6e. The five moDON monomers were mixed and the mixture halved, in one half the $MgCl_2$ concentration was increased and in to the other half the connector strands added. The result was again analyzed by TEM imaging: As seen in Figure 3.8b, the DNA origami assembled depending on the trigger added either into the xy-pentamer or the z-pentamer. The yield for the xy-pentamer was 33.7 % and the yield of the z-pentamer was 44.0 %, somewhat reduced compared to the yield in the normal assembly (65.9 %).

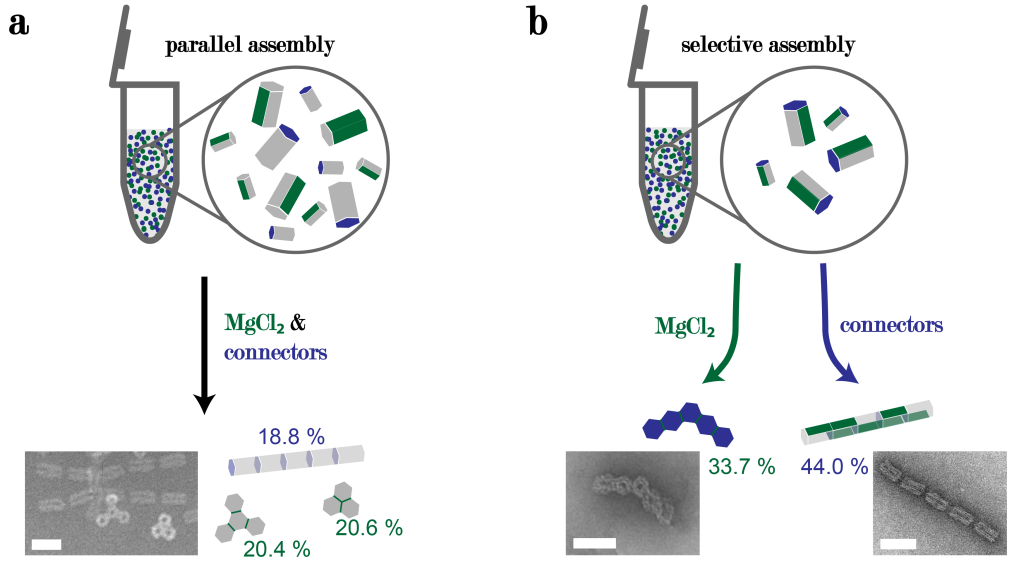

Figure 3.8: Parallel and Selective Assembly of Superstructures

(**a**) parallel and (**b**) selective assembly of moDON superstructures. In (**a**) the parallel assembly, three different DNA origami are constructed at the same time in the same tube. The respective structures assemble upon the increase of $MgCl_2$ and addition of connector strands with nearly no cross-talk. This is possible due to the high orthogonality of the connection sites. The yield of the structures combined is approximately 60 %. In the (**b**) selective assembly, five moDON monomers are assembled into two different structures depending on the assembly trigger added: An xy-pentamer is constructed by elevation of the $MgCl_2$ concentration and a z-pentamer is constructed by the addition of connector strands. The yield of the xy-pentamer is 33.7 % and the yield of the z-pentamer is 44.0 %. Scale bars are 50 nm. Panels were partially adapted and reprinted with permission from [114], copyright 2025 Springer Nature Ltd.

3.4.4 Selective Disassembly

Orthogonality in connection sites and assembly triggers implies also an orthogonality in disassembly. The disassembly trigger for the xy-connections is a reduced $MgCl_2$ concentration, as described in section 3.2, and the disassembly trigger for the z-connections are sequence-specific invader strands, as introduced in sections 2.3.2 and 3.3.

First, we tested whether we can specifically disassemble z-connections, through invader strands. To an initially constructed z-pentamer, different invader strands were added to disassemble specific connections in the structure. As seen in Figure 3.9a, the superstructure was disassembled with high precision into smaller structures. Depending on the added invader strands, the split either left a monomer and a tetramer, of a dimer and a trimer. Also, the addition of two invader strands simultaneously was tested, which cleaved the structure, for example, into two dimers and a monomer.

Having tested the specificity and orthogonality of the z-disassembly, we next tested the disassembly of larger structures. For this we again constructed tubes with monomeric subunits or with a dimeric subunit (dimeric in z-direction). The structures were assembled properly, as suggested by AGE (Figure B.16, and could again be cleanly disassembled into their respective subunits upon the addition of the respective invader as a trigger.

Then we constructed a large xyz-20-mer, to test the specific disassembly of xy- and z-connections. The 20-mer consisted of a central z-pentamer, and to each moDON monomer in this central pentamer were three moDONs in xy-direction attached, creating a pentamer of tetramers. The 20-mer structure is depicted in Figure 3.9b. The sample was then split, one part was diluted to decrease the $MgCl_2$ concentration, to the second part invader I was added, and invader II was added to the last part. As designed, the reduced $MgCl_2$ concentration disassembled exclusively the xy-connections leaving only z-pentamers and monomers. Similarly, the invader strands split the 20-mer at the designed positions, resulting in a tetramer and a 16-mer for invader I, and in an octamer and a dodecamer for invader II, depicted in Figure 3.9b.

3.4.5 Retained Addressability

A central feature that multimeric DNA nanostructures need to achieve is retaining the high addressability, which distinguishes DNA origami from other nanoparticles in the first place. To verify that the superstructures constructed here are still addressable at each position, we site-specifically attached AuNPs to them.

For this, we elongated a few staples on parts of the origami with a specific sequence, and modified AuNPs with the respective complementary sequence. The AuNPs were produced and modified as described in the appendix, sections A.1.4 and A.1.5, and the DNA origami were modified with AuNPs following the protocol detailed in section A.1.6. A sketch of this is depicted in Figure 3.10.

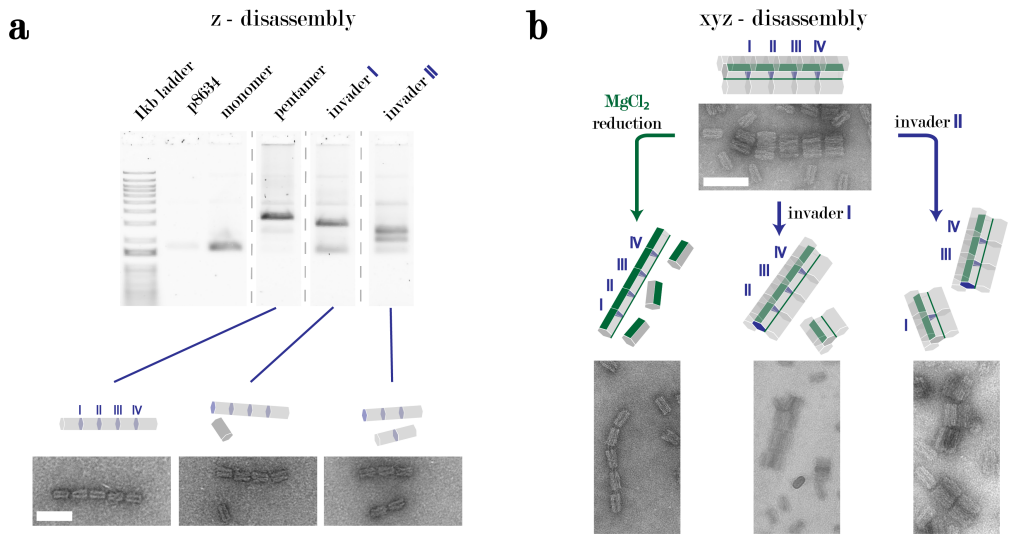

Figure 3.9: Selective Disassembly of moDON Superstructures

(**a**) AGE and TEM analysis of the selective disassembly in z-direction. An initial z-pentamer is disassembled into either a tetramer and a monomer through the addition of invader I, or a trimer and a dimer through the addition of invader II. The structures show a migration speed through the agarose gel, antiproportional to their size. (**b**) Disassembly of xyz-structures: An initial xyz-20-mer was disassembled either in a z-pentamer, and many monomers, by reduction of the $MgCl_2$ concentration, or into a tetramer and a 16-mer by addition of invader I, or into an octamer and a dodecamer by addition of invader strand II. The scale bar in (**a**) is 50 nm and holds for all micrographs in the subfigure, and the scale bar in (**b**) is 100 nm and also holds for all micrographs in the sub-figure. Panels were partially adapted and reprinted with permission from [114], copyright 2025 Springer Nature Ltd.

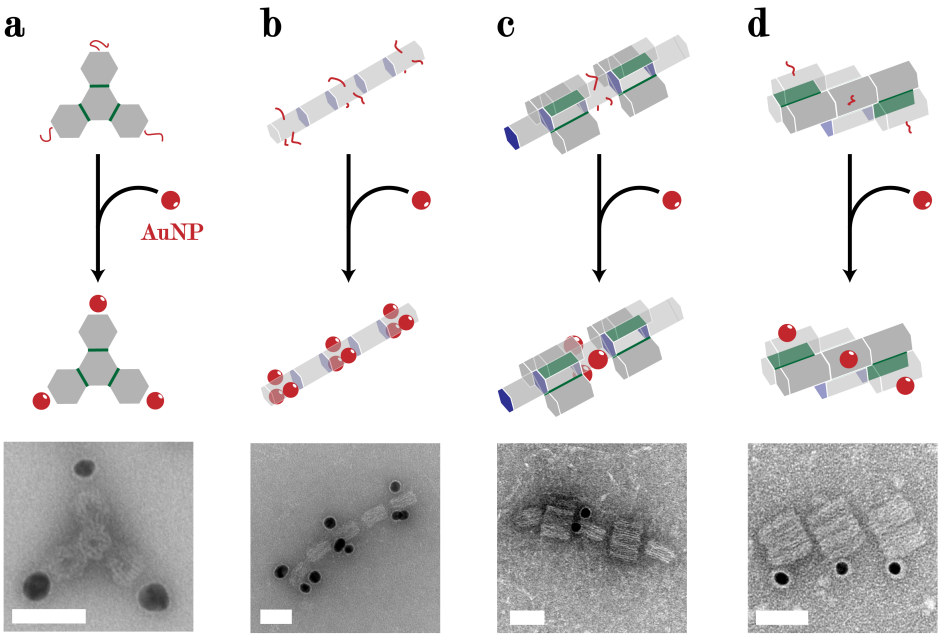

Figure 3.10: Addressability is Retained in moDON Superstructures

The addressability of the moDON superstructures is shown by site-specifically attaching AuNP (red balls) onto the structures. The moDON superstructures are modified with ssDNA handles (red lines), complementary to ssDNA sequences attached to AuNP. Through sequence-complementary hybridization, the AuNPs are attached only to the specifically designed sites. The used structures shown are (**a**) an xy-tetramer, (**b**) a z-pentamer, (**c**) an xyz-undecamer, and (**d**) a hierarchically assembled nonamer. Scale bars are 50 nm. Panels were partially adapted and reprinted with permission from [114], copyright 2025 Springer Nature Ltd.

Firstly, we constructed an xy-tetramer with AuNPs at its tips, seen in Figure 3.10a. Further, a z-pentamer was constructed with three attachment sites at the first, middle, and end moDON (Figure 3.10b. Additionally, an undecamer with attachment sites at its middle unit and a twisted trimeric trimer with AuNPs at its tips were constructed (Figure 3.10c,d. In general, the precision of the AuNPs was fully retained, even though the occupation of binding sites was often not fully given. This again is probably due to low AuNP excess, to short incubation time, to fewer handles for attachment, resulting in defective sites due to imperfect incorporation or even allowing detachment of AuNPs.

3.5 Conclusion

In this chapter, two approaches to modular DNA origami design were explored. Both were incorporated into the same DNA origami structure, which enabled a large number of constructible monomers with combinatorially different connection sites. The number of combinatorially possible monomers is given in equation 3.2 by the product of the combinatorially possible xy- and z-connections:

$$(2xy - configs. + passive)^{6sites}(8z - configs. + passive)^{2sites} = 59049 \quad (3.2)$$

Both types of connections between DNA origami used in the moDON are based on existing methods. Foundational for those methods is the joining of DNA with either sticky ends or blunt ends. These were already introduced for biochemical ligation of plasmid DNA, and then used to create higher-order DNA structures like tubes[133] or crystal-like 2D sheets [49]. Later for DNA origami, as discussed in section 3.1.1, these approaches were adapted. In this work, a novel modularity was introduced to protrusions and indentations with re-routable scaffold parts and the inherently modular three-strand connections were simplified.

Rothemund, 2004
Winfree, 1998

The modular protrusions and indentations were able to be reconfigured, fully independent from one another, while retaining full functionality, just as designed. They yielded strong, if not more durable connections than their antetype. The yield for dimers was at ≈ 95%, judged by AGE analyses, and stayed at that level even for some higher-order structures (Figure 3.3). The short staple intrusions proved to be significantly more effective than blunt ends, as used in reference [96]. We hypothesize that this is due to the overall increase in connection strength. However, an increased length of the staple intrusions can again have downsides, like unwanted interactions or unshaped monomers.

Gerling, 2015

Three-strand systems are modular by default, however, in this work several problems associated with it were significantly improved: We demonstrated that only low amounts of one kind of short ssDNA connector was needed to establish rigid (*c.f.* Figure B.15) and directional (*c.f.* Figure 3.6) connections. These connections also did not show any branching behaviors and were fully orthogonal to each other. The connections were also dynamically alterable through toehold-mediated strand displacement and thus were the structures.

Both connection types were orthogonal to one another concerning their connection triggers. This allowed for the assembly and disassembly of a large variety of fully addressable, finite 3D structures (see Figures 3.7 and 3.9). These structures were also fully addressable and could also be modified site-specifically with AuNPs. It also allowed for very large, periodic structures (Figure 3.7), and for the parallel or selective assembly of superstructures (Figure 3.8). These features predestine our assemblies for all applications that rely on precision and dynamic alterability on different scales, for example synthetic biology.

Through the easily achievable large number of connection sites, the number of DNA origami monomers in one-pot connection reactions can be increased. This

allows for the easier assembly of larger superstructures by removing the need for intermediate extraction and purification.

In comparison to other methods of nanoscale assembly, it has advantages and drawbacks: The largest, finite, and fully addressable superstructures to date were constructed by Wintersinger *et al.* in the laboratory of William Shih[157]. These structures consist of ensembles of long 6HB or 12HB, that are layered in a criss-cross pattern and held by short, complementary ssDNA handles which connect the DNA origami with a two-strand system. The structures span μM in size and are of GDa weight, while still being fully addressable. However, the criss-cross superstructures are quite error-prone, and tedious to purify, as illustrated by the TEM micrographs in the paper. These connections are also floppy, which limits potential applications. Further, the large number of individual connection sites that have to be pipetted separately for each monomer increases the difficulty of construction tremendously. Wintersinger, 2023

The here presented method of modular construction and subsequent assembly of the moDON excels in yield and ease of use. The monomers used in Wintersinger *et al.* partially only fold with 10 % yield, lowering the *effective yield* of the superstructures. The monetary cost is comparable, as only a few staples need to be exchanged in both methods. However, Shih and coworkers' superstructure size could not be achieved with the modularly modified connections presented here.

Other assembly methods, using three-strand systems, were able to construct superstructures with large structural fidelity. Two examples of this approach were published in *Angewandte Chemie*[136] and *Science Robotics*[141]. The former used a multitude of additional staples in a pseudo-scaffold approach to follow the helical pacing and fuse monomers at their edges. The latter used a large number of ssDNA connectors in a three-strand system to connect monomers and fix them in position. Zhou, 2022 Luu, 2024

These methods generally have a good yield, but somewhat lower than the yield we achieved with our modular approaches, especially when also considering the structural integrity and effective yield. The three-strand-system approach by Luu *et al.* yielded slightly larger finite structures than the ones shown in this dissertation. Additionally, the reconfigurability of their structures is remarkable: Through ssDNA tethers, which are made up of unfolded scaffold parts in the structures, single connections can be dissolved, or established, while keeping the monomers connected. The connections in our superstructures dissolve selectively and completely, while those in the work of Zhou *et al.* cannot be altered at all. However, Zhou *et al.* and Luu *et al.* use a large number of unique ssDNA strands for each connection, which renders them unusable for incorporation into dynamic networks, controlled by strand displacement circuits.

In summary, modularity does not explicitly increase the size, range, or scope of the constructible superstructures; it just simplifies the construction. The approach of modular scaffold routing will be a very useful option for future DNA origami designs and the presented insights into the three-strand-connection designs will prove an asset in dynamic nanoscale assembly of larger superstructures.

Chapter 4

Origami of Death

In this chapter, the interaction of FasL and FasR with respect to the spationumerical and geometric FasL presentation and its effect on cancer cells in 2D and cancer spheroids in 3D is examined. Firstly, apoptosis induction is probed by positioning FasL proteins on DNA origami and presenting them to adherent, 2D cancer cells. Next, the applicability of DNA origami-FasL *nanoagent* therapeutics is tested by examining their ability to induce apoptosis in a large 3D spheroid model. The first part, section 4.1, has been published in 2021 in the journal *Small*, here as reference [158]:

Ricarda M. L. Berger, ***Johann M. Weck****, Simon M. Kempe, Oliver Hill, Tim Liedl, Joachim O. Rädler, Cornelia Monzel, Amelie Heuer- Jungemann. Nanoscale FasL Organization on DNA Origami to Decipher Apoptosis Signal Activation in Cells. Small, 17, 2101678, 2021*

The biochemical production of the modified FasL was published in 2025 in *BMC Biotechnology*, here as reference [159]:

Xiaoyue Shang, Nina Bartels, ***Johann Moritz Weck****, Sabine Suppmann, Jérôme Basquin, Amelie Heuer-Jungemann, Cornelia Monzel. High yield purification of an isoleucine zipper-modified CD95 ligand for efficient cell apoptosis initiation and with biotin or DNA-oligomer binding domain to probe ligand functionalization effects. BMC Biotechnology, 25, 64, 2025*

The work on spheroid penetration and apoptosis induction with DNA origami nanoagents was published in 2025 in *Small*, here as refence [160]:

Johann M. Weck*, Riya Nair, Merve-Z. Kesici, Xiaoyue Shang, Cornelia Monzel, Amelie Heuer-Jungemann. Effects of DNA Origami-Based Nanoagent Design on Apoptosis Induction in a Large 3D Cancer Spheroid Model. Small, 21 (24), 2502490, 2025*

4.1 Examining FasL:FasR Clustering

4.1.1 Introduction: FasL-FasR Interaction

The extrinsic apoptosis pathway constitutes a crucial focal point of innate and adaptive immunity. In this case, effector cells of the immune system, NK cells for innate immunity, or T cells for adaptive immunity can induce apoptosis to specific cells, as already touched upon in section 2.1.4. The effector cells recognize the cells as malignant to the host system, due to *e.g.* pathogen infection or degeneration to cancer cells. Then the effector cells present death signals to the malignant cells, inducing PCD through the extrinsic apoptosis pathway, followed by formation of the DISC and the caspase cascade, described in the introductory section 2.1.4, and shown in Figure 2.2b. But to set the apoptosis pathway into motion, it has to be induced with a *Kiss of Death* [161].

Berke, 1995

Ligand:Receptor Clustering

The *Kiss of Death* describes the interaction between the death receptors on the to-be apoptotic cell and the ligands inducing the apoptosis on the effector cell. Just as all other signal transduction mechanisms[1], the receiving cell needs to discriminate between signal and noise. Necessarily so, as otherwise all cells possessing the apoptosis mechanism would die spontaneously. The discrimination between signal and noise on a biological scale happens through the temporal and spatial clustering of proteins[2]. The outer signal needs to be "strong" enough to spatiotemporally cluster a number of receptors on the receiving cell, that transduce the signal to its inside. The transduction itself is done by positional fixation and/or conformational change of the receptor, which opens the binding sites for downstream proteins. Thermal fluctuation or short-lived interactions with other molecules could induce these conformational changes in the receptor and erroneously start the signaling cascade. To avoid this, the signal is only transduced and the downstream cascade only starts if enough receptors are activated at the same position, at the same time. The unlikelihood of spontaneous activation then exponentiates by the number of required receptors, decreasing the likelihood for spontaneous activation significantly. The key to the mechanisms behind this, however, lies in the structure of the ligands and receptors, which is also the case for FasL and FasR.

FasL and FasR Structure

Fundamental for the understanding of the interactions between proteins is their three-dimensional structure. Proteins consist of a linear chain of amino acids (aa) called the primary structure, which interact with each other (secondary structure) to form a distinct three dimensional shape (tertiary structure). The quaternary

[1] not only in biology, but also in the information technology

[2] with some exceptions, *e.g.* pMHCs as T-cell antigens, see Hellmeier *et al.*[113]

structure describes interactions with proteins of a different aa chain. As the function of a protein is dictated by its form and the arrangement of its aa in 3D, protein structure determination is a focus point of scientific research. Structure determination is usually achieved with crystallography, NMR spectroscopy, or CryoEM[3]. The interactions between proteins can be described as a *lock and key* mechanism of shape and structurally complementary proteins, fitting into another's binding sites[162]. Tripathi, 2018

This *lock and key* mechanism is also the mode of operation for FasL and FasR, and their structurally homologous family members. FasL and FasR[4] are members of the tumor necrosis[5] factor (receptor) super family (TNFSF and TNFRSF). The TNFSF has 19 members, and the TNFRSF has 29 members. While all members of both TNFSF and TNFRSF have a high structural homology within their family, their function within the cellular context can differ greatly. The TNFRSF is roughly split into three parts; the death receptors, the TRAF-interacting receptors, and the decoy receptors. While the death receptors induce downstream apoptosis (or necroptosis), the TRAF-interacting receptors are able to inhibit apoptosis and induce cell survival, or even proliferation. Thirdly, the decoy receptors can bind ligands and interrupt the signaling processes. An overview over interaction partners and their function in the cell is shown in Figure 4.1.

Even though the function within the cellular context might be different, the mode of binding interaction has been supposed to be very similar for all members of the superfamilies: The ligand binds to the extracellular part of the receptor, which transduces the signal through the cell membrane. Structural analysis of the ligands has shown, that they exist as homo- (or hetero-) trimers[164][165](Figure 4.2a). As shown in Figure 4.2a, the receptors (blue) bind into the moieties between the ligand (red) monomers in the trimer, making the multimerization of the ligand mandatory for receptor binding in the first place. Several studies showed dimeric and trimeric connections of receptors without ligand interactions, occuring at different parts of the protein: The extracellular part was found to form dimers[166](Figure 4.2b). Structural studies indicated trimeric motifs of the transmembrane domain of the receptor [167] (Figure 4.2c). Further, the FADD, binding intracellularly to the DD of Fas, was found to induce dimers of the FasDD [168] (Figure 4.2d). The form of the cluster, which transduces the signal to the inner of the cell, is governed by the protein structures and their mode of interaction. Eck & Sprang, 1989 Monkgolsapaya, 1999 Naismith, 1995 Zhao, 2020 Scott, 2008

Knowing the homology of the TNF(R)SF, as well as the dimeric (receptor dimers, FADD dimerization) and trimeric (trimeric ligands, trimeric receptor transmembrane domain) motifs of ligands and receptors, the clusters were proposed

[3]also: structure prediction from amino acid sequences can be done with machine-learning-based approaches, such as Alpha Fold. The Nobel Prize in Chemistry was awarded for this in 2024 to Demis Hassabis and John M. Jumper

[4]Fas is acronym for *FS-7-associated surface antigen*, also known as CD95, APO-1, or TNFRSF-6

[5]the *necrosis* part of TNF(R)SF being a historical nomenclature error

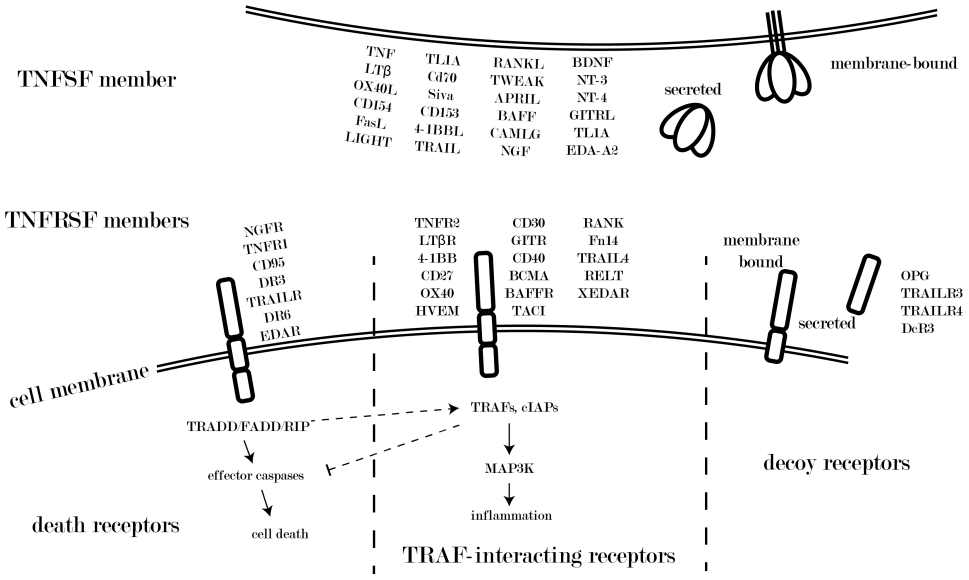

Figure 4.1: Interaction of TNF(R)SF Members

The ligands, members of the TNFSF, shown on top, can interact with the receptors, members of the TNFRSF, displayed on the bottom. The names of the ligands and the receptors are listed next to the respective sketches. The receptors can be roughly divided into *death receptors*, *TRAIL-interacting receptors*, and *decoy receptors*. The ligands, which can be membrane-bound or secreted in solution, interact specifically with the respective receptors and induce either cell death, inflammation, or be deterred from either, when they are intercepted by decoy receptors. The Figure is adapted from [163].

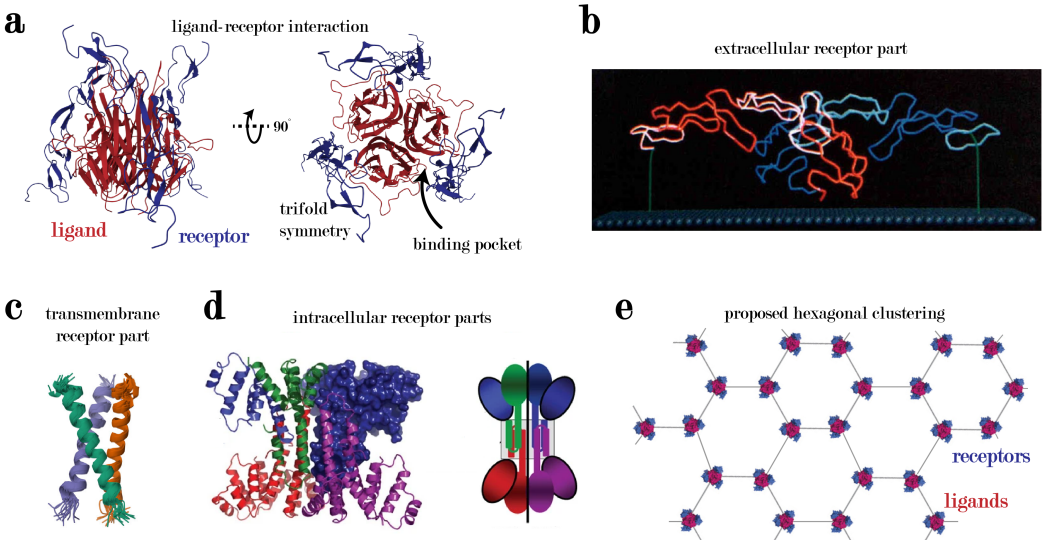

Figure 4.2: Structural Components of the TNF(R)SF

Several structural motifs were found to be consistently present in members of the TNF families. Here, some examples for these motifs are shown. (**a**) The members of the TNFSF are mostly trimeric, and form moieties between their monomers in which receptors of the TNFRSF can bind (pdb: 1D4V[165]). (**b**) The receptors were found to form dimers at their extracellular parts when no ligands were present [166], and (**c**) their intramembrane parts were found to form trimers (pdb: 7K7A[167]), and (**d**) FADD would induce dimerization of the intracellular FasDD when activated by ligand binding[168]. (**e**) From those dimeric and trimeric motifs, the clustering in a hexagonal, honeycomb-like 2D structure was proposed [169]. Panel (**b**) is reprinted and adapted with permission from [166], copyright 1982 Elsevier. Panel (**d**) is reprinted and adapted with permission from [168], copyright 2008 Springer Nature Ltd. Panel (**e**) is reprinted and adapted with permission from [169], copyright 2008 The American Association for the Advancement of Science.

Vanamee & Faustmann, 2018

Graves, 2014

Vanamee, 2022

to be hexagonal, honeycomb-like with an inter-ligand-distance (ILD) of roughly 10 nm[169]. The proposed cluster is shown in Figure 4.2e. This was also supported by a study that co-administered a stabilizing Ab to FasL, which connects the ligand-receptor complexes, supposedly in cluster formation, and thus increases the efficacy of apoptosis induction [170]. There is a further geometric argument for hexagonal cluster formation [171] : Information relay through the cell membrane presupposes dimerization of the FasDD on the intracellular part of the DISC, thus pro-caspase 8 can be cleaved into caspase 8 at the death effector domain. This presupposes two FasL coming together at a certain distance to facilitate the formation of an intracellular FasDD dimer for a minimal DISC. Two incoming ligands would relay the information by creation of one DISC. Depending on the cluster geometry, the number of additional DISCs with each additional ligands varies, but generally scales with the amount of edges coming from one ligands as vertex and the dimensionality of the cluster. In a triangular lattice this would be a maximum of six, in a square lattice four, and in a hexagonal lattice three. This can also only be the case for clusters spanning in 2D, not 1D, as linear clusters won't allow for as many connections. Given the trimeric nature of the central FasL, only the hexagonal pattern is possible, where in the two-dimensional cluster the ratio of FasL to DISCs becomes 1.45, with large numbers of ligands.

However, the proposed hexagonal structure of the clusters was not shown yet in a cellular context. Here, we approached this question indirectly. We utilized DNA origami's unique programmability to position FasL on the origami at different valencies and distances. These *nanoagents* were then presented to cancer cells whose response, *i.e.* their apoptosis kinetics were recorded.

The experiments were conducted under the working hypothesis that the closer the ligand pattern reflects the proposed hexagonal cluster with 10 nm inter ligand distance (ILD), the more effective the apoptosis induction would be.

4.1.2 Experimental Setup and Results

A special experimental setup needed to be established to analyze the efficacy of extrinsic apoptosis induction. Since the activation of this pathway *in vivo* happens at a cell-cell interface, it was supposed that the activation would be different when FasL is presented on a lipid membrane. This notion is supported by the low efficacy of TNF-based drugs, which are in solution by design. To test this, the setup needed to enable the display of the FasL on the DNA origami on the lipid membrane.

Experimental Setup

The experimental setup was established within a flow chamber, shown in Figure 4.3. The flow chamber consisted of a microscopy slide with six microfluidic chambers and a high-precision glass slide at its bottom. In the flow chambers, a lipid bilayer was established (a detailed description is found in the method section

A.1.12). On top of that bilayer, first, cholesterol-labeled DNA *anchor strands* were added, where the cholesterol moieties inserted themselves into the lipid membrane and the ssDNA anchor strands were thus able to freely diffuse in 2D. Next, DNA origami were attached to the *anchor strands*, as they bore complementary *anchor handles* (see Figure 4.3b,c). Then the streptavidin (SA) was attached to biotins, which were incorporated into the DNA origami structure, making up the *pattern* of the FasL later. Different biotin patterns were constructed by using biotin modifications on different positions on the origami. Lastly, the FasL was attached to the streptavidin, in the exact pattern given by the biotins on the DNA origami. Then cells were flushed into the flow chamber and their apoptosis kinetics were monitored with a fluorescence microscope over 24 h.

This experimental setup was partially changed for the different variations of the experiment. For variations of linker length and flexibility, the wild type (wt) streptavidin was exchanged for a monovalent streptavidin (mSA)[172]. The mSA[6] was modified with a ssDNA strand, for attachment to a complementary ssDNA handle on the DNA origami, instead of the biotin. Alternatively, the DNA origami-FasL nanoagent could be assembled outside the chamber, for administration in solution. A detailed description of the experimental setup is given in the method section A.1.13. Freitag, 1998

The FasL used was acquired from the company *Apogenix*. This FasL construct was the modified version of the naturally occurring FasL, presented in Kleber *et al.*[173], which is shown in Figure B.17: Firstly, it merely consisted of the extracellular part of FasL, as only this part interacts with the Fas receptor. Further, it was trimerized through the addition of a T4 foldon[7]. Kleber, 2008

The cell line used in these experiments is called *HeLa Apo mGFP* and was provided by the group of Cornelia Monzel. The Fas receptors in this cell line are overexpressed, and it also carries an internal mGFP tag. Tests by the group of Cornelia Monzel showed that the mGFP tag does not influence the downstream signaling. They further analyzed that the overexpression of these cells was ≈ 20 times higher than in wt HeLa cells, which guaranteed the transduction of the apoptosis signal.

DNA Origami-FasL Nanoagents

The successful construction of DNA origami-FasL nanoagents and their attachment to the lipid membrane was verified with several methods. Firstly, the structure DNA origami folding was verified via gel-electrophoresis, as displayed in Figure B.18. The purified as well as the unpurified DNA origami showed a strongly reduced electrophoretic mobility in comparison to the p7249 scaffold strand alone. This indicates a change in the Stokes radius of the structure, by folding into the wide Rothemund rectangle origami structure[57]. Rothemund, 2006

[6] produced under the supervision of Steffen Sedlak in the group of Herman Gaub

[7] which is the trimerization domain of the T4 phages' tail

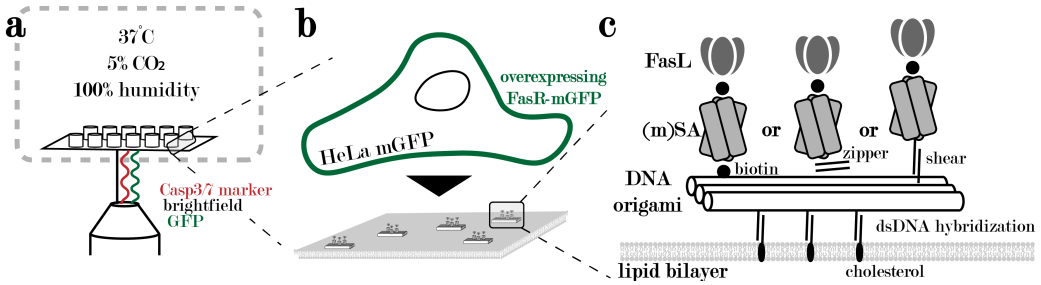

Figure 4.3: Experimental Setup for Apoptosis Tests

(**a**) The experiments were conducted in a 6-well slide, in a chamber with a controlled environment. The temperature was set to 37 °C, the humidity to 100 % (or with sealed chambers), and the CO_2 was set to 5 % (or L15 medium was used). (**b**) In the slide, a lipid bilayer with DNA origami for positioning the ligands was established and the HeLa mGFP cells settled on top. (**c**) The architecture of the DNA origami-FasL nanoagents is shown. The DNA origami was anchored to the lipid membrane by cholesterol anchors, attached to ssDNA, which hybridized to complementary strands on the DNA origami to dsDNA. The DNA origami carry specific connectors to connect to (m)SA, which then attach the biotinylated FasL. The specific connector on the origami for the (m)SA was either a biotin, for SA, or a ssDNA strand to connect to a, with complementary ssDNA, modified monovalent streptavidin (mSA), either in a zipper or a shear configuration.

Even though the formation of the DNA origami can be verified by the gel electrophoresis shift assay, the attachment of proteins could not be detected (protocol in section A.1.2). As seen in Figure B.18, the attachment of SA to the DNA origami did not evoke a large shift in electrophoretic mobility. This can be explained by the position of the protein on the DNA origami and the difference in molecular weight. The proteins are positioned in the very middle of the large, rectangular DNA origami, which does not alter the Stokes radius much. Additionally, each SA protein is just above 1 % of the molecular weight of the DNA origami[8].

The attachment of the proteins can be detected with microscopy techniques. For this purpose, both atomic force microscopy (AFM) and transmission electron microscopy (TEM) were employed. For the AFM measurements, the DNA origami was attached to a mica surface, by incubating it on the mica in solution. Subsequently, SA and FasL were attached to the DNA origami on the mica surface. The DNA origami as well as the protein pattern can be easily identified, as seen in Figure 4.4a. But also the height of the proteins can be extracted from the AFM data: As proteins attached to the DNA origami raise the contour in the z-direction, it was possible to distinguish between the attachment of SA or SA plus FasL (see Figure B.19).

For TEM, the DNA origami were negatively stained on a copper-coated carbon grid, described in detail in section A.1.3. The contour of the negatively stained rectangular DNA origami is visible in TEM, while the proteins can be identified as small white dots within the rectangle, see Figure 4.4b. The protein position can be clearly identified as a hexagon. Since the proteins SA and FasL cannot be discriminated between in TEM images, the attachment efficiency was estimated via the attachment of SA to the origami to be approximately 70 %[158] . Berger/Weck, 2021

For the experiments in this project, the position, valency, and attachment strategy of FasL were varied. As seen in Figure 4.4c, DNA origami were constructed with several different FasL patterns: with six FasL, in a hexagonal pattern of 5, 10, or 30 nm ILD, or with two FasL in 10 and 20 nm ILD, or only with one FasL. Further, the attachment strategy of FasL to the DNA origami was varied: Either with a rigid SA linker or with a flexible dsDNA linker attached to a mSA either in the zipper conformation or in the even more flexible shear conformation.

Apoptosis Kinetics Experiments

Initially, it was examined, whether the FasL conformation does change the apoptosis kinetics of the cells. Especially, the question arose, whether "pre-clustering" the ligands on the DNA origami achieved a better apoptosis induction. For this purpose, FasL was presented to the cells either on DNA origami, in a 10 nm ILD hexagon, or with FasL bound to a membrane, or in solution. As seen in Figure 4.5 the cells would settle onto the prepared lipid membrane, with FasL or nanoagents either between the cells and the lipid membrane or in solution. The cell mor-

[8]SA size: 60 kDa *cf.* rro size: 4,712 kDa

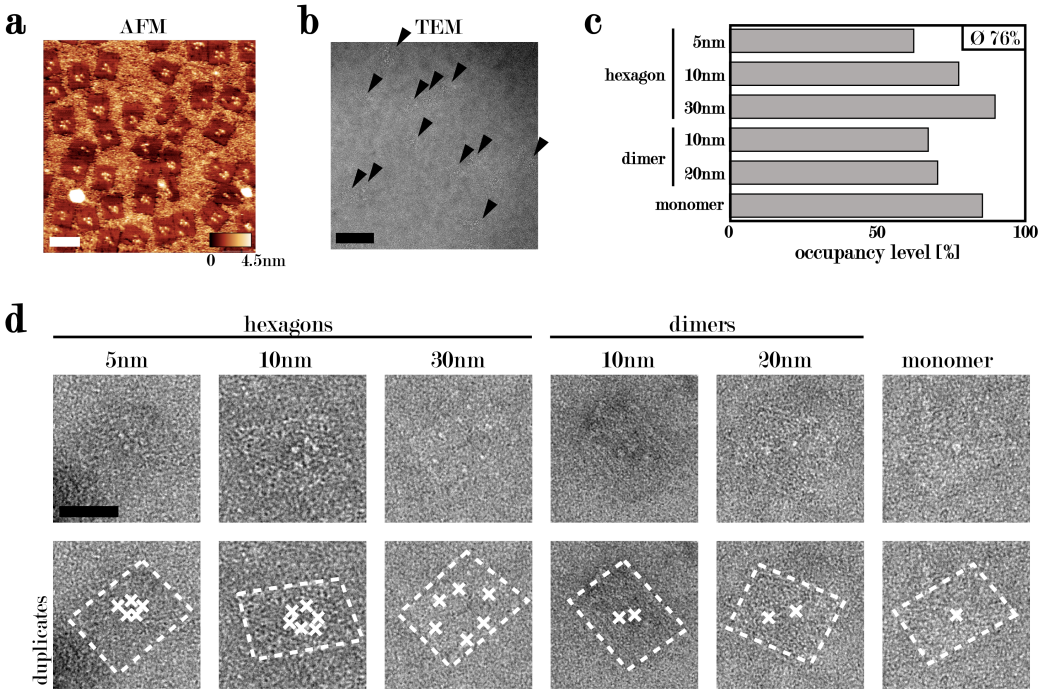

Figure 4.4: Nanoagent Characterization and Patterns

(**a**) AFM images of nanoagents: The image shows the height profile of the DNA origami-FasL nanoagents. The scale bar indicates the height, with higher structures being displayed in a brighter color. The DNA origami are easily visible as rectangles, with the proteins shown as bright, even higher dots on the rectangles. (**b**) TEM micrographs of nanoagents: The outlines of the DNA origami rectangles are dimly visible, and the proteins are visible as bright spots. The low contrast is a result of the similarly low diversion of the electron beam, by the small and thin molecules. (**c**) Occupancy statistics for the nanoagents. The average occupancy of the nanoagents was 76 %, with larger distance generally resulting in higher occupancy levels: Hexagons with 5 nm ILD: 66 %, 10 nm ILD: 82 %, 30 nm ILD: 94 %, dimers with 10 nm ILD: 71 % and 20 nm ILD 74 %. Nanoagents with FasL as monomers had 90 % occupancy. (**d**) TEM characterization of different DNA origami-FasL nanoagents: Cropped micrographs of each structure are shown with a duplicate below them having DNA origami and protein outlined in white for better visibility. The scale bar in (**a**) is 100 nm and in (**b**) is 200 nm, and the scale bar in (**d**) is 50 nm and holds for all micrographs. Panels were partially adapted and reprinted, all with permission from [158], copyright 2021 John Wiley & Sons.

phology was then observed every 10 min (or 20 min) for 24 h, giving information about cell fate. While healthy cells would spread and move around, apoptotic cells would round up, and then form well-visible membrane blebs, as shown in Figure 4.5a. The cell was marked as *apoptotic* as soon as the blebs occurred, thus at a late-apoptotic stage (*cf.* 2.1.4).

The cells showed drastically different responses to the different FasL presentations. Firstly, the control of only DNA origami on the lipid bilayer, depicted in grey in Figure 4.5b, did not induce any apoptosis in the HeLa cells. When FasL was administered in solution (light blue lines), cells underwent apoptosis, but only slowly. For 1 nM FasL the apoptosis started to show only about 20 h into the experiment and also only about 10 % of the cells in the population underwent apoptosis. Increasing the concentration (to 10 nM) increased the number of cells undergoing apoptosis to about 50 % and also shifted the first apoptosis events to an earlier time point, around 12 h after the start of the experiment. When 10 nM of FasL were presented on the lipid bilayer (dark blue lines), and not in solution, the apoptosis kinetics changed again. The first cells became apoptotic already in the first 2-3 h after the start of the experiments, and the amount of apoptotic cells at the end of the experiment was about 70 %. An increase in FasL concentration (to 100 nM) again shifted the onset of apoptosis kinetics a little bit earlier and increased the number of dead cells to just above 80 %.

However, the fastest apoptosis kinetics were observed for FasL which were presented on the DNA origami in a hexagonal pattern of 10 nm inter-ligand-distance (ILD). Already 1 nM of DNA origami-FasL nanoagent (equivalent to 6 nM of FasL) resulted in the quickest apoptosis kinetics, starting around 1 h into the experiment(red lines). It further resulted in the full annihilation of all cells in the population, after having induced apoptosis in approximately 90 % of the population after already 10 h. Impressively, the kinetics were also the same when only using 0.1 nM of the nanoagent. Comparing only the concentrations of FasL, this showed that (0.6 nM) of FasL pre-clustered on the nanoagent was more than 100-fold as effective as (100 nM) unclustered FasL.

This experiment showed a strong dependence of the kind of presentation of FasL on its ability to induce apoptosis. Firstly, FasL on the lipid surface was better in inducing apoptosis than the one in solution. Similar observations like this were also made in later experiments, determining dose-response curves for the 10 nm ILD hexagon nanaogent (not shown here but in [158] Figure 5). This could be the result of an effect caused by the organization in different dimensions: FasL in solution needs to diffuse through a -comparably- large 3D volume and be attach to the cell at the same time, at the same position. Whereas the FasL attached to the surface can only diffuse in two dimensions and thus also in much less space. There would simply be more FasL close to the cells' surface at any time.

Berger/Weck, 2021

Secondly, the nanometer-precise clustered FasL was again much more effective in inducing apoptosis. This led to the question of to what degree the apoptosis induction is dependent on the ILD between the FasL proteins.

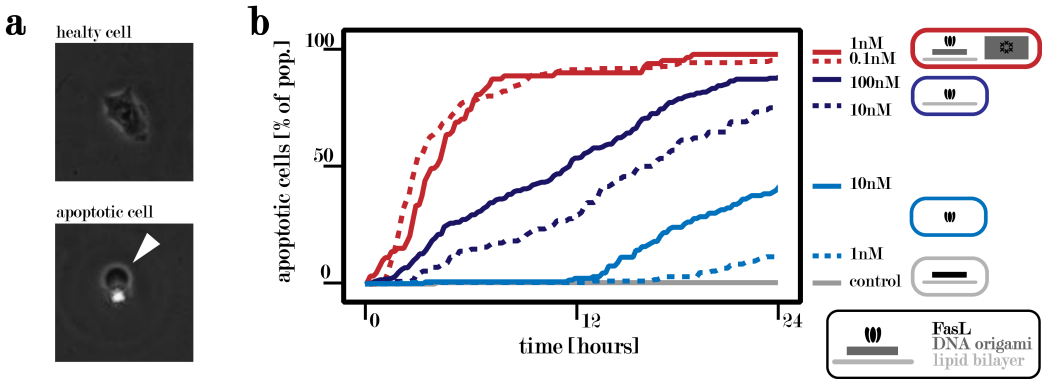

Figure 4.5: FasL Pre-Clustering Induces Strong Apoptosis Signal

(**a**) Morphological differences in healthy and apoptotic cells: The apoptotic bleb (indicated with a white arrow) serves as an easy visual indicator for apoptotic cells, while healthy cells spread on the surface. (**b**) The pre-clustered FasL on the DNA origami induces apoptosis efficiently in cells. The colors of the curves indicate the respective presentation of FasL, while the solidity of the curves indicates relative concentrations: The grey line is a control, with origami, without FasL. The light blue lines indicate FasL administered in solution, solid (10 nM) and dotted (1 nM). The dark blue lines show FasL presented on a lipid surface, solid (100 nM) and dotted (10 nM). The red curves are FasL pre-clustered on a DNA origami in a hexagon shape with 10 nm ILD, the solid line is for 1 nM, and the dotted line 0.1 nM. Panels were partially adapted and reprinted, all with permission from [158], copyright 2021 John Wiley & Sons.

Variations of FasL Pattern

Having shown that an ILD of 10 nm was much more effective in inducing apoptosis than unclustered FasL, the ILD was varied to test the dependence on the exact positioning. With this, the hypothesis was examined, that the prepositioning only in the exactly correct pattern would support apoptosis induction. To test this hypothesis, several more FasL patterns on the DNA origami were created: Versions of the hexagonal pattern with increased or decreased ILD, and dimeric and monomeric, as described above.

The distance and pattern of the FasL made a significant difference in apoptosis kinetics. When the ILD of the hexagon was varied, the number of apoptotic cells plummeted, and the onset of the apoptosis kinetics shifted to later points in time, as seen in Figure 4.6. This was the case for both, increasing the ILD to 30 nm, and decreasing the ILD to only 5 nm. Also, apoptotic cells only started occurring several hours into the experiment. This was in stark contrast to the 10 nm ILD hexagons, which induced apoptosis very quickly, *i.e.* already in the first hour of the experiment, and also annihilated the whole cell population. This experiment proved a strong dependence of apoptosis induction on the ILD of the FasL: The correct distance, mimicking the naturally found 10 nm IDL, seemed to be a requirement for effective apoptosis induction.

Next, the influence of FasL valency on apoptosis induction was tested: The valency of the nanoagent was reduced to two FasL, in 10 or 20 nm ILD. Surprisingly, both nanoagents had a subfraction of the cells undergoing apoptosis at early stages, almost as fast as the 10 nm ILD nanoagents, but in general had apoptotic events more spread out on the temporal axis. These nanoagents were also able to induce apoptosis in most of the cells in the population.

These observations could be interpreted in the following way: With the dimer interpreted as the main signalling unit, the main upside of the hexagonal arrangement is raising the probability of two FasL being attached in 10 nm ILD. The connection efficiency of 70 % on average, would result in only about 50 %[9] of all "dimeric" nanoagents being occupied by two FasL. This is tantamount to a reduction of the effective concentration of nanoagents of 1/2, disregarding monovalent nanoagents. On the other hand, six attachment sides in hexagonal arrangement with an ILD of 10 nm reduce the probability of not having two FasL in 10-20 nm ILD to merely 1 %[10]. This indicates that large, hexagonal clusters of FasL and FasR are not necessarily required for a strong transduction of the apoptosis signal.

Variations of FasL Attachment

Lastly, the mode of attachment of FasL to the DNA origami was varied. This was done initially to rule out effects of double-binding of FasL to the tetravalent SA molecule, but then the flexibility of the attachment mode turned out to have a

[9] this is the counterprobability of having both FasL attached; 1 - 0.7^2

[10] this is the sum of the probabilities for no FasL or only 1 FasL; $0.3^6 + 6 * 0.7 * 0.3^5$

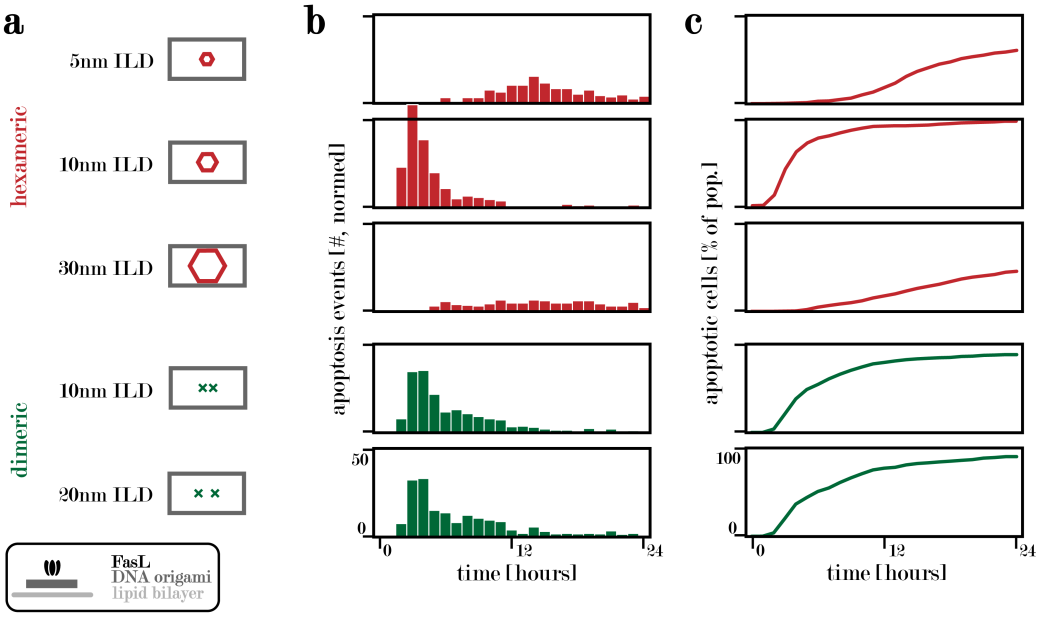

Figure 4.6: Impact of FasL Pattern Variations

(**a**) Schematic representation of the different FasL patterns on the DNA origami. Red indicates hexameric patterns in a hexagonal structure with 5 nm, 10 nm, or 30 nm ILD. Green indicates dimeric patterns with either 10 nm or 20 nm ILD. (**b**) Histograms on apoptosis events until the respective hour during the experiment. Apoptosis events were recorded upon the cells' morphological change, *i.e.* bleb formation. Red histograms show the behavior of cells exposed to the respective hexameric patterns, corresponding to the sketches on the left, and green histograms show cell behavior when exposed to dimeric patterns. The total number of cells in the respective groups was normalized to 100, for better graphical visibility of the nanoagent impact. (**c**) Amount of apoptotic cells as percentage of the total number of cells in the respective populations over time. Colors indicate results of the respective FasL patterns on the left. (**b**) and (**c**) are based upon the same set of data. Panels were partially adapted and reprinted, all with permission from [158], copyright 2021 John Wiley & Sons.

direct effect on the apoptosis induction. Instead, a modified version of it, a monovalent streptavidin [174], consisting of three inactivated and one active streptavidin monomer. The mSA has one active binding site and a cysteine on the opposite side of the molecule, which was subsequently labeled with a DNA strand. In this way, only one biotin-binding pocket is active for the FasL-biotin to connect to, while the mSA itself was attached to the DNA origami through dsDNA hybridization. Sedlak, 2018

The dsDNA connection was designed to have one of two geometries. The two different dsDNA geometries are shown in Figure 4.7b and c, one being a *zipper* geometry, with the dsDNA bulging out to the side, the other being a *shear* geometry with the full length of the dsDNA between origami and mSA. The shear conformation connects the mSA and thus the FasL much more loosely to the DNA origami, than the zipper conformation, which itself is more loose and flexible than the initial bioting-SA-biotin-FasL connection used above.

The geometry of the dsDNA linker between origami and mSA had a direct influence on the effectivity of apoptosis induction. As seen in Figure 4.7, the higher the flexibility of the linker, the later and fewer apoptosis events were recorded. The peak at 2 h in apoptosis events for the 10 nm ILD hexagon pattern vanished and the apoptosis event distribution became flatter when decreasing the linker rigidity. This effect was observed for all of the configurations and increased with increasing linker flexibility. Apoptosis event distributions which were already flat when SA was used, *e.g.* the 5 nm and 30 nm, became even more flat and, especially for the shear conformation of the dsDNA, had a much later onset. The distributions for 10 nm and 20 nm ILD dimers also suffered the same loss of the initial apoptosis peak and flattening of the curve, as observed for the 10 nm ILD hexagon. This indicated a strong dependence of apoptosis induction capability on the positional accuracy of the FasL on the nanoagent.

This leads to the question, whether the detrimental effects are caused by a positional or a directional inaccuracy of the more flexible linkers. Here, positional inaccuracy means fluctuations in the ILD and pattern geometry of the FasL on the 2D nanoagents surface. And directional inaccuracy means fluctuations of the angles/directions with respect to the FasR and the other FasL. 10 nm and 20 nm distances in the dimer patterns both inducing apoptosis similarly well, indicating a certain distance *range* for optimal apoptosis induction. This would mean that a mere fluctuation in position, but not angle/direction, would not be as detrimental as we observed the effect to be. Similarly, the 5 nm hexagon would then profit from an increased positional inaccuracy, enabling its FasL to arrange properly. However, this was not observed. The increased linker fluctuation caused a decrease of apoptosis signalling for each FasL pattern. This indicates that most probably an inaccuracy in the FasL *angles* or *directions*, relative to all other proteins partaking in the interaction, is the main cause for the less effective signalling.

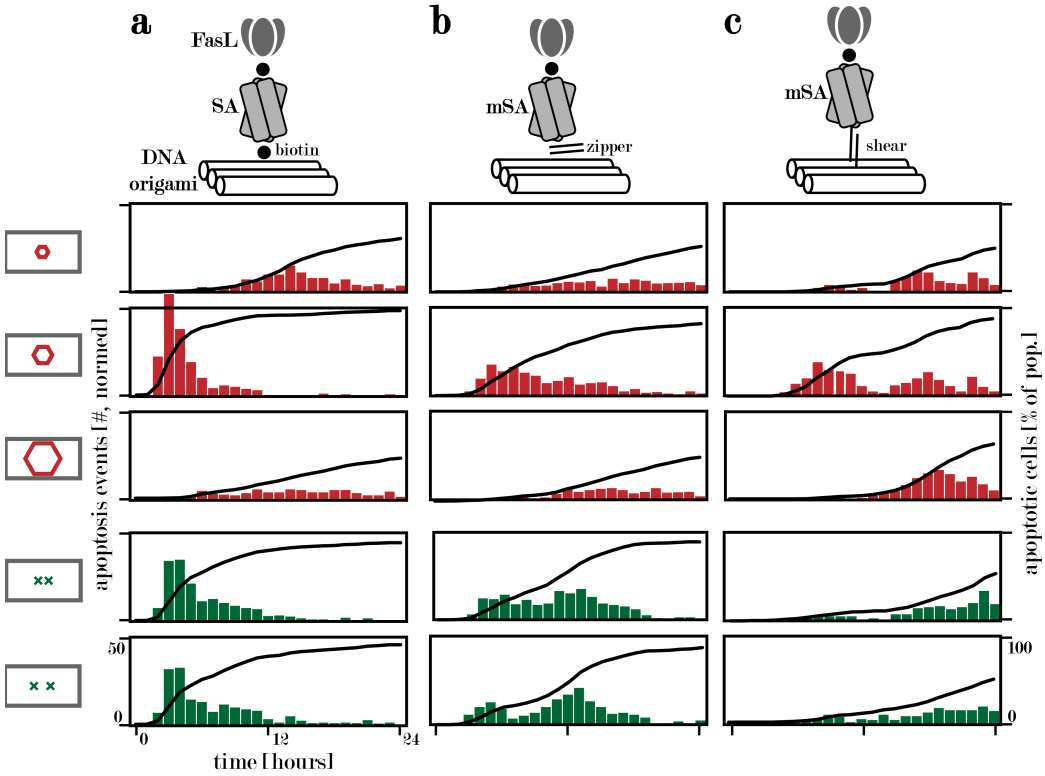

Figure 4.7: Impact of FasL Linker Variations

Histograms of apoptosis events and percentages of dead cells in the populations over the 24-h experiment. The linkers between DNA origami and FasL and the ligand patterns on the DNA origami were varied. The respective linkers are shown on top of the graphs, and the respective ligand patterns are on the left of the graphs. Colors indicate the respective geometrical patterns of ligands on the DNA origami: red indicates hexameric, hexagonal patterns, green indicates dimeric patterns. (**a**) Shows the same graphs as in Figure 4.6. These nanoagents were constructed with FasL linked via SA-biotin connections to the DNA origami. The apoptosis histograms and dead percentage are shown in the same graph. (**b**) Nanoagents with a zipper dsDNA conformation between the DNA origami and the mSA, attaching the FasL. (**c**) Nanoagents with a shear dsDNA conformation between the DNA origami and the mSA, attaching the FasL. Panels were partially adapted and reprinted, all with permission from [158], copyright 2021 John Wiley & Sons.

Further Experiments and Controls

Cell death can have several causes. To ensure that the observed cell death events were indeed due to apoptosis, the formation of blebs were correlated with the occurrence of biochemical processes in the cells. This was achieved with a commercially available caspase 3/7 marker. As seen in Figure B.20 the fluorescence signal from the caspase marker appeared approximately 4 h before the cells showed membrane blebbing. The correlation of blebbing and the early apoptosis marker for caspase 3/7, proved that the mode of cell death was indeed apoptosis and that the appearance of the bleb can be reliably used as a simple morphological indication for apoptosis events.

It was ruled out that apoptosis was caused by a different cause than the nanoagent. It was reported that apoptosis can be caused by a lack of cellular adhesion points[16], but the combination of cholesterol DNA and serum in the cell media was enough for the cells to attach to the otherwise passivated surface. Experiments without FasL present showed negligible apoptosis events during the whole experiment. Frisch, 1994

It was also ruled out that the nanoagents were causing apoptosis through a different effect. For this, non-cancerous HuH7 lacking the FasR overexpression, were used to conduct the same experiment, but ended up with less than 10 % of dead cells even after 30 h.

4.1.3 Other Work

Similar experiments were conducted on the TRAIL-DR4/5 system, another member of the TNF(R)SF[175]. The used TRAIL peptide showed similar dependency on ligand distance when positioned on the DNA origami and presented to cells. Here, the most optimal spacing found was 5 nm ILD, which varied from our findings for the related FasL-FasR system. Wang, 2021

However, there are several differences between our study and the study of Wang *et al.*: Instead of the TRAIL protein, a peptide was used, whose mode of binding to the receptor is not known [11]. Thus the natural binding mode of one receptor -in the moiety between two ligands of the ligand homotrimer (see section 4.1.1 and Figure 4.2a)- might not be given. Thus the ligand does not need to be trimeric in the first place to facilitate receptor binding, as it is in nature. The mode/position of binding being unknown has even further implications: The peptide does not necessarily need to bind at the same region of the receptor as the natural ligand. Also, the direction of C- and N-termini is unclear, and thus is the position of the dsDNA handle, which in turn can lead to an unnatural position/conformation of the receptors. The receptors could be pulled by the dsDNA handle and/or squeezed by the adjacent DNA origami, in such a way that the position of the receptor is altered in comparison with its natural state. Additionally, similar results had been

[11] the first author told me in our Email correspondence

Lamanna, 2012 reported for the chemical linkage of TRAIL peptides [176].

The TRAIL peptides were also employed later in the construction of a pH-
Wang, 2024 responsive dynamic DNA origami [177], effective against tumors *in vivo*. Further, the use of peptides instead of proteins simplifies the experimental setup. The te-
Shang/Bartels/Weck, dious protein expression, purification, and functionalization [159] is circumvented.
2025 This makes the use of peptides easier to handle by the experimenter and also better scalable and therefore better suited for medical applications.

4.1.4 Conclusion

In this section, unambiguous data on the ligand organization-dependent nature of the apoptosis signal transduction was shown. Four factors determined nanoagent efficacy: (i) nanoagent presentation, (ii) positional accuracy, (iii) ligand spacing, and (iv) ligand valency.

The arrangement of FasL on the DNA origami in 10 nm or 20 nm distance increased the number of cells in the population undergoing apoptosis and shifted the onset of the apoptosis events to an earlier time. Deviation from this most optimal ILD, diminished the apoptosis efficiency again tremendously.

However, these indirect experiments are -in the best case- only indicators for hexagonal clusters with 10 nm ILD, but no evidence. Since the experimental setup is indirect, it cannot be inferred whether we provoked large-area clustering in the HeLa cells. The dimers in 10 nm and 20 nm were also able to evoke quicker apoptosis kinetics in the cells, just not as quickly as the hexagonal structure with FasL on the origami.

A different approach is needed to determine the *actual* mode of clustering. The most optimal approach for this purpose is super-resolution microscopy. From structural data and the data shown in this thesis, one would expect ILDs from 5-20 nm, which is far below Abbes' limit for light microscopy. This can only be done with super-resolution microscopy, which already reached resolutions on the Angström level.

Bartels, 2023 A first paper on super-resolving the Fas system was published in 2023[178]. Bartels *et al.* employed a Förster resonance energy transfer-based approach to determine the fraction of monomers and oligomers in different stages of the apoptosis induction process. They found almost exclusive monomeric FasR on the surface, without external cues. The amount of FasR in a dimerized state was below 5 % and showed a distance of $\approx$ 12 nm, indicating their dimerized state being tip-to-tip of the extracellular part of the FasR. Upon the addition of FasL the receptors formed dimers and trimers, but only about 15 % of them, and no higher-order structures. They also proposed a model for the ligand receptor interactions here, where the receptors attach to one ligand alone, and thus maximally form trimers.

However, the organization of FasL on the surface of lymphocytes is unknown. The respective ligand and receptor organization on the signaling cells and the receiving cell could interact to form larger or again different kinds of patterns.

Also for this problem, super-resolved imaging would be the optimal approach.

Lastly, the highly artificial nature of the experimental setup used needs to be considered. *In vivo* cancer forms solid tumors and the cells find themselves in a different environment, only in contact with other cells and surrounded by somatic stimuli. This might lead to different behavior towards the previously apoptosis-inducing cues. In the next section, this will be explored further, together with the ability of the nanoagents to penetrate through tumor tissue, which both are prerequisites for the use of DNA origami-FasL nanoagents as nanotherapeutics.

4.2 DNA Origami-FasL Nanotherapeutics

4.2.1 Introduction: Nanotherapeutics

Extrinsic apoptosis induction is a directed process, with close to no spill-over to healthy tissue, including non-immunogenicity of the debris from the apoptotic cell. Apoptosis is a very frequent bodily process; it is estimated that about 50 billion cells undergo apoptosis per day in an adult human[179] [12]. Apoptosis is such a frequent process and the fact that it takes place without disturbing other somatic functions makes it a very attractive therapeutic approach. This therapeutic could be able to pick out specific cells and harness the extrinsic apoptosis induction pathway to clear them from the organism.

Kolb, 2017

However, therapeutics for apoptosis induction through the extrinsic pathway did prove to be not very effective so far. As already mentioned in section 4.1.1 the lack of efficacy of those therapeutics was suspected to be due to a lack of ability to form ordered clusters of the respective receptors. This was supported by the fact that an increase in efficacy was obtained when conformation-stabilizing antibodies were co-administered [170]. These antibodies would stabilize two ligand-receptor pairs in position with respect to the other pair.

Graves, 2014

Another study showed that FasL arranged on lipid nanoparticles was able to eradicate cancer cells in 2D, but a tumoroid grafted into a mouse was not[180]. Contrariwise, these tumoroids even increased in size, compared to the controls without FasL nanoparticles. The authors attributed this behavior-switching to the higher tyrosine phosphorylation when in cell-cell contact.

GülcülerBalta, 2019

We supposed, that the most effective nanoagents, presented in section 4.1 could overcome the barrier to apoptosis induction in 3D tumoroid models seen in [180]. A nanoagent able to do so could pave the way for new therapeutic approaches in medicine. However, the use of nanotherapeutics *in vivo* faces several more problems.

Challenges for Nanotherapeutics

Firstly, there is the problem of delivering the therapeutic through the organism, to the desired site. A straightforward approach is administering directly into the site. But that site might be inaccessible from the outside, span large areas, or the respective cells are scattered through the body. Additionally, this method is *invasive*, can damage tissue and harm the patient, and thus should be avoided as far as possible. Another approach is using the vascular systems of the organism to deliver the therapeutic. This is either done by intravenous injection, which again is somewhat invasive, or by oral or topical administration. Therapeutics administered orally face harsh pH values in the stomach and the additional hurdle of crossing the intestinal barrier to the bloodstream. Topically administered therapeutics

[12] *cf.* the human body has around 30 trillion cells

need to penetrate through the even tougher dermis and into the bloodstream.

Secondly, therapeutics in the bloodstream can be cleared again from the organism. The spine filters out nanoparticles from the blood of 100-200 nm and larger [181]. The kidney is also able to filter out nanoparticles of small sizes and translocate them to the bladder [182]. Additionally, antibodies can mark nanoparticles for opsonization, leading to recognition and digestion by macrophages. Cataldi, 2017 Du, 2018

Thirdly, the therapeutics need to be target specific in their effect. They need to again be able to exit the bloodstream, move through tissue and arrive at their specific target, avoiding unwanted interactions. Specificity for a certain target can be accomplished by certain surface markers on the nanoparticle; protein ligands or chemical modifications which interact specifically with the target cells [13]. Also, target cells positioned deep in tissue can only be reached by penetration of the nanoparticle through the tissue. This is especially important for the targeting cells deep in organs or elimination of cancer tissue. All this while evading the engagement with the wrong cells and thus evoking off-target effects.

Lastly, the nanoparticle needs to have a therapeutic effect. This can be an agent that the nanoparticle only transports to the desired site, like the cytotoxic agent doxorubicin, which is frequently used as cancer therapeutics. This could also be biomolecules like siRNA, knocking down cellular functions, mRNA encoding for proteins, or proteins acting as cues for cellular recognition apparatus.

In summary, the aim is to minimally-invasive administer the nanoparticle, which migrates to the target site and exclusively engages with the desired cells. These aims partially contradict each other, which makes the respective design process challenging. The nanotherapeutic needs to have a certain size, too large it would be filtered out by the spleen, too small it would be filtered by the kidney. And all this, while it needs to have the capacity to carry modifications for specific cell targeting, and the effective agents at the same time. The modifications for targeting and affecting the cell also should not impede their respective properties. The nanoparticle needs to be robust enough to withstand the respective kind of administration, on the other hand, a prolonged circulation time would increase the risk of off-target effects. Then again, its size, structure and modifications might alter its ability to penetrate tissue.

This Work

In this doctoral thesis, the viability of DNA origami-FasL nanoagents as cancer therapeutics was examined. For this purpose, we studied the ability of DNA origami to penetrate through cancer spheroids, as a tumor tissue model, and the ability of DNA origami-FasL nanoagents to induce apoptosis in this large, 3D spheroid model. Both parts revealed the effect of DNA origami design choices on the nanoparticle behavior. The biodistribution and administration pathways were

[13] *e.g.* Ma *et al.*[183] used folic acid modification on DNA origami to target polarized M1 macrophages specifically

explicitly not examined, as we deem the process of nanoparticle design stepwise and iterative.

4.2.2 Experimental Results

This study can be roughly divided into three parts. The penetration of the different DNA origami through large spheroids was initially analyzed to pinpoint the design parameters for DNA origami influencing it. Then the influence of DNA origami structure and attachment strategy of FasL on the nanoagents' ability to induce apoptosis in such cancer spheroids was examined. Finally, the fate of all cells in the spheroids was analyzed.

DNA Origami Design

Three different DNA origami were designed, varying in their size and flexibility. The prior study (in section 4.1 above and the publication[158]) used Rothemunds rectangle origami (in the following abbreviated as *rro*) [57]. This large rectangular sheet has been used widely as a standardized peg-board structure since the ssDNA staple ends are positioned evenly with a distance of quite exactly 5 nm from each other. It was chosen as the first DNA origami structure for the study, its structure is depicted in Figure 4.8 and Figure B.21. To test the influence of DNA origami size, we designed a miniature version (in the following abbreviated as *mini*) of the rro origami. This DNA origami, as can be seen in Figure 4.8 has a much smaller size than the rro but is also designed in a square lattice, and with an almost identical staple routing (better seen in Figure B.22). To test the influence of DNA origami flexibility on its ability to penetrate spheroid tissue, we designed a third DNA origami, of the same size as the rro, but of different internal structure. For this purpose, the wireframe DNA origami design method was employed [61], which has a much higher flexibility than lattice-based designs. A wireframe DNA origami (in the following abbreviated as *wf*) was designed with the same dimensions as the rro origami, so it would only differ in the internal structure, seen in Figure B.23. The design process is also described in section A.1.16. The respective scaffold and staple sequences for the structures can be found in sections A.2.1 and A.2.2.

Berger/Weck, 2021

Rothemund, 2006

Benson, 2015

Characterization of the DNA Origami

To verify the differences in size and flexibility of the structures, the DNA origami structures were characterized. The size of the rro was determined to be 87.4 ± 4.2 nm by 64.2 ± 3.6 nm, similar to the size of the wf origami with 77.9 ± 5.5 nm by 50.5 ± 4.2 nm. The mini origami was much smaller with 33.9 ± 3.1 nm by 24.9 ± 2.1 nm. The areas of the respective DNA origami were then roughly 5600 nm^2 for the rro, 3900 nm^2 for the wf (disregarding the corners), and 850 nm^2

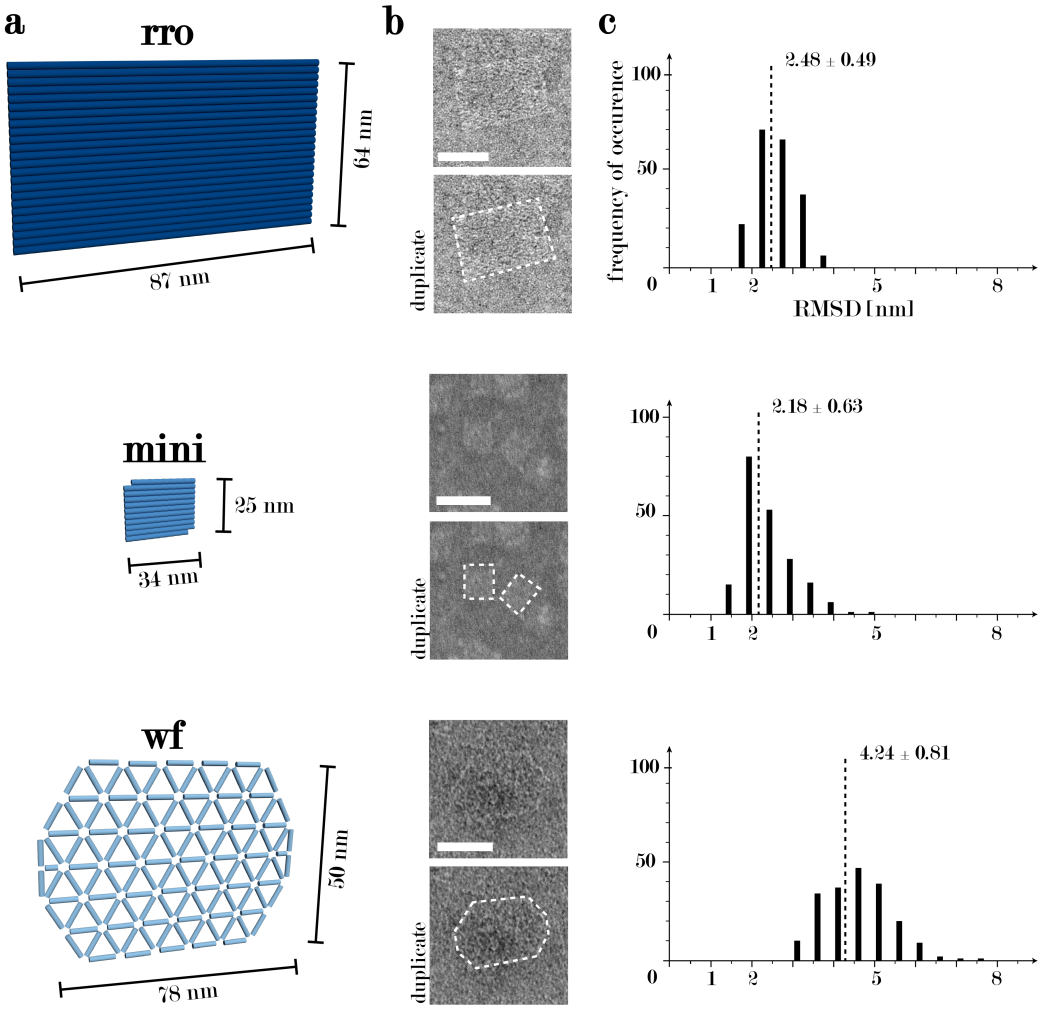

Figure 4.8: Three DNA Origami with Different Structural Properties

(**a**) Sketches and sizes of the three DNA origami structures. The rro DNA origami has a size of 87x64 nm, the mini DNA origami approximately 34x25 nm, and the wf DNA origami has a size of 78x50 nm. The respective colors of the DNA origami hold for all graphics in this section. (**b**) Cropped TEM micrographs displaying the respective DNA origami structures on the left. The upper image is duplicated and the outlines are indicated in white on the lower micrograph. (**c**) Histograms of the structural fluctuation of the DNA origami as RMSD from oxDNA simulations. The rro and the mini DNA origami show low fluctuations, with 2.48 nm and 2.18 nm RMSD. The wf DNA origami showed larger fluctuations with 4.24 nm RMSD. The respective averages are indicated with a dotted line in the histograms. The scale bars are 50 nm and hold for all TEM micrographs. Panels were partially adapted and reprinted with permission from [160], copyright 2025 John Wiley & Sons.

for the mini DNA origami [14]. The protocol for TEM analysis is described in section A.1.3.

To determine the flexibility of the DNA origami, molecular dynamics were employed. The three structures were simulated with oxDNA and the molecular fluctuations were extracted and analyzed (see section A.1.17). The root mean square fluctuation (RMSF) for the rro and the mini origami were very similar: The RMSF of the rro was 2.48 ± 0.49 nm and the RMSF of the mini was 2.18 ± 0.63 nm. The flexibility of the wf DNA origami was approximately double that with 4.24 ± 0.81 nm.

Effects on Penetration

Having analyzed the structural properties of the three DNA origami, their penetration into spheroid tissue was determined. For this purpose, large, 3D spheroids were grown. On the third day, the spheroids reached a diameter of approximately 0.5 mm, visible by the naked eye, and resembling real tumors *in vivo* much more than adherent cells in 2D. The DNA origami were added to the spheroids and their penetration progress was measured at different points in time.

Since tissue of that size is not penetrable by light microscopy, two advanced microscopy methods were combined to yield proper fluorescence signals. Firstly, the spheroids were chemically cleared after their incubation with the DNA origami. This altered the cellular diffraction limit and aligned it with the diffraction index of the surrounding medium. With this, we were able to use confocal microscopy to scan through the whole spheroid without signal loss. Secondly, the signal from the DNA origami was amplified by FISH[42]. A version of fluorescent FISH probes was employed, DNA origami FISH, developed in the laboratory of Leo Chou[177]. Here, DNA hairpins labeled with a fluorophore, hybridize to a target sequence. The hybridization of the hairpin opens a binding site for another hairpin, a process that repeats and then leads to the accumulation of hairpins and thus fluorophores at the target. This process is shown in Figure 4.9a. This way, the fluorescence signal is amplified manifold compared to labeling with single fluorophores. The protocol for spheroid seeding, growth, and the DNA origami penetration tests can be found in appendix sections A.1.7 and A.1.8.

Langer, 1982

Wang, 2024

The penetration depth was then analyzed for the different DNA origami at various incubation times. 0.5 pmol of DNA origami were added to each spheroid and the salt conditions were harmonized across the different origami samples. The penetration was stopped by fixation of the spheroid, follwoed by permeabilization, incubation with the fluorescence probes, and clearing. The cleared spheroids were then imaged at different vertical positions on a confocal microscope, shown as a sketch in Figure 4.9b. This experiment was repeated for each origami and each incubation time at least three times.

[14] Interestingly, the calculated electron density of the respective structures was very similar: rro ≈ 0.99 e/nm^2, wf ≈ 0.97 e/nm^2, mini ≈ 1.29 e/nm^2

Information on penetration depth was extracted from the fluorescence images. Chemically clearing the spheroids leads to a strongly reduced contrast in the bright-field (BF) channel, which can be seen in Figure 4.9c. The bright blob-like artifacts seen in the Brightfield channel, vanish in the fluorescence channels. Hoechst stain renders the cell nuclei well visible as large spots throughout the whole spheroid. As the overexpressed FasR in the respective cell line carries a mGFP on its intracellular part, the outlines of the cell membrane.

Both fluorescence signals are easily visible with no quality loss across the whole spheroid (see also the montage of the z-series in Figure B.24). This proves that the chemical clearing method worked, and the origami's fluorescence signal will not be diminished deep into the tissue.

The penetration depth of the DNA origami was extracted from the position of the fluorescence ring inside the spheroid. The fluorescence channel of the DNA origami (Alexa 647) showed three distinctly different shaped/sized signals: There is a very even, low fluorescence background, a few very small, but comparably bright spots, and a granular fluorescence ring at the outside of the spheroid. The even fluorescence background and the bright spots could also be seen in the control (*cf.* Figure 4.9), while the fluorescent ring was only seen in the samples with DNA origami. This fluorescent ring was thus identified as the positional signal of the DNA origami[15].

The position and thickness of fluorescent rings gave information on the penetration progress of the origami. With all DNA origami, the depth of the fluorescent ring increased with time, spreading further and further into the spheroid. The rate at which the ring spread into the tumor was, however, different for the different DNA origami, indicating a structure-dependent behavior, see Figure 4.10. The penetration depth was highly consistent for the respective structures and incubation times. After one hour all DNA origami showed a fluorescence signal approximately 40 μm into the spheroid. Similarly, the penetration depth of all origami after 4 h was approximately 50 μm deep. From these data points no difference in penetration behavior could be determined. The difference in penetration behavior appeared only for longer incubation times: After 16 h the fluorescent ring reached a depth of 70 μm of the rro, 65 μm for the wf, and 140 μm for the mini origami. This trend was the same for the penetration depth after 32 h: The rro penetrated roughly 100 μm through the spheroid, the wf about 90 μm, while the mini DNA origami did not even show a fluorescent ring anymore. This suggests full penetration of the mini origami after 32 h, which is further supported by comparing the penetration speeds.

The speed of the DNA origami penetration through the spheroid was calculated from the penetration depths. For this, the data points of the penetration depths were fitted linearly, and the incline was extracted. The speed of the rro was 1.99 μm/h, the speed of the wf was 1.69 μm/h and the speed of the mini DNA

[15]the number of bright fluorescence spots was reduced by using filtered buffers and media, but unfortunately never fully eradicated

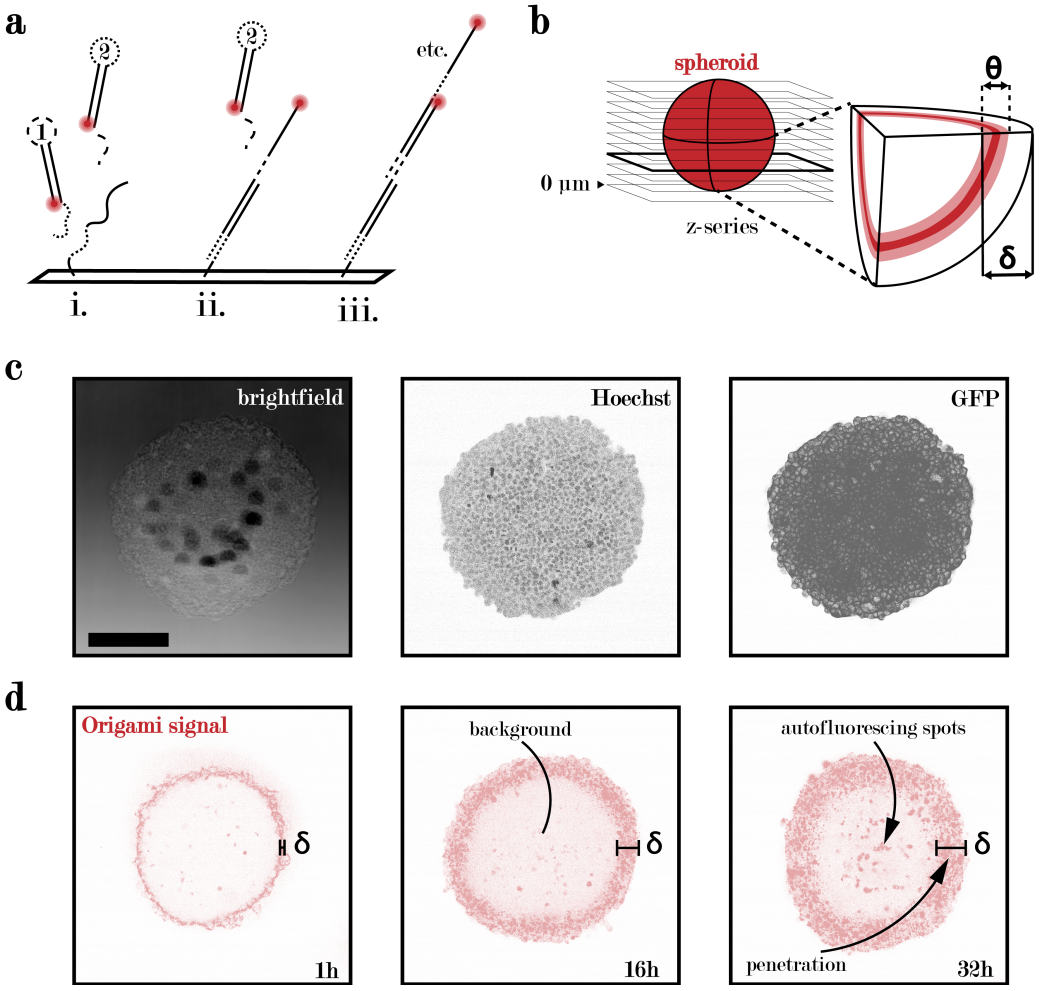

Figure 4.9: Spheroid Penetration Experiment

(**a**) The principle behind DNA origami FISH: (i) To an ssDNA strand on the DNA origami, a first, fluorescent hairpin binds, (ii) opening a binding position for the second fluorescent hairpin in the process. (iii) The second hairpin binds to this newly opened position, again opening a position for the first kind of hairpin to bind to. (**b**) Sketch of the confocal scan through the spheroid. For analyzing the penetration behavior of the DNA origami the thickest point of the spheroid was chosen. From these images, the penetration depth δ and the ring thickness θ was extracted. (**c**) Different signals through an exemplary spheroid: Brightfield signal, Hoechst signal, indicating the cell nuclei, and GFP signal, showing the cell outlines via the mGFP labeled FasR. The fluorescence signal in the middle of the spheroid showed no qualitative difference, compared to the signal at the outside, indicating successful clearing of the spheroid. (**d**) Exemplary images of DNA origami penetration through the spheroid. The penetration depth of the DNA origami increases proportionally with incubation time. Indicated are the three different fluorescence patterns: Dim and diffuse background, unspecifically autofluorescing spots, and the penetration signal from the DNA origami, as a thick and coarse ring around the spheroid. The scale bar is 200 μm and holds for all fluorescence images. Panels were partially adapted and reprinted with permission from [160], copyright 2025 John Wiley & Sons.

origami was 6.79 μm/h, more than three times as fast as the larger structures. This supports the above claim, that after 32 h the mini has penetrated the whole spheroid, as the calculated penetration depth of 220 μm is approximately the radius of the spheroid.

The offset of around 40 μm was disregarded for the calculation of the penetration speed. This offset could be due to an inherent spread of the fluorescence signal, and/or the spheroid being much more loose on its outside, thus much better penetrable to the DNA origami.

Interestingly, the ring thickness and penetration depth were not always the same. As can be seen in Figure B.25, and as data in Figure 4.10, the ring thickness of the rro and the mini origami was less than the penetration depth in the case of 16 and 32 h incubation times. Careful investigation of the fluorescence images revealed that for rro and mini origami, the fluorescence at the outer part of the spheroid was vanishing again. This effect was only present for the two DNA origami in square-lattice but not for the wf origami, whose ring thickness and penetration depth were approximately the same in each experiment. This was suspected to be the result of ingestion and/or destruction of the square-lattice DNA origami. The tighter structure of the square-lattice origami could increase the ability of cells to interact with them and thus internalize and digest them in the endosome, then the lysosome. In this way, the anchor points for the FISH hairpins on the DNA origami would be inaccessible, or destroyed. It follows that the hairpins would not be able to attach (anymore) and no fluorescence signal would be present, different from the unspecific background of the mere hairpins. The DNA origami were also similarly stable in medium, see Figure B.26, so a different, structure-dependent degradation in solution can be ruled out.

Summarizing, the size of the DNA origami structure is the main determining factor behind its ability to penetrate spheroid tissue. If any, the flexible wf structure had a slight detrimental effect, as the slightly larger rro origami penetrated just a little faster (wf: 1.69 μm/h vs. rro: 1.99 μm/h). The wf structure, however, seemed to be interacting less with the cells, increasing its circulation time.

We next investigated how these findings translate to nanoagent efficiency in apoptosis induction: Whether the faster penetration of the mini origami, or the longer circulation time of the wf origami, would be the determining factors in the efficacy of apoptosis induction. For this purpose, different DNA origami-FasL nanoagents were constructed with the three different DNA origami:

FasL Modification

The FasL used for the nanoagents were expressed as described in [159]. The construct consists of the extramembrane part of the FasL, the part that binds to FasR, and an isoleucine zipper (IZ) region, which trimerizes the FasL monomers into a FasL homotrimer, resembling the naturally occurring FasL. This homotrimer was modified as described in the same paper and also in section A.1.14, either with a biotin or a ssDNA oligomer. The labeling rate for FasL with ssDNA was

Shang/Bartels/Weck, 2025

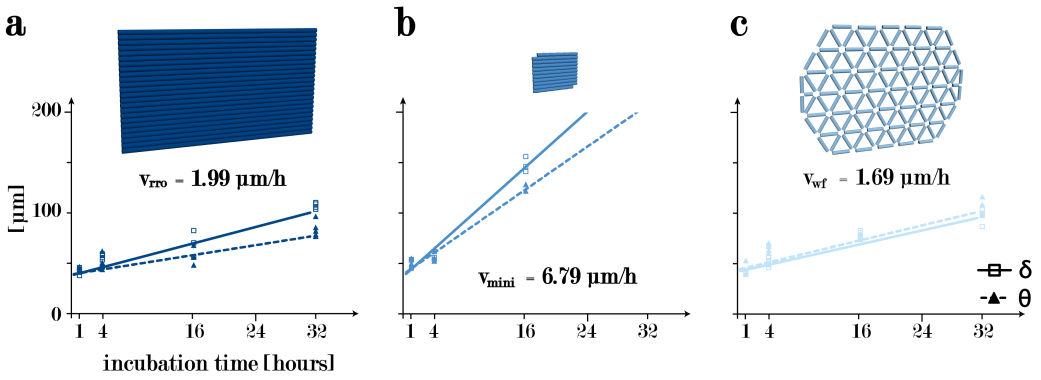

Figure 4.10: Penetration of Different DNA Origami through Spheroids

Different DNA origami structures penetrate differently through spheroid tissue. The graphs show the penetration depth and the ring thickness at different time points for the different DNA origami structures: (**a**) rro, (**b**) mini, and (**c**) wf DNA origami structures. The penetration depth is shown as solid lines, with single datapoints as dotted lines and the thickness of the ring is shown as a dotted line, with the individual data points shown as triangles. The penetration through the spheroids is different for each DNA origami. The rro DNA origami penetrated with an approximate speed of 1.99 μm/h, the mini with 6.79 μm/h, and the wf DNA origami with 1.69 μm/h. Panels were partially adapted and reprinted with permission from [160], copyright 2025 John Wiley & Sons.

determined from band intensities of a denaturing PAGE gel A.1.2. In Figure B.27 the upper band, tantamount to labeled FasL, has a slightly lower intensity than the lower (unlabeled) FasL band[16]. From this the labeling rate of each homotrimer can be calculated under the assumption of equal, non-impairing probabilities of labeling once, twice, or thrice [17] with the following formula:

$$P_{labeled} = 1 - P_{unlabeled} = 1 - \left(\frac{3}{5}\right)^3 = 78.4\% \tag{4.1}$$

with the 3/5 being the fraction of unlabeled monomers, approximated from the gel band intensities. The labeling rate for FasL with biotin modification could not be determined, as the molecular weight of the biotin modification was too low to show a distinct band. However, a band shift is clearly visible, indicating successful labeling. It can be supposed, that the labeling might be even better for the FasL-biotin construct; As firstly, the maleimide-biotin molecule is much smaller than the maleimide-DNA, which would lead to less steric hindrance during attachment. And secondly, both bands are shifted upwards, without smearing or left-over unlabeled bands, indicating full modification. With those modified FasL, the DNA origami were then decorated to create the different DNA origami-FasL nanoagents.

Nanoagent Characterization

Nanoagents with different DNA origami chassis and different FasL attachment strategies were constructed. In the following, nanoagents with FasL attached to them via a dsDNA linker are abbreviated "OF", and with FasL attached to them via an intermediated neutravidin are abbreviated "ONF" nanoagents, indicating the neutravidin in the middle.

The nanoagents were characterized by TEM imaging, analogously to the characterization of the DNA origami above. Cropped micrographs of each nanoagent are shown in Figure 4.11. The FasL can be identified in the TEM images as white spots on the DNA origami and indicated with red crosses. However, its shape can not be distinguished from the white spots by the neutravidin, which are indicated by white rings, identified only by their position.

The attachment efficiency of the OF nanoagents was determined in [159] to be 71.4 %, as calculated from combinatorics: Shang/Bartels/Weck, 2025

$$2\left(P_{attached}\left(1 - P_{attached}\right)\right) = \frac{N_{one}}{N} \tag{4.2}$$

$$\left(P_{attached}\right)^2 = \frac{N_{two}}{N} \tag{4.3}$$

with $N_{one} = 18$, $N_{two} = 23$ and $N = N_{one} + N_{two}$, the number of origami with one or two FasL attached to them. The attachment efficiency of ONF nanoagents was already determined in [158] to be roughly 76%[18]. The protocol for DNA Berger/Weck, 2021

[16] *N.B.:* there are no higher bands visible, indicating precise, single labeling of each FasL

[17] which might not be the case, but then the labeling rate would be even higher

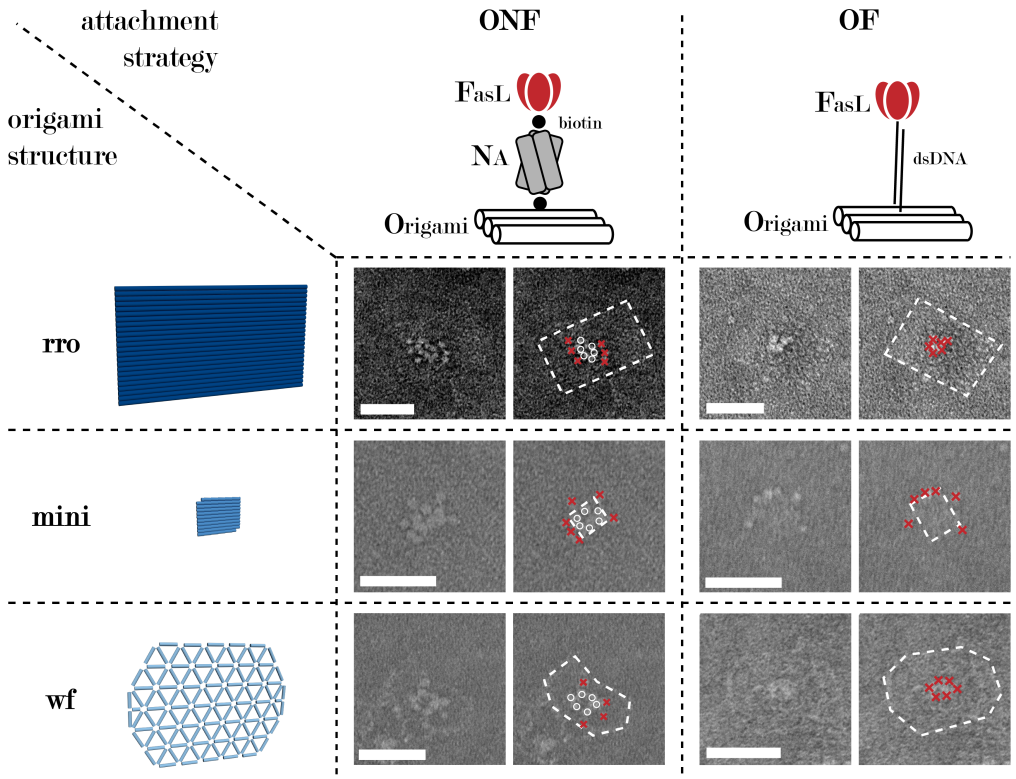

Figure 4.11: The Six Different Nanoagents Constructed

Through variation of the DNA origami structure and the attachment strategy of FasL to the DNA origami, six different nanoagents were constructed. The three different DNA origami, analyzed in Figure 4.8, were functionalized with FasL, either through an NA linker, creating ONF nanoagents, or via a dsDNA linker, creating OF nanoagents. One cropped TEM micrograph of the respective nanoagent is shown for each structure. The crop is duplicated and in the right one the DNA origami, as well as neutravidin and FasL are indicated with white lines, white circles and red crosses, respectively. The scale bars are 50 nm and hold for the respective DNA origami. Panels were partially adapted and reprinted with permission from [160], copyright 2025 John Wiley & Sons.

origami-FasL nanoagents construction is described in section A.1.15.

Apoptosis Induction in 3D Spheroids

To assess the effect of the nanoagents on the spheroids, their morphological changes after nanoagent addition were examined.

The spheroids were grown as described above (and in section A.1.7) for three days, when they reached a size of approximately 0.5 mm diameter. Then the respective nanoagent, or soluble FasL, was added to the spheroids. The spheroids were then imaged every day for an additional seven days in BF, GFP and TXred channel, recording their morphology, the expression of FasR, and apoptosis events, made visible by an Annexin V (AnxV) stain. The development of spheroid size over time is shown in Figure 4.12b, as *projected size* of the spheroid onto a 2D surface. The controls showed homogenous, linear growth to a final size of approximately 0.7 mm^2, indicating undisturbed proliferation of the cancer cells in the spheroid. The behavior was the same when controlled for the addition of DNA origami, increased amounts of storage buffer, or the addition of AnxV marker (see Figure B.28). However, when (300 fmol) FasL was added to the spheroids, their behavior changed: Beginning one day after addition, the size of the spheroids increased drastically and rose quickly to more than 1 mm^2, then plateauing starting on the seventh day at approximately 1.3 mm^2. When (50 fmol) of rroOF nanoagent was added (since it carries 6 FasL) the behavior was similar. The projected size of the spheroids increased quickly, then the size plateaued just over 1 mm^2. Contrariwise, the spheroid with rroONF nanoagent behaved again very differently: When the rroONF was administered to the spheroids, their size initially only increased slightly, peaked at day 4, and then ever so slightly shrunk again. The final size of the spheroids was less than 0.3 mm^2, approximately its size on day 3.

In addition to the development of size, the morphology and the fluorescence signal from the spheroids were also characteristically different. This is shown in Figure 4.12c. The control spheroids grew evenly, and so was their morphology: almost perfectly round and smooth at the sides across the whole experiment. The GFP signal was also bright and even, indicating the strong expression of fluorescence signal. Later, the fluorescence signal at the center dimmed down, as the spheroid grew too thick for the normal light microscope, used for all life-cell experiments, to penetrate through.

The images of the spheroids incubated with FasL or rroOF administered showed that those spheroids did not grow as much as they *fell apart*. Starting on day 4, the sides of the spheroids roughened and frayed, and then moved away from the spheroid. This would cause the stark increase in projected size, seen above. Char-

[18] *N.B.* The precise determination of attachment efficiencies is comparably difficult. Any bulk-fluorescence based methods are difficult, as fluorescence scales linearly only in some cases and a large influence of fluorescence distribution inside a band can be assumed. The combinatorial/mathematical approach used here is comparably reliable.

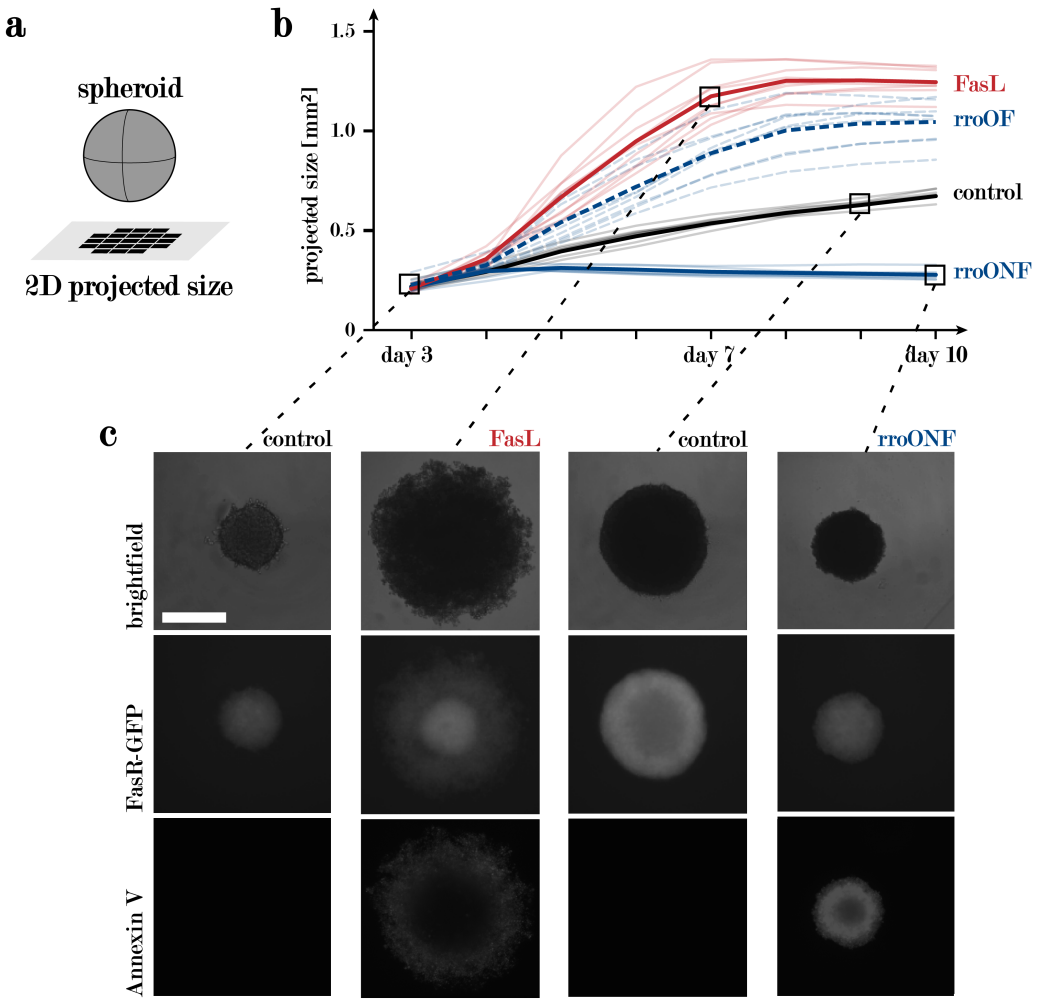

Figure 4.12: Spheroid Development after Nanoagent Addition

(**a**) Sketch of the experimental setup and evaluation method: The size of the spheroids is extracted from its 2D projection, as the spheroid is imaged on a simple fluorescence microscope. (**b**) Development of spheroid sizes after the addition of the respective nanoagents: Development of spheroids with 300 fmol FasL are shown in red, with 50 fmol rroOF as shown as blue dotted lines, and with 50 fmol rroONF as solid blue lines. Controls are shown in black. Thick lines indicate averages and thin lines indicate single experiments. (**c**) Fluorescence images of different spheroids at different time points: A control spheroid at day 3, a fraying spheroid at day 7 with addition of FasL, a control spheroid at day 9, and a spheroid with rroONF at day 10. The scale bar in (**c**) is 200 μm and holds for all microscopy images. Panels were partially adapted and reprinted with permission from [160], copyright 2025 John Wiley & Sons.

acteristically, these fallen-off parts would not change their morphology, indicating that the cells were dead. This was further confirmed by the fluorescence signals: While the GFP signal in the core was still bright and homogenous, indicating thickness in 3D and cell survival, the GFP signal on the frayed parts was much lower, indicating thin parts with dead cells. The AnxV signal also showed a dim, red halo following the outlines of the frayed sides, which were dim in GFP. This showed, as indicated, apoptosis occurring in the very outside layers of the spheroids.

The rroONF nanoagent induced again a different morphology. The spheroids incubated with rroONF added did not grow in size, stayed round and their sides stayed smooth. There were no real morphological changes after day 4, one day after nanoagent administration. The GFP signal also stayed the same brightness for the whole experiment. The apoptosis signal was however very strong, and increasingly so over the whole week. The decreased brightness in the middle can be attributed to the thicker parts of the spheroid dimming the light of the conventional light microscope used for these experiments. Having found this stark contrast in spheroid behavior depending only on attachment strategy, we next sought to analyze the effects of the underlying DNA origami structure.

When varying the underlying DNA origami structure, the effect was minute. OF nanoagents with the mini origami, which was found to penetrate the spheroid best, or the wf origami, which was assumed to be more stable, induced the same behavior as rroOF nanoagent in the spheroids. As seen in Figure 4.13 both nanoagents induced a quick increase in projected size, followed by a plateauing of the projected spheroid size at around 1 mm^2. Similarly, changing the underlying DNA origami for the ONF nanoagent evoked the same spheroid behavior as with the rroONF nanaogent: Their sizes peaked at day 4 or 5, and then declined again slowly. In both cases the microscopy images also revealed strikingly similar behavior, independent of the underlying DNA origami.

The ONF nanoagents seemed to be simply more effective than the OF nanoagents. This sparked the hypothesis, that the qualitative effect of growth halt and spheroid shrinkage for ONF nanoagents could be evoked by an increase in the amount of OF (or FasL) or vice versa: Whether the fraying of the spheroids observed with OF nanoagents and FasL could be evoked through low doses of ONF nanoagent. To test this hypothesis, the amount of nanoagent was titrated: Double the amount (100 fmol of OF nanoagents or 600 fmol FasL), half the amount (25 fmol, 150 fmol), a tenth (5 fmol, 30 fmol) or a twentieth (2.5 fmol, 15 fmol) of the initial amount were added to the spheroid, and their behavior recorded.

Strikingly, the spheroid behavior was still characteristic of the respective nanoagent. The curves for these spheroids are depicted in Figure 4.13. Low amounts of ONF were not able to evoke the fraying behavior, and high amounts of OF nanoagent or FasL still lead to the fraying of the spheroid, and not the halt and shrinkage. However, the amount of nanoagent added affected the magnitude of spheroid behavior. Larger amounts of OF nanoagent lead to stronger and earlier fraying, and lower amounts to less and later fraying. Half the amount of the ONF

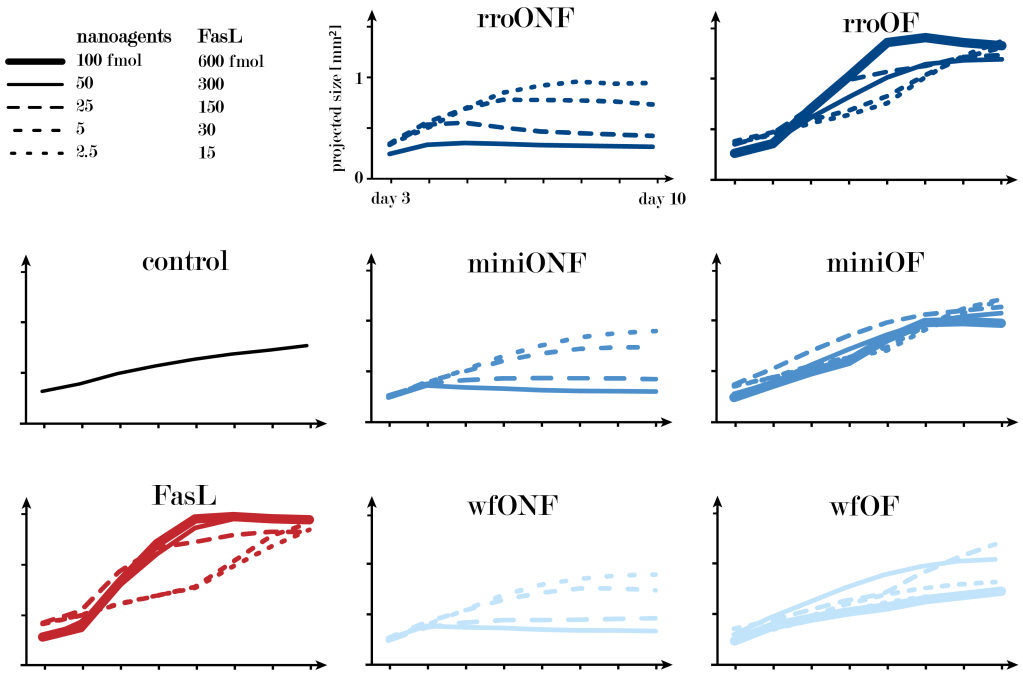

Figure 4.13: Effects of Nanoagent Variation on Spheroid Fate

Average growth curves for all nanoagents tested. The spheroid size is displayed on the ordinate, and the day of the experiment is shown on the abscissa. The different line thicknesses indicate different concentrations, specified by the table in the upper left corner. Colors indicate the different agents: The control is black, FasL is red, and the DNA origami nanoagents are shown in blue, with varying shades for the different DNA origami structures. Dark blue for the rro DNA origami, medium blue for the mini, and light blue for the wf DNA origami. Panels were partially adapted and reprinted with permission from [160], copyright 2025 John Wiley & Sons.

nanoagent still led to an early peak and then a halt in spheroid growth, but lower amounts only led to a halt in growth. The onset of the halt in growth shifted to a later time point with decreasing nanoagent amounts. The lower the amount of any nanoagent, the closer the spheroids' growth curve was to the controls. Interestingly, the wfOF nanoagent behaved somewhat differently to the general rules outlined above. The 100 fmol wfOF induced an almost linear increase in size of the spheroid, similar to the controls, however, microscopy images revealed many apoptotic events, just with a comparably smaller corona of dead, fallen-of cells.

To visualize this, a pseudo-phase diagram was made. This pseudo-phase diagram is shown in Figure 4.14, with the opening angle of the growth curve on the ordinate and the final spheroid size on the abscissa. Four distinctly different zones of behavior were identified. There are linearly growing, halting, and fraying spheroids, with the fraying population divided in those who plateau in size early and those who don't. The FasL and the OF nanogents are located in the fraying zones, a small amount of nanoagent in the zone of linearly growing spheroids, just as the controls. The ONF nanoagents are all halting, showing no overlap with any of the other characterized growth curves.

Having characterized the effect of different nanoagent architectures on spheroid behavior, *i.e.* that the underlying DNA origami -if so- only minutely influences spheroid fate, while attachment strategy completely changes it, the effects on the cells were examined next. For simplicity's sake and since the DNA origami structure did not affect the spheroids' response, the following experiments were done with rro DNA origami only.

Quantifying the Apoptosis Efficiency

The fate of the cells in the spheroids was analyzed with two methods. The cell morphology was analyzed in a fluorescence-activated cell sorter (FACS) and their survival was monitored by reseeding the cells in 2D. The protocols can be found in sections A.1.10 and A.1.11.

After incubation with the respective nanoagent (or FasL) for seven days, the spheroids were dissociated and analyzed by FACS. When running healthy, adherent cells through the FACS, the cells were mainly in one distinct population, at low sideward scatter (SSC) and medium forward scatter (FSC) values. The transition into 3D (spheroids incubated for 10 days) shifted the population of healthy cells to slightly lower SSC and FSC values. Additionally, a population of low SSC and FSC appeared, separate from the first population. The first observation was interpreted as a shift in cell morphology, the second observation indicates the appearance of dead cells inside the spheroid. These dead cells could potentially have their origin in the nutrient-depraved spheroid core, the so-called *necrotic core*.

The number of viable cells decreased and the amount of dead cells increased when FasL or nanoagents were added. As seen in Figure 4.15 (and also Figure B.29) a distinct population of dead cells formed. The ratio between the number

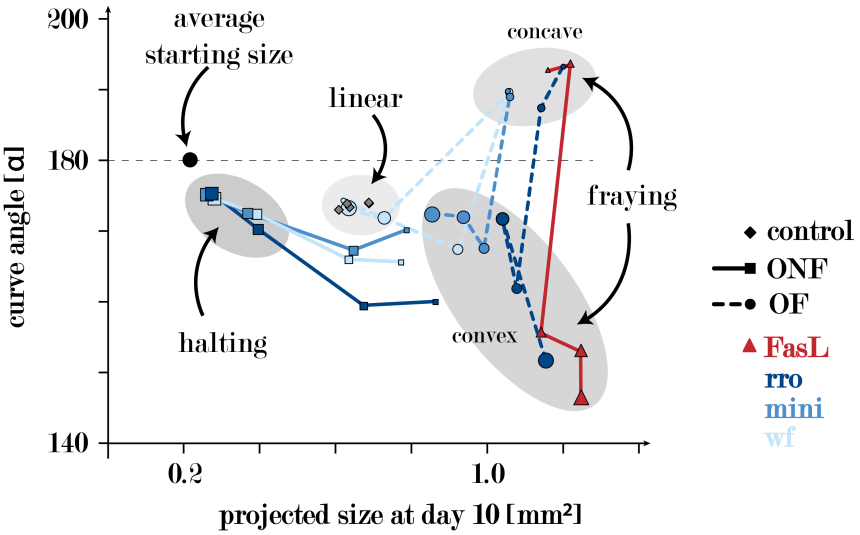

Figure 4.14: Pseudo-Phase Diagram of Spheroid Fate

The pseudo-phase diagram summarizes spheroid behavior. The angle of the spheroid growth curve is on the ordinate, and the final size as 2D projection on the abscissa. The colors indicate the kind of administered agent, with black for the control, red for FasL, and blue for rro, mini, and wf DNA origami, with decreasing color intensity. The icon shape and lines indicate the kind of attachment strategy, with dashed lines and circle icons for OF nanoagents and solid lines with diamond icons for the ONF nanoagents. FasL is shown with triangles. The size of the icons indicate agent concentrations, with larger icons correspond to higher concentrations. Four different areas can be identified: a linear growth, halting, and two fraying areas, one with a concave and one with a convex growth curve. Panels were partially adapted and reprinted with permission from [160], copyright 2025 John Wiley & Sons.

of cells in the viable and the dead population was used as an indicator for the efficacy of the respective nanoagent.

While for the 2D control, almost 100 % of the cells were located in the viable gate, this was drastically reduced in the 3D control, to only about 40 %, a result of the morphology shift and dead cells in the spheroid. When incubated with (300 fmol) FasL, the amount of cells in the viable gate shrunk to only 16.9 %, while incubation with (50 fmol) rroOF nanoagent reduced it to 4.6 % and the rroONF nanoagent (50 fmol) reduced it to 1.2 %. These results were consistent for both datasets recorded.

FACS data thus showed an increased apoptosis induction efficacy of OF compared to FasL of the same concentration. Measured by the ratio of viable to dead cells, this efficacy was almost quadrupled. The apoptosis induction efficacy of the ONF compared to the OF almost quadrupled, as an insignificant amount of only 1.2 % of cells were found in the viable gate, which were not even recognizable as a separate population. Next, we tested whether the population changes also translated to actual cell fate.

To examine the actual cell fate of the cells in the spheroids after incubation with the nanoagents, the dissociated spheroids were reseeded onto a 2D surface in fresh medium to recover. The remaining viable cells would adhere and form new colonies in 2D that were easily identifiable. The dissociated control spheroids, without further addition, formed an overgrown cell lawn after two days of incubation, as seen in Figure 4.16a. The number of surviving cells was somewhat reduced for spheroids previously incubated with (300 fmol) FasL, showing many islands of regrowth, but no continuous layer. For (50 fmol) rroOF nanoagents, the number of cells regrowing was again much more sparse than for FasL. For the (50 fmol) rroONF nanoagents, not a single cell survived, in either of the three repetitions of the experiment. This extended analysis of cell fate showed that the ONF nanoagent was able to eradicate the whole spheroids.

It was further explored, how the amount of rroONF nanoagent influenced the regrowth of 2D cell populations from the dissociated spheroids. As shown in Figure 4.16b, when the amount of rroONF nanoagent was halved (to 25 fmol), still in two out of three cases, no regrowth was observed. However, lower amounts (5 fmol or 2.5 fmol) of the rroONF nanoagent were not sufficient to kill off all cells in the spheroids.

4.2.3 Conclusion

In this section, the effects of nanoagent design on its ability to penetrate and induce apoptosis in a large, 3D spheroid model were examined.

For this, three different DNA origami (rro, mini, and wf), varying in size and/or flexibility, were designed and characterized. It was found that the ability to penetrate a spheroid tissue is mainly dependent on DNA origami size, not its flexibility, which is given by its internal structure. Further evidence was found

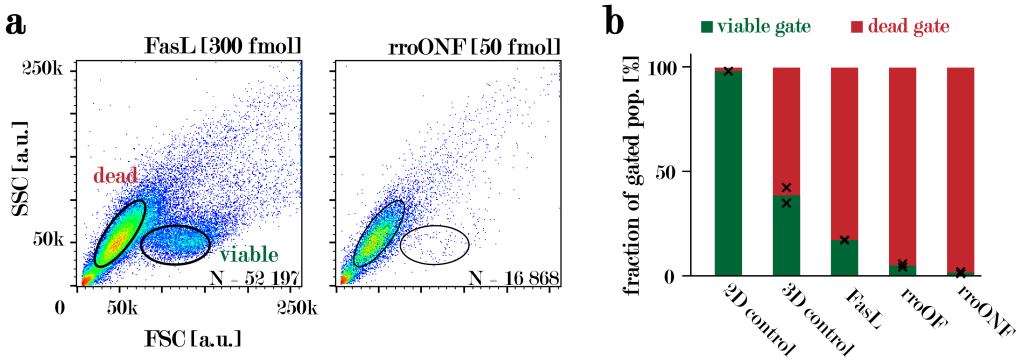

Figure 4.15: FACS Analysis of Dissociated Spheroids

(**a**) Exemplary FACS graphs of spheroids with either (300 fmol) FasL, or (50 fmol) rroONF. Two gates were defined around distinct populations in the plane spanned by the SSC and FSC values: dead and viable. The effectivity of the respective agent was characterized by the ratio of cells in the respective gates. (**b**) Fractions of cells in viable and dead gates. The 2D control showed nearly no dead cells, and almost only viable cells, while the 3D control had only 40 % viable cells. When 300 fmol FasL were added, amount of viable cells dropped to 16.9 %, with 50 fmol of rroOF it dropped to 4.6 %, and with 50 fmol of rroONF the amount of events in the viable gate was only 1.2 %. Single measurements are shown as black crosses. Panels were partially adapted and reprinted with permission from [160], copyright 2025 John Wiley & Sons.

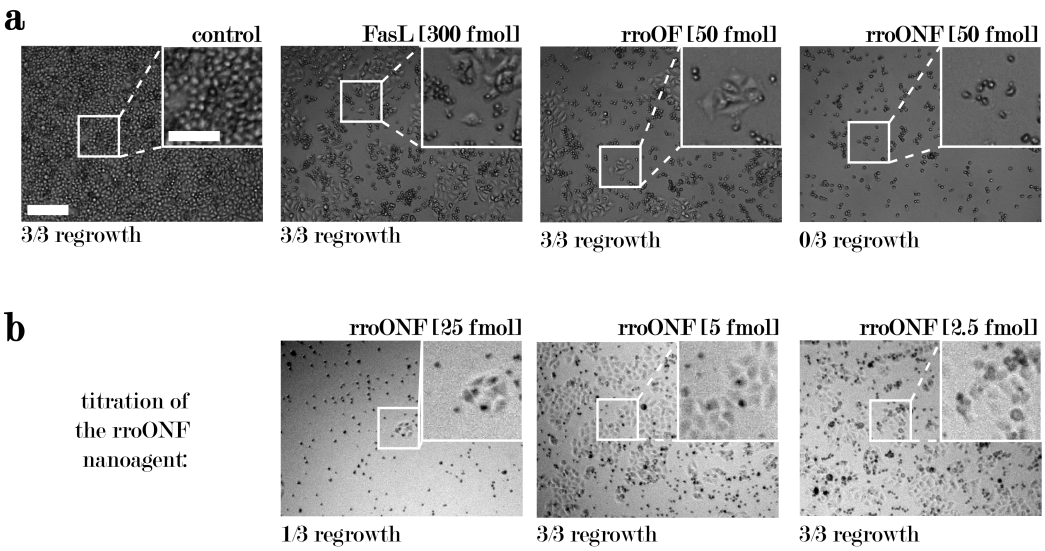

Figure 4.16: Reseeding Assay on Cell in Spheroids

Results of the reseeding experiments and exemplary microscopy images: (**a**) Control spheroids without any additions showed regrowth in 2D in 3 out of 3 cases. Similarly, when 300 fmol FasL, or 50 fmol rroOF nanoagent were added, all three repeats of this experiment showed regrowth in 2D, but with less confluency of the cells. Spheroids with 50 fmol of rroONF added showed no regrowth of cells in 2D in any case. (**b**) Titration of the rroONF concentration added to the spheroids and the effect on the regrowth in 2D: Spheroids with 25 fmol of rroONF added, only showed regrowth in one of three cases, while lower concentrations in all experiments showed regrowth again. The scale bar for the wide-field image is 200 μm and for the zoomed-in crops 100 μm, both hold for all of the respective images. Panels were partially adapted and reprinted with permission from [160], copyright 2025 John Wiley & Sons.

that an internal wireframe structure indeed increases the circulation time of DNA origami in a cellular context.

The most probable explanation for this is an increased capability of diffusion. The smaller the DNA origami structure, the better it can fit through the intercellular space and the cell-cell junctions. Also, the diffusion constant is inversely proportional to the square of the particle diameter, generally increasing the diffusion speed with decreased particle size.

Wang, 2021

These findings somewhat contradict the observations of a prior study[184], that wireframe structures would better penetrate through tissue. These deviating results could be attributed to structural differences of their tubular DNA origami and our flat, sheet-like structures. It could also be attributed to the different types of data analysis: The fluorescence signal was enhanced through the use of FISH, and, more importantly, the tissue thickness did not limit our ability to view through the spheroid.

Further, the notion that lower charge density increases the ability to penetrate tissue[184], was not supported by our data, as rro and wf had a very similar charge density, but the mini DNA origami, with an elevated charge density, penetrates the spheroid tissue much faster. On the other hand, this data was calculated from the size of the DNA origami adherent to TEM grids in 2D, which probably have different dimensions in solution.

To test the effects of nanoagent structure on its capability to induce apoptosis in spheroids, a total of six different nanoagents were constructed and characterized. These nanoagents varied in their underlying DNA origami structure (rro, mini, and wf) and their attachment strategy of FasL to the DNA origami (via a dsDNA linker or via neutravidin). However, the underlying DNA origami did not seem to make a significant difference in the ability of the nanoagents to induce apoptosis. The main factor was the attachment of the FasL via a specific linker: Neutravidin linkers proved more effective than dsDNA linkers concerning the nanoagents apoptosis induction efficacy.

This effect is probably owed to the fact that the neutravidin linker is less flexible than the dsDNA linker: Different attachment efficiencies can be ruled out as the cause of the effect, as both OF and ONF showed similar FasL attachment rates (71 % and 76 %). Faulty FasL modifications can also be ruled out, as Figure B.27 showed only single labeling of FasL monomers. Another reason could be the increased stability of the neutravidin-biotin connection compared to the dsDNA connection. Connections of lower stability would have a higher probability of either dissociating or being plugged off the origami by the cell's ingestion apparatus. On the other hand, in the previous section 4.1 the zipper configuration of the dsDNA proved more effective than the bar configuration but should be much less stable

Strunz, 1999

[185]. Another factor could be the different charge of the connectors, however, compared to the high charge of the origami itself, this is negligible. Also, in direct vicinity to the binding site is only the extracellular part of the FasL, and then a comparably long isoleucine zipper. Having these parameters eliminated as

cause, the flexibility of the linkers seems the only viable reason behind the different apoptosis induction efficacy. This was also the suspected reason for the different apoptosis kinetics in section 4.1.

Somewhat contrary to this hypothesis, the flexibility of the underlying DNA origami structure did not have a major influence. The increased flexibility of the wf DNA origami did not have a detrimental effect on apoptosis induction of the wfONF nanaogent. The reason behind this could be either the DNA origami fluctuating not enough to have an effect, and/or the flexibility of the connector having not only caused a positional inaccuracy but directional inaccuracy, as already discussed above in section 4.1.

However, the increased positional accuracy cannot explain the different phenotypical behavior of the spheroids. The -more flexible- OF nanoagents did induce cell detachment, as did the freely diffusing FasL controls, but the -less flexible- ONF nanoagents did not. The spheroids with ONF nanoagents did not undergo major morphological changes, besides growing in size; the spheroid did not fray on its sides, as in the other cases. The reason behind this difference in behavior was not examined in this doctoral thesis and is left as subject for subsequent studies.

Our findings have several implications for the construction of therapeutic nanoagents from DNA origami. Since smaller DNA origami penetrate better through spheroid tissue, this work suggests the use of small (20-30 nm diameter) DNA origami as nanoagent chassis. This on the other hand limits the amount of space to position proteins on, or carry cargo inside of the origami.

There are still several problems for nanotherapeutics that have not been examined here. The first of which is the problem of administration, and their traversal through the skin or the intestinal barrier. The second problem is the migration through the bodily choke points, which are the filtering organs (kidney and spleen), the traversal from the bloodstream to tissue, and the crossing of the blood-brain barrier. The third problem is the targeting of specific cells. For our system, this can be done by targeting the overexpressed receptor, which is also transducing the signal. For other systems, where both aspects do not coincide, this is an engineering task. Another engineering problem would be the circulation time, which needs to be optimal for targeting and delivery, but with planned obsolescence, such that the particles do not stay in the body and cause harm. However, these problems will be tackled in the future by nanoscale therapeutics, which promise that these aspects are engineerable, a trait that other therapeutics do not have (to this degree).

The trailblazer of engineering these aspects is the minimal tetrahedron structure. This DNA tetrahedron, a miniature structure made from a few, short ssDNA strands, is easy to synthesize and quick to modify [186]. It has been used to target specific cells, deliver various cargo, and can be used without further stabilization in a somatic context [187][188]. Larger structures, like DNA origami, on the other hand, promise more programmability, more complex functions, higher loading capacity, and precise presentation of several proteins, as done in the here presented

Tian, 2023

Hu, 2017

Yan, 2021

work.

The findings on the penetration behavior of DNA origami presented in this work promise to be translatable to other DNA origami-based therapeutics. The examined structural features of size and flexibility are universal for DNA origami structures, and the finding that the penetration behavior is governed by origami size, not their flexibility, is applicable to future designs. This, however, means that future designs will face a trade-off between the ability to penetrate tissue and the amount of cargo, the number of ligands displayed, or structural complexity, which are all connected to increased structure size.

Chapter 5

Outlook

DNA nanotechnology has been described as a *solution without a problem*. Even though DNA nanotechnologists have dabbled into different fields, examined biological systems, created plasmonic arrangements, nanorulers, and nanomotors, a *definite* application for DNA origami is not apparent.

Is it worth the effort for biomedicine? The question is, whether the nanoscale precision of DNA nanotech is actually *needed* to yield good results, sufficient results. The years of corona have shown the large impact on biomedicine, which lipid nanoparticles alone can make, and the question arises, whether DNA nanotechnology is needed anyway. Especially when this is weighed up against the additional costs in synthesis, modification, and stabilization that DNA origami require. Lipid vesicles, just as gold nanoparticles, or silica nanoparticles, can be synthesized easily and quickly, in large batches, with high yields, and afterwards easily purified and functionalized. And if the result with those is similarly good, which pharma company would use DNA nanotechnology?

Another development sidelined DNA nanotechnology further: The creation of *de novo* designed proteins made significant progress due to AI-supported design. Those *de novo* proteins promise even more versatility and precision on the nanoscale than DNA origami, while simultaneously being easily expressed and purified with methods that are already established and easily scaled up. Further, they are implicitly biocompatible and promise the direct fulfillment of roles within cells, just like any other protein.

Some aspects, however, are encouraging: While the bodily immune system can develop an aversion towards protein scaffolds, that would be used in *de novo* designed agents, the probability that this happens with DNA chassis is minute[112]. Wamhoff, 2024
The fact that the extrinsic activation of some functions needs larger scaffold and comparably stiff connections[90] and that the hexameric FasL assemblies Veneziano, 2020
still worked much better than the dimeric assemblies (see section 4) makes DNA origami-sized structures necessary for some applications. Also, the small, tetrahedral DNA structures, Itamar Willner is famous for[189], are easy to produce, Ouyang, 2024
and already much closer to clinical trials and medical use than any larger DNA

origami-based nanoagents.

Other uses for DNA origami are limited by the scope of the applications and/or by the inherent limits of DNA origami themselves. Nanorulers for AFM and optical super-resolution are constructed with great precision from DNA origami, but there is no room for improvement beyond the current application. The nanomotors created with DNA nanotechnology are not remotely comparable to the motors found in nature, with regards to programmability and the performable work. The hotspots that can be created between plasmonic particles arranged with DNA origami, can be used for biosensing, but compete, similarly to the problems above, with quicker and easier methods.

Even though, in this dissertation, as in several other publications, the range of DNA origami design is extended, both with regards to methods and to structure size, in the end, there seem to be insuperable obstacles. An ultra complex machine as protein-made nanomotors, will not be constructed with DNA origami, as DNA itself is not versatile enough and the programmability is too crude. Micrometer-sized 3D structures that remain fully addressable cannot be constructed to date with DNA origami. Closest to this were the crisscross slats [157], but the structures were only in 2D and suffered from defects. The modularities for DNA origami nanostructure design developed in this dissertation are probably most effective either for smaller assemblies, as an alternative for the use of longer or orthogonal scaffolds (xy-structures), and for larger, semi-ordered assemblies, as an alternative for tiled DNA tubes (z-assemblies).

Wintersinger, 2023

However, DNA origami has carved itself a niche as a *testing* and construction framework. The simplicity of construction and modification of -comparably- large structures comes in handy to *test* a plethora of different nanoscale assemblies. Plasmonic structures are easily assembled and *tested*, from which the knowledge can then be translated for applications built with lithography or other nanoscale assembly methods, better suited. DNA nanotechnology can easily *test* the most optimal assemblies of ligands in biology, for other methods to pick these insights up and apply them for medical use. And as such, DNA nanotechnology is destined to be at the forefront of new scientific discoveries.

Appendix A

Supplementary Methods

A.1 Methods & Materials

A.1.1 Scaffold Production

The protocols for the production of single-stranded DNA scaffold were adapted from the book *Molecular Cloning*[190]. Bacteriophages with different inserts derived from the M13mp18 genome were a gift by the Liedl laboratory. The respective insert sizes define scaffold length in the M13mp18-derived phages. The wild-type M13 phage was purchased from the DSMZ[115] and has a length of 6407 nt. The M13mp18 variants have the following sizes: 7249, 7308, 7560, 8064, 8634 nt. Annually, phages were purified and new inoculation stocks were made, with which ssDNA scaffold was produced on a large scale: To purify phage stocks from potential contaminants, such as miniphages [191], phages were diluted in power of 10 down to 10^{-16}, and 100 μl of each dilution was mixed with 100 μl overnight cultured bacteria (Top10F' cell line) and 2.5 ml top agar (0.6 % (w/v) agarose in LB medium), plated on regular agar plates (1.5 % (w/v) agarose in LB medium), and incubated overnight at 37 °C. Several single phage plaques were picked and incubated in 2 ml LB medium overnight. Bacteria were pelleted by centrifugation for 10 min at 5000 rcf and discarded. To check the quality of the phage plaques picked, 50 μl of the supernatant was mixed with 10 μl of phage denaturation buffer, incubated at 65 °C for 15 min, and then analyzed via AGE.

Sambrook & Russel, 2001

DSMZ

Hewitt, 1975

A.1.2 Gel Electrophoresis

Agarose gels were prepared with 1 % ultra-pure agarose, and TAE buffer supplemented with 11 mM $MgCl_2$ and 1X SYBR safe, if not further specified.

The usual running conditions were 70 V for 90 min, cooled in an ice bath.

PAGE gels for DNA were prepared at 20 % acrylamide and PAGE gels for proteins were prepared at 15 % acrylamide. Further, the gels contained 1X TBE buffer, 10 % APS, and 0.05 % TEMED, which were added to induce polymerization, then filled to the desired volume with mQ water. For denaturating protein gels, 1 % SDS was added. Gels were run at constant 150 V for $\approx$ 1 h in an ice bath.

Post-staining of previously unstained gels was done using 10 μl SYBR gold diluted in 100 ml mQ water for 20 min. All gels were imaged on a Typhoon FLA 9000 laserscanner. Gels were analyzed with the Fiji software
Schindelin, 2012 [192].

A.1.3 TEM imaging

Copper-coated carbon grids were glow-discharged in oxygen plasma to increase their hydrophilicity. The grid was then gripped with a reverse tweezer and (usually) 10 μl of 1 nM sample was applied for 5 min, then the excess sample was blotted away with a filter paper. Optionally, one washing step with 10 μl mQ water followed, which was blotted away immediately after application. The grid was stained with 2 % uranyl formate (UFO), usually with one drop of 5 μl, immediately blotted away and a second drop of 5 μl stain for 10 s. The prepared grid was then air-dried and afterward stored in a grid box until further use.

A.1.4 AuNP Synthesis

Eneston, 1963 Gold Nanoparticles were synthesized as previously described in [193]. In short, 1 mM hydrogentetrachloroaurate in mQ water was heated to a rolling simmer and 2 % hot trisodium citrate solution was added quickly. The solution was further heated for approximately 15 min, during which several color changes occurred, and then the heat was cut and the solution was stirred until it cooled to RT. During the whole procedure, the solution was mixed quickly and evenly with a magnetic stir-bar. All hardware articles used in this procedure were cleaned thoroughly with Aqua Regia before and after use.

The AuNP were then purified from aggregates by centrifugation for 10 min at 10,000 rcf[1], their concentration was determined with *nanopdrop 1000* spectral photometer, and stored at 4 °C until further use.

[1] an additional centrifugation step at 20,000 rcf allows for a cleaner size-cut-off of AuNP

A.1.5 AuNP Functionalization

AuNP were functionalized with ssDNA strands by the freezing method: In mQ water resuspended thiolated DNA strands were mixed with AuNP in a 12,500:1 ratio. The mixture was frozen for 3 h minimum at -20 °C. The then functionalized AuNPs were again purified via centrifugation at 20,000 rcf for 10 min, the supernatant was removed and replenished several times with mQ water, to get rid of excess DNA strands. The concentration was again measured on a nanodrop 1000 spectral photometer and stored at 4 °C until further use.

A.1.6 DNA Origami Functionalization with AuNP

DNA origami was functionalized with AuNP by the addition of AuNP in 5x excess over the number of binding sites on the DNA origami. The AuNPs were added to the DNA origami quickly, and under constant agitation. Subsequently, the solution was incubated shaking for 1 h.

A.1.7 Cultivation of Cells & Spheroids

The HeLa Apo12 mGFP cell line, overexpressing FasR tagged with an mGFP, was provided by the Laboratory of Cornelia Monzel. The standard cell medium consists of 10 % FBS and 1 % PenStrep in DMEM glutamax. Cells were incubated at 37 °C, 5 % CO_2, and 100 % humidity The cells were split every Monday and Wednesday (500,000 cells in 10 ml standard medium), as well as Fridays (200,000 cells) to achieve constant $\approx$ 70 % confluency for the next split. Cells were stored long-term as cryo stocks at -80 °C or in liquid nitrogen in a mixture of 20 % FBS, 10 % DMSO in DMEM glutamax cell medium. When required, the cryo stocks were thawed in a 37 °C warm water bath, diluted in 10ml standard cell medium, then centrifuged for 5 min at 300 rcf to pellet the cells. Then the medium was discarded and the cells resuspended in standard cell medium, with the FBS content elevated to 20 %, then the cells were plated. Dead cells were removed from the culture after one day, by exchange of the medium.

The same cells as for 2D experiments were used for 3D experiments. Spheroids were cultured in 96 well low adhesion plates. The 2D cells were split and diluted in standard cell medium to 8000 cells per ml. 50 μl cell medium, containing 400 cells were seeded in each well of the plate, but the outermost wells were filled with $\approx$ 200 μl PBS to prevent evaporation of the spheroid medium. The cells were then centrifuged for 3 min at 1000 rcf and room temperature to cluster them. The plate was then incubated at 37 °C,

5 % CO_2, and 100 % humidity for the spheroids to form.

A.1.8 Spheroid Penetration Experiments

For the spheroid penetration experiments the spheroids were seeded as described above (section A.1.7) and grown for three days. The resulting spheroids were spherical and had an approximate diameter of 0.5 mm, visible by the naked eye. 500fmol of the respective nanoagent was added to the spheroid and incubated for set time intervals (1, 4, 16 or 32 h). The penetration was stopped by fixing the spheroids in 50 μl 4 % paraformaldehyde (PFA) for 30 min in the incubator. Then the spheroids were permeabilized in 50 μl, 2 % tween, 2 % PBST (0.05 % (w/v) NaAc, 2 % (v/v) Triton X 100 in 1x PBS) for 15 min in the incubator. The two kinds of FISH hairpins (B1, Molecular Instruments) were added and incubated together with the spheroids in the "hybridization buffer" (Molecular Instruments) overnight at RT. Previously, the FISH hairpins had been prepared by snap-heating and -cooling to 95 °C for 90 seconds and again to RT, separately from the other. The spheroids were washed in the "washing buffer" from Molecular Instruments. Optionally, at this point in the protocol, the spheroid was stained with 0.5 % Hoechst 33342 for 20 min at RT. In between the above steps, the spheroids were usually washed with PBS. Lastly, they were then transferred to microscopy slides, cleared with 8-10 μl RapiClear 1.47 (Sunjin Biolabs), and then imaged on a Stellaris 8 confocal microscope.

Z-stacks through the tumoroids were recorded with a confocal microscope. The penetration depth was extracted from the fluorescence signal of the hairpins. The relevant signal could be distinguished from background and autofluorescing artifacts by their form and size: The artifacts had a concentrated, high fluorescence intensity at cell-sized spots, while the background fluorescence of only hairpins showed a very even fluorescence distribution. The signal from the DNA origami was granular and positioned ring-like around the edges of the spheroid. To analyze the penetration depth, the intensity was recorded with the Fiji[192] clockscan plugin[194].

Schindelin, 2012
Dobretsov, 2017

A.1.9 Spheroid Apoptosis Assays

For the spheroid apoptosis assays the spheroids were seeded as described above (section A.1.7) and grown for three days. On the third day, the respective amount (50, 25, 5, or 2.5 fmol) of the nanoagents was administered. Additionally, for some experiments, 1 μl of Annexin V (AnxV) marker was added. Images in BF, GFP (Fas receptor), and Texas Red (AnxV) channels were taken every day for the next week on an EVOS fluorescence microscope.

The size of the spheroids was extracted from the BF channel, while GFP and Texas Red channels gave cues about cell states in the spheroid.

A.1.10 FACS Experiments

The FACS experiments were conducted with spheroids incubated for 10 days. The spheroids were washed with PBS thrice and then incubated in 50 μl Trypsin-EDTA (TE) for 30 min to release the cell-cell connections. The spheroid was then dissolved mechanically, through pipetting. The cells were then washed twice and resuspended in PBS for imaging on a FACS Fortessa.

A.1.11 Reseeding Experiments

Similar to the FACS experiments, the spheroids were incubated in 50 μl TE for 30 min and then dissolved mechanically. They were then resuspended in 200 μl standard cell medium and reseeded in a cell-culture-treated 96-well plate. After incubating for 2 days, they were imaged and scanned for populations of surviving cells.

A.1.12 Lipid Handling

For the construction of the lipid bilayer, 39 μl of 18:1 (Δ9-cis) DOPC lipids were pipetted into a glass beaker, which was cleaned with chloroform prior to use. The chloroform in the lipid mixture was evaporated under a low nitrogen stream, such that only dry lipids remained. Optionally, the lipids were dried overnight in a desiccator. To the dry lipids 1 ml of PBS was added, and then sonicated with a tip sonicator until the milkiness disappeared from the solution. This process formed small lipid vesicles from the lipids in the solution. To get rid of impurities, the lipids were then diluted $\approx$ 1:10 in PBS, centrifuged and only the upper 9/10 was used further.

A.1.13 2D Flow Chamber Experiments

The flow chamber was constructed in a sterile flow hood, from a ibidi 6 well slide with a sticky bottom, to which an isopropanol-cleaned precision microscopy slide was glued. Each channel of the slide was cleaned with PBS, and then 100 μl of the lipid solution prepared above in section A.1.12 were added and incubated for 1 h for the lipids to settle. The lipid vesicles were then popped and a lipid bilayer formed by an osmotic shock from 100 μl mQ water, which was added and incubated for 2 min. Then the nanoagent was formed *in situ*, by first incubating 100 nM cholesterol DNA for 15 min, then

the DNA origami were incubated for 30 min, SA (or mSA) was incubated for 10 min, and the FasL was incubated for another 10 min. These steps were followed by at least two washing steps of 100 μl with the respective buffer. In each channel 2000 HeLa Apo12 mGFP cells were added, in L15 or standard culturing medium, supplemented with 10 % FBS. Finally, the channels were sealed with anti-evaporation oil. The slides were incubated and imaged every 10 min (or 20 min) for 24 h on a heat-controlled fluorescence microscope. The data was analyzed with Microsoft Excel.

A.1.14 FasL Functionalization

The FasL protein was functionalized either with a DNA strand or with biotin, each via a thiol-maleimide click chemistry. Firstly, potential disulfide bridges between the cysteines on the IZ were reduced by adding tris(2-chloroethyl)phosphate (TCEP) to 2 mM and incubation for 30 min at 4° C. The buffer was then exchanged to "coupling buffer" (A.12). The FasL was then functionalized by adding maleimide-DNA (5x excess over FasL) or maleimide-biotin (30x excess), followed by incubation overnight. The product was then purified via ultracentrifugation. [2]

A.1.15 Construction of Nanoagents

DNA origami based nanoagents were constructed by attaching FasL, either through DNA hybridization and formation of a dsDNA linker, or by connection to an intermediate neutravidin. The neutravidin for ONF nanoagents was attached to the DNA origami by incubating it in 50x excess over each biotin at 4 °C over-night, then filtering it through a 0.22 μm centrifugal filter, and afterwards purifying it via high pressure liquid chromatography (HPLC) (*confer* [195]), followed by a concentration by amicon ultrafiltration. For both ONF and OF, the FasL-biotin and the FasL-DNA was added in 5x excess over each binding site, and incubated over night at 4 °C. The construct was filtered with a 0.22 μm centrifugal filter, purified via HPLC, and concentrated with Amicon ultracentrifugation. As cryopreservative, glycerol was added to a concentration of 10 %, after which the sample was sterile filtered through a 0.22 μm centrifugal filter, its concentration measured, and

Shaw, 2015

[2] The concentration for FasL-DNA conjugates however, was determined by the absorption spectra for ssDNA in the nanodrop, as the protein absorbs far less than the DNA. This was done under the assumption that all three cysteines of the trimeric FasL have ssDNA modifications. The *final* concentration of both FasL-biotin and FasL-DNA was always calculated for the trimer. This implies that the actual FasL concentration was somewhat higher than the calculated one.

finally aliquotted and rapidly frozen in liquid N_2. It was stored at -80 °C until further use.

A.1.16 DNA Origami Design

The DNA origami in this work were constructed using computer-aided design (CAD) software. Lattice based structures were designed in caDNAno 2.4.10 [64], and the wireframe structure was designed with vHelix [61].

Douglas, 2009
Benson, 2015

A.1.17 Simulation of DNA Origami

The DNA Origami structures were then simulated using the oxDNA software [196][73][197]. The DNA origami were relaxed in oxView (5,000 CPU and 100,000 GPU iterations), and then simulated on the oxView server for 100,000,000 iterations. To extract the RMSF the structures were simulated again for 100,000,000 iterations[3], and the data points were extracted with the built-in function on oxDNA.org. Those were then further analyzed with Microsoft Excel.

Henrich, 2018
Poppleton, 2021
Doye, 2023

A.1.18 DNA Origami Folding Conditions

The DNA origami used in chapters 3 and 4 were folded with the following folding mixtures:

constituent	concentration in folding mixture
scaffold	10.0 nM
core staples	50.0 nM
z-connectors	50.0 nM
xy-structure	75.0 nM
xy-connections	100.0 nM
$MgCl_2$	15 mM
TAE	1 X

Table A.1: Folding Conditions of the moDON DNA Origami

[3] this was done to avoid bias from initial out-of-equilibrium states

constituent	concentration in folding mixture
scaffold	12.5 nM
staples	50.0 nM
staples with handles	200.0 nM
$MgCl_2$	12.5 mM
TAE	1 X

Table A.2: Folding Conditions of the RRO origami

constituent	concentration in folding mixture
scaffold	10 nM
staples	40.0 nM
staples with handles	160.0 nM
$MgCl_2$	7.5 mM
TAE	1 X

Table A.3: Folding Conditions for the wf DNA Origami

constituent	concentration in folding mixture
scaffold	10.0 nM
staples	40.0 nM
staples with handles	160.0 nM
$MgCl_2$	4.0 mM
TAE	1 X

Table A.4: Folding Conditions for the mini DNA Origami

A.1.19 Buffers and Media

Table A.5: 2X YT Medium

constituent	concentration
NaCl	10 g/l
yeast extract	5 g/l
trypton/pepton	10 g/l
$MgCl_2$	5 mM

Table A.6: LB Miller Medium

constituent	concentration
NaCl	10 g/l
yeast extract	5 g/l
trypton/pepton	10 g/l

Table A.7: Phage Denaturation Buffer

constituent	concentration
SDS	0.4 % (w/v)
EDTA	30 mM
orange G	until orange

Table A.8: TAE Buffer

constituent	concentration
tris	40 mM
acetic acid	20 mM
EDTA	1 mM
pH to 8.0	

Table A.9: TBE Buffer

constituent	concentration
tris	40 mM
boric acid	20 mM
EDTA	1 mM
pH to 8.0	

Table A.10: PBS Buffer

constituent	concentration
Na_2HPO_4	10 mM
KH_2PO_4	2 mM
NaCl	140 mM
KCl	3 mM
pH to 7.4	

Table A.11: Buffer A

constituent	concentration
NaCl	50 mM
EDTA	10 mM
Na_2HPO_4	50 mM
pH to 8.0	
filtered through a 0.22 μm mesh	

Table A.12: Coupling Buffer

constituent	concentration
tris	10 mM
NaCl	100 mM
pH to 7.2	

A.2 DNA Sequences

A.2.1 Scaffold Sequences

Scaffold p8634

AATGCTACTACTATTAGTAGAATTGATGCCACCTTTTCAGCTCGCGCCCCAAATGAAAATATAGCTAAACAG
GTTATTGACCATTTGCGAAATGTATCTAATGGTCAAACTAAATCTACTCGTTCGCAGAATTGGGAATCAACT
GTTATATGGAATGAAACTTCCAGACACCGTACTTTAGTTGCATATTTAAAACATGTTGAGCTACAGCATTAT
ATTCAGCAATTAAGCTCTAAGCCATCCGCAAAAATGACCTCTTATCAAAAGGAGCAATTAAAGGTACTCTCTA
ATCCTGACCTGTTGGAGTTTGCTTCCGGTCTGGTTCGCTTTGAAGCTCGAATTAAAACGCGATATTTGAAGT
CTTTCGGGCTTCCTCTTAATCTTTTTGATGCAATCCGCTTTGCTTCTGACTATAATAGTCAGGGTAAAGACCT
GATTTTTGATTTATGGTCATTCTCGTTTTCTGAACTGTTTAAAGCATTTGAGGGGGATTCAATGAATATTTA
TGACGATTCCGCAGTATTGGACGCTATCCAGTCTAAACATTTTACTATTACCCCCTCTGGCAAAACTTCTTTT
GCAAAAGCCTCTCGCTATTTTGGTTTTTATCGTCGTCTGGTAAACGAGGGTTATGATAGTGTTGCTCTTACT
ATGCCTCGTAATTCCTTTTGGCGTTATGTATCTGCATTAGTTGAATGTGGTATTCCTAAATCTCAACTGATGA
ATCTTTCTACCTGTAATAATGTTGTTCCGTTAGTTCGTTTTATTAACGTAGATTTTTCTTCCCAACGTCCTGA
CTGGTATAATGAGCCAGTTCTTAAAATCGCATAAGGTAATTCACAATGATTAAAGTTGAAATTAAACCATCT
CAAGCCCAATTTACTACTCGTTCTGGTGTTTCTCGTCAGGGCAAGCCTTATTCACTGAATGAGCAGCTTTGT
TACGTTGATTTGGGTAATGAATATCCGGTTCTTGTCAAGATTACTCTTGATGAAGGTCAGCCAGCCTATGCG
CCTGGTCTGTACACCGTTCATCTGTCCTCTTTCAAAGTTGGTCAGTTCGGTTCCCTTATGATTGACCGTCTGC
GCCTCGTTCCGGCTAAGTAACATGGAGCAGGTCGCGGATTTCGACACAATTTATCAGGCGATGATACAAATC
TCCGTTGTACTTTGTTTCGCGCTTGGTATAATCGCTGGGGGTCAAAGATGAGTGTTTTAGTGTATTCTTTTG
CCTCTTTCGTTTTAGGTTGGTGCCTTCGTAGTGGCATTACGTATTTTACCCGTTTAATGGAAACTTCCTCATG
AAAAAGTCTTTAGTCCTCAAAGCCTCTGTAGCCGTTGCTACCCTCGTTCCGATGCTGTCTTTCGCTGCTGAG
GGTGACGATCCCGCAAAAGCGGCCTTTAACTCCCTGCAAGCCTCAGCGACCGAATATATCGGTTATGCGTGG
GCGATGGTTGTTGTCATTGTCGGCGCAACTATCGGTATCAAGCTGTTTAAGAAATTCACCTCGAAAGCAAGC
TGATAAACCGATACAATTAAAGGCTCCTTTTGGAGCCTTTTTTTTGGAGATTTTCAACGTGAAAAAATTATT
ATTCGCAATTCCTTTAGTTGTTCCTTTCTATTCTCACTCCGCTGAAACTGTTGAAAGTTGTTTAGCAAAATCC
CATACAGAAAATTCATTTACTAACGTCTGGAAAGACGACAAAACTTTAGATCGTTACGCTAACTATGAGGGC
TGTCTGTGGAATGCTACAGGCGTTGTAGTTTGTACTGGTGACGAAACTCAGTGTTACGGTACATGGGTTCCT
ATTGGGCTTGCTATCCCTGAAAATGAGGGTGGTGGCTCTGAGGGTGGCGGTTCTGAGGGTGGCGGTTCTGA
GGGTGGCGGTACTAAACCTCCTGAGTACGGTGATACACCTATTCCGGGCTATACTTATATCAACCCTCTCGA
CGGCACTTATCCGCCTGGTACTGAGCAAAACCCCGCTAATCCTAATCCTTCTCTTGAGGAGTCTCAGCCTCTT
AATACTTTCATGTTTCAGAATAATAGGTTCCGAAATAGGCAGGGGGCATTAACTGTTTATACGGGCACTGTT
ACTCAAGGCACTGACCCCGTTAAAACTTATTACCAGTACACTCCTGTATCATCAAAAGCCATGTATGACGCTT
ACTGGAACGGTAAATTCAGAGACTGCGCTTTCCATTCTGGCTTTAATGAGGATTTATTTGTTTGTGAATATC
AAGGCCAATCGTCTGACCTGCCTCAACCTCCTGTCAATGCTGGCGGCGGCTCTGGTGGTGGTTCTGGTGGCG
GCTCTGAGGGTGGTGGCTCTGAGGGTGGCGGTTCTGAGGGTGGCGGCTCTGAGGGAGGCGGTTCCGGTGGT
GGCTCTGGTTCCGGTGATTTTGATTATGAAAAGATGGCAAACGCTAATAAGGGGGCTATGACCGAAAATGCC
GATGAAAACGCGCTACAGTCTGACGCTAAAGGCAAACTTGATTCTGTCGCTACTGATTACGGTGCTGCTATC
GATGGTTTCATTGGTGACGTTTCCGGCCTTGCTAATGGTAATGGTGCTACTGGTGATTTTGCTGGCTCTAAT
TCCCAAATGGCTCAAGTCGGTGACGGTGATAATTCACCTTTAATGAATAATTTCCGTCAATATTTACCTTCCC
TCCCTCAATCGGTTGAATGTCGCCCTTTTGTCTTTGGCGCTGGTAAACCATATGAATTTTCTATTGATTGTG
ACAAAATAAACTTATTCCGTGGTGTCTTTGCGTTTCTTTTATATGTTGCCACCTTTATGTATGTATTTTCTAC
GTTTGCTAACATACTGCGTAATAAGGAGTCTTAATCATGCCAGTTCTTTTGGGTATTCCGTTATTATTGCGT
TTCCTCGGTTTCCTTCTGGTAACTTTGTTCGGCTATCTGCTTACTTTTCTTAAAAAGGGCTTCGGTAAGATAG
CTATTGCTATTTCATTGTTTCTTGCTCTTATTATTGGGCTTAACTCAATTCTTGTGGGTTATCTCTCTGATAT

TAGCGCTCAATTACCCTCTGACTTTGTTCAGGGTGTTCAGTTAATTCTCCCGTCTAATGCGCTTCCCTGTTTT
TATGTTATTCTCTCTGTAAAGGCTGCTATTTTCATTTTTGACGTTAAACAAAAAATCGTTTCTTATTTGGATT
GGGATAAATAATATGGCTGTTTATTTTGTAACTGGCAAATTAGGCTCTGGAAAGACGCTCGTTAGCGTTGGT
AAGATTCAGGATAAAATTGTAGCTGGGTGCAAAATAGCAACTAATCTTGATTTAAGGCTTCAAAACCTCCCG
CAAGTCGGGAGGTTCGCTAAAACGCCTCGCGTTCTTAGAATACCGGATAAGCCTTCTATATCTGATTTGCTT
GCTATTGGGCGCGGTAATGATTCCTACGATGAAAATAAAAACGGCTTGCTTGTTCTCGATGAGTGCGGTACT
TGGTTTAATACCCGTTCTTGGAATGATAAGGAAAGACAGCCGATTATTGATTGGTTTCTACATGCTCGTAAA
TTAGGATGGGATATTATTTTTCTTGTTCAGGACTTATCTATTGTTGATAAACAGGCGCGTTCTGCATTAGCT
GAACATGTTGTTTATTGTCGTCGTCTGGACAGAATTACTTTACCTTTTGTCGGTACTTTATATTCTCTTATTA
CTGGCTCGAAAATGCCTCTGCCTAAATTACATGTTGGCGTTGTTAAATATGGCGATTCTCAATTAAGCCCTA
CTGTTGAGCGTTGGCTTTATACTGGTAAGAATTTGTATAACGCATATGATACTAAACAGGCTTTTTCTAGTA
ATTATGATTCCGGTGTTTATTCTTATTTAACGCCTTATTTATCACACGGTCGGTATTTCAAACCATTAAATTT
AGGTCAGAAGATGAAATTAACTAAAATATATTTGAAAAAGTTTTCTCGCGTTCTTTGTCTTGCGATTGGATT
TGCATCAGCATTTACATATAGTTATATAACCCAACCTAAGCCGGAGGTTAAAAAGGTAGTCTCTCAGACCTA
TGATTTTGATAAATTCACTATTGACTCTTCTCAGCGTCTTAATCTAAGCTATCGCTATGTTTTCAAGGATTCT
AAGGGAAAATTAATTAATAGCGACGATTTACAGAAGCAAGGTTATTCACTCACATATATTGATTTATGTACT
GTTTCCATTAAAAAAGGTAATTCAAATGAAATTGTTAAATGTAATTAATTTTGTTTTCTTGATGTTTGTTTCA
TCATCTTCTTTTGCTCAGGTAATTGAAATGAATAATTCGCCTCTGCGCGATTTTGTAACTTGGTATTCAAAGC
AATCAGGCGAATCCGTTATTGTTTCTCCCGATGTAAAAGGTACTGTTACTGTATATTCATCTGACGTTAAAC
CTGAAAATCTACGCAATTTCTTTATTTCTGTTTTACGTGCAAATAATTTTGATATGGTAGGTTCTAACCCTTC
CATTATTCAGAAGTATAATCCAAACAATCAGGATTATATTGATGAATTGCCATCATCTGATAATCAGGAATA
TGATGATAATTCCGCTCCTTCTGGTGGTTTCTTTGTTCCGCAAAATGATAATGTTACTCAAACTTTTAAAATT
AATAACGTTCGGGCAAAGGATTTAATACGAGTTGTCGAATTGTTTGTAAAGTCTAATACTTCTAAATCCTCA
AATGTATTATCTATTGACGGCTCTAATCTATTAGTTGTTAGTGCTCCTAAAGATATTTTAGATAACCTTCCTC
AATTCCTTTCAACTGTTGATTTGCCAACTGACCAGATATTGATTGAGGGTTTGATATTTGAGGTTCAGCAAG
GTGATGCTTTAGATTTTTCATTTGCTGCTGGCTCTCAGCGTGGCACTGTTGCAGGCGGTGTTAATACTGACC
GCCTCACCTCTGTTTTATCTTCTGCTGGTGGTTCGTTCGGTATTTTTAATGGCGATGTTTTAGGGCTATCAG
TTCGCGCATTAAAGACTAATAGCCATTCAAAAATATTGTCTGTGCCACGTATTCTTACGCTTTCAGGTCAGAA
GGGTTCTATCTCTGTTGGCCAGAATGTCCCTTTTATTACTGGTCGTGTGACTGGTGAATCTGCCAATGTAAA
TAATCCATTTCAGACGATTGAGCGTCAAAATGTAGGTATTTCCATGAGCGTTTTTCCTGTTGCAATGGCTGG
CGGTAATATTGTTCTGGATATTACCAGCAAGGCCGATAGTTTGAGTTCTTCTACTCAGGCAAGTGATGTTAT
TACTAATCAAAGAAGTATTGCTACAACGGTTAATTTGCGTGATGGACAGACTCTTTTACTCGGTGGCCTCAC
TGATTATAAAAACACTTCTCAGGATTCTGGCGTACCGTTCCTGTCTAAAATCCCTTTAATCGGCCTCCTGTTT
AGCTCCCGCTCTGATTCTAACGAGGAAAGCACGTTATACGTGCTCGTCAAAGCAACCATAGTACGCGCCCTG
TAGCGGCGCATTAAGCGCGGCGGGTGTGGTGGTTACGCGCAGCGTGACCGCTACACTTGCCAGCGCCCTAGC
GCCCGCTCCTTTCGCTTTCTTCCCTTCCTTTCTCGCCACGTTCGCCGGCTTTCCCCGTCAAGCTCTAAATCGG
GGGCTCCCTTTAGGGTTCCGATTTAGTGCTTTACGGCACCTCGACCCCAAAAAACTTGATTTGGGTGATGGT
TCACGTAGTGGGCCATCGCCCTGATAGACGGTTTTTCGCCCTTTGACGTTGGAGTCCACGTTCTTTAATAGT
GGACTCTTGTTCCAAACTGGAACAACACTCAACCCTATCTCGGGCTATTCTTTTGATTTATAAGGGATTTTGC
CGATTTCGGAACCACCATCAAACAGGATTTTCGCCTGCTGGGGCAAACCAGCGTGGACCGCTTGCTGCAACT
CTCTCAGGGCCAGGCGGTGAAGGGCAATCAGCTGTTGCCCGTCTCACTGGTGAAAAGAAAAACCACCCTGGC
GCCCAATACGCAAACCGCCTCTCCCCGCGCGTTGGCCGATTCATTAATGCAGCTGGCACGACAGGTTTCCCG
ACTGGAAAGCGGGCAGTGAGCGCAACGCAATTAATGTGAGTTAGCTCACTCATTAGGCACCCCAGGCTTTAC
ACTTTATGCTTCCGGCTCGTATGTTGTGTGGAATTGTGAGCGGATAACAATTTCACACAGGAAACAGCTATG
ACCATGATTACGAATTCGAGCTCGGTACCCGGGGATCCATTCTCCTGTGACTCGGAAGTGCATTTATCATCT
CCATAAAACAAAACCCGCCGTAGCGAGTTCAGATAAAATAAATCCCCGCGAGTGCGAGGATTGTTATGTAAT
ATTGGGTTTAATCATCTATATGTTTTGTACAGAGAGGGCAAGTATCGTTTCCACCGTACTCGTGATAATAAT
TTTGCACGGTATCAGTCATTTCTCGCACATTGCAGAATGGGGATTTGTCTTCATTAGACTTATAAACCTTCAT
GGAATATTTGTATGCCGACTCTATATCTATACCTTCATCTACATAAACACCTTCGTGATGTCTGCATGGAGAC
AAGACACCGGATCTGCACAACATTGATAACGCCCAATCTTTTTGCTCAGACTCTAACTCATTGATACTCATTT
ATAAACTCCTTGCAATGTATGTCGTTTCAGCTAAACGGTATCAGCAATGTTTATGTAAAGAAACAGTAAGAT
AATACTCAACCCGATGTTTGAGTACGGTCATCATCTGACACTACAGACTCTGGCATCGCTGTGAAGACGACG
CGAAATTCAGCATTTTCACAAGCGTTATCTTTTACAAAACCGATCTCACTCTCCTTTGATGCGAATGCCAGCG
TCAGACATCATATGCAGATACTCACCTGCATCCTGAACCCATTGACCTCCAACCCCGTAATAGCGATGCGTAA
TGATGTCGATAGTTACTAACGGGTCTTGTTCGATTAACTGCCGCAGAAACTCTTCCAGGTCACCAGTGCAGT
GCTTGATAACAGGAGTCTTCCCAGGATGGCGAACAACAAGAAACTGGTTTCCGTCTTCACGGACTTCGTTGC
TTTCCAGTTTAGCAATACGCTTACTCCCATCCGAGATAACACCTTCGTAATACTCACGCTGCTCGTTGAGTTT
TGATTTTGCTGTTTCAAGCTCAACACGCAGTTTCCCTACTGTTAGCGCAATATCCTCGTTCTCCTGGTCGCGG
CGTTTGATGTATTGCTGGTTTCTTTCCCGTTCATCCAGCAGTTCCAGCACAATCGATGGTGTTACCAATTCAT
GGAAAAGGTCTGCGTCAAATCCCCAGTCGTCATGCATTGCCTGCTCTGCCGCTTCACGCAGTGCCTGAGAGT
TAATTTCGCTCACTTCGAACCTCTCTGTTTACTGATAAGTTCCAGATCCTCCTGGCAACTTGCACAAGTCCGA
CAACCCTGAACGACCAGGCGTCTTCGTTCATCTATCGGATCGCCACACTCACAACAATGAGTGGCAGATATA
GCCTGGTGGTTCAGGCGGCGCATTTTTATTGCTGTGTTGCGCTGTAATTCTTCTATTTCTGATGCTGAATCA
ATGATGTCTGCCATCTTTCATTAATCCCTGAACTGTTGGTTAATACGCATGAGGGTGAATGCGAATAATAAA
GCTTGGCACTGGCCGTCGTTTTACAACGTCGTGACTGGGAAAACCCTGGCGTTACCCAACTTAATCGCCTTG
CAGCACATCCCCCTTTCGCCAGCTGGCGTAATAGCGAAGAGGCCCGCACCGATCGCCCTTCCCAACAGTTGC
GCAGCCTGAATGGCGAATGGCGCTTTGCCTGGTTTCCGGCACCAGAAGCGGTGCCGGAAAGCTGGCTGGAGT
GCGATCTTCCTGAGGCCGATACTGTCGTCGTCCCCTCAAACTGGCAGATGCACGGTTACGATGCGCCCATCT
ACACCAACGTGACCTATCCCATTACGGTCAATCCGCCGTTTGTTCCCACGGAGAATCCGACGGGTTGTTACT
CGCTCACATTTAATGTTGATGAAAGCTGGCTACAGGAAGGCCAGACGCGAATTATTTTTGATGGCGTTCCTA
TTGGTTAAAAAATGAGCTGATTTAACAAAAATTTAATGCGAATTTTAACAAAATATTAACGTTTACAATTTAA
ATATTTGCTTATACAATCTTCCTGTTTTTGGGGCTTTTCTGATTATCAACCGGGGTACATATGATTGACATGC
TAGTTTTACGATTACCGTTCATCGATTCTCTTGTTTGCTCCAGACTCTCAGGCAATGACCTGATAGCCTTTGT
AGATCTCTCAAAAATAGCTACCCTCTCCGGCATTAATTTATCAGCTAGAACGGTTGAATATCATATTGATGGT
GATTTGACTGTCTCCGGCCTTTCTCACCCTTTTGAATCTTTACCTACACATTACTCAGGCATTGCATTTAAAA
TATATGAGGGTTCTAAAAATTTTTATCCTTGCGTTGAAATAAAGGCTTCTCCCGCAAAAGTATTACAGGGTC
ATAATGTTTTTGGTACAACCGATTTAGCTTTATGCTCTGAGGCTTTATTGCTTAATTTTGCTAATTCTTTGCC
TTGCCTGTATGATTTATTGGATGTT

Scaffold p7249

AATGCTACTACTATTAGTAGAATTGATGCCACCTTTTCAGCTCGCGCCCCAAATGAAAATATAGCTAAACAG
GTTATTGACCATTTGCGAAATGTATCTAATGGTCAAACTAAATCTACTCGTTCGCAGAATTGGGAATCAACT

GTTATATGGAATGAAACTTCCAGACACCGTACTTTAGTTGCATATTTAAAACATGTTGAGCTACAGCATTAT
ATTCAGCAATTAAGCTCTAAGCCATCCGCAAAAATGACCTCTTATCAAAAGGAGCAATTAAAGGTACTCTCTA
ATCCTGACCTGTTGGAGTTTGCTTCCGGTCTGGTTCGCTTTGAAGCTCGAATTAAAACGCGATATTTGAAGT
CTTTCGGGCTTCCTCTTAATCTTTTTGATGCAATCCGCTTTGCTTCTGACTATAATAGTCAGGGTAAAGACCT
GATTTTTGATTTATGGTCATTCTCGTTTTCTGAACTGTTTAAAGCATTTGAGGGGGATTCAATGAATATTTA
TGACGATTCCGCAGTATTGGACGCTATCCAGTCTAAACATTTTACTATTACCCCCTCTGGCAAAACTTCTTTT
GCAAAAGCCTCTCGCTATTTTGGTTTTTATCGTCGTCTGGTAAACGAGGGTTATGATAGTGTTGCTCTTACT
ATGCCTCGTAATTCCTTTTGGCGTTATGTATCTGCATTAGTTGAATGTGGTATTCCTAAATCTCAACTGATGA
ATCTTTCTACCTGTAATAATGTTGTTCCGTTAGTTCGTTTTATTAACGTAGATTTTTCTTCCCAACGTCCTGA
CTGGTATAATGAGCCAGTTCTTAAAATCGCATAAGGTAATTCACAATGATTAAAGTTGAAATTAAACCATCT
CAAGCCCAATTTACTACTCGTTCTGGTGTTTCTCGTCAGGGCAAGCCTTATTCACTGAATGAGCAGCTTTGT
TACGTTGATTTGGGTAATGAATATCCGGTTCTTGTCAAGATTACTCTTGATGAAGGTCAGCCAGCCTATGCG
CCTGGTCTGTACACCGTTCATCTGTCCTCTTTCAAAGTTGGTCAGTTCGGTTCCCTTATGATTGACCGTCTGC
GCCTCGTTCCGGCTAAGTAACATGGAGCAGGTCGCGGATTTCGACACAATTTATCAGGCGATGATACAAATC
TCCGTTGTACTTTGTTTCGCGCTTGGTATAATCGCTGGGGGTCAAAGATGAGTGTTTTAGTGTATTCTTTTG
CCTCTTTCGTTTTAGGTTGGTGCCTTCGTAGTGGCATTACGTATTTTACCCGTTTAATGGAAACTTCCTCATG
AAAAAGTCTTTAGTCCTCAAAGCCTCTGTAGCCGTTGCTACCCTCGTTCCGATGCTGTCTTTCGCTGCTGAG
GGTGACGATCCCGCAAAAGCGGCCTTTAACTCCCTGCAAGCCTCAGCGACCGAATATATCGGTTATGCGTGG
GCGATGGTTGTTGTCATTGTCGGCGCAACTATCGGTATCAAGCTGTTTAAGAAATTCACCTCGAAAGCAAGC
TGATAAACCGATACAATTAAAGGCTCCTTTTGGAGCCTTTTTTTTGGAGATTTTCAACGTGAAAAAATTATT
ATTCGCAATTCCTTTAGTTGTTCCTTTCTATTCTCACTCCGCTGAAACTGTTGAAAGTTGTTTAGCAAAATCC
CATACAGAAAATTCATTTACTAACGTCTGGAAAGACGACAAAACTTTAGATCGTTACGCTAACTATGAGGGC
TGTCTGTGGAATGCTACAGGCGTTGTAGTTTGTACTGGTGACGAAACTCAGTGTTACGGTACATGGGTTCCT
ATTGGGCTTGCTATCCCTGAAAATGAGGGTGGTGGCTCTGAGGGTGGCGGTTCTGAGGGTGGCGGTTCTGA
GGGTGGCGGTACTAAACCTCCTGAGTACGGTGATACACCTATTCCGGGCTATACTTATATCAACCCTCTCGA
CGGCACTTATCCGCCTGGTACTGAGCAAAACCCCGCTAATCCTAATCCTTCTCTTGAGGAGTCTCAGCCTCTT
AATACTTTCATGTTTCAGAATAATAGGTTCCGAAATAGGCAGGGGGCATTAACTGTTTATACGGGCACTGTT
ACTCAAGGCACTGACCCCGTTAAAACTTATTACCAGTACACTCCTGTATCATCAAAAGCCATGTATGACGCTT
ACTGGAACGGTAAATTCAGAGACTGCGCTTTCCATTCTGGCTTTAATGAGGATTTATTTGTTTGTGAATATC
AAGGCCAATCGTCTGACCTGCCTCAACCTCCTGTCAATGCTGGCGGCGGCTCTGGTGGTGGTTCTGGTGGCG
GCTCTGAGGGTGGTGGCTCTGAGGGTGGCGGTTCTGAGGGTGGCGGCTCTGAGGGAGGCGGTTCCGGTGGT
GGCTCTGGTTCCGGTGATTTTGATTATGAAAAGATGGCAAACGCTAATAAGGGGGCTATGACCGAAAATGCC
GATGAAAACGCGCTACAGTCTGACGCTAAAGGCAAACTTGATTCTGTCGCTACTGATTACGGTGCTGCTATC
GATGGTTTCATTGGTGACGTTTCCGGCCTTGCTAATGGTAATGGTGCTACTGGTGATTTTGCTGGCTCTAAT
TCCCAAATGGCTCAAGTCGGTGACGGTGATAATTCACCTTTAATGAATAATTTCCGTCAATATTTACCTTCCC
TCCCTCAATCGGTTGAATGTCGCCCTTTTGTCTTTGGCGCTGGTAAACCATATGAATTTTCTATTGATTGTGA
CAAAATAAACTTATTCCGTGGTGTCTTTGCGTTTCTTTTATATGTTGCCACCTTTATGTATGTATTTTCTACG
TTTGCTAACATACTGCGTAATAAGGAGTCTTAATCATGCCAGTTCTTTTGGGTATTCCGTTATTATTGCGTTT
CCTCGGTTTCCTTCTGGTAACTTTGTTCGGCTATCTGCTTACTTTTCTTAAAAAGGGCTTCGGTAAGATAGCT
ATTGCTATTTCATTGTTTCTTGCTCTTATTATTGGGCTTAACTCAATTCTTGTGGGTTATCTCTCTGATATTA
GCGCTCAATTACCCTCTGACTTTGTTCAGGGTGTTCAGTTAATTCTCCCGTCTAATGCGCTTCCCTGTTTTTA
TGTTATTCTCTCTGTAAAGGCTGCTATTTTCATTTTTGACGTTAAACAAAAAATCGTTTCTTATTTGGATTGG
GATAAATAATATGGCTGTTTATTTTGTAACTGGCAAATTAGGCTCTGGAAAGACGCTCGTTAGCGTTGGTAA
GATTCAGGATAAAATTGTAGCTGGGTGCAAAATAGCAACTAATCTTGATTTAAGGCTTCAAAACCTCCCGCA
AGTCGGGAGGTTCGCTAAAACGCCTCGCGTTCTTAGAATACCGGATAAGCCTTCTATATCTGATTTGCTTGC
TATTGGGCGCGGTAATGATTCCTACGATGAAAATAAAAACGGCTTGCTTGTTCTCGATGAGTGCGGTACTTG
GTTTAATACCCGTTCTTGGAATGATAAGGAAAGACAGCCGATTATTGATTGGTTTCTACATGCTCGTAAATT
AGGATGGGATATTATTTTTCTTGTTCAGGACTTATCTATTGTTGATAAACAGGCGCGTTCTGCATTAGCTGA
ACATGTTGTTTATTGTCGTCGTCTGGACAGAATTACTTTACCTTTTGTCGGTACTTTATATTCTCTTATTACT
GGCTCGAAAATGCCTCTGCCTAAATTACATGTTGGCGTTGTTAAATATGGCGATTCTCAATTAAGCCCTACT
GTTGAGCGTTGGCTTTATACTGGTAAGAATTTGTATAACGCATATGATACTAAACAGGCTTTTTCTAGTAAT
TATGATTCCGGTGTTTATTCTTATTTAACGCCTTATTTATCACACGGTCGGTATTTCAAACCATTAAATTTAG
GTCAGAAGATGAAATTAACTAAAATATATTTGAAAAAGTTTTCTCGCGTTCTTTGTCTTGCGATTGGATTTG
CATCAGCATTTACATATAGTTATATAACCCAACCTAAGCCGGAGGTTAAAAAGGTAGTCTCTCAGACCTATG
ATTTTGATAAATTCACTATTGACTCTTCTCAGCGTCTTAATCTAAGCTATCGCTATGTTTTCAAGGATTCTAA
GGGAAAATTAATTAATAGCGACGATTTACAGAAGCAAGGTTATTCACTCACATATATTGATTTATGTACTGT
TTCCATTAAAAAAGGTAATTCAAATGAAATTGTTAAATGTAATTAATTTTGTTTTCTTGATGTTTGTTTCATC
ATCTTCTTTTGCTCAGGTAATTGAAATGAATAATTCGCCTCTGCGCGATTTTGTAACTTGGTATTCAAAGCAA
TCAGGCGAATCCGTTATTGTTTCTCCCGATGTAAAAGGTACTGTTACTGTATATTCATCTGACGTTAAACCTG
AAAATCTACGCAATTTCTTTATTTCTGTTTTACGTGCAAATAATTTTGATATGGTAGGTTCTAACCCTTCCAT
TATTCAGAAGTATAATCCAAACAATCAGGATTATATTGATGAATTGCCATCATCTGATAATCAGGAATATGA
TGATAATTCCGCTCCTTCTGGTGGTTTCTTTGTTCCGCAAAATGATAATGTTACTCAAACTTTTAAAATTAAT
AACGTTCGGGCAAAGGATTTAATACGAGTTGTCGAATTGTTTTGTAAAGTCTAATACTTCTAAATCCTCAAAT
GTATTATCTATTGACGGCTCTAATCTATTAGTTGTTAGTGCTCCTAAAGATATTTTAGATAACCTTCCTCAAT
TCCTTTCAACTGTTGATTTGCCAACTGACCAGATATTGATTGAGGGTTTGATATTTGAGGTTCAGCAAGGTG
ATGCTTTAGATTTTTCATTTGCTGCTGGCTCTCAGCGTGGCACTGTTGCAGGCGGTGTTAATACTGACCGCC
TCACCTCTGTTTTTATCTTCTGCTGGTGGTTCGTTCGGTATTTTTAATGGCGATGTTTTAGGGCTATCAGTTC
GCGCATTAAAGACTAATAGCCATTCAAAAATATTGTCTGTGCCACGTATTCTTACGCTTTCAGGTCAGAAGG
GTTCTATCTCTGTTGGCCAGAATGTCCCTTTTATTACTGGTCGTGTGACTGGTGAATCTGCCAATGTAAATA
ATCCATTTCAGACGATTGAGCGTCAAAATGTAGGTATTTCCATGAGCGTTTTTCCTGTTGCAATGGCTGGCG
GTAATATTGTTCTGGATATTACCAGCAAGGCCGATAGTTTGAGTTCTTCTACTCAGGCAAGTGATGTTATTA
CTAATCAAAGAAGTATTGCTACAACGGTTAATTTGCGTGATGGACAGACTCTTTTACTCGGTGGCCTCACTG
ATTATAAAAACACTTCTCAGGATTCTGGCGTACCGTTCCTGTCTAAAATCCCTTTAATCGGCCTCCTGTTTAG
CTCCCGCTCTGATTCTAACGAGGAAAGCACGTTATACGTGCTCGTCAAAGCAACCATAGTACGCGCCCTGTA
GCGGCGCATTAAGCGCGGCGGGTGTGGTGGTTACGCGCAGCGTGACCGCTACACTTGCCAGCGCCCTAGCGC
CCGCTCCTTTCGCTTTCTTCCCTTCCTTTCTCGCCACGTTCGCCGGCTTTCCCCGTCAAGCTCTAAATCGGGG
GCTCCCTTTAGGGTTCCGATTTAGTGCTTTACGGCACCTCGACCCCAAAAAACTTGATTTGGGTGATGGTTC
ACGTAGTGGGCCATCGCCCTGATAGACGGTTTTTCGCCCTTTGACGTTGGAGTCCACGTTCTTTAATAGTGG
ACTCTTGTTCCAAACTGGAACAACACTCAACCCTATCTCGGGCTATTCTTTTGATTTATAAGGGATTTTGCCG
ATTTCGGAACCACCATCAAACAGGATTTTCGCCTGCTGGGGCAAACCAGCGTGGACCGCTTGCTGCAACTCT
CTCAGGGCCAGGCGGTGAAGGGCAATCAGCTGTTGCCCGTCTCACTGGTGAAAAGAAAAACCACCCTGGCGC
CCAATACGCAAACCGCCTCTCCCCGCGCGTTGGCCGATTCATTAATGCAGCTGGCACGACAGGTTTCCCGAC
TGGAAAGCGGGCAGTGAGCGCAACGCAATTAATGTGAGTTAGCTCACTCATTAGGCACCCCAGGCTTTACAC

TTTATGCTTCCGGCTCGTATGTTGTGTGGAATTGTGAGCGGATAACAATTTCACACAGGAAACAGCTATGAC
CATGATTACGAATTCGAGCTCGGTACCCGGGGATCCTCTAGAGTCGACCTGCAGGCATGCAAGCTTGGCACT
GGCCGTCGTTTTACAACGTCGTGACTGGGAAAACCCTGGCGTTACCCAACTTAATCGCCTTGCAGCACATCC
CCCTTTCGCCAGCTGGCGTAATAGCGAAGAGGCCCGCACCGATCGCCCTTCCCAACAGTTGCGCAGCCTGAA
TGGCGAATGGCGCTTTGCCTGGTTTCCGGCACCAGAAGCGGTGCCGGAAAGCTGGCTGGAGTGCGATCTTCC
TGAGGCCGATACTGTCGTCGTCCCCTCAAACTGGCAGATGCACGGTTACGATGCGCCCATCTACACCAACGT
GACCTATCCCATTACGGTCAATCCGCCGTTTGTTCCCACGGAGAATCCGACGGGTTGTTACTCGCTCACATTT
AATGTTGATGAAAGCTGGCTACAGGAAGGCCAGACGCGAATTATTTTTGATGGCGTTCCTATTGGTTAAAAA
ATGAGCTGATTTAACAAAAATTTAATGCGAATTTTAACAAAATATTAACGTTTACAATTTAAATATTTGCTTA
TACAATCTTCCTGTTTTTGGGGCTTTTCTGATTATCAACCGGGGTACATATGATTGACATGCTAGTTTTACG
ATTACCGTTCATCGATTCTCTTGTTTGCTCCAGACTCTCAGGCAATGACCTGATAGCCTTTGTAGATCTCTCA
AAAATAGCTACCCTCTCCGGCATTAATTTATCAGCTAGAACGGTTGAATATCATATTGATGGTGATTTGACT
GTCTCCGGCCTTTCTCACCCTTTTGAATCTTTACCTACACATTACTCAGGCATTGCATTTAAAATATATGAGG
GTTCTAAAAATTTTTATCCTTGCGTTGAAATAAAGGCTTCTCCCGCAAAAGTATTACAGGGTCATAATGTTTT
TGGTACAACCGATTTAGCTTTATGCTCTGAGGCTTTATTGCTTAATTTTGCTAATTCTTTGCCTTGCCTGTAT
GATTTATTGGATGTT

Scaffold p4844

CTTTTCGGGGAAATGTGCGCGGAACCTTGATCGGGCACGTAAGAGGTTCCAACTTTCACCATAATGAAATAA
GATCACTACCGGGCGTATTTTTTGAGTTATCGAGATTTTCAGGAGCTAAGGAAGCTAAAATGGAGAAAAAAA
TCACTGGATATACCACCGTTGATATATCCCAATGGCATCGTAAAGAACATTTTGAGGCATTTCAGTCAGTTG
CTCAATGTACCTATAACCAGACCGTTCAGCTGGATATTACGGCCTTTTTAAAGACCGTAAAGAAAAATAAGC
ACAAGTTTTATCCGGCCTTTATTCACATTCTTGCCCGCCTGATGAATGCTCATCCGGAATTTCGTATGGCAAT
GAAAGACGGTGAGCTGGTGATATGGGATAGTGTTCACCCTTGTTACACCGTTTTCCATGAGCAAACTGAAAC
GTTTTCATCGCTCTGGAGTGAATACCACGACGATTTCCGGCAGTTTCTACACATATATTCGCAAGATGTGGC
GTGTTACGGTGAAAACCTGGCCTATTTCCCTAAAGGGTTTATTGAGAATATGTTTTTCGTCTCAGCCAATCC
CTGGGTGAGTTTCACCAGTTTTGATTTAAACGTGGCCAATATGGACAACTTCTTCGCCCCCGTTTTCACCATG
GGCAAATATTATACGCAAGGCGACAAGGTGCTGATGCCGCTGGCGATTCAGGTTCATCATGCCGTTTGTGAT
GGCTTCCATGTCGGCAGAATGCTTAATGAATTACAACAGTACTGCGATGAGTGGCAGGGCGGGGCGTAATTT
GATATCGAGCTCGCTTGGACTCCTGTTGATAGATCCAGTAATGACCTCAGAACTCCATCTGGATTTGTTCAG
AACGCTCGGTTGCCGCCGGGCGTTTTTTATTGGTGAGAATCCAAGCCTCGAGCTGTCAGACCAAGTTTACTC
ATATATACTTTAGATTGATTTAAAACTTCATTTTTAATTTAAAAGGATCTAGGTGAAGATCCTTTTTGATAAT
CTCATGACCAAAATCCCTTAACGTGAGTTTTCGTTCCACTGAGCGTCAGACCCCGTAGAAAAGATCAAAGGA
TCTTCTTGAGATCCTTTTTTTTCTGCGCGTAATCTGCTGCTTGCAAACAAAAAAACCACCGCTACCAGCGGTGG
TTTGTTTGCCGGATCAAGAGCTACCAACTCTTTTTCCGAAGGTAACTGGCTTCAGCAGAGCGCAGATACCAA
ATACTGTTCTTCTAGTGTAGCCGTAGTTAGGCCACCACTTCAAGAACTCTGTAGCACCGCCTACATACCTCGC
TCTGCTAATCCTGTTACCAGTGGCTGCTGCCAGTGGCGATAAGTCGTGTCTTACCGGGTTGGACTCAAGACG
ATAGTTACCGGATAAGGCGCAGCGGTCGGGCTGAACGGGGGGTTCGTGCACACAGCCCAGCTTGGAGCGAA
CGACCTACACCGAACTGAGATACCTACAGCGTGAGCTATGAGAAAGCGCCACGCTTCCCGAAGGGAGAAAGG
CGGACAGGTATCCGGTAAGCGGCAGGGTCGGAACAGGAGAGCGCACGAGGGAGCTTCCAGGGGGAAACGCC
TGGTATCTTTATAGTCCTGTCGGGTTTCGCCACCTCTGACTTGAGCGTCGATTTTTGTGATGCTCGTCAGGG
GGGCGGAGCCTATGGAAAAACGCCAGCAACGCGGCCTTTTTACGGTTCCTGGCCTTTTGCTGGCCTTTTGCT
CACGAAATTCACCTCGAAAGCAAGCTGATAAACCGATACAATTAAAGGCTCCTTTTGGAGCCTTTTTTTTTTG
GAGATTTTCAACGTGAAAAAATTATTATTCGCAATTCCTTTAGTTGTTCCTTTCTATTCTCACTCCGCTGAAA
CTGTTGAAAGTTGTTTAGCAAAACCCCATACAGAAAATTCATTTACTAACGTCTGGAAAGACGACAAAACTT
TAGATCGTTACGCTAACTATGAGGGCTGTCTGTGGAATGCTACAGGCGTTGTAGTTTGTACTGGTGACGAAA
CTCAGTGTTACGGTACATGGGTTCCTATTGGGCTTGCTATCCCTGAAAATGAGGGTGGTGGCTCTGAGGGTG
GCGGTTCTGAGGGTGGCGGTTCTGAGGGTGGCGGTACTAAACCTCCTGAGTACGGTGATACACCTATTCCGG
GCTATACTTATATCAACCCTCTCGACGGCACTTATCCGCCTGGTACTGAGCAAAACCCCGCTAATCCTAATCC
TTCTCTTGAGGAGTCTCAGCCTCTTAATACTTTCATGTTTCAGAATAATAGGTTCCGAAATAGGCAGGGGGC
ATTAACTGTTTATACGGGCACTGTTACTCAAGGCACTGACCCCGTTAAAACTTATTACCAGTACACTCCTGTA
TCATCAAAAGCCATGTATGACGCTTACTGGAACGGTAAATTCAGAGACTGCGCTTTCCATTCTGGCTTTAAT
GAGGATCCATTCGTTTGTGAATATCAAGGCCAATCGTCTGACCTGCCTCAACCTCCTGTCAATGCTGGCGGC
GGCTCTGGTGGTGGTTCTGGTGGCGGCTCTGAGGGTGGTGGCTCTGAGGGTGGCGGTTCTGAGGGTGGCGG
CTCTGAGGGAGGCGGTTCCGGTGGTGGCTCTGGTTCCGGTGATTTTGATTATGAAAAGATGGCAAACGCTAA
TAAGGGGGCTATGACCGAAAATGCCGATGAAAACGCGCTACAGTCTGACGCTAAAGGCAAACTTGATTCTGT
CGCTACTGATTACGGTGCTGCTATCGATGGTTTCATTGGTGACGTTTCCGGCCTTGCTAATGGTAATGGTGC
TACTGGTGATTTTGCTGGCTCTAATTCCCAAATGGCTCAAGTCGGTGACGGTGATAATTCACCTTTAATGAA
TAATTTCCGTCAATATTTACCTTCCCTCCCTCAATCGGTTGAATGTCGCCCTTTTGTCTTTGGCGCTGGTAAA
CCATATGAATTTTCTATTGATTGTGACAAAATAAACTTATTCCGTGGTGTCTTTGCGTTTCTTTTATATGTTG
CCACCTTTATGTATGTATTTTCTACGTTTGCTAACATACTGCGTAATAAGGAGTCTTAATCATGCCAGTTCTT
TTGGGTTAAGTAACTAAGGAGCTTTAACTCCTACTTTCATACGCCACCGCACAGACTTCATTGACCACGTATC
TGAGACTCCTTGTAAACTGACTACTCCAGCTCCATCAACAATCTTGAAGAAGTTCTATCCGATCACGGTTATC
GCGAGTCTTAGCGTAGCCAATGCTGGGCCGTAGCGTCTACTTAACGGAAAGAAGGGTGAAAGCTGCCACAGA
AAATAAATTACTATTTACATTTGTAAGACAAAGTTAGTATGGTTAAATACTGGCTTAGTCTGCGGGAAACTT
AGCCATACGACTTGGTTTGCCTATCGTTACAGCGTACGACCCGTTCACCAATCGCATTTGCGATGCAGATAA
CAACTCGGACGAAGTAACCACGGAGTATCCTATCTCTTACGAGTGTTATTCTCATTATAAAGTGCATTGGCA
GGGGGTGTGCGGGTATACTAAACGTAATAAGGGATTACCATGAAGGTAAATGTTCAGGACAACTCTGTGTAT
TGCGTTAGGATAGCGGAAAAACTGCGCGTATGTGGTACCGAATGGTTGTTGGAAGACCGTAGTCGTGTCTGC
TTTAAGTTTTCGTCCGTTGCTGGATGTAGAATTAAAATAGGGCCCTCAGATGCCATCTGGTGCTACTGTTTC
ATGGAGAGGAGGGTCTCCAGGTGACGTGCCGTGGCGCCGATGAGTCAAAAGGCACAAGCAGAAATCATATG
ACTATGGCCGCCTGAATCCCCCGTCACGAACCGGTAGCATCAACCCAGTTGACAGCTTCTGACCTTCCAACAC
TTAACAGGCCAGCGCAGTAGGCGGCGTCTTCACAGTCCCTAAGAGCCAAACCTCTAGTGGGGAGCTGCACCA
GAGTTCCTCGGATCGCTGAGCGCCCTGTAGCGGCGCATTAAGCGCGGCGGGTGTGGTGGTTACGCGCAGCGT
GACCGCTACACTTGCCAGCGCCCTAGCGCCCGCTCCTTTCGCTTTCTTCCCTTCCTTTCTCGCCACGTTCGCC
GGCTTTCCCCGTCAAGCTCTAAATCGGGGGCTCCCTTTAGGGTTCCGATTTAGTGCTTTACGGCACCTCGAC
CCCAAAAAACTTGATTAGGGTGATGGTTCACGTAGTGGGCCATCGCCCTGATAGACGGTTTTTCGCCCTTTG
ACGTTGGAGTCCACGTTCTTTAATAGTGGACTCTTGTTCCAAACTGGAACAACACTCAACCCTATCTCGGTCC
AAGTCTATTAGCCTAGCTCCTTGCCCCTTTTTGTGAAACAAATTTTATCGAAAGAACTTCGAGCAATTCCCAC
ATGCTCTCGTACTTTGGGTTACACACGCTTGGTCATCGTTCGCCCATACAGACATTTGCAGCCCGCATGTCCT

GGGAACATCCGCTGTCGGCAAAGCCGGCTGAGCGATTCAATACCCGACTCCCGGGGCATAACGGGCTAATCG
GGACGCACGTCGCGCTAGGTTTGAGGTCGATCTTTCCGAGAAGCTATATAGTACGGCCTCCGGACCAAGATA
CGCGGTGGACTGATAATGATGGGCGACCCTGCCTTATGCAACGACACCGCGAGGCTCGCAAGGAATATTTCT
TGATCCATTCGGTTCTACATAGAGATTTACTCGACGGTCCACCTACCTGTACAATCTAACTACGTTTAGACTT
GTAAGCGTGAGACGATATCACTGGCTTAGTTAATTGAACGCCACTAGATCAGTGATTGTCAGCACTCACCCC
AATG

Scaffold p1033

AGACTTCCGGCTTAAGCTCTGAAAGGGTTCTATATCTCCAGGTAGATCTGCTCCCAATGTAACATGCTCGGG
ACCTACAAGGTGTCAGGATCGAAGATTGCACGACGATGACTTACGGACAGCCGGACGTACTCCCTGAACAAT
GCGATTCGATATACACGGTGGTGTTCTGTTTGGGCCTTCTGACTCAAAGCCAAGCCTGGATAACAGTGTCCT
TCGGGTCCTCCGTGTTATGGAGCACGGCTGCTTAGAGCATTGCCACGGAGCCTTTGAAGGCAGCGAGGGCGT
GGCCTCCCGACCGCACTAGCACAACACAGGAGAGGACCGGCGACATACCTGGGTGGAAGTTTCATCGGAATA
CTCGTCAAACGACTAACCCATCAGCCATCGATCGTATGAATATGTATAATCCATCCGTACCTAGAGTCGCGG
GCCAGCATCAACGCATGTGGTAAATTGGTTGGATCCGCGAGCAGTAAGAACCCTTAAATCAAGCTTCCCGGC
ACAGCGTCAGTGGCGGATACGCGCGATGTCTGCCGTGCTGAAGTAGGGTAAGGGCCCTCCATGCGGACTTCT
TGGTAGCTCCAAGAGTGGATTCCCTCGTAAGTTCGGCTACGTCATTTACTGCAGCCTCTGCAAGCGGAGGAA
CTCCACTATGCACTTAGGGACTACTGATATCAAATTCGCCGCCGAAACCCGCAAGATGGTGCTCTTTAACTG
GCCAATACATAGCCCAGTGAAACTGTTCGCATATGGCGAACCTTTCTGCGCCACTTGTTTCGCGCACGTTTA
GGAGCTTATTAGCTAAATGAACCAGTTCTCTGGAGTGATACAGACTTGCGGCGTCCCGTAAACCGAGAGTAA
CTTAACCATAAAGCTGGTGGGTATAGAACATATAGCGATCAGTACGGCCATTTGACGGCAAATACCGTCTGG
CTGGCAAGTCGGGCTGATGAAATGCCTGACAGAACTTGAACTGACCAGAAGTGAGCAAAGGCGGTCTCAATT
AACACTTTCCTATACGACACGTTGA

A.2.2 Oligomer Sequences

Table A.13: Core Staple Strands for the moDON DNA Origami

sequence name	sequence
core_001	GGAGAATGGATCCCGCCAGTGTGTGCTG
core_002	TAAATGCATCCTCGGAGAAATGACTGATACCGTGAATATTA
core_003	GGTTTTGTATTTTATCTGAACTCTTTTT
core_004	CATAACAACTTCCGTCGCATTCACCCTCATTCAG
core_005	TTTTTCCGCTCACAATTGAGTGAGCTAACTCACATTTTTTT
core_006	TAAACCCCAAAATTATTATCAGGCCAACGGATTTA
core_007	TCGACATTACTTCTAATAACATCACTTGATCTCGG
core_008	GTAACTAGTTTTGTAAAAGATCTTCACAGAGTCTG
core_009	AATCAGATATAATCCAATATTACCGCCATCGTCTG
core_010	AGGATGCAGGTTAGCCTCGTGTATTAA
core_011	AGGTCAAGATGTCTGACGCTGGTAGCGG
core_012	GTAGCAACATTACGCATCGCTATTACGGGCAAATTAGAAGAA
core_013	CTGAGAAGTGTTTTGCGGGAGCTAAACAGGAGGCC
core_014	GTAAAAGCTTGCTGGACAGTCAAATCACATTTGGG
core_015	GGAAGACATTGCTAAACTGGAATACATCGTACCCC
core_016	ATGGGAGAGGAGAACGAGGATATTGCGCAGGTGTTCCTGAGTAACCGTT
core_017	AAATGGATGGCAGAACAAAATAAACAGC
core_018	GAGCAGCTATCGGCAGTCTGTCCATCACGGTTGG
core_019	TTACGATAACAGTATCGATTAGTTGCTATTTTGCGCGAGGCAAAAA
core_020	GCGACCTAAGCGTTCTTAGTTTGACTGTTATCAAGCACTGCATCCTG
core_021	TTTTTAAGAAACCAGCAAAGCAAC
core_022	TGAAACATCTGACCAATACCGAACGAAC
core_023	TTTTTTAAAAGGGACATTCTGGTCACACCGCTCAAGCCATTG
core_024	GCCAACAAGAAGATGAGAGCCTGCTGAA
core_025	CACCAGCGAGATAGAACCCTGCTACATTTATTAACCAGAA
core_026	TGATAGCCACAGACAATATTTTTGAATGTTTAATGCGAAGTGATGAACG
core_027	CTCAGGCACTGCGTGATGCAACTTTTTC
core_028	AACAGTGGCATCTGCCTTTTT
core_029	AAGACGCACTAATAGATTAGAGATAATATTATTATAGTCACA
core_030	TGCCACTCATTGTTGTGAGTGTGGCGATAGAAATA
core_031	ACTTGTGGGAGGATTGGGATAGGTCACGATGAGAA
core_032	GAAGAATATCATTGATGCGTATTAACCATTTAACA
core_033	GCAAATCAACAGTTGAAAGGAATCACCTAGCAGCAAGATGGG
core_034	AAGGTTAAATTCGACAACTCGGGGAAACTTCACCGGTTCCG
core_035	CTAACACTGGTCGTAAACAGAGAGGTTCGCGAAC
core_036	TTTTTCAAATCCCCACCGAACTGTTTTTT
core_037	CACAATAGCCGTTCCCGATAGAGCGAAATTAACT
core_038	TTTTTTTAATGAAAGATTAATGAAGATTTTT
core_039	GAAGTATAACGACGCGGGTAC
core_040	TTTTTTTTAAAAGTTTGAGTACCCGAACCTCACTG
core_041	CATTTTGGAAACCACGCCATTAGCCAGCTCGGCCTCAGGAAG
core_042	TTTTTAAATTAATTACAACAGTTCAGGGATTTTT
core_043	CAGTACATCTGTAAAGGTTGGGTTATATAACTATTTTT
core_044	TTTTTTGCCGGAAACCACCTCAAA
core_045	CGCAACTGATTAAGGAGTCAATAGTGAATTTATCAAAATCA
core_046	ATCGTCGCTATTAATTAATTTTACCTTT
core_047	TTTTTAGTGAATAACCTTGCTTAAATCA
core_048	ACGCTCGCACTCCCGCCATTTAAAGCATTGAGG
core_049	TTTTTAGTTTGAGGGGACGACTAACCGTCCACGCTAAAACAG
core_050	TTTTTTATGTAAATGCTGAAGCGGGACGCAGACCTTTTAACTGCT
core_051	CGCATCGGACAGTATTTCCGGCACCGCTTCTGGTTTTT
core_052	TTGGTGTAATGAAAAATGCCACAAGTTCCAGGCTG
core_053	CGGATTGACCGTAACTGGAACTTATCAGTTCAGGGAGGGCGACAAGGC
core_054	AAATATATTTTAGTTATTTTT
core_055	TTTTTCTTATCATTCCATTTATTTTCATCGTAGGAATTTTT
core_056	CCAGCTTTAATTCGGTAAGAATACGTGGCCTAAAACATCGCCATTAAA
core_057	AAATCAGATCGATTGTGCTGGCCATGAA
core_058	TTTTTAAAATTCGCGGATGAACGGGATTTTT
core_059	AGTTAAAATATGTTTTGAAGCCTTAAATCCCGACTTTAACCGAGTAAC
core_060	CCAATAGGAGCGTCTTTCCTTTTT
core_061	GTCCATGATATTATTTGTGCACATAAACATTGCTAAGAAAG
core_062	ATAAGTCGGCAGACTACAGCGCAACACA
core_063	TTTTTAATTGCGTTGCGGTTATTAATTTTTT
core_064	TGCCAGCTACAAACTCTAAAATATCTTTAGGAGCA
core_065	TGCATTAGACGGGCAACAGCTGATTGCCCCTGTCG
core_066	GCGCGGGGTTTTTCAAAGATTGGGCGTTATCAATGTGGGCGC
core_067	TTTTTAGCCCCAAAAACAGGAGGTTGATAATCAGAAATTTTT
core_068	TTTATCCTGAATCTTACCAA
core_069	AATCGTAAAACTAGCATGTCAGAGCCG
core_070	TTTTTAGAGCCTAATTTGCCAGTTTTCACCA
core_071	TTTTTTCATATGGTAACCGATTGAGGTTTTT
core_072	CAAAGGCCAAGAGAAGGGAAACTGCGTG
core_073	TTAATCATATTCATATAGCAGCACCGTGCGTCAG
core_074	TTTTTAGTAATGTGTAGGTAATTAAATGCAATGCCTGTTTTT
core_075	GGCCGGAGTAATATAATCAAAACTCAACTTGAGCT
core_076	ATGATATTCAACCGCACCGTCACGTCAC
core_077	TTTTTGAGGGAAGGTAAATATTGACGGAAATAAAGGGC

core_078	TTTTTGCGGGAGAAGCCTTTATTTCAACGCAAAACATTATGACCC
core_079	AGGATAAAACCCTCATATATTAGATTCAAAAGGGTTCCAAAT
core_080	CACCAGTAGCTAAACCACCGA
core_081	GCCGGAAACCGACTTGAGCCCATCAATCTCAAACGTGAGTA
core_082	TTTTTATCAAGTTTCGGCATTTTCGGTTTTT
core_083	TAGCGCGTCGCAAATGGTCAATAACCTGTTTAGC
core_084	TTTTTGCCCGTATATGTAATACTTTTTTTTT
core_085	TTTTTTTAGTTTGACCATTAGCTGCGAACGAGTAGATTTTTT
core_086	GGGCGCGAGCTGAACGAGAGG
core_087	CCCAATTATACATTTTTTCATGCCTTTAAATCAGTAGCGACAGATTTTT
core_088	TAAGTATTCATTTGCTAATAGTAGTAGCATTAACATCCAAT
core_089	CAGGGTGGAGAGGCGGTTTGC
core_090	AGATATAGAGTCGGCATACAAAAGGTTT
core_091	GAGTTGCGCGAAAAAATAGCCCGAGATATCCACTA
core_092	CAGTGAATGAATCCGAGTACACATATAGATGAT
core_093	CTCAGAGGCTCAGTGAGGCTGAGACTCCGTATAACAATGCGC
core_094	GAGCTTAATTGCTGAGGAGCGGAGATCG
core_095	TTTTTAGCAAGCCCGGGCGCGTACTATTTTT
core_096	AACTACAGAAGCAAGACCATATTGAATCCCCCTCAGATAGCG
core_097	TTTTTCATAATGCCTCGCCTGATAAATTTAGCCGGGTGTCTT
core_098	TTTTTACCCTGACTATTATAGTCAACGCCTGTAGCATTTTT
core_099	TTTTTAAACGGGTAAAATACGTGAGGAACTTACTGTAGTGTC
core_100	ACACTAAAACACTCTAAGAGGAAGCCCGGATTAGA
core_101	TTTTTCATAAATATTCAAATCAAAAATCAGGTCTTTTTTTT
core_102	TTTTTCCTGCTCCATGTTACTGTGTCGAAATCCGCGATTTTT
core_103	TAGACTGAATGCTCAGAAAACGAGAATAGCGGATTTATAAACTCCAAC
core_104	AAAAACCAAACGGCGCAGAATGTATCAACTACG
core_105	TTTTTTTCAACTAATGCAGATACACTGCGGAATCGTTTTTT
core_106	AAAAGGACTGGGGTTCCAGTCTATTAAATCCTTTGACATTAT
core_107	GTCTCCAGTATTATGTTTCCATTTTTTT
core_108	TGATGGTGCCTGGCCCTGAGACCCGCTT
core_109	AATGAGTTGCAAGGAGTTTATAAGGCAAAAATCATAAATGTT
core_110	AATCCCTGCATCAAAAAGAT
core_111	CGTGCCAGCGAAAAATATAATGCTGTCTTTGAG
core_112	TTAAAGAACGTGGATCAAAAGTCCTGTT
core_113	GTCAAAGCACCCGCCGCGCTTGTGCTTT
core_114	CGAGAAAGGGCGCTTGGCTTAAGGTTTAGTACCGC
core_115	GCGTCGTAACGCTTAACAAGACCCGTTA
core_116	TTTTTCTGAATTTCCATGTTTTAAATTTTTT
core_117	GCGCGTAACCACCAGGCGAAAAACCGTCTATCAAGCCGGCGA
core_118	TCACGCTATAAGAGGTCATTTAGGTCAGAAAGACT
core_119	GGCAAGTGCATTCGCATCAAATATATTTAGCCCGGAATAGGTACTCAGG
core_120	GGAGAGTGGCGCTAGGAAGGGGATACCGTTTAGCTGAAACGAACGTGG
core_121	TTTTTTGGTTGCTTTGACGAGCACTCAAGAGAAGGATTTTT
core_122	GAGTATCTGCATATTGGGTTC
core_123	CAGAATCCAACAGGAAAAACGCTCATTTTTT
core_124	AGGTGAGGCGGTCAGTATTTTTTT
core_125	TTTTTTTTCTGCGGCAGTTAATCGGTGAAAATGTTTTT
core_126	TTTTTGAAACCAGTTTCTTGTGAAGTCCGTGAAGACGTTTTT
core_127	TTTTTTTTATGTAGATGAAGGTAT
core_128	TTTGGAAATACCTACATTTTGAGACCAGTAATTTTT
core_129	TTTAATATCTGGTCAGTTGTATCAAA
core_130	TGTTCGCCACTGGTGACCTGGAAGAGTTT
core_131	GCAATAAAAATGCGCCGCCTTT
core_132	AGATGATGACCGTACTCAATTT

Table A.14: Connector Staple Strands for the moDON DNA Origami

sequence name	sequence
hh50_ C* A_shell_01	CGAGCTCGTACAAAGGTGGAAACGATACTTAAAGTAGCATGC
hh50_ C* A_shell_02	CCTCTCTGAATTCGTAATCATGGTCATAGCCGGAGTAAAGC
hh50_ C* A_shell_03	GCCTAATCCACACATAACGGAACAACATTATTATTTTT
hh50_ C* A_shell_04	ATCAGTTTTAAACTTTGACCCAATAGTAGAGTATC
hh50_ C* A_shell_05	TGCAAAAGAAGTTTTGAGCAATTTTCAC
hh50_ C* A_shell_06	TCCAATATAACGCCTTCAGTTTTCATATACCAGTC
hh50_ C* A_shell_07	TCAATCACAAATCATGACAAGAACCGGA
hh50_ C* A_shell_08	AGGCGCAGGGGATTTTTTATGGAGATGA
hh50_ C* A_shell_09	TTTTTTGAACGGTGTACAGACCTATTGAAAGAGGACAGATTTTT
hh50_ C* A_shell_10	AACGAACACATACGAGCTGTTTCCTGTG
hh50_ C* A_shell_11	TTTTTCAGGTAGAAAGAGAGATTTAGGAATACCACATTTTT
hh50_ C* A_shell_12	ACCAACTTTCATTACCTAAGGGAATTCTGC
hh50_ C* A_shell_13	CCTTATGTAAGAGCAACACTAAGGGGGTCCAGCGA
hh50_ C* A_shell_14	TTTCTTTAGATCCGAACGAGG
hh50_ C* A_shell_15	CATACATTAGAGTCTGCCAGTCATAACATCATTGTGAATTA
hh50_ C* A_passive_ C*_01	AATGTGCCACTCGCTAGGCTGGCTGACCTTCATTTTTT
hh50_ C* A_passive_ C*_02	ATTACGAGGCATAGCGATTTTTGGGAAGAATTTTT
hh50_ C* A_passive_ C*_03	TTTTTAAATCTACGTTAATAAAGGACGTAAGAACTGGCTCA
hh50_ C* A_passive_ C*_04	TTTTTCAAGAGTAATCTACGTAACAAAGCTGCTCATTC
hh50_ C* A_2nt_intr_ C*_01	AATGTGCCACTCGCTAGGCTGGCTGACCTTCATGC
hh50_ C* A_2nt_intr_ C*_02	ATTACGAGGCATAGCGATTTTTGGGAAGAAGC
hh50_ C* A_2nt_intr_ C*_03	CCCAAGAGTAATCTACGTAACAAAGCTGCTCATTC

hh50_ C* A_2nt_intr_ C*_04	TGAAATCTACGTTAATAAAGGACGTAAGAACTGGCTCA
hh50_ C* A_passive_ A_01	GTACAACACCAGAAAATAAGGCTTGCCCTGTTTTT
hh50_ C* A_passive_ A_02	AGATTTCGTTTATGCGAGTAGTAAATTGGGTTTTT
hh50_ C* A_passive_ A_03	TTTTTCTTGAGATGAACTTTACCTCGTTTACCAGA
hh50_ C* A_passive_ A_04	TTTTTACGAGAAACGGAGATTTAGCGAGAGGCTTTCGACGAT
hh50_ C* A_2nt_intr_ A_01	GTACAACACCAGAAAATAAGGCTTGCCCTGTA
hh50_ C* A_2nt_intr_ A_02	AGATTTCGTTTATGCGAGTAGTAAATTGGGTG
hh50_ C* A_2nt_intr_ A_03	AAACGAGAAACGGAGATTTAGCGAGAGGCTTTCGACGAT
hh50_ C* A_2nt_intr_ A_04	CCCTTGAGATGAACTTTACCTCGTTTACCAGA
hh55_ A B*_shell_01	ACCAGGCGGATAATCAGAACGTTTGCTTTTAATT
hh55_ A B*_shell_02	TTTTTATGCAACTAAAGAGGCCGCTTTTTTT
hh55_ A B*_shell_03	ACACTGACGCCACCTTCTGTATGGGATT
hh55_ A B*_shell_04	TTTTTGAGGGTAGCAACGGCTAAGACAGCATCGGAACTTTTT
hh55_ A B*_shell_05	CGTCACGAATAATAGAAAGGAACAACTATGAATT
hh55_ A B*_shell_06	ATCGCGTAAGCAAACCGACAA
hh55_ A B*_shell_07	AAAGAATTTATACCAAGCGCGAAACAAAAAACGAAAGCTTGC
hh55_ A B*_shell_08	CGATAGTTGGGCTCAAAACGCTCCAACTTGCGGA
hh55_ A B*_shell_09	GCAGCGAACAGAGGAGCTCAA
hh55_ A B*_shell_10	TTTTTTTCCACAGACAGTAGCGTAACGATCTAAAGTTTTTT
hh55_ A B*_shell_11	TTTTTTTGCGGGATCGTCACCGAGTTAATACGGTG
hh55_ A B*_shell_12	AAATAGTCCCTCAGGAATTGCCAGTACATACCGTA
hh55_ A B*_shell_13	TGAGAATAATTTTTTCACGTTGAGTACCCCTTTTG
hh55_ A B*_shell_14	TTTTTTTTGTCGTCTTTTTCAGGGATTTTTT
hh55_ A B*_shell_15	CGCTACAAATAGGACCTCATTCCAGACGTTAGTAA
hh55_ A B*_passive_ A_01	TTTTTTTAATTGTATCGGTTTATCAGAGGCATCAAAT
hh55_ A B*_passive_ A_02	TTTTTTTAAACAGCAACCATCGCGAACCAGACCGGTTTAATTCAACCTA
hh55_ A B*_passive_ A_03	TGACAACTTGATACTTTCGAGGTGAATTTCTTTTT
hh55_ A B*_passive_ A_04	GAAAATCTCCAAAACAAAAGGAGCCTTTTTT
hh55_ A B*_2nt_intr_ A_01	TGACAACTTGATACTTTCGAGGTGAATTTCCA
hh55_ A B*_2nt_intr_ A_02	GAAAATCTCCAAAACAAAAGGAGCCTCG
hh55_ A B*_2nt_intr_ A_03	ATTAAACAGCAACCATCGCGAACCAGACCGGTTTAATTCAACCTA
hh55_ A B*_2nt_intr_ A_04	AGTTAATTGTATCGGTTTATCAGAGGCATCAAAT
hh55_ A B*_passive_ B_01	GTTGATACACCCTCAGAACCACAACTTTCTTTTT
hh55_ A B*_passive_ B_02	AAGGCACCGAGCTTCAAAGACGACTAAAGCCCACGATATTCGGTTTTTT
hh55_ A B*_passive_ B_03	TTTTTAACAGTTTCAGCGGAGTTGCTAAGCCACCCGTGCCGT
hh55_ A B*_passive_ B_04	TTTTTCGCTGAGGCTTGCAGGCTCCGATCATAACA
hh55_ A B*_2nt_intr_ B_01	GTTGATACACCCTCAGAACCACAACTT
hh55_ A B*_2nt_intr_ B_02	AAGGCACCGAGCTTCAAAGACGACTAAAGCCCACGATATTCGGTTC
hh55_ A B*_2nt_intr_ B_03	CACGCTGAGGCTTGCAGGCTCCGATCATAACA
hh55_ A B*_2nt_intr_ B_04	TCAACAGTTTCAGCGGAGTTGCTAAGCCACCCGTGCCGT
hh60_ B* C_shell_01	AGTGAGGTCGGTTATTTCGGTCTGAATTTACCGT
hh60_ B* C_shell_02	ACATACAAAATCTGTCAGAGGCCGCCACCCTCAG
hh60_ B* C_shell_03	AATGAAATATTCGGTGGCATCGCCAGAA
hh60_ B* C_shell_04	TTTTTTTAGGATTAGCGGGAGTGTACTGGTAATAAGTTTTT
hh60_ B* C_shell_05	CCGGAACGTTGATTTCTGGAAGTTTCATTCACCGTGTATCCA
hh60_ B* C_shell_06	TTTTTTTCATAATCAAAATCAAAGCGTTTATTACCGCCACCC
hh60_ B* C_shell_07	TTTTTTTTTAACGGGGTAGTAACAGTTTTTT
hh60_ B* C_shell_08	GCCGCCACCATCCTAATAAAGGGAGGTT
hh60_ B* C_shell_09	TTTTTTCATAGCCCCCTTGCCATCTTTTTTT
hh60_ B* C_shell_10	TCCAGTAAATGCCCCCTGCCTGTACCAA
hh60_ B* C_shell_11	TGGAAAGCGCAGTCAACCTATCATGAAA
hh60_ B* C_shell_12	GAGGCAGTAGCAAGCAATAAAGCCTCAGAGCATAA
hh60_ B* C_passive_ B*_01	AACAGTTAGCCTTGCAGTGCGTCATACATGGCTTTTTT
hh60_ B* C_passive_ B*_02	TATAACACAGAGCCACCACCGGAACCTTTTT
hh60_ B* C_passive_ B*_03	TTTTTTTTGATGATACAGGGTTTTCCACCACACCCATG
hh60_ B* C_passive_ B*_04	TTTTTGCCTCCCTCAGACCACCACCCTCAGA
hh60_ B* C_2nt_intr_ B*_01	AACAGTTAGCCTTGCAGTGCGTCATACATGG
hh60_ B* C_2nt_intr_ B*_02	TATAACACAGAGCCACCACCGGAA
hh60_ B* C_2nt_intr_ B*_03	TGATGATACAGGGTTTTCCACCACACCCATG
hh60_ B* C_2nt_intr_ B*_04	CTCCCTCAGACCACCACCCTCAGA
hh60_ B* C_passive_ C_01	TTACCATGTCAGACGATTGTTTTT
hh60_ B* C_passive_ C_02	TTTTTGCCTTGATATTCACAAACACATTAAAAATTCTA
hh60_ B* C_passive_ C_03	ATTGACAAACCACCACCAGAGCCTTTTT
hh60_ B* C_passive_ C_04	TTTTTGCCGCCAGCCAATGAACAAAGAATTAGCAAAATTAAG
hh60_ B* C_2nt_intr_ C_01	TTACCATGTCAGACGAT
hh60_ B* C_2nt_intr_ C_02	CTTGATATTCACAAACACATTAAAAATTCTA
hh60_ B* C_2nt_intr_ C_03	ATTGACAAACCACCACCAGAG
hh60_ B* C_2nt_intr_ C_04	CGCCAGCCAATGAACAAAGAATTAGCAAAATTAAG
hh65_ C A*_shell_01	AGATTGTACGCAAAGACACCACGGAATTTTT
hh65_ C A*_shell_02	GAGCAAATATCAGGTCATTGCAATAAGA
hh65_ C A*_shell_03	TTTTGAGAGATCTAAATAGCA
hh65_ C A*_shell_04	GAATTATTTCTAGCTGATAAAGAGAGGGTTAGCAAA
hh65_ C A*_shell_05	GAGGAAACTATCTTACCGAAGACAATGA
hh65_ C A*_shell_06	CGTAGAAAATACACGCCAAAATCATATAAACGCC
hh65_ C A*_shell_07	TTTTTAAAATGAAAATAGGGAAGCGCTTTTT
hh65_ C A*_shell_08	TTACAGAAAGAAACGATTTTTTGTTTAACGTCATTTTT
hh65_ C A*_shell_09	GAAATTGACAAGGAATAACATAACTGAACGCTAACCAAGCAAAGCCGTT
hh65_ C A*_shell_10	GCCCAATCTTATTTATCCCAAGAGAAA
hh65_ C A*_shell_11	GCAAGAACCCTTTTACCAGAAGGAAACC
hh65_ C A*_shell_12	ATTTACGCCTTAAGCGCAATAATAACGG
hh65_ C A*_shell_13	TTTTTTAAGTTTATTTTATAGAAAATTTTTT
hh65_ C A*_shell_14	TTTTTATTAGACGGGAGAATTAAAAACAGCAGCCT
hh65_ C A*_shell_15	CACCCTGAACAAAGATAACCCAGTTAA

hh65_ C A*_passive_ C_01	AGCACCAAATTAGACAAAGTTTAAGAAAAGTAAGCAGTTTTT
hh65_ C A*_passive_ C_02	GGCAAGGACCATCGTAAAGGTAATACCCAAAAGTTTTT
hh65_ C A*_passive_ C_03	TTTTTATAGCCGAAGCCAGCAAATTTAGAAATTAT
hh65_ C A*_passive_ C_04	TTTTTAACTGGCATGATTAAGACTCAGTATGTAGCTAT
hh65_ C A*_2nt_intr_ C_01	AGCACCAAATTAGACAAAGTTTAAGAAAAGTAAGCAGCT
hh65_ C A*_2nt_intr_ C_02	GGCAAGGACCATCGTAAAGGTAATACCCAAAAGAG
hh65_ C A*_2nt_intr_ C_03	AGAACTGGCATGATTAAGACTCAGTATGTAGCTAT
hh65_ C A*_2nt_intr_ C_04	TTATAGCCGAAGCCAGCAAATTTAGAAATTAT
hh65_ C A*_passive_ A*_01	CATATGAGAGTCTGCTACAATGTAATTGAGTTTTT
hh65_ C A*_passive_ A*_02	GACATTCTTACCAGTAAATCAGTCACCATAAAGGTGGCAATTTTT
hh65_ C A*_passive_ A*_03	TTTTTCGCTAATATCAGAGAGTCAGAGG
hh65_ C A*_passive_ A*_04	TTTTTCATATAAAAGAAATAAGCAATTGTAATTTTGTT
hh65_ C A*_2nt_intr_ A*_01	CATATGAGAGTCTGCTACAATGTAATTG
hh65_ C A*_2nt_intr_ A*_02	GACATTCTTACCAGTAAATCAGTCACCATAAAGGTGGC
hh65_ C A*_2nt_intr_ A*_03	CTAATATCAGAGAGTCAGAGG
hh65_ C A*_2nt_intr_ A*_04	TATAAAAGAAATAAGCAATTGTAATTTTGTT
hh70_ A* B_shell_01	TGAAAGCCGTCTGGCGGTATTATAGATAAGTCCTGCATGTTC
hh70_ A* B_shell_02	TTGGTAACATAGTCGCTATCCCTCATTTTTGCGGG
hh70_ A* B_shell_03	TTAACCTCGCAAGACGTCGGAACCCAAGCCTGTT
hh70_ A* B_shell_04	AGAACGGGTATTAAGTAATTCACGACAA
hh70_ A* B_shell_05	TCATCAACATTAAATTATACA
hh70_ A* B_shell_06	ATCGAGAACAAGCAATCAGATAAAATAA
hh70_ A* B_shell_07	ACGCCATCGTTTTAGCGAACCTCAAGATGAACGGT
hh70_ A* B_shell_08	TTTTTTCATTACCGCGCTTACGAGCATTTTT
hh70_ A* B_shell_09	TTTTTAATACCGACCGTGTATTTTGTTTTTTT
hh70_ A* B_shell_10	TATCCCATAAGACGTGTCCATCGGCTGTCTTTCTTTTT
hh70_ A* B_shell_11	TTTTTTGTAGAAACCAATCAATCCTAAT
hh70_ A* B_shell_12	TAAACAAAACAAGAATAGAAGGCTTATCCCCACTC
hh70_ A* B_shell_13	TAGTATCATATGCGTGTGAGCAATAGGA
hh70_ A* B_shell_14	AGAAAAAAGAACGCGAGAAAAATCCAATCCGGCTT
hh70_ A* B_shell_15	ATTTCATCTTCTGACCTAATCATCCGGAAATTTAATGGTTTGATTTTT
hh70_ A* B_shell_16	AATAAGAGTAATTGGCTTAATTGAGAA
hh70_ A* B_shell_17	TCGCCATGGCATTTTCGAGCCAGAATAT
hh70_ A* B_passive_ A*_01	CCTGTAGAAAGTACAGCTAATGCAGAACGCGCCTTTTT
hh70_ A* B_passive_ A*_02	ATTAAATACGTTAATGATAAATAAGGCGTTAAATTTTT
hh70_ A* B_passive_ A*_03	TTTTTTGTTTATCAACACTAAGAACACCCAG
hh70_ A* B_passive_ A*_04	TTTTTTAAGAATAAACAAATTACT
hh70_ A* B_2nt_intr_ A*_01	CCTGTAGAAAGTACAGCTAATGCAGAACGCG
hh70_ A* B_2nt_intr_ A*_02	ATTAAATACGTTAATGATAAATAAGGCGTTA
hh70_ A* B_2nt_intr_ A*_03	TTTATCAACACTAAGAACACCCAG
hh70_ A* B_2nt_intr_ A*_04	AGAATAAACAAATTACT
hh70_ A* B_passive_ B_01	CGACAAAAGGCAGAATTTAACAACGCCAACTTTTT
hh70_ A* B_passive_ B_02	TTTTTATGTAATTTAGGTAAAACCAAGTACCGTT
hh70_ A* B_passive_ B_03	TTTTTCAACGCTCATAGGTCTGTGGGAACAAACGG
hh70_ A* B_passive_ B_04	ACAGTAGCTTACCAGTATAAAGCTTTTT
hh70_ A* B_2nt_intr_ B_01	CCCAACGCTCATAGGTCTGTGGGAACAAACGG
hh70_ A* B_2nt_intr_ B_02	CTATGTAATTTAGGTAAAACCAAGTACCGTT
hh70_ A* B_2nt_intr_ B_03	CGACAAAAGGCAGAATTTAACAACGCCAACTT
hh70_ A* B_2nt_intr_ B_04	ACAGTAGCTTACCAGTATAAAGCGC
hh75_ B C*_shell_01	TTTTTGCTACGGCGCCTGAGCAATTTTT
hh75_ B C*_shell_02	TCACGACTTGGGTAACGCCAGATTATTT
hh75_ B C*_shell_03	TTCGCTATGGCGAACGGATTCGCCTGATTGCTTTTTGAATTACCCAGC
hh75_ B C*_shell_04	GGCAAAGCCAGAAGGATAGAAAGGGTTGATGGCAATTCATTTTTT
hh75_ B C*_shell_05	TCGGTGCTGAAAACATAGCGATAGCTTAGTTGGGATTGTCGG
hh75_ B C*_shell_06	TTTTTATATTCCTGATTATCAGAGCGGAATTATCATCTTTTT
hh75_ B C*_shell_07	TATCAAAGGACAAACGGATTTTCCCAG
hh75_ B C*_shell_08	GCACGTAAAACAGAGATTAAGGTTGTAATAGACTT
hh75_ B C*_shell_09	TTTTTAAGAAGATGATGAAACTCAATTA
hh75_ B C*_shell_10	TTTTTCAATATAATCCTTGAAATTGTTATTTTTT
hh75_ B C*_passive_ B_01	ATTCTCCGAGAGACTCCCTTAGTACCTTTTACATTTTT
hh75_ B C*_passive_ B_02	TTTTTAGATGAATATACAGTAACAGAATCCTGGGCCTC
hh75_ B C*_passive_ B_03	TTTTTTCGGGAGAAACAATTTTTCGTAGAAAAGGGGGACCAAGCTCATTTGA
hh75_ B C*_passive_ B_04	AATAAAGAAATTGCAGGTTTAACGTCTTTTT
hh75_ B C*_2nt_intr_ B_01	ATTCTCCGAGAGACTCCCTTAGTACCTTTTA
hh75_ B C*_2nt_intr_ B_02	TCAGATGAATATACAGTAACAGAATCCTGGGCCTC
hh75_ B C*_2nt_intr_ B_03	GGGAGAAACAATTTTTCGTAGAAAAGGGGGACCAAGCTCATTTGA
hh75_ B C*_2nt_intr_ B_04	AATAAAGAAATTGCAGGTTTAACG
hh75_ B C*_passive_ C*_01	TTACGCTTTTTTAATGGAAAATTTCATGAATACCATCGCGCAGTTTTT
hh75_ B C*_passive_ C*_02	TTTTTCTGAATAATGGACCTACCA
hh75_ B C*_passive_ C*_03	TTTTTAGGCGAATTATTCATTAAACAAAAAGTTACATCAAGAAAACATTTTT
hh75_ B C*_passive_ C*_04	GATTGTTTGGATTATACTTTTTTT
hh75_ B C*_2nt_intr_ C*_01	TTACGCTTTTTTAATGGAAAATTTCATGAATACCATCGCGC
hh75_ B C*_2nt_intr_ C*_02	GAATAATGGACCTACCA
hh75_ B C*_2nt_intr_ C*_03	GCGAATTATTCATTAAACAAAAAGTTACATCAAGAAAACATTTTT
hh75_ B C*_2nt_intr_ C*_04	GATTGTTTGGATTATAC
hh50_F*D_shell_01	TAATCATGGTCATAGCCGGAGTAAAGC
hh50_F*D_shell_02	CGAGCTCGTACAAAGGTGGAAACGATACTTAAAGTAGCATGCATCTACG
hh50_F*D_shell_03	GTACAACGGAGATTTAGCGAGAGGCTTTCGACGAT
hh50_F*D_shell_04	TCCAATATAACGCCCGCAGTTTTCATATTTTAAGA
hh50_F*D_shell_05	TACCAGATGCAAAAGAAGTTTTGAGCAATTTTCAC
hh50_F*D_shell_06	TTTTTGAACGGTGTACAGACCAGATTTGAAAGAGGACAGATTTTTTT
hh50_F*D_shell_07	TTAATAAACTGGCTGAATTACCTTATG

hh50_F*D_shell_08	TATTCATTACCCAAATCAACGTAACAAAGCTGCTCCCTCGTT
hh50_F*D_shell_09	TTTTTACCAACTCTTGACAAGTAAGGGAATTCTGC
hh50_F*D_shell_10	GCTTGAATAAGAGCAACACTAAGGGGGTCCAGCGA
hh50_F*D_shell_11	TTTCTTTAGATCCGAACGAGGTCAATCAAACCGGA
hh50_F*D_shell_12	CATACATTAGAGTCTGCCAGTCATAACATTCAGTGAATAAG
hh50_F*D_passive_F*_01	AATGTGCCACTCGCGGCTGGCTGTTTTT
hh50_F*D_passive_F*_02	ATTACGAGGCATAGTCATTGTCATTATACCAGTCAGGACGTTTTT
hh50_F*D_passive_F*_03	TTTTTTTGGGAAGAAAACCTCTCTGAATTCG
hh50_F*D_passive_F*_04	TTTTTACCTTCATCAAGAGTAGCGCATAGGGGATTTTTTATGGAGATGA
hh50_F*D_2nt_intr_F*_01	AATGTGCCACTCGCGGCTGGCTGAC
hh50_F*D_2nt_intr_F*_02	ATTACGAGGCATAGTCATTGTCATTATACCAGTCAGGACGGT
hh50_F*D_2nt_intr_F*_03	CCACCTTCATCAAGAGTAGCGCATAGGGGATTTTTTATGGAGATGA
hh50_F*D_2nt_intr_F*_04	AGTTGGGAAGAAAACCTCTCTGAATTCG
hh50_F*D_passive_D_01	ATCAGTTTTAAACTGCTTGAGATGGTTTTTT
hh50_F*D_passive_D_02	TTTTTTTAATTTCAACTTTCCCTGACGAGAAACACCTTTTT
hh50_F*D_passive_D_03	TTTTTAGAACGAGTAGTAAATTGGTTGACCCAATAGTAGAGTATC
hh50_F*D_2nt_intr_D_01	ATCAGTTTTAAACTGCTTGAGATGGTGA
hh50_F*D_2nt_intr_D_02	TAAGAACGAGTAGTAAATTGGTTGACCCAATAGTAGAGTATC
hh50_F*D_2nt_intr_D_03	AATTAATTTCAACTTTCCCTGACGAGAAACACCGA
hh55_DE*_shell_01	ACCAGGCGGATAATCAGAAC
hh55_DE*_shell_02	GTTGATACACCCTCAGAACCGCCACCCGTGCCGT
hh55_DE*_shell_03	GTTTGCTTTTAATTCGTCACTTCAGCG
hh55_DE*_shell_04	AAGGCACCGAGCTTCAAAGACGACTAAAAGCTTGATGCGCCG
hh55_DE*_shell_05	AAAGAATTTATACCAAGCGCGAAACAAAAAACGAAAAAAAAG
hh55_DE*_shell_06	ATCAGCTTGTGCGAGAATCTCTCCAACTTGCGGA
hh55_DE*_shell_07	GAGTGAGAATAGAAGAGTACCCCTTTTG
hh55_DE*_shell_08	ACAATGATCGGTCGCTGAGGCTTGCAGGCTATAGTTACCGCA
hh55_DE*_shell_09	CTATAGTCCCTCTTCAACAGTCAGTACATACCGTA
hh55_DE*_passive_E_01	TTTTTTCACGTTGAAAATCTCCAAAGAGGCATCAAAT
hh55_DE*_passive_E_02	TTTTTTTAATTGTACTTAAACGCGAACCAGACCGGTTTAATTCAACCTA
hh55_DE*_passive_E_03	TGAATTTTCGGTTTGCTCCAAAAGGAGCCTTTTTT
hh55_DE*_passive_E_04	AGGAACAACTAAAGATAATAATTTTTTTTTT
hh55_DE*_2nt_intr_E_01	TGAATTTTCGGTTTGCTCCAAAAGGAGCCTCA
hh55_DE*_2nt_intr_E_02	AGGAACAACTAAAGATAATAATTTTTCG
hh55_DE*_2nt_intr_E_03	AATTAATTGTACTTAAACGCGAACCAGACCGGTTTAATTCAACCTA
hh55_DE*_2nt_intr_E_04	AGTCACGTTGAAAATCTCCAAAGAGGCATCAAAT
hh55_DE*_passive_D*_02	ATCGCGTAAGCAAATTCGAGGCATCGCCCATTTTT
hh55_DE*_passive_D*_03	TTTTTGGATTTTGCTAAACAAATGAATT
hh55_DE*_passive_D*_04	TTTTTTCGCATAACCGATATATCAACAAC
hh55_DE*_2nt_intr_D*_01	ACACTGACGCCACCTTCTGTATGTA
hh55_DE*_2nt_intr_D*_02	ATCGCGTAAGCAAATTCGAGGCATCGCC
hh55_DE*_2nt_intr_D*_03	ATTTTGCTAAACAAATGAATT
hh55_DE*_2nt_intr_D*_04	ATCGCATAACCGATATATCAACAAC
hh60_E*F_shell_01	TTACCATTAGCAAGCAATAAAGCCTCAGAGCATAA
hh60_E*F_shell_02	AATGAAATATTCGGTGGCATC
hh60_E*F_shell_03	GCCAGAATGGAAAGCGCAGTCAACCTATCATGAAA
hh60_E*F_passive_E*_04	TTTTTGCCTCCCTCAGACCACCACCCTCACA
hh60_E*F_2nt_intr_E*_04	CTCCCTCAGACCACCACCCTCACA
hh60_E*F_passive_F_01	AACAAATAAATCCTTTGGCCTCAGGAGGTTGAGGCAGTTTTT
hh60_E*F_passive_F_02	TTTTTGTCAGACGACATTAAAAATTCTA
hh60_E*F_passive_F_03	GCATTGATGATATTCAGAGCCGCCACCAGAACCTTTTT
hh60_E*F_passive_F_04	TTTTTACCACCAGAGCCGCCGCCACAATGAACAAAGAATTAGCAAAATTAAG
hh60_E*F_2nt_intr_F_01	AACAAATAAATCCTTTGGCCTCAGGAGGTTGAGGC
hh60_E*F_2nt_intr_F_02	CAGACGACATTAAAAATTCTA
hh60_E*F_2nt_intr_F_03	GCATTGATGATATTCAGAGCCGCCACCAGAA
hh60_E*F_2nt_intr_F_04	CACCAGAGCCGCCGCCACAATGAACAAAGAATTAGCAAAATTAAG
hh70_D*E_shell_01	TGAAAGCCGTCTGGCGGTATTCTAAGAACACCCAG
hh70_D*E_shell_02	TTGGTAACATAGTCGCTATCCCTCATTTTTGCGGGTAAGAAT
hh70_D*E_shell_03	TTAACCTCGCAAGACGTCGGAACCCAAAGGGCTT
hh70_D*E_shell_04	TCATCAACATTAAAATATTTA
hh70_D*E_shell_05	ATTAAATACGTTAATGTGATAAATAAGGCGTTAAA
hh70_D*E_shell_06	ACAAGCAATCAGATATAGAAGGCTTATCCCCACTCATCGAGA
hh70_D*E_shell_07	AAACACCTATCATAAATTGAGAATCGCCTGTGAGCAATAGGA
hh70_D*E_shell_08	TTTTTAAATACCGACCGTATTTTGTTTTTTT
hh70_D*E_shell_09	TGCGTTATACAAATTCTTACCCAACGCT
hh70_D*E_shell_10	CAACAGTAGAACGCGAGAAAAATCCAATCCGGCTT
hh70_D*E_shell_11	TTTTTATTTCATCTTCTGACCTAAAAGCAGTATAATTTAATGGTTTGTTTTT
hh70_D*E_shell_12	ATAGAATCGGCTGTCTTTCTTTTT
hh70_D*E_shell_13	ACACATAAACAAAGAGCCAGTAATAAG
hh70_D*E_shell_14	AGAATATCAGACGACGACAATGTTCAGC
hh70_D*E_passive_D*_01	AGAACGGGTATTAAATCAACACCTGAACAATTTTT
hh70_D*E_passive_D*_02	ACGCCATCGTTTTATAATTACTATTTTT
hh70_D*E_passive_D*_03	TTTTTGAAAAATAATATCCCATATAAGT
hh70_D*E_passive_D*_04	TTTTTGAAAAAGCCTGTTTAGGGAATCAGCGAACCTCAAGATGAACGGT
hh70_D*E_2nt_intr_D*_01	AGAACGGGTATTAAATCAACACCTGAAC
hh70_D*E_2nt_intr_D*_02	ACGCCATCGTTTTATAATTAC
hh70_D*E_2nt_intr_D*_03	AAAATAATATCCCATATAAGT
hh70_D*E_2nt_intr_D*_04	AAAAGCCTGTTTAGGGAATCAGCGAACCTCAAGATGAACGGT
hh70_D*E_passive_E_01	GAACGCGTTCTGTCAAAGTACCGACAAAAGTTTTT
hh70_D*E_passive_E_02	TTTTTGTAAAGTAACCTGTTTACCAAGTACCGTTCCTGTAGTAATGCA
hh70_D*E_passive_E_03	TTTTTAGGCAGAGGTAGGTCTGTGGGAACAAACGG
hh70_D*E_passive_E_04	CATTTTCCGCCAACATGTAATTTTTTTT
hh70_D*E_2nt_intr_E_01	CCAGGCAGAGGTAGGTCTGTGGGAACAAACGG

hh70_D*E_2nt_intr_E_02	CTGTAAAGTAACCTGTTTACCAAGTACCGTTCCTGTAGTAATGCA
hh70_D*E_2nt_intr_E_03	GAACGCGTTCTGTCAAAGTACCGACAAAAGTT
hh70_D*E_2nt_intr_E_04	CATTTTCCGCCAACATGTAATTTGC
hh75_EF*_shell_01	ATTCTCCGAGAGACTCCCTTAGAATCCTGGGCCTC
hh75_EF*_shell_02	TTACATCGGGAGAAACAATAAAGGGGGACCAAGCTCATTTGA
hh75_EF*_passive_E_01	TCGGTGCTGAAAACATAGCGATCAGATGAATATTTTTT
hh75_EF*_passive_E_02	TTTTTTAGATTTTCAGGTTTAACGTAGCTTAGTTGGGATTGTCGG
hh75_EF*_passive_E_03	TTTTTACAGTAACAGTACCGAAATAAACATTGATTAAGGTTGTAATAGACTT
hh75_EF*_passive_E_04	GCACGTAAAAGAAATTGCGTTTTT
hh75_EF*_2nt_intr_E_01	TCGGTGCTGAAAACATAGCGATCAGATGAAT
hh75_EF*_2nt_intr_E_02	CAACAGTAACAGTACCGAAATAAACATTGATTAAGGTTGTAATAGACTT
hh75_EF*_2nt_intr_E_03	GATTTTCAGGTTTAACGTAGCTTAGTTGGGATTGTCGG
hh75_EF*_2nt_intr_E_04	GCACGTAAAAGAAATTGCGGG
hh50_ C*D_shell_01	TACCAGATGCAAAAGAAGTTTGAGCAATTTTCA
hh50_ C*D_shell_02	TTTTTGAACGGTGTACAGACCAGTTTTGAAAGAGGACAGATTTTTT
hh50_ C*D_shell_03	CCGGATAGCGCATAGGGGATTTTTTATGGAGATGA
hh50_ C*D_shell_04	AGCTGCTCATTCAGTGAATAAGGCTTGCCCTCGTT
hh50_ C*D_shell_05	TTTTTACCAACTCATTACCCATAAGGGAATTCTGC
hh50_ C*D_shell_06	CCAGATGTAAGAGCAACACTAAGGGGGTCCAGCGA
hh50_ C*D_shell_07	TTTCTTTAGATCCGAACGAGGTCAATCAAATCAACACAAGAA
hh50_ C*D_shell_08	CATACATTAGAGTCTTGCCAGTCATAACCCTGACGAGAAACA
hh50_ C*D_passive_ C*_01	AATGTGCCACTCGCGGCTGGCTGACCTTCATCATTTTT
hh50_ C*D_passive_ C*_04	TTTTTAGAGTAATCTTGGTAACAA
hh50_ C*D_2nt_intr_ C*_01	AATGTGCCACTCGCGGCTGGCTGACCTTCATCAGC
hh50_ C*D_2nt_intr_ C*_02	ATTACGAGGCATAGCGATTTTTGGGAAGAAGC
hh50_ C*D_2nt_intr_ C*_03	TGAAATCTACGTTAATAAAGGACGTAAGAACTGGCTCA
hh50_ C*D_2nt_intr_ C*_04	CCAGAGTAATCTTGGTAACAA
hh50_ C*D_passive_D_01	ATCAGTTTTAAACTAACTTTAATCATTTTTT
hh50_ C*D_passive_D_02	TTTTTTGTGAATTACCTTAACGAGTAGTAAATTGGGTTTTT
hh50_ C*D_passive_D_03	TTTTTCTTGAGATGGTTTAATTTCTTGACCCAATAGTAGAGTATC
hh50_ C*D_2nt_intr_D_01	ATCAGTTTTAAACTAACTTTAATCATGA
hh50_ C*D_2nt_intr_D_02	AATGTGAATTACCTTAACGAGTAGTAAATTGGGGA
hh50_ C*D_2nt_intr_D_03	TACTTGAGATGGTTTAATTTCTTGACCCAATAGTAGAGTATC
hh50_F* A_shell_01	TACCAGATGCAAAAGAAGTTTGAGCAATTTTCA
hh50_F* A_shell_02	TTTTTGAACGGTGTACAGACCTATTGAAAGAGGACAGATTTTTT
hh50_F* A_shell_03	GATATTCATTACCCAAATCAACGATTGGGCTTGAGCCTCGTT
hh50_F* A_shell_04	TTTTTACCAACTATCTTGACATAAGGGAATTCTGC
hh50_F* A_shell_05	ACTTTAATAAGAGCAACACTAAGGGGGTCCAGCGA
hh50_F* A_shell_06	TTTCTTTAGATCCGAACGAGGTCAATCAAGAACCG
hh50_F* A_shell_07	CATACATTAGAGTCTTGCCAGTCATAACATGGTTTAATTTCA
hh50_F* A_passive_F*_01	AATGTGCCACTCGCTAGGCTGGCTTTTT
hh50_F* A_passive_F*_04	TTTTTTGACCTTCATCAAGAGAGGCGCAGGGGATTTTTTATGGAGATGA
hh50_F* A_2nt_intr_F*_01	AATGTGCCACTCGCTAGGCTGGCAC
hh50_F* A_2nt_intr_F*_02	ATTACGAGGCATAGTCATTGTCATTATACCAGTCAGGACGGT
hh50_F* A_2nt_intr_F*_03	AGTTGGGAAGAAAACCTCTCTGAATTCG
hh50_F* A_2nt_intr_F*_04	CCTGACCTTCATCAAGAGAGGCGCAGGGGATTTTTTATGGAGATGA
hh50_F* A_passive_ A_01	GTACAACGGCTTGCCCTGACGAGAAACACCTTTTT
hh50_F* A_passive_ A_02	TTTTTAGAACGAGTAGTAATAACAAAGCTGCTCATTCTTTTT
hh50_F* A_passive_ A_03	TTTTTAGTGAATAAGGAGATTTAGCGAGAGGCTTTCGACGAT
hh50_F* A_2nt_intr_ A_01	GTACAACGGCTTGCCCTGACGAGAAACACCTG
hh50_F* A_2nt_intr_ A_02	CCAGAACGAGTAGTAATAACAAAGCTGCTCATTCTA
hh50_F* A_2nt_intr_ A_03	AAAGTGAATAAGGAGATTTAGCGAGAGGCTTTCGACGAT
left_passive_01	TTTTTGACAGGAACGGTACGCGATTAAAGGGATTTTATTTTT
left_passive_02	TTTTTGGAAATACCTACATTTTGAGACCAGTAATTTTT
left_passive_03	TTTTTAACACCGCCTGCCCCTCAATCTTTTT
left_passive_04	TTTTTAATATCTGGTCAGTTGTATCAAA
left_passive_05	TTTTTTGGTTTGCCCCAGCAGAGCAAGCGGTCCACGCTTTTT
left_passive_06	TTTTTCAGTTTGGAACAAGAGGGGTTGAGTGTTGTTCTTTTT
right_passive_01	TGTTCGCCACTGGTGACCTGGAAGAGTTTTT
right_passive_02	TTTTTTGACGACTGGGGATTTCAGAGCAGGCAATGCATTTTT
right_passive_03	TTTTTTGAACCACCAGGCTATATCATATATGTGTTTTT
right_passive_04	GCAATAAAAATGCGCCGCCTTTTT
right_passive_05	TTTTTACATCGGGTTGATGCAGACATCACGAAGGTGTTTTT
right_passive_06	AGATGATGACCGTACTCAATTTTT
zI_left_5'_01	TGTAGTAATGGACAGGAACGGTACGCGATTAAAGGGATTTTATTT
zI_left_5'_02	TGTAGTAATGGGAAATACCTACATTTTGAGACCAGTAATTTTT
zI_left_5'_03	TGTAGTAATGAACACCGCCTGCCCCTCAATCTTT
zI_left_5'_04	TGTAGTAATGAATATCTGGTCAGTTGTATCAAA
zI_left_5'_05	TGTAGTAATGTGGTTTGCCCCAGCAGAGCAAGCGGTCCACGCTTT
zI_left_5'_06	TGTAGTAATGCAGTTTGGAACAAGAGGGGTTGAGTGTTGTTCTTT
zI_right_3'_01	TGTTCGCCACTGGTGACCTGGAAGAGGTGGTAGTAGA
zI_right_3'_02	TTTGAAACCAGTTTCTTGTGAAGTCCGTGAAGACGGTGGTAGTAGA
zI_right_3'_03	TTTTGACGACTGGGGATTTCAGAGCAGGCAATGCAGTGGTAGTAGA
zI_right_3'_04	GCAATAAAAATGCGCCGCCGTGGTAGTAGA
zI_right_3'_05	TTTACATCGGGTTGATGCAGACATCACGAAGGTGGTGGTAGTAGA
zI_right_3'_06	AGATGATGACCGTACTCAAGTGGTAGTAGA
zII_left_5'_01	AGTAGATTGAGACAGGAACGGTACGCGATTAAAGGGATTTTATTT
zII_left_5'_02	AGTAGATTGAGGAAATACCTACATTTTGAGACCAGTAATTTTT
zII_left_5'_03	AGTAGATTGAAACACCGCCTGCCCCTCAATCTTT
zII_left_5'_04	AGTAGATTGAAATATCTGGTCAGTTGTATCAAA
zII_left_5'_05	AGTAGATTGATGGTTTGCCCCAGCAGAGCAAGCGGTCCACGCTTT
zII_left_5'_06	AGTAGATTGACAGTTTGGAACAAGAGGGGTTGAGTGTTGTTCTTT
zII_right_3'_01	TGTTCGCCACTGGTGACCTGGAAGAGGTAGTAGTGAT

zII_right_3'_02	TTTGAAACCAGTTTCTTGTGAAGTCCGTGAAGACGGTAGTAGTGAT
zII_right_3'_03	TTTTGACGACTGGGGATTTCAGAGCAGGCAATGCAGTAGTAGTGAT
zII_right_3'_04	GCAATAAAAATGCGCCGCCGTAGTAGTGAT
zII_right_3'_05	TTTACATCGGGTTGATGCAGACATCACGAAGGTGGTAGTAGTGAT
zII_right_3'_06	AGATGATGACCGTACTCAAGTAGTAGTGAT
zIII_left_5'_01	GTTAGAAGTGGACAGGAACGGTACGCGATTAAAGGGATTTTATTT
zIII_left_5'_02	GTTAGAAGTGGGAAATACCTACATTTTGAGACCAGTAATTTTT
zIII_left_5'_03	GTTAGAAGTGAACACCGCCTGCCCCTCAATCTTT
zIII_left_5'_04	GTTAGAAGTGAATATCTGGTCAGTTGTATCAAA
zIII_left_5'_05	GTTAGAAGTGTGGTTTGCCCCAGCAGAGCAAGCGGTCCACGCTTT
zIII_left_5'_06	GTTAGAAGTGCAGTTTGGAACAAGAGGGGTTGAGTGTTGTTCTTT
zIII_right_3'_01	TGTTCGCCACTGGTGACCTGGAAGAGGATGGGAAGAT
zIII_right_3'_02	TTTGAAACCAGTTTCTTGTGAAGTCCGTGAAGACGGATGGGAAGAT
zIII_right_3'_03	TTTTGACGACTGGGGATTTCAGAGCAGGCAATGCAGATGGGAAGAT
zIII_right_3'_04	GCAATAAAAATGCGCCGCCGATGGGAAGAT
zIII_right_3'_05	TTTACATCGGGTTGATGCAGACATCACGAAGGTGGATGGGAAGAT
zIII_right_3'_06	AGATGATGACCGTACTCAAGATGGGAAGAT
zIV_left_5'_01	TGAGGTAGAAGACAGGAACGGTACGCGATTAAAGGGATTTTATTT
zIV_left_5'_02	TGAGGTAGAAGGAAATACCTACATTTTGAGACCAGTAATTTTT
zIV_left_5'_03	TGAGGTAGAAAACACCGCCTGCCCCTCAATCTTT
zIV_left_5'_04	TGAGGTAGAAAATATCTGGTCAGTTGTATCAAA
zIV_left_5'_05	TGAGGTAGAATGGTTTGCCCCAGCAGAGCAAGCGGTCCACGCTTT
zIV_left_5'_06	TGAGGTAGAACAGTTTGGAACAAGAGGGGTTGAGTGTTGTTCTTT
zIV_right_3'_01	TGTTCGCCACTGGTGACCTGGAAGAGGTAAAGAGATA
zIV_right_3'_02	TTTGAAACCAGTTTCTTGTGAAGTCCGTGAAGACGGTAAAGAGATA
zIV_right_3'_03	TTTTGACGACTGGGGATTTCAGAGCAGGCAATGCAGTAAAGAGATA
zIV_right_3'_04	GCAATAAAAATGCGCCGCCGTAAAGAGATA
zIV_right_3'_05	TTTACATCGGGTTGATGCAGACATCACGAAGGTGGTAAAGAGATA
zIV_right_3'_06	AGATGATGACCGTACTCAAGTAAAGAGATA
zI_left_3'_01	CAGAATCCAACAGGAAAAACGCTCATGTGGTAGTAGA
zI_left_3'_02	TTTGACAGGAACGGTACGCGATTAAAGGGATTTTAGTGGTAGTAGA
zI_left_3'_03	AGGTGAGGCGGTCAGTATTGTGGTAGTAGA
zI_left_3'_04	TTTAACACCGCCTGCCCCTCAATCGTGGTAGTAGA
zI_left_3'_05	TTTTGGTTTGCCCCAGCAGAGCAAGCGGTCCACGCGTGGTAGTAGA
zI_left_3'_06	TTTCAGTTTGGAACAAGAGGGGTTGAGTGTTGTTCGTGGTAGTAGA
zI_right_5'_01	TGTAGTAATGTTTCTGCGGCAGTTAATCGGTGAAAATGTTTTT
zI_ right_5'_02	TGTAGTAATGGAAACCAGTTTCTTGTGAAGTCCGTGAAGACGTTT
zI_ right_5'_03	TGTAGTAATGTGACGACTGGGGATTTCAGAGCAGGCAATGCATTT
zI_ right_5'_04	TGTAGTAATGTGAACCACCAGGCTATATCATATATGTGTTTTT
zI_ right_5'_05	TGTAGTAATGTTTATGTAGATGAAGGTAT
zI_ right_5'_06	TGTAGTAATGACATCGGGTTGATGCAGACATCACGAAGGTGTTT
zII_left_3'_01	CAGAATCCAACAGGAAAAACGCTCATGTAGTAGTGAT
zII_left_3'_02	TTTGACAGGAACGGTACGCGATTAAAGGGATTTTAGTAGTAGTGAT
zII_left_3'_03	AGGTGAGGCGGTCAGTATTGTAGTAGTGAT
zII_left_3'_04	TTTAACACCGCCTGCCCCTCAATCGTAGTAGTGAT
zII_left_3'_05	TTTTGGTTTGCCCCAGCAGAGCAAGCGGTCCACGCGTAGTAGTGAT
zII_left_3'_06	TTTCAGTTTGGAACAAGAGGGGTTGAGTGTTGTTCGTAGTAGTGAT
zII_right_5'_01	AGTAGATTGATTTCTGCGGCAGTTAATCGGTGAAAATGTTTTT
zII_ right_5'_02	AGTAGATTGAGAAACCAGTTTCTTGTGAAGTCCGTGAAGACGTTT
zII_ right_5'_03	AGTAGATTGATGACGACTGGGGATTTCAGAGCAGGCAATGCATTT
zII_ right_5'_04	AGTAGATTGATGAACCACCAGGCTATATCATATATGTGTTTTT
zII_ right_5'_05	AGTAGATTGATTTATGTAGATGAAGGTAT
zII_ right_5'_06	AGTAGATTGAACATCGGGTTGATGCAGACATCACGAAGGTGTTT
zIII_left_3'_01	CAGAATCCAACAGGAAAAACGCTCATGATGGGAAGAT
zIII_left_3'_02	TTTGACAGGAACGGTACGCGATTAAAGGGATTTTAGATGGGAAGAT
zIII_left_3'_03	AGGTGAGGCGGTCAGTATTGATGGGAAGAT
zIII_left_3'_04	TTTAACACCGCCTGCCCCTCAATCGATGGGAAGAT
zIII_left_3'_05	TTTTGGTTTGCCCCAGCAGAGCAAGCGGTCCACGCGATGGGAAGAT
zIII_left_3'_06	TTTCAGTTTGGAACAAGAGGGGTTGAGTGTTGTTCGATGGGAAGAT
zIII_right_5'_01	GTTAGAAGTGTTTCTGCGGCAGTTAATCGGTGAAAATGTTTTT
zIII_ right_5'_02	GTTAGAAGTGGAAACCAGTTTCTTGTGAAGTCCGTGAAGACGTTT
zIII_ right_5'_03	GTTAGAAGTGTGACGACTGGGGATTTCAGAGCAGGCAATGCATTT
zIII_ right_5'_04	GTTAGAAGTGTGAACCACCAGGCTATATCATATATGTGTTTTT
zIII_ right_5'_05	GTTAGAAGTGTTTATGTAGATGAAGGTAT
zIII_ right_5'_06	GTTAGAAGTGACATCGGGTTGATGCAGACATCACGAAGGTGTTT
zIV_left_3'_01	CAGAATCCAACAGGAAAAACGCTCATGTAAAGAGATA
zIV_left_3'_02	TTTGACAGGAACGGTACGCGATTAAAGGGATTTTAGTAAAGAGATA
zIV_left_3'_03	AGGTGAGGCGGTCAGTATTGTAAAGAGATA
zIV_left_3'_04	TTTAACACCGCCTGCCCCTCAATCGTAAAGAGATA
zIV_left_3'_05	TTTTGGTTTGCCCCAGCAGAGCAAGCGGTCCACGCGTAAAGAGATA
zIV_left_3'_06	TTTCAGTTTGGAACAAGAGGGGTTGAGTGTTGTTCGTAAAGAGATA
zIV_right_5'_01	TGAGGTAGAATTTCTGCGGCAGTTAATCGGTGAAAATGTTTTT
zIV_ right_5'_02	TGAGGTAGAAGAAACCAGTTTCTTGTGAAGTCCGTGAAGACGTTT
zIV_ right_5'_03	TGAGGTAGAATGACGACTGGGGATTTCAGAGCAGGCAATGCATTT
zIV_ right_5'_04	TGAGGTAGAATGAACCACCAGGCTATATCATATATGTGTTTTT
zIV_ right_5'_05	TGAGGTAGAATTTATGTAGATGAAGGTAT
zIV_ right_5'_06	TGAGGTAGAAACATCGGGTTGATGCAGACATCACGAAGGTGTTT
z_connector_I	CATTACTACATCTACTACCAC
z_connector_II	TCAATCTACTATCACTACTAC
z_connector_III	CACTTCTAACATCTTCCCATC
z_connector_IV	TTCTACCTCATATCTCTTTAC
z_connector_I-th7	CTACTATCATTACTACATCTACTACCAC
z_connector_II-th7	ACACTGCTCAATCTACTATCACTACTAC

z_connector_III-th7	CTACCAACACTTCTAACATCTTCCCATC
z_connector_IV-th7	AACTCCATTCTACCTCATATCTCTTTAC
z_invader_I-th7	GTGGTAGTAGATGTAGTAATGATAGTAG
z_invader_II-th7	GTAGTAGTGATAGTAGATTGAGCAGTGT
z_invader_III-th7	GATGGGAAGATGTTAGAAGTGTTGGTAG
z_invader_IV-th7	GTAAAGAGATATGAGGTAGAATGGAGTT
AuNP_handle_hh50_ A	GTACAACACCAGAAAATAAGGCTTGCCCTG TT ATGTAGGTGGTAGAG
AuNP_handle_hh55_ A	TGACAACTTGATACTTTCGAGGTGAATTTC TT ATGTAGGTGGTAGAG
AuNP_handle_hh60_ C	ATTGACAAACCACCACCAGAGCC TT ATGTAGGTGGTAGAG
AuNP_handle_hh65_ C	GGCAAGGACCATCGTAAAGGTAATACCCAAAAG TT ATGTAGGTGGTAGAG
AuNP_handle_hh70_ B	ACAGTAGCTTACCAGTATAAAGC TT ATGTAGGTGGTAGAG
AuNP_handle_hh75_ B	ATTCTCCGAGAGACTCCCTTAGTACCTTTTACA TT ATGTAGGTGGTAGAG
AuNP_sequence	[thiol-C6] - TT CTCTACCACCTACAT

Table A.15: Staple Strands for the rro DNA Origami

sequence name	sequence
rro_core_001	TTTTCACTCAAAGGGCGAAAAACCATCACC
rro_core_002	GTCGACTTCGGCCAACGCGCGGGGTTTTTC
rro_core_003	TGCATCTTTCCCAGTCACGACGGCCTGCAG
rro_core_004	TAATCAGCGGATTGACCGTAATCGTAACCG
rro_core_005	AACGCAAAATCGATGAACGGTACCGGTTGA
rro_core_006	AACAGTTTTGTACCAAAAACATTTTATTTC
rro_core_007	TTTACCCCAACATGTTTTAAATTTCCATAT
rro_core_008	TTTAGGACAAATGCTTTAAACAATCAGGTC
rro_core_009	CATCAAGTAAAACGAACTAACGAGTTGAGA
rro_core_010	AATACGTTTGAAAGAGGACAGACTGACCTT
rro_core_011	AGGCTCCAGAGGCTTTGAGGACACGGGTAA
rro_core_012	AGAAAGGAACAACTAAAGGAATTCAAAAAAA
rro_core_013	CAAATCAAGTTTTTTGGGGTCGAAACGTGGA
rro_core_014	CTCCAACGCAGTGAGACGGGCAACCAGCTGCA
rro_core_015	TTAATGAACTAGAGGATCCCCGGGGGGTAACG
rro_core_016	CCAGGGTTGCCAGTTTGAGGGGACCCGTGGGA
rro_core_017	ACAAACGGAAAAGCCCCAAAAACACTGGAGCA
rro_core_018	AACAAGAGGGATAAAAATTTTTAGCATAAAGC
rro_core_019	TAAATCGGGATTCCCAATTCTGCGATATAATG
rro_core_020	CTGTAGCTTGACTATTATAGTCAGTTCATTGA
rro_core_021	ATCCCCCTATACCACATTCAACTAGAAAAATC
rro_core_022	TACGTTAAAGTAATCTTGACAAGAACCGAACT
rro_core_023	GACCAACTAATGCCACTACGAAGGGGGTAGCA
rro_core_024	ACGGCTACAAAAGGAGCCTTTAATGTGAGAAT
rro_core_025	AGCTGATTGCCCTTCAGAGTCCACTATTAAAGGGTGCCGT
rro_core_026	GTATAAGCCAACCCGTCGGATTCTGACGACAGTATCGGCCGCAAGGCG
rro_core_027	TATATTTTGTCATTGCCTGAGAGTGGAAGATT
rro_core_028	GATTTAGTCAATAAAGCCTCAGAGAACCCTCA
rro_core_029	CGGATTGCAGAGCTTAATTGCTGAAACGAGTA
rro_core_030	ATGCAGATACATAACGGGAATCGTCATAAATAAAGCAAAG
rro_core_031	TTTATCAGGACAGCATCGGAACGACACCAACCTAAAACGAGGTCAATC
rro_core_032	ACAACTTTCAACAGTTTCAGCGGATGTATCGG
rro_core_033	AAAGCACTAAATCGGAACCCTAATCCAGTT
rro_core_034	TGGAACAACCGCCTGGCCCTGAGGCCCGCT
rro_core_035	TTCCAGTCGTAATCATGGTCATAAAAGGGG
rro_core_036	GATGTGCTTCAGGAAGATCGCACAATGTGA
rro_core_037	GCGAGTAAAAATATTTAAATTGTTACAAAG
rro_core_038	GCTATCAGAAATGCAATGCCTGAATTAGCA
rro_core_039	AAATTAAGTTGACCATTAGATACTTTTGCG
rro_core_040	GATGGCTTATCAAAAAGATTAAGAGCGTCC
rro_core_041	AATACTGCCCAAAAGGAATTACGTGGCTCA
rro_core_042	TTATACCACCAAATCAACGTAACGAACGAG
rro_core_043	GCGCAGACAAGAGGCAAAAGAATCCCTCAG
rro_core_044	CAGCGAAACTTGCTTTCGAGGTGTTGCTAA
rro_core_045	AGCAAGCGTAGGGTTGAGTGTTGTAGGGAGCC
rro_core_046	CTGTGTGATTGCGTTGCGCTCACTAGAGTTGC
rro_core_047	GCTTTCCGATTACGCCAGCTGGCGGCTGTTTC
rro_core_048	ATATTTTGGCTTTCATCAACATTATCCAGCCA
rro_core_049	TAGGTAAACTATTTTTGAGAGATCAAACGTTA
rro_core_050	AATGGTCAACAGGCAAGGCAAAGAGTAATGTG
rro_core_051	TAAGAGCAAATGTTTAGACTGGATAGGAAGCC
rro_core_052	TCATTCAGATGCGATTTTAAGAACAGGCATAG
rro_core_053	ACACTCATCCATGTTACTTAGCCGAAAGCTGC
rro_core_054	AAACAGCTTTTTGCGGGATCGTCAACACTAAA
rro_core_055	TAAATGAATTTTCTGTATGGGATTAATTTCTT
rro_core_056	CCCGATTTAGAGCTTGACGGGGAAAAAGAATA
rro_core_057	GCCCGAGAGTCCACGCTGGTTTGCAGCTAACT
rro_core_058	CACATTAAAATTGTTATCCGCTCATGCGGGCC
rro_core_059	TCTTCGCTGCACCGCTTCTGGTGCGGCCTTCC
rro_core_060	GAGGGTAGGATTCAAAAGGGTGAGACATCCAA
rro_core_061	TAAATCATATAACCTGTTTAGCTAACCTTTAA
rro_core_062	AATAGTAAACACTATCATAACCCTCATTGTGA
rro_core_063	ATTACCTTTGAATAAGGCTTGCCCAAATCCGC
rro_core_064	GACCTGCTCTTTGACCCCCAGCGAGGGAGTTA

rro_core_065	AAGGCCGCTGATACCGATAGTTGCGACGTTAG
rro_core_066	CCCAGCAGGCGAAAAATCCCTTATAAATCAAGCCGGCG
rro_core_067	TAAATCAAAATAATTCGCGTCTCGGAAACCAGGCAAAGGGAAGG
rro_core_068	GAGACAGCTAGCTGATAAATTAATTTTTGT
rro_core_069	TTTGGGGATAGTAGTAGCATTAAAAGGCCG
rro_core_070	GCTTCAATCAGGATTAGAGAGTTATTTTCA
rro_core_071	CGTTTACCAGACGACAAAGAAGTTTTGCCATAATTCGA
rro_core_072	TGACAACTCGCTGAGGCTTGCATTATACCAAGCGCGATGATAAA
rro_core_073	TCTAAAGTTTTGTCGTCTTTCCAGCCGACAA
rro_core_074	TCAATATCGAACCTCAAATATCAATTCCGAAA
rro_core_075	GCAATTCACATATTCCTGATTATCAAAGTGTA
rro_core_076	AGAAAACAAAGAAGATGATGAAACAGGCTGCG
rro_core_077	ATCGCAAGTATGTAAATGCTGATGATAGGAAC
rro_core_078	CCAATAGCTCATCGTAGGAATCATGGCATCAA
rro_core_079	AGAGAGAAAAAAATGAAAATAGCAAGCAAACT
rro_core_080	GCAAGGCCTCACCAGTAGCACCATGGGCTTGA
rro_core_081	TTGACAGGCCACCACCAGAGCCGCGATTTGTA
rro_core_082	TTAGGATTGGCTGAGACTCCTCAATAACCGAT
rro_core_083	TCCACAGACAGCCCTCATAGTTAGCGTAACGA
rro_core_084	AACGTGGCGAGAAAGGAAGGGAAACCAGTAA
rro_core_085	TCGGCAAATCCTGTTTGATGGTGGACCCTCAA
rro_core_086	AAGCCTGGTACGAGCCGGAAGCATAGATGATG
rro_core_087	CAACTGTTGCGCCATTCGCCATTCAAACATCA
rro_core_088	GCCATCAAGCTCATTTTTTAACCACAAATCCA
rro_core_089	CAACCGTTTCAAATCACCATCAATTCGAGCCA
rro_core_090	CCAACAGGAGCGAACCAGACCGGAGCCTTTAC
rro_core_091	CTTTTGCAGATAAAAACCAAAATAAAGACTCC
rro_core_092	GATGGTTTGAACGAGTAGTAAATTTACCATTA
rro_core_093	TCATCGCCAACAAAGTACAACGGACGCCAGCA
rro_core_094	ATATTCGGAACCATCGCCCACGCAGAGAAGGA
rro_core_095	TAAAAGGGACATTCTGGCCAACAAAGCATC
rro_core_096	ACCTTGCTTGGTCAGTTGGCAAAGAGCGGA
rro_core_097	ATTATCATTCAATATAATCCTGACAATTAC
rro_core_098	CTGAGCAAAAATTAATTACATTTTGGGTTA
rro_core_099	TATAACTAACAAAGAACGCGAGAACGCCAA
rro_core_100	CATGTAATAGAATATAAAGTACCAAGCCGT
rro_core_101	TTTTATTTAAGCAAATCAGATATTTTTTGT
rro_core_102	TTAACGTCTAACATAAAAACAGGTAACGGA
rro_core_103	ATACCCAACAGTATGTTAGCAAATTAGAGC
rro_core_104	CAGCAAAAGGAAACGTCACCAATGAGCCGC
rro_core_105	CACCAGAAAGGTTGAGGCAGGTCATGAAAG
rro_core_106	TATTAAGAAGCGGGGTTTTGCTCGTAGCAT
rro_core_107	TCAACAGTTGAAAGGAGCAAATGAAAAATCTAGAGATAGA
rro_core_108	TCAAATATAACCTCCGGCTTAGGTAACAATTTCATTTGAAGGCGAATT
rro_core_109	GTAAAGTAATCGCCATATTTAACAAAACTTTT
rro_core_110	TATCCGGTCTCATCGAGAACAAGCGACAAAAG
rro_core_111	TTAGACGGCCAAATAAGAAACGATAGAAGGCT
rro_core_112	CGTAGAAAATACATACCGAGGAAACGCAATAAGAAGCGCA
rro_core_113	GCGGATAACCTATTATTCTGAAACAGACGATTGGCCTTGAAGAGCCAC
rro_core_114	TCACCAGTACAAACTACAACGCCTAGTACCAG
rro_core_115	ACCCTTCTGACCTGAAAGCGTAAGACGCTGAG
rro_core_116	AGCCAGCAATTGAGGAAGGTTATCATCATTTT
rro_core_117	GCGGAACATCTGAATAATGGAAGGTACAAAAT
rro_core_118	CGCGCAGATTACCTTTTTTAATGGGAGAGACT
rro_core_119	ACCTTTTTATTTTAGTTAATTTCATAGGGCTT
rro_core_120	AATTGAGAATTCTGTCCAGACGACTAAACCAA
rro_core_121	GTACCGCAATTCTAAGAACGCGAGTATTATTT
rro_core_122	ATCCCAATGAGAATTAACTGAACAGTTACCAG
rro_core_123	AAGGAAACATAAAGGTGGCAACATTATCACCG
rro_core_124	TCACCGACGCACCGTAATCAGTAGCAGAACCG
rro_core_125	CCACCCTCTATTCACAAACAAATACCTGCCTA
rro_core_126	TTTCGGAAGTGCCGTCGAGAGGGTGAGTTTCG
rro_core_127	CTTTAGGGCCTGCAACAGTGCCAATACGTG
rro_core_128	CTACCATAGTTTGAGTAACATTTAAAATAT
rro_core_129	CATAAATCTTTGAATACCAAGTGTTAGAAC
rro_core_130	CCTAAATCAAAATCATAGGTCTAAACAGTA
rro_core_131	ACAACATGCCAACGCTCAACAGTCTTCTGA
rro_core_132	GCGAACCTCCAAGAACGGGTATGACAATAA
rro_core_133	AAAGTCACAAAATAAACAGCCAGCGTTTTA
rro_core_134	AACGCAAAGATAGCCGAACAAACCCTGAAC
rro_core_135	TCAAGTTTCATTAAAGGTGAATATAAAAGA
rro_core_136	TTAAAGCCAGAGCCGCCACCCTCGACAGAA
rro_core_137	GTATAGCAAACAGTTAATGCCCAATCCTCA
rro_core_138	AGGAACCCATGTACCGTAACACTTGATATAA
rro_core_139	GCACAGACAATATTTTTGAATGGGGTCAGTA
rro_core_140	TTAACACCAGCACTAACAACTAATCGTTATTA
rro_core_141	ATTTTAAAATCAAAATTATTTGCACGGATTCG
rro_core_142	CCTGATTGCAATATATGTGAGTGATCAATAGT
rro_core_143	GAATTTATTTAATGGTTTGAAATATTCTTACC
rro_core_144	AGTATAAAGTTCAGCTAATGCAGATGTCTTTC
rro_core_145	CTTATCATTCCCGACTTGCGGGAGCCTAATTT
rro_core_146	GCCAGTTAGAGGGTAATTGAGCGCTTTAAGAA
rro_core_147	AAGTAAGCAGACACCACGGAATAATATTGACG

rro_core_148	GAAATTATTGCCTTTAGCGTCAGACCGGAACC
rro_core_149	GCCTCCCTCAGAATGGAAAGCGCAGTAACAGT
rro_core_150	GCCCGTATCCGGAATAGGTGTATCAGCCCAAT
rro_core_151	AGATTAGAGCCGTCAAAAAACAGAGGTGAGGCCTATTAGT
rro_core_152	GTGATAAAAAGACGCTGAGAAGAGATAACCTTGCTTCTGTTCGGGAGA
rro_core_153	GTTTATCAATATGCGTTATACAAACCGACCGT
rro_core_154	GCCTTAAACCAATCAATAATCGGCACGCGCCT
rro_core_155	GAGAGATAGAGCGTCTTTCCAGAGGTTTTGAA
rro_core_156	GTTTATTTTGTCACAATCTTACCGAAGCCCTTTAATATCA
rro_core_157	CAGGAGGTGGGGTCAGTGCCTTGAGTCTCTGAATTTACCGGGAACCAG
rro_core_158	CCACCCTCATTTTCAGGGATAGCAACCGTACT
rro_core_159	CTTTAATGCGCGAACTGATAGCCCCACCAG
rro_core_160	CAGAAGATTAGATAATACATTTGTCGACAA
rro_core_161	CTCGTATTAGAAATTGCGTAGATACAGTAC
rro_core_162	CTTTTACAAAATCGTCGCTATTAGCGATAG
rro_core_163	CTTAGATTTAAGGCGTTAAATAAAGCCTGT
rro_core_164	TTAGTATCACAATAGATAAGTCCACGAGCA
rro_core_165	TGTAGAAATCAAGATTAGTTGCTCTTACCA
rro_core_166	ACGCTAACACCCACAAGAATTGAAAATAGC
rro_core_167	AATAGCTATCAATAGAAAATTCAACATTCA
rro_core_168	ACCGATTGTCGGCATTTTCGGTCATAATCA
rro_core_169	AAATCACCTTCCAGTAAGCGTCAGTAATAA
rro_core_170	GTTTTAACTTAGTACCGCCACCCAGAGCCA
rro_anchor_01	CATTCTCCTATTACTACCTTGTGTCGTGACGAGAAACACCAAATTTCA ACTTTAAT
rro_anchor_02	CATTCTCCTATTACTACCGCGATCGGCAATTCCACACAACAGGTGCCT AATGAGTG
rro_anchor_03	CATTCTCCTATTACTACCCACCCTCAGAAACCATCGATAGCATTGAGC CATTTGGGAA
rro_anchor_04	CATTCTCCTATTACTACCAACAATAACGTAAAACAGAAATAAAAATCC TTTGCCCGAA
rro_anchor_05	CATTCTCCTATTACTACCATTAAGTTTACCGAGCTCGAATTCGGGAAA CCTGTCGTGC
rro_anchor_06	CATTCTCCTATTACTACCCACCCTCAGAAACCATCGATAGCATTGAGC CATTTGGGAA
rro_anchor_07	CATTCTCCTATTACTACCATAAGGGAACCGGATATTCATTACGTCAG GACGTTGGGAA
rro_anchor_08	CATTCTCCTATTACTACCAGCCACCACTGTAGCGCGTTTTCAAGGGA GGGAAGGTAAA
rro_FasL_handle_01	CGAAAGACTTTGATAAGAGGTCATATTTCGCATTTTCATTCTCCTATT ACTACC
rro_FasL_handle_02	TGTAGCCATTAAAATTCGCATTAAATGCCGGATTTTCATTCTCCTATT ACTACC
rro_FasL_handle_03	TTGCTCCTTTCAAATATCGCGTTTGAGGGGGTTTTTCATTCTCCTATT ACTACC
rro_FasL_handle_04	GTAATAAGTTAGGCAGAGGCATTTATGATATTTTTTCATTCTCCTAT TACTACC
rro_FasL_handle_05	TTATTACGAAGAACTGGCATGATTGCGAGAGGTTTTCATTCTCCTAT TACTACC
rro_FasL_handle_06	TTCTACTACGCGAGCTGAAAAGGTTACCGCGCTTTTCATTCTCCTATT ACTACC
rro_biotin_handle_01	CGAAAGACTTTGATAAGAGGTCATATTTCGCATT[biotin]
rro_biotin_handle_02	TGTAGCCATTAAAATTCGCATTAAATGCCGGATT[biotin]
rro_biotin_handle_03	TTGCTCCTTTCAAATATCGCGTTTGAGGGGGTTT[biotin]
rro_biotin_handle_04	GTAATAAGTTAGGCAGAGGCATTTATGATATTTT[biotin]
rro_biotin_handle_05	TTATTACGAAGAACTGGCATGATTGCGAGAGGTT[biotin]
rro_biotin_handle_06	TTCTACTACGCGAGCTGAAAAGGTTACCGCGCTT[biotin]
rro_FISH_handle_01	CGAAAGACTTTGATAAGAGGTCATATTTCGCAGCATTCTTTCTTGAG GAGGGCAGCAAACGGGAAGAG
rro_FISH_handle_02	TGTAGCCATTAAAATTCGCATTAAATGCCGGAGCATTCTTTCTTGAG GAGGGCAGCAAACGGGAAGAG
rro_FISH_handle_03	TTGCTCCTTTCAAATATCGCGTTTGAGGGGGTGCATTCTTTCTTGAG GAGGGCAGCAAACGGGAAGAG
rro_FISH_handle_04	GTAATAAGTTAGGCAGAGGCATTTATGATATTGCATTCTTTCTTGAG GAGGGCAGCAAACGGGAAGAG
rro_FISH_handle_05	TTATTACGAAGAACTGGCATGATTGCGAGAGGGCATTCTTTCTTGAG GAGGGCAGCAAACGGGAAGAG
rro_FISH_handle_06	TTCTACTACGCGAGCTGAAAAGGTTACCGCGCGCATTCTTTCTTGAG GAGGGCAGCAAACGGGAAGAG

Table A.16: Staple Strands for the wf DNA Origami

sequence name	sequence
wf_core_001	CGCCGCCAGCATTGACACCCCCCGTTCAGCCC
wf_core_002	GGTTTGGCTCTTAGGGGAACCACCACCAGAGC
wf_core_003	CCCTCAGAGCCGCCACCACACCGGAACCAGA
wf_core_004	TCAGACGATTGGCCTTGCCACCCTCAGAGCCACCA
wf_core_005	CGCCACCCTCAGAACCGATATTCACAAAC
wf_core_006	TGGCTCCGCCTCCCTCAGAGC
wf_core_007	GCCACCACCGGAAATCGGCATTTTCGG
wf_core_008	TTTTCATAATCAAAATACTGTGAAGACGC
wf_core_009	TTGGAAGGTCAGAATTAGCGTTTGCCATC
wf_core_010	TCATAGCCCCCTTCCGTAATCAGTAG
wf_core_011	ACTGTAGCGCGTTTTCTTTGATGATACAG
wf_core_012	GTGCCTTGAGTAACAGTGTTTGCCTTTAGCGTCAG
wf_core_013	CGACAGAATCAAGAGCACCATTACCA
wf_core_014	ACCATCGATAGCAGCAAGCTGTCAACTGGGTT
wf_core_015	AAGTAGGAGTTAAAGCAAACGTCACCAATGAA
wf_core_016	TTAGCAAGGCCGGAATTATCACCGTC
wf_core_017	CAGCAAAATCACCAGTCCCGTATAAACAGTTA
wf_core_018	GTATCACCGTACTCAGATTTGGGAATTAGAGC
wf_core_019	ACCGACTTGAGCCCATTCAACCGATT
wf_core_020	TTATTCATTAAAGGTGTCCTTAGTTACTT
wf_core_021	ACTCCTTATTACGTAAATATTGACGGAAA
wf_core_022	GAGGGAGGGAAGGTTTGTCACAATCA
wf_core_023	AAAGACAAAAGGGCGAGAGGTTTAGTACC
wf_core_024	CCCTCAGAGCCACCACCCTCAATGGTTTACCAGCGCC
wf_core_025	ATAGAAAATTCATTTTTCAGGGATAGCAAGCC
wf_core_026	GGAATAAGTTTATCAGTATGTTAGCA
wf_core_027	CAATAGGAACCCATGTACGCAAAGACACCAC
wf_core_028	AACATATAAAAGAAACCGTAACACTGAGTTTCGTC
wf_core_029	CCAAGTCGTATGGCTACATACATAAAGGTGGC
wf_core_030	AACGTAGAAAATATCACCCTTCTTTCCGT
wf_core_031	TAAGTAGACGCTACGGTGGCATGATTAAG
wf_core_032	GATGCTACCGGTTCGTGTGCGGTGGCGTATGA
wf_core_033	GTCAATGAAGTCTCCTCCTCTCCATGAAA
wf_core_034	CAGTAGCACCAGATGGAGCTGGAGTAGTC
wf_core_035	TCAAGATTGTTGATGGCGGTACCACATAC
wf_core_036	TCTGTGGCAGCTTAGTTTCCCGCAGA
wf_core_037	GTCTTACAAATGTAAAGTCCTGAACATTTACCTTC
wf_core_038	GCACACCCCCTGCTAACCATACTAACTTT
wf_core_039	CTAAGCCAGTATTATGCGATTGGTGA
wf_core_040	ACCAGTACAAACTACAACTGTAACGATAGGCAAA
wf_core_041	ACGGGTCGTACGCGCCTGTAGCATTCCACAGA
wf_core_042	ATCTGCATCGCAACAATGCACTTTAT
wf_core_043	CAGCCCTCATAGTTAGCGCGTCCGAGTTGTT
wf_core_044	TACTCCGTGGTTACTTTAACGATCTAAAGTTT
wf_core_045	TTTTCTGTATGGGCTCGTAAGAGATAGGA
wf_core_046	AATGAGAATAACATTTAAAAAGGCCGTAA
wf_core_047	TATCCAGCTGAACGGTGTTTAGTATACCC
wf_core_048	ATGGTAATCCCTTATTACTTTTCTCCATTTTAGC
wf_core_049	TCCAACAACCATTCATCTGAGGGCCC
wf_core_050	TGCCTTTTGACTCATCTCACGCTGCGCGT
wf_core_051	CGCCGCTACAGGGATATGATTTCTGCTTG
wf_core_052	GGCGGCCATAGTCGGCCTGTTAAGTG
wf_core_053	CGCCTACTGCGCTCGCTCAGCGATCC
wf_core_054	GACCGCTGCGCCTTATGCAGCTCCCCACTAGA
wf_core_055	GAGGAACTCTGGTAGGCGGTGCTACAGAG
wf_core_056	TTCTTGAAGTGGTGGCGCCGCGCTTAATG
wf_core_057	AACCACCACACCCCTTGATCCGGCAAACA
wf_core_058	AACCACCGCTGGTAGCCGCTAGGGCGCTG
wf_core_059	CGAAAGGAGCGGGCGCTCAGTGGAACGAA
wf_core_060	CGTGGCGAGAAAGTGCCGTAAAGCAC
wf_core_061	AACTCACGTTAAGGGAGAAAGCCGGCGAA
wf_core_062	TTTAGAGCTTGACGGGATGAGTAAACTTGGTC
wf_core_063	GCGGCATCAGCACCTTTAAAGGGAGCCCCCGA
wf_core_064	TAAATCGGAACCCTGGAACCTCTTAC
wf_core_065	GTGCCCGATCAAGAATCTCGATAACT
wf_core_066	TCATTATGGTGAAAGTGTCGCCTTGCGTATAATAT
wf_core_067	TGTCCATATTGGCCGGTAGTGATCTTATT
wf_core_068	CAAAAAATACGCCATCAACGGTGGTA
wf_core_069	TATCCAGTGATTTCTGGTTATAGGTACATTGA
wf_core_070	GATGCCATTGGGATATCACGTTTAAATCAAAA
wf_core_071	AACAAGGGTGAACACTTCAAAATGTTCTTTAC
wf_core_072	GCAACTGACTGAAATGCCACTTGTGCTTATT
wf_core_073	TTTCTTTACGGTCGTTTTGCTAAACAACT
wf_core_074	AAGGCCGGATAAAATCCCATATCACCAGCTCA
wf_core_075	TTCAACAGTTTCAGCGAAGAATGTGAATA
wf_core_076	CATTCATCAGGCGGGCAAGGCTCCAAAAGGAGC
wf_core_077	CTTTAATTGTATCGGTCGAAATTCCGGATGAG
wf_core_078	CCGTCTTTCATTGCCATAAGAGCGATGAAAA
wf_core_079	CTGGTGAAACTCACCCTCATGGAAAACGGTGT
wf_core_080	CGTTTCAGTTTGCGCGAATAT

wf__core__081	TCGTGGTATTCACTCCTTATCAGCTTGCTTTCG
wf__core__082	AGGTGAATTTCGTGAGAAACTGCCGGAAATCG
wf__core__083	ATGTGTAGCAAAAGGCCAGCA
wf__core__084	CACGCCACATCTTAGGGATTGGCTGA
wf__core__085	AAAGGCCAGGAACGTTTTCACCGTAA
wf__core__086	TAGGGAAATAGGCCAGCGTAAAAAGGCCGCGTTGC
wf__core__087	TTAAGCATTCTGCCGATTCTCAATAAACCCTT
wf__core__088	GACGAAAAACATAGGGGCGAAGAAGT
wf__core__089	TTGCCCATGGTGAAAACGCATGGAAGCCATC
wf__core__090	TGACAGCTCGAGGCTTTGAACCTGAATCGCCA
wf__core__091	ACAAACGGCATGACGATATCAAATTACGCCCC
wf__core__092	TGGCGTTTTTCCATAGGCGTACTGTTGTAATTCA
wf__core__093	GCCCTGCCACTCATCGCATCCGCCCCCCTGACGAGCA
wf__core__094	ACAGGAGTCCAAGCGAGCTGGATTCTCACCAA
wf__core__095	TCACAAAAATCGACGCTCGTCATTACTGGATCTATCA
wf__core__096	AAATCCAGATGGAGTTCTGAGAAGTCAGAGGTGGCGAAACCC
wf__core__097	GACAGGACTATAAAGATACCAGCGGCAACCGAGCGTTCTGAAC
wf__core__098	TAAAAAACGCCCGAAGTTTTAAATCA
wf__core__099	ATCTAAAGTATATTTTTGGTCATGAG
wf__core__100	TTTTAAATTAAAAATGGGCGTTTCCCCCTGGA
wf__core__101	AGCTCCCTCGTGCGCTATCTTCACCTAGATCC
wf__core__102	ATTATCAAAAAGGTCCTTTGATCTTTT
wf__core__103	CTACGGGGTCTGAGGTGGTTTTTTTGT
wf__core__104	AAGGATCTCAAGAAGACTCCTGTTCCGACCCT
wf__core__105	GCCGCTTACCGGATACATTACGCGCAGAAAAA
wf__core__106	TTGCAAGCAGCAGTACCTTCGGAAAA
wf__core__107	AGAGTTGGTAGCTCTAACTACGGCTA
wf__core__108	CTCTGCTGAAGCCAGTCTGTCCGCCTTTCTCC
wf__core__109	CTTCGGGAAGCGTGGCGTATTTGGTATCTGCG
wf__core__110	CACTAGAAGAACAAACAGGATTAGCA
wf__core__111	GAGCGAGGTATGTCCGGTAACTATCG
wf__core__112	CCACTGGCAGCAGCCACTGGTGCTTTCTCATAGCTCACGCTGT
wf__core__113	AGGTATCTCAGTTCGGTGTAGCCGGTAAGACACGACTTATCG
wf__core__114	TCTTGAGTCCAACGTCGTTCGCTCCAAGC
wf__core__115	TGGGCTGTGTGCACGAAGGAGGTTGAGGCAGG
wf__core__116	GAAAATCTCCAAAAAAAAGAGTGAGAATAGAAAGGAA
wf__core__117	TGTCGTCTTTCCAGACATAATAATTTTTTCACGTT
wf__core__118	CAACTAAAGGAATTGCGAGTTAGTAAATGAA
wf__core__119	CGGGGTTTTGCTCAGTACCCGCCACCCTCAGAACCGCCA
wf__core__120	GCCACCCTCAGAACAGGCGGATAAGTGCCGTC
wf__core__121	ATGCCCCCTGCCTATTATAGCCCGGAATAGGT
wf__core__122	GAGAGGGTTGATATAAGTAGAGAAGGATTAGGATTAG
wf__core__123	CTGAGACTCCTCATCGGAACCTATTA
wf__core__124	GGAAAGCGCAGTCAAGTATTAAGAGG
wf__core__125	TTCTGAAACATGAATAAGTTTTAACGGGGTCA
wf__core__126	GAGTGTACTGGTATCTGAATTTACCG
wf__core__127	GAATGGATCCTCACATACA
wf__core__128	TTCCAGTAAGCGTTTAAAGCCAGAAT
wf__core__129	ATACACAGAGTTATCGGATAGAACTTCT
wf__core__130	ACTCGCGATAACCGTGTAGTAATTTATTT
wf__core__131	CGTCACCTGGAGACGACGGGGGATTCA
wf__core__132	ACGAAAACTTAAAGCAGACGAAGGGAAGAAAG
wf__core__133	TTCCCCGAAAAGGTCGAGGACGACTACGGTCT
wf__FasL__handle__01	TATTTTAATTCTAGGCGCCACGGCA TTTTCATTCTCCTATTACTACC
wf__FasL__handle__02	AACCCAAAAGAACTCTCAGATACGTG TTTTCATTCTCCTATTACTACC
wf__FasL__handle__03	AGTTTACAAGGAGCCCAGCATTGGCTACGCTAAG TTTTCATTCTCC-TATTACTACC
wf__FasL__handle__04	TTCCTTAGCTCCTGAAGCTATCCTAACGCA TTTTCATTCTCCTATTAC-TACC
wf__FasL__handle__05	GCGCAGTTTTTCCGTTCCGCGCACA TTTTTCATTCTCCTATTACTACC
wf__FasL__handle__06	GCAAGTGTAGCGGCATCCAGCAACGG TTTTCATTCTCCTATTACTACC
wf__biotin__handle__01	TATTTTAATTCTAGGCGCCACGGCA [biotin]
wf__biotin__handle__02	AACCCAAAAGAACTCTCAGATACGTG [biotin]
wf__biotin__handle__03	AGTTTACAAGGAGCCCAGCATTGGCTACGCTAAG [biotin]
wf__biotin__handle__04	TTCCTTAGCTCCTGAAGCTATCCTAACGCA [biotin]
wf__biotin__handle__05	GCGCAGTTTTTCCGTTCCGCGCACA [biotin]
wf__biotin__handle__06	GCAAGTGTAGCGGCATCCAGCAACGG [biotin]
wf__FISH__handle__01	TATTTTAATTCTAGGCGCCACGGCA GCATTCTTTCTTGAG-GAGGGCAGCAAACGGGAAGAG
wf__FISH__handle__02	AACCCAAAAGAACTCTCAGATACGTG GCATTCTTTCTTGAG-GAGGGCAGCAAACGGGAAGAG
wf__FISH__handle__03	AGTTTACAAGGAGCCCAGCATTGGCTACGCTAAG GCATTCTTTCTTGAGGAGGGCAGCAAACGGGAAGAG
wf__FISH__handle__04	TTCCTTAGCTCCTGAAGCTATCCTAACGCA GCATTCTTTCTTGAG-GAGGGCAGCAAACGGGAAGAG
wf__FISH__handle__05	GCGCAGTTTTTCCGTTCCGCGCACA GCATTCTTTCTTGAG-GAGGGCAGCAAACGGGAAGAG
wf__FISH__handle__06	GCAAGTGTAGCGGCATCCAGCAACGG GCATTCTTTCTTGAG-GAGGGCAGCAAACGGGAAGAG

Table A.17: Staple Strands for the mini DNA Origami

sequence name	sequence
mini_core_01	ACTCTCGGGTTAAAGAGCACCATCCGGCGGC
mini_core_02	ATCACTCCGCGAACAGTTTCACTGGTGCATAG
mini_core_03	AGCCCGACTAGCTAATAAGCTCCTGAAACAAGTGGCGCAGTGCAGTA
mini_core_04	CAGACGGTATTTGCCGTCAAATGGAGTCTGT
mini_core_05	GATCGCTATATGTTCTATACCCACGTTAAGTT
mini_core_06	CCTGACACCCGAGCATGTTACATTGGGAGCA
mini_core_07	TGTCCGTATGGAGATATAGAACCCTTTCAGAG
mini_core_08	AGGACCCGCCACGCCCTCGCTGCCATTATAC
mini_core_09	GCTTTGAGCTCTCCTGTGTTGTGCGGGTTAGT
mini_core_10	CGCCGGTCTCAGAAGGCCCAAACAGTGTATATCGAATCGCGGAAGTCT
mini_core_11	GCTCCGTGAAGCAGCCGTGCTCCATCTTCGAT
mini_core_12	TCGGGAGGAAGGACACTGTTATCCGTCCGGC
mini_core_13	ATATTCATGGATCCAACCAATTTATTGGAGCT
mini_core_14	CGTTTGACGAAGCTTGATTTAAGGCTTACCC
mini_core_15	TGTGCCGGGAGTATTCCGATGAAAGGTATGT
mini_core_16	GTTGATGCCTCTAGGTACGGATGGTTCAAAG
mini_core_17	CTGCTCGCACGATCGATGGCTGATTAGTGCGG
mini_core_18	TGGAGTTCGTCCGCATGGAGGGCCGTTCTTA
mini_core_19	CGCCATATAGAGAACTGGTTCATTTTGCCAGC
mini_core_20	ATTGGCCATTTACGGGACGCCGCACCGTACT
mini_FasL_handle_01	GATCTACCAGTCATCGTCGTGCAATAACACGG TTTTCATTCTCCTATTACTACC
mini_FasL_handle_02	CTTAAGCCATTGTTCAGGGAGTACAGGCTTG TTTTCATTCTCCTATTACTACC
mini_FasL_handle_03	ACCAAGAACTCCGCTTGCAGAGGCAAAGGTT TTTTCATTCTCCTATTACTACC
mini_FasL_handle_04	TACTTCAGTATCAGTAGTCCCTAAGGCTATGT TTTTCATTCTCCTATTACTACC
mini_FasL_handle_05	GAATTTGACACGGCAGACATCGCGACTGACGC TTTTCATTCTCCTATTACTACC
mini_FasL_handle_06	AATGACGTACGAGGGAATCCACTCCCACATGC TTTTCATTCTCCTATTACTACC
mini_biotin_handle_01	GATCTACCAGTCATCGTCGTGCAATAACACGG [biotin]
mini_biotin_handle_02	CTTAAGCCATTGTTCAGGGAGTACAGGCTTG [biotin]
mini_biotin_handle_03	ACCAAGAACTCCGCTTGCAGAGGCAAAGGTT [biotin]
mini_biotin_handle_04	TACTTCAGTATCAGTAGTCCCTAAGGCTATGT [biotin]
mini_biotin_handle_05	GAATTTGACACGGCAGACATCGCGACTGACGC [biotin]
mini_biotin_handle_06	AATGACGTACGAGGGAATCCACTCCCACATGC [biotin]
mini_FISH_handle_01	GATCTACCAGTCATCGTCGTGCAATAACACGG GCATTCTTTCTTGAGGAGGGCAGCAAACGGGAAGAG
mini_FISH_handle_02	CTTAAGCCATTGTTCAGGGAGTACAGGCTTG GCATTCTTTCTTGAGGAGGGCAGCAAACGGGAAGAG
mini_FISH_handle_03	ACCAAGAACTCCGCTTGCAGAGGCAAAGGTT GCATTCTTTCTTGAGGAGGGCAGCAAACGGGAAGAG
mini_FISH_handle_04	TACTTCAGTATCAGTAGTCCCTAAGGCTATGT GCATTCTTTCTTGAGGAGGGCAGCAAACGGGAAGAG
mini_FISH_handle_05	GAATTTGACACGGCAGACATCGCGACTGACGC GCATTCTTTCTTGAGGAGGGCAGCAAACGGGAAGAG
mini_FISH_handle_06	AATGACGTACGAGGGAATCCACTCCCACATGC GCATTCTTTCTTGAGGAGGGCAGCAAACGGGAAGAG

Appendix B

Supplementary Figures

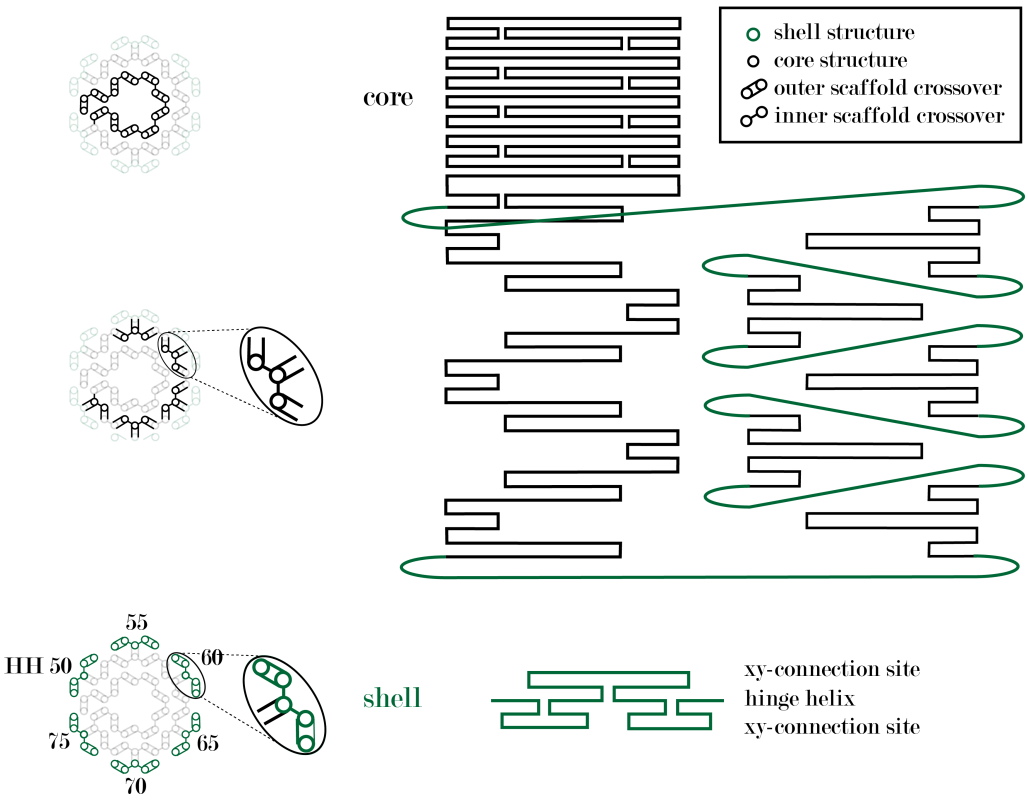

Figure B.1: Scaffold Routing for Modular xy-Connections

Scaffold routing follows the inside-outside crossovers for the core structure (indicated black), then it changes the pacing to allow for the re-routable scaffold parts for the modular shell (green). The respective hinge helices (HH) are indicated at the lower right. Panels were partially adapted and reprinted with permission from [114], copyright 2025 Springer Nature Ltd.

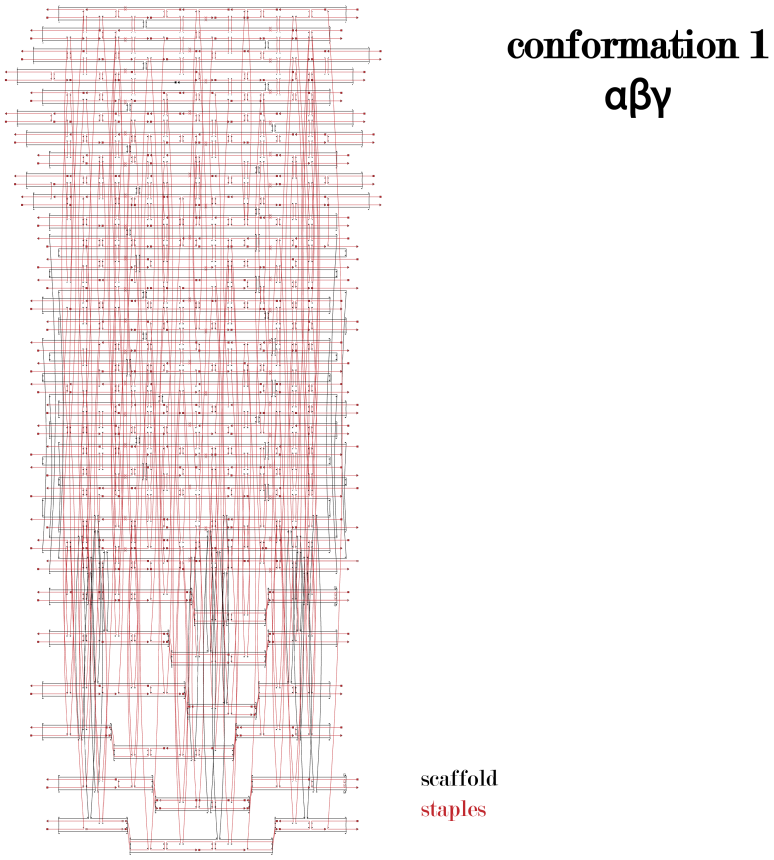

Figure B.2: caDNAno Routing of the moDON in Conformation 1

caDNAno routing of the structure in conformation 1 ($\alpha\beta\gamma$). Scaffold is indicated in black, staples are indicated in red. Panels were partially adapted and reprinted with permission from [114], copyright 2025 Springer Nature Ltd.

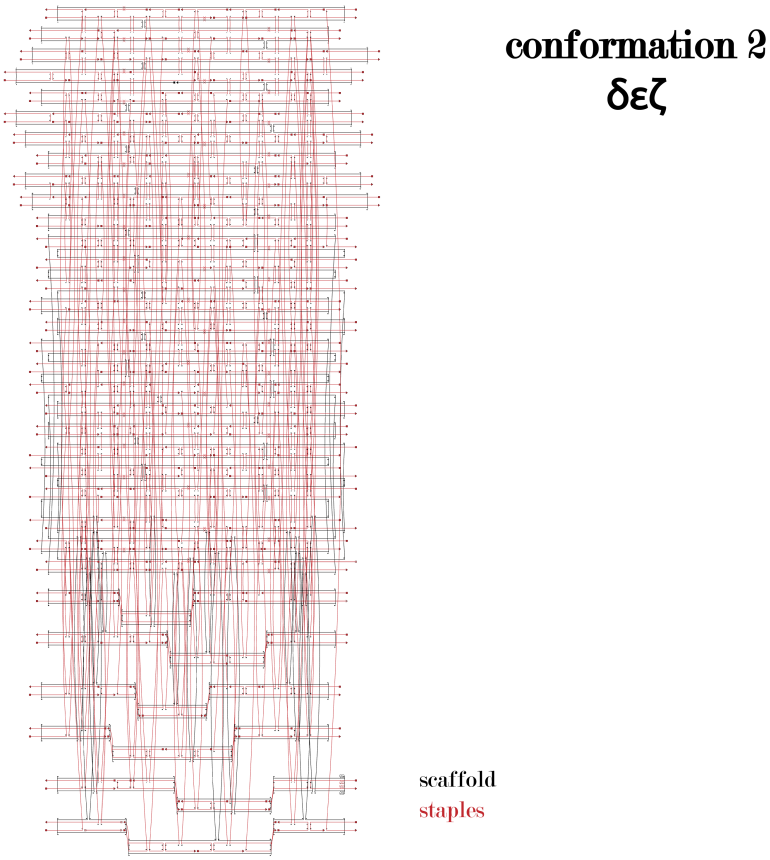

Figure B.3: caDNAno Routing of the moDON in Conformation 2

caDNAno routing of the structure in conformation 2 ($\delta\epsilon\zeta$). Scaffold is indicated in black, staples are indicated in red. Panels were partially adapted and reprinted with permission from [114], copyright 2025 Springer Nature Ltd.

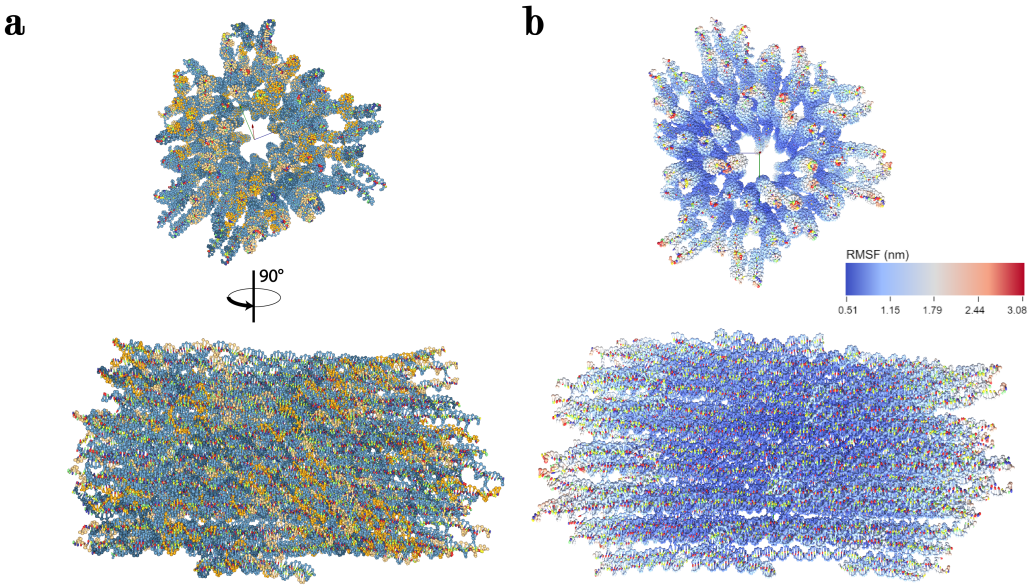

Figure B.4: oxDNA Simulation of the moDON in Configuration 1

(**a**) Mean structure of the oxDNA-simulated moDON in z- and 90° turned, in xy-direction. (**b**) same structure with RMSF indicated as colors from blue (low) to red (high) fluctuations. The moDON shows very low overall fluctuations, speaking for its structural rigidity. Panels were partially adapted and reprinted with permission from [114], copyright 2025 Springer Nature Ltd.

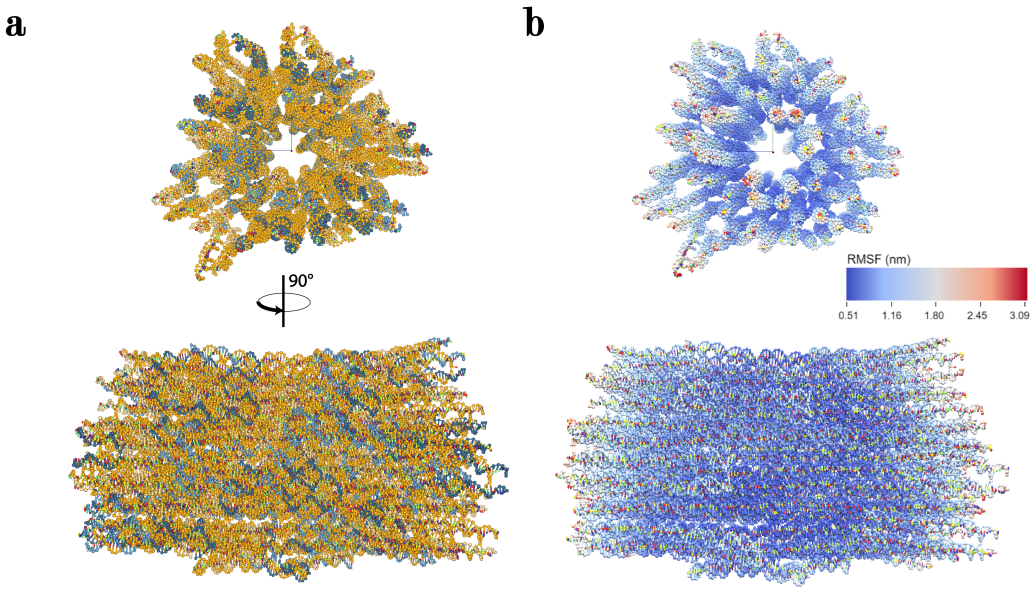

Figure B.5: oxDNA Simulation of the moDON in Configuration 2

(**a**) Mean structure of the oxDNA-simulated moDON in z- and 90° turned, in xy-direction. (**b**) same structure with RMSF indicated as colors from blue (low) to red (high) fluctuations. The moDON shows very low overall fluctuations, speaking for its structural rigidity.

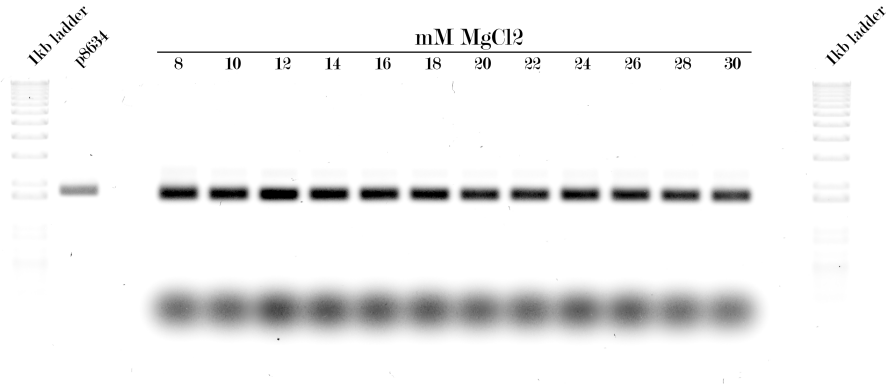

Figure B.6: AGE Analysis of the moDON folds

The moDON monomer folded with high yield across a wide range of $MgCl_2$ concentrations. The monomer migrates slightly faster through the gel than the scaffold p8634. The yield was almost quantitative with approximately 98.5 % AGE yield across all bands. Further tests on NaCl and $MgCl_2$ combinations yielded the same result, but are not shown here. Panels were partially adapted and reprinted with permission from [114], copyright 2025 Springer Nature Ltd.

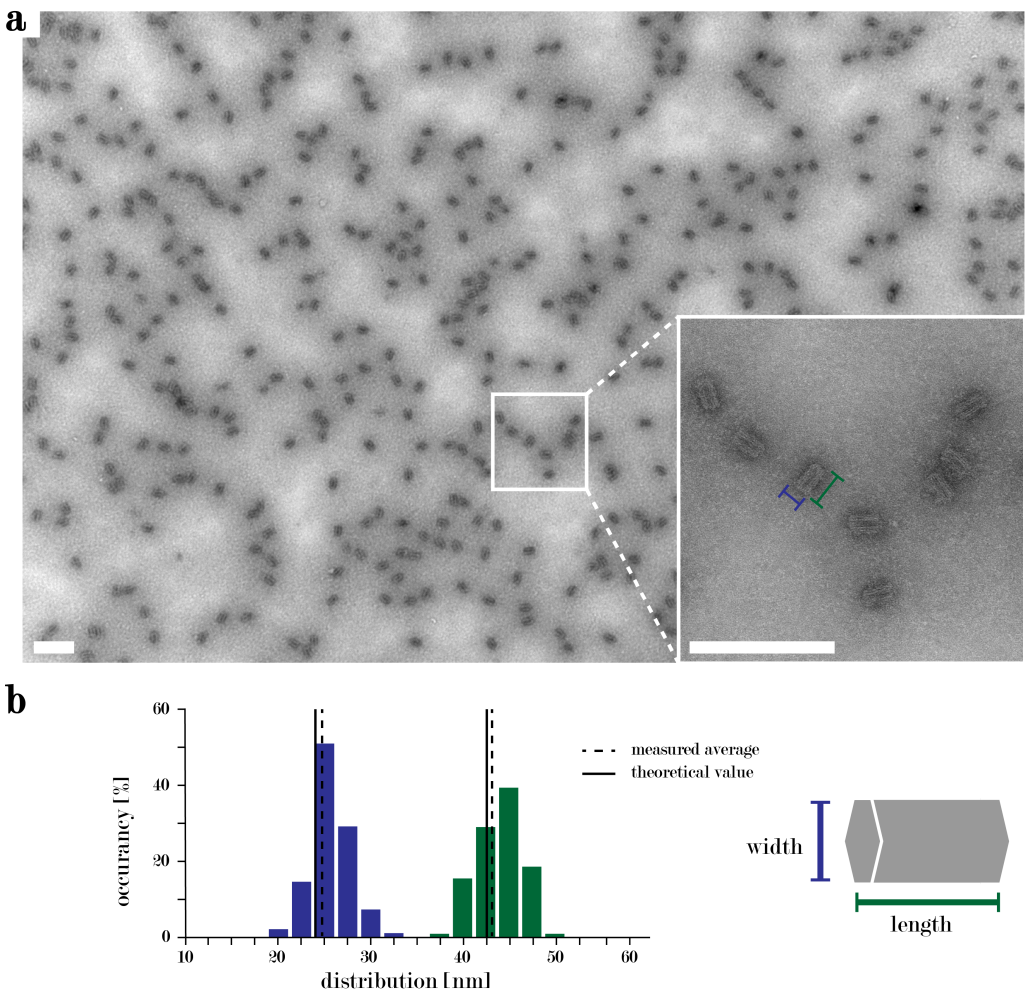

Figure B.7: Analysis of moDON Dimensions

(**a**) Wide-field TEM micrograph of moDON monomers. (**b**) Analysis of the moDONs dimensions for N > 100 monomers. The histograms show the values for width and length in blue and green. Averages (width: 24.5 nm, length: 43.0 nm) are roughly in accordance with the theoretical values (width: 24.0 nm, length: 42.5 nm). Scale bar in (**a**) are 200 nm. Panels were partially adapted and reprinted with permission from [114], copyright 2025 Springer Nature Ltd.

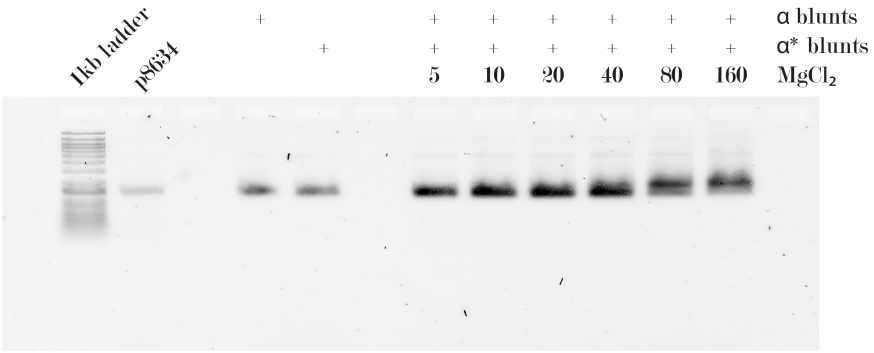

Figure B.8: Testing Blunt End Connections

Blunt end moDON structure at different $MgCl_2$ concentrations incubated for 24 h. Only moDON structures incubated with 80 and 160 mM $MgCl_2$ show some minor dimerization

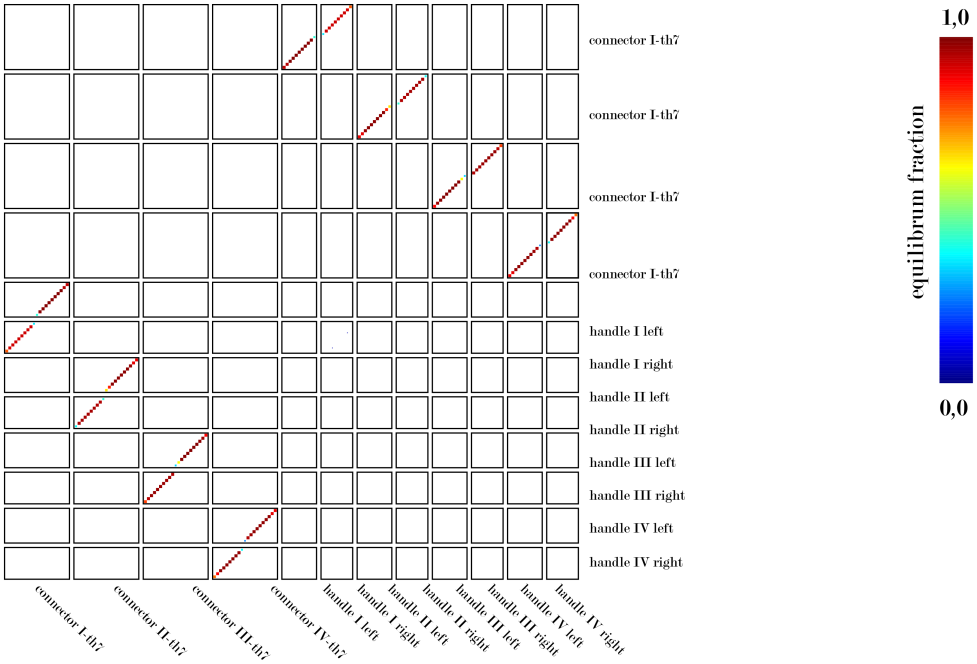

Figure B.9: NUPACK Simulation of z-Connections

Probability matrix for interactions in an ensemble with all handles and connectors: The red squares indicate high probability of interaction between the designed, sequence complementary connectors and handles. The absence of other markers indicates the unlikelihood of off-target interactions. Panels were partially adapted and reprinted with permission from [114], copyright 2025 Springer Nature Ltd.

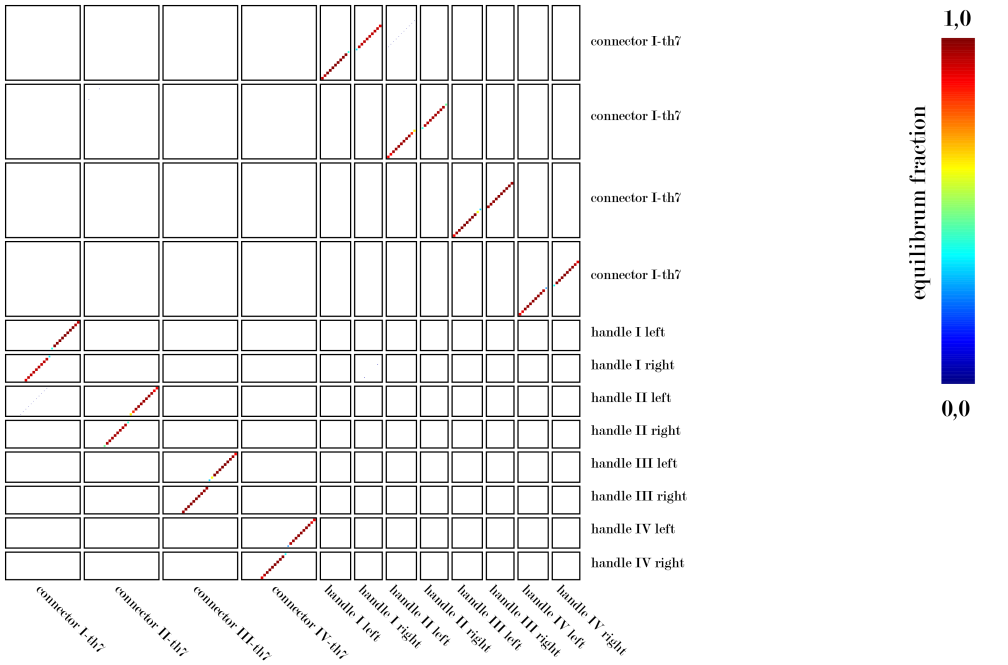

Figure B.10: NUPACK Simulation of z-Connections with Toeholds

Probability matrix for interactions in an ensemble with all handles and connectors: The red squares indicate high probability of interaction between the designed, sequence-complementary connectors and handles. The absence of other markers indicates the unlikelihood of off-target interactions. Panels were partially adapted and reprinted with permission from [114], copyright 2025 Springer Nature Ltd.

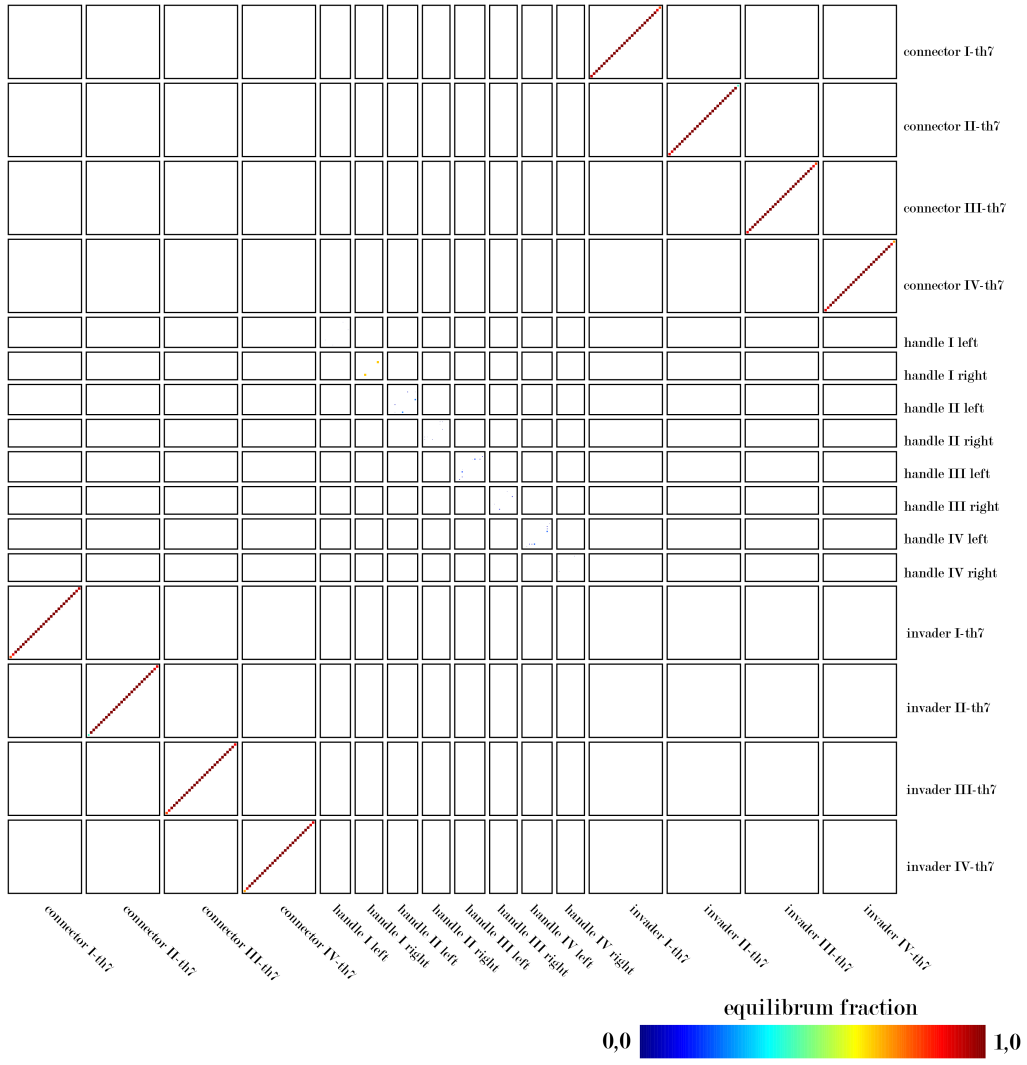

Figure B.11: NUPACK Simulation of z-Connections with Invaders

Probability matrix for interactions in an ensemble with all handles and connectors: The red squares indicate high probability of interaction between the designed, sequence complementary connectors and handles. The absence of other markers indicates the unlikelihood of off-target interactions. If invader strands are introduced to the ensemble, the most likely connections shift to those between connectors and invaders, not between connectors and handles, anymore. Panels were partially adapted and reprinted with permission from [114], copyright 2025 Springer Nature Ltd.

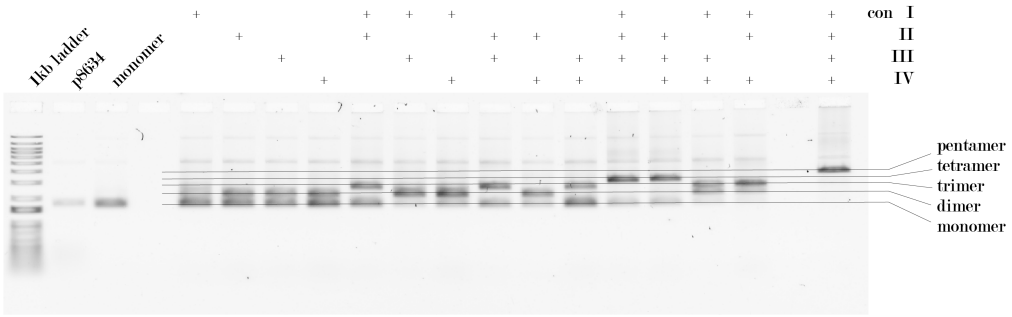

Figure B.12: AGE Analysis of the Orthogonality of z-Connections

The orthogonality of z-connections is tested by AGE: Different subsets of connectors are added to the same ensemble of five moDONs, and different moDON structures arise. The size of the moDON superstructures is anti-proportional to the migration speed through the gel. The defined bands indicate high specificity of the connections. Panels were partially adapted and reprinted with permission from [114], copyright 2025 Springer Nature Ltd.

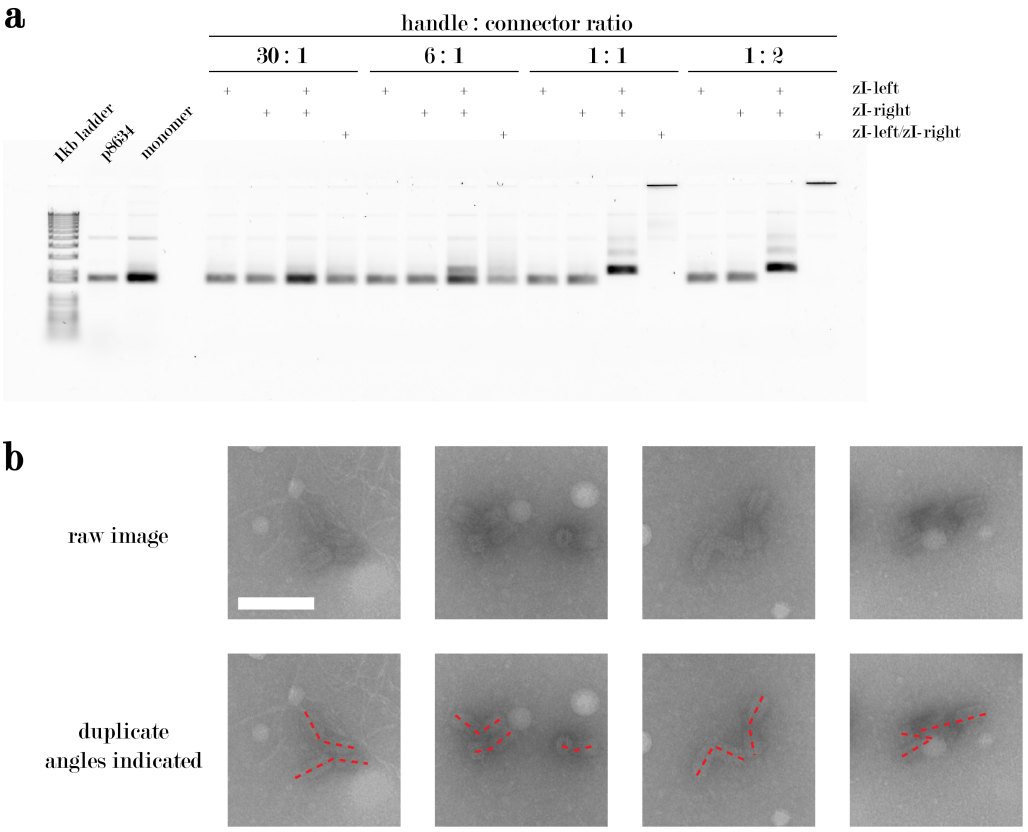

Figure B.13: Low Connector Excess Leads to Kinked Assemblies

(**a**) AGE analysis of z-connections with low amounts of connectors: Already six times less connectors than handles present (or 1:1 over each moDON monomer) are able to connect a subfraction of the origami, but full dimerization is only reached with a 1:1 ratio of handles to connectors. (**b**) However, as shown in the TEM micrographs, the connectors of moDON monomers with a 1:1 ratio of handles to connectors are kinked (angles indicated in red at the duplicates). Larger excesses of connectors are needed for straight connections.. Scale bar is 100 nm and holds for all micrographs. Panels were partially adapted and reprinted with permission from [114], copyright 2025 Springer Nature Ltd.

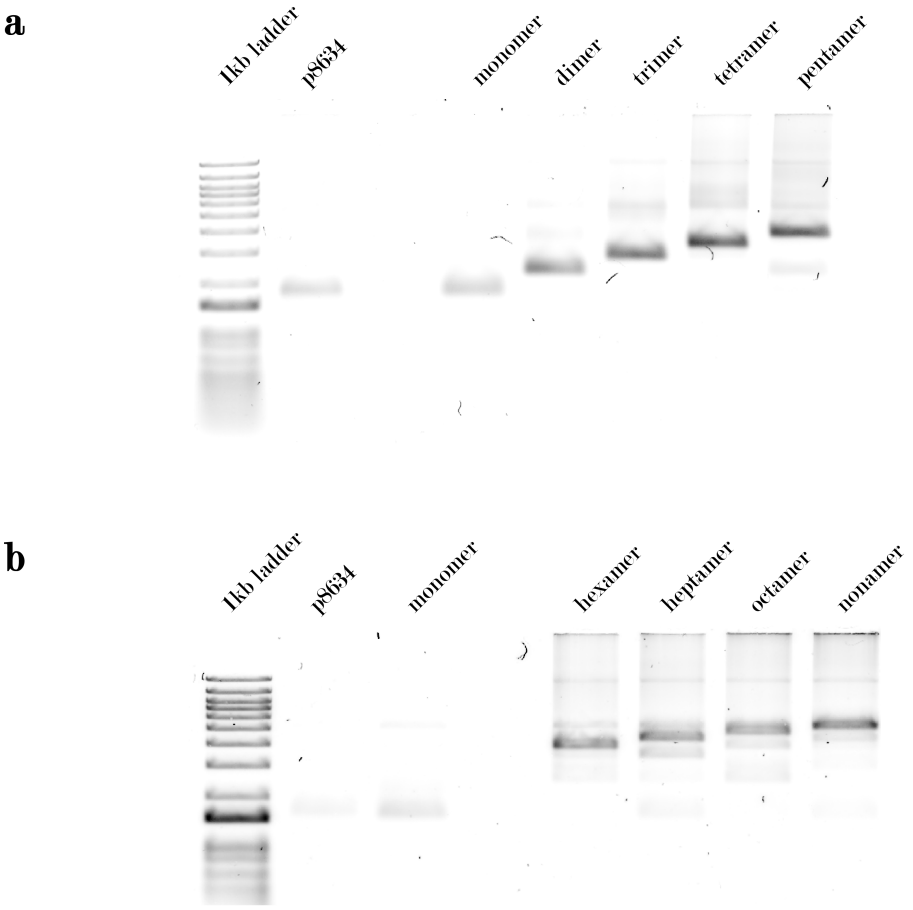

Figure B.14: AGE Analysis of Assemblies with z-Connections

(**a**) monomers to pentamers assembled in the z-direction with unidirectional connectors. (**b**) symmetric assemblies with connectors going in both directions, 5' to 3' from a central symmetric connection part. Panels were partially adapted and reprinted with permission from [114], copyright 2025 Springer Nature Ltd.

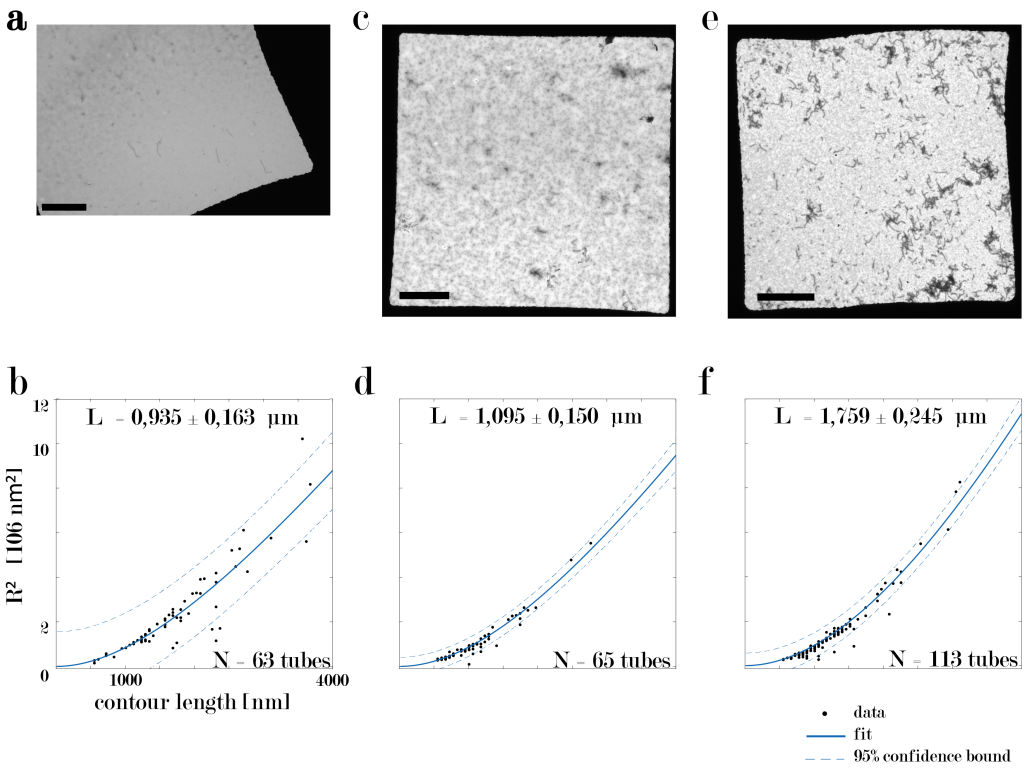

Figure B.15: Persistence Length Analysis of Periodic Structures

Wide-field TEM images and persistence length analysis plots of (**a**)/(**b**) the periodic tube with a monomeric subunit, (**c**)/(**d**) the periodic tube with a trimeric subunit, and (**e**)/(**f**) the periodic tube with a tetrameric subunit. Numbers of tubes N for the analysis and the calculated persistence length L_p are indicated in the respective plot. Scale bars are 10 μm. Panels were partially adapted and reprinted with permission from [114], copyright 2025 Springer Nature Ltd.

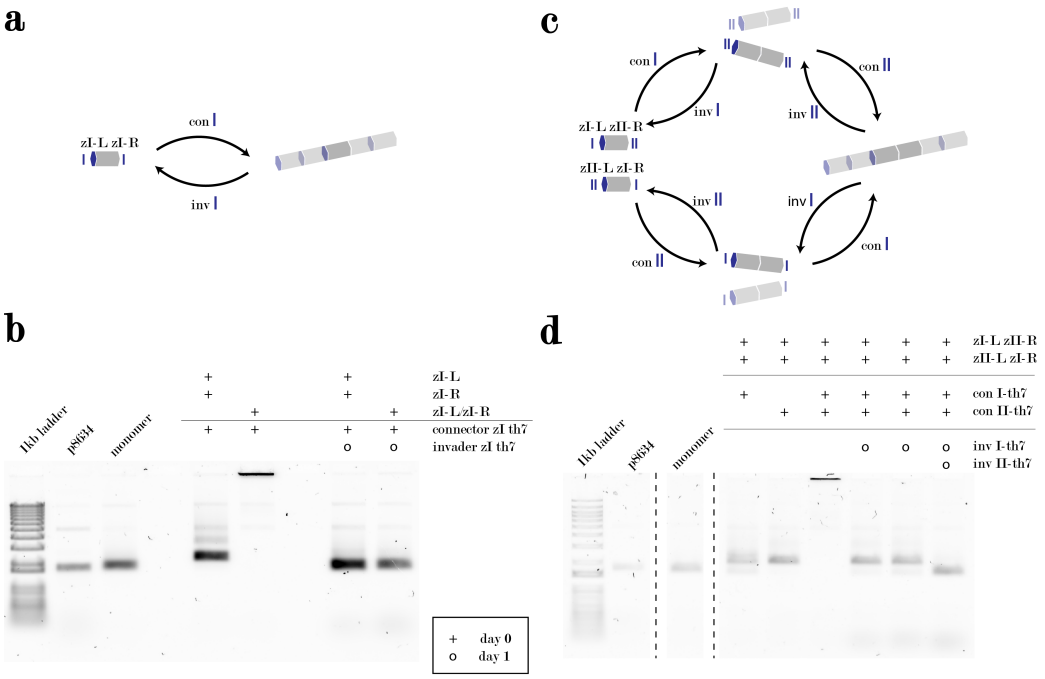

Figure B.16: Disassembly of Periodic Structures

Sketch and AGE analysis of the controlled assembly and disassembly of (**a**)/(**b**) a periodic tube with a monomeric subunit, and (**c**)/(**d**) a periodic tube with a dimeric z-subunit. Panels were partially adapted and reprinted with permission from [114], copyright 2025 Springer Nature Ltd.

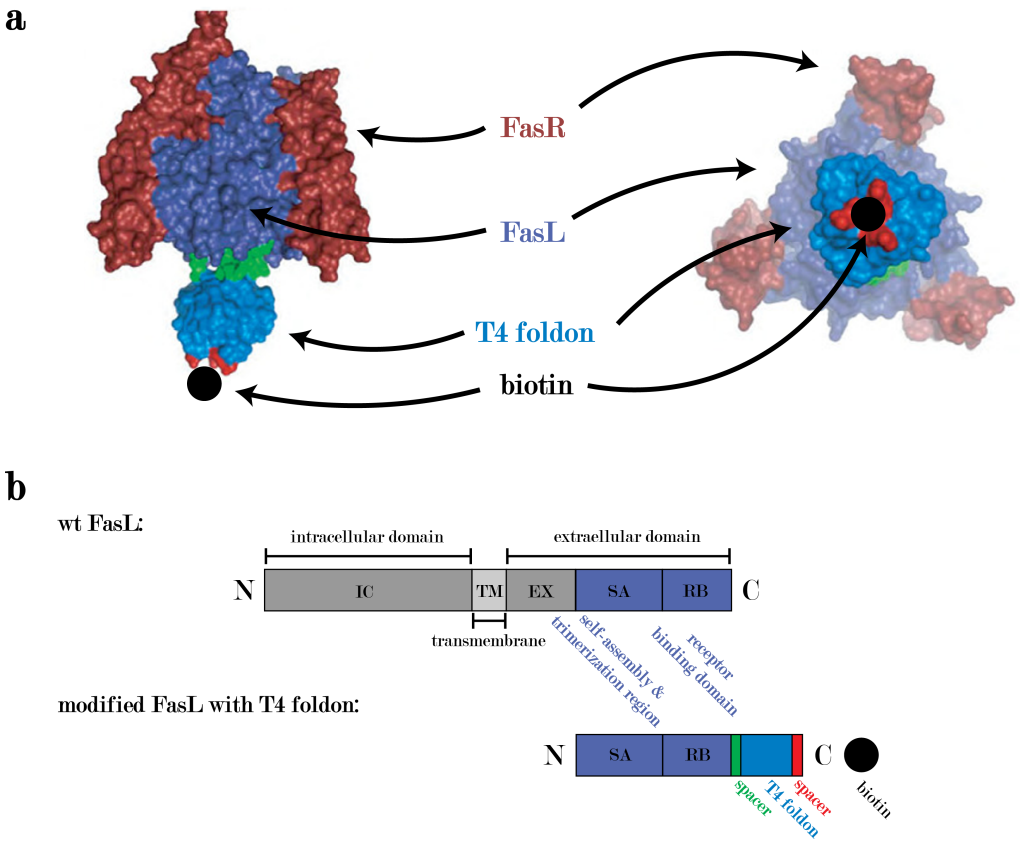

Figure B.17: The FasL from Apogenix

(**a**) Three-dimensional rendering of the modified FasL from Apogenix, based upon the construct of Kleber *et al.*[173]. The FasR is indicated red, FasL dark blue, linkers in green and bright red, the T4 foldon in light blue, and lastly the position of the biotin modification is indicated as a big black circle. (**b**) Comparison of the wt FasL and the modified FasL constructs. The wt FasL has an intracellular domain (IC), a transmembrane domain (TM), and some part of the extracellular domain (EX), which are truncated in the modified version. Both FasL share the self-assembly and trimerization region (SA), as well as the receptor binding domain (RB). The modified FasL has additionally a T4 foldon engulfed by two linkers at the C-terminus of the construct, where also the biotin modification will attach. Panel (**a**) is adapted and reprinted with permission from [173], copyright 2008 Elsevier.

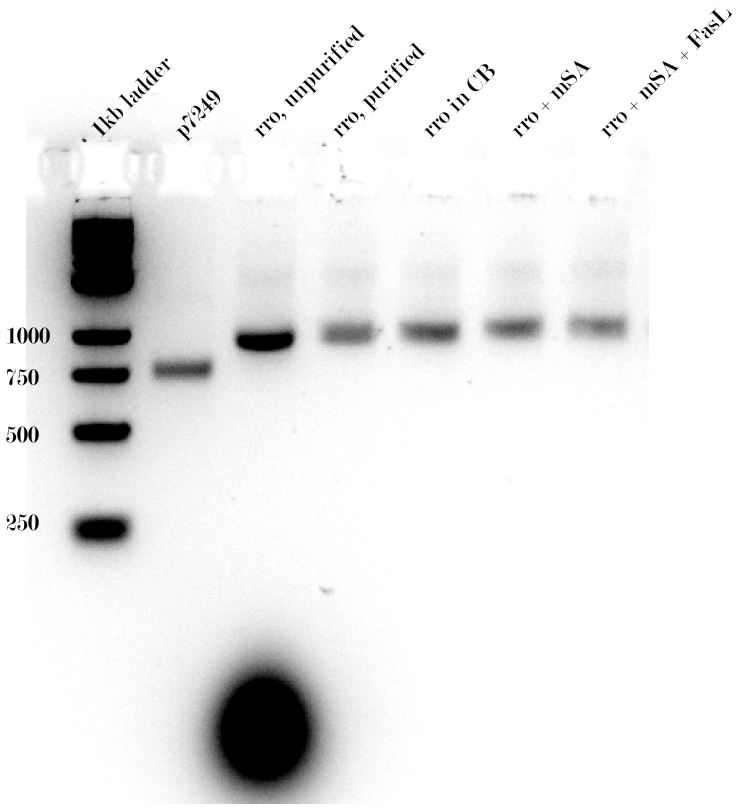

Figure B.18: AGE of the DNA Origami and the Nanoagent

Agarose gel electrophoresis of the nanoagent in different stages. From left to right: 1 kb ladder, p7249 scaffold, unpurified origami, purified origami, origami purified and in CB, origami with mSA attached, and the origami with mSA and FasL attached. The DNA origami shows less electrophoretic motility than the p7249 scaffold, indicating successful folding. The larger constructs show again less electrophoretic motility, indicating successful protein attachment. Panels were partially adapted and reprinted with permission from [158], copyright 2021 John Wiley & Sons.

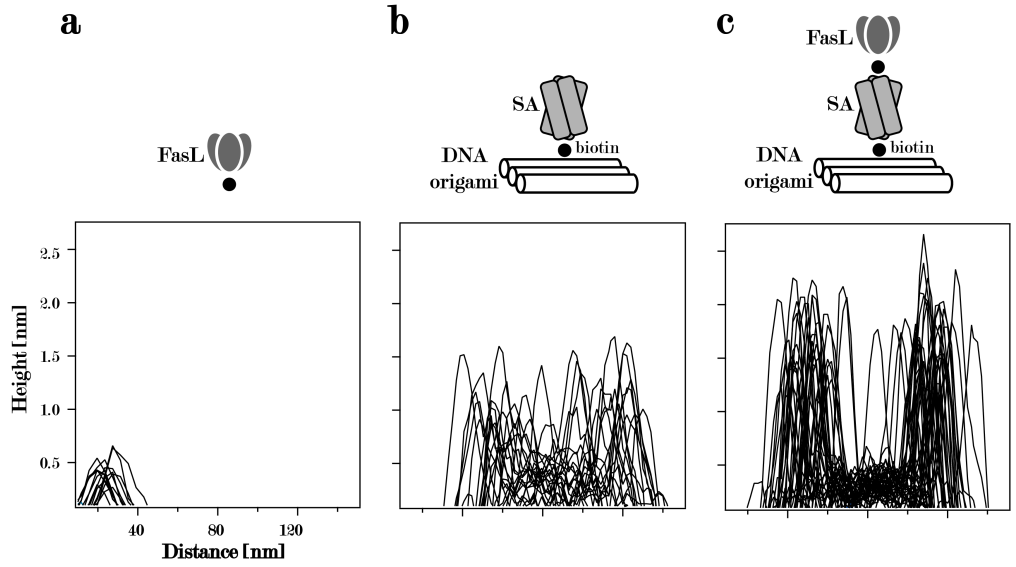

Figure B.19: AFM Height Analysis of Nanoagents

AFM profiles and heights of different constituents and full nanoagent. (**a**) FasL height of approximately 0.5 nm. (**b**) DNA origami and streptavidin height of approximately 1.5 nm. (**c**) Full nanoagent height is with 2.0 nm a sum of its constituents. Double peaks are due to DNA origami having several binding spots. Panels were partially adapted and reprinted with permission from [158], copyright 2021 John Wiley & Sons.

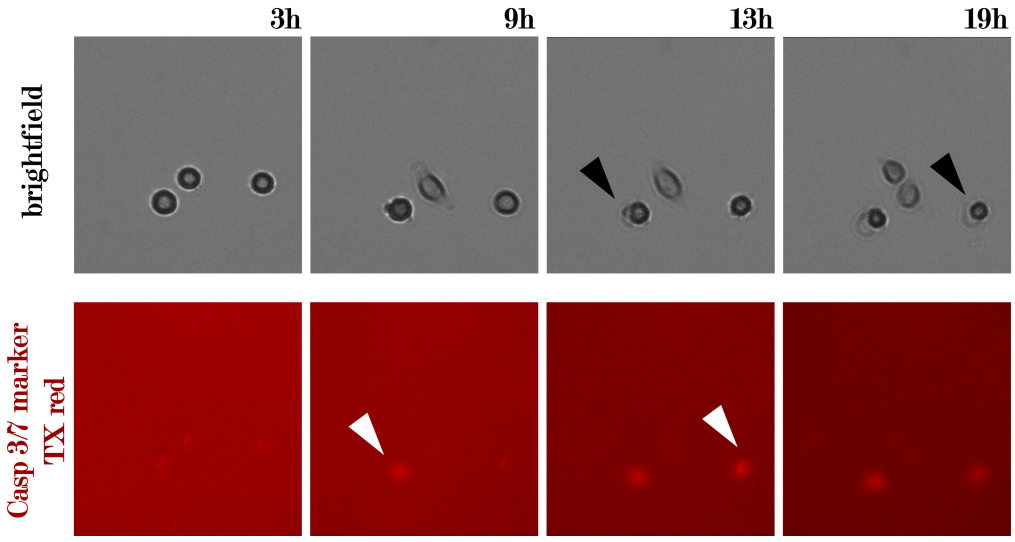

Figure B.20: Caspase 3/7 Activation and Cell Blebbing

BF and TXred images of cells undergoing apoptosis. The morphological changes of apoptotic cells correlate with the fluorescence signal from caspase 3/7 activation. The caspase 3/7 marker is an early apoptosis marker, and signals from it are approximately 4 h earlier than the occurrence of the bleb. Blebs in the BF channel are indicated by black arrows, and caspase 3/7 signal is indicated with white arrows. Panels were partially adapted and reprinted with permission from [158], copyright 2021 John Wiley & Sons.

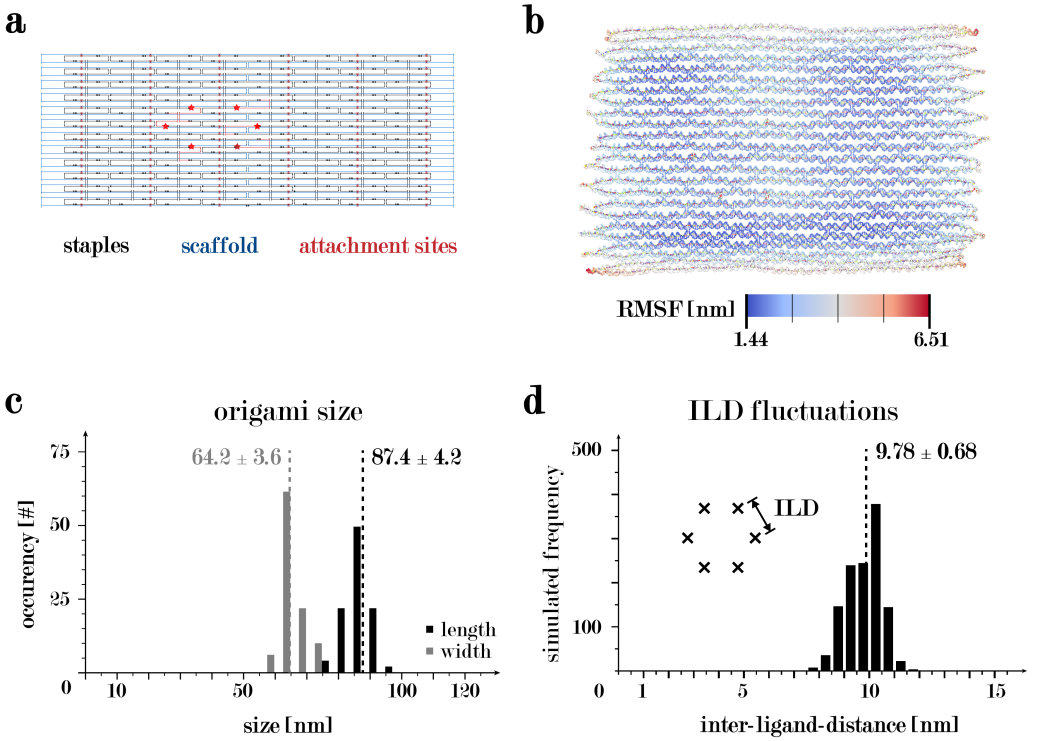

Figure B.21: Structure and *in silico* Analysis of the rro DNA Origami

(**a**) Scaffold and staple layout of the rro DNA origami. The scaffold strand is shown in blue, staples strands are shown in black, and the connection sites for FasL are indicated by red stars. (**b**) Averaged structure from oxDNA simulations with RMSF color-coded from blue to red. (**c**) Size distribution of the DNA origami extracted from TEM micrographs. Length is shown in black, and width is shown in grey, and average values are annotated at the respective dotted lines. (**d**) ILD distribution of the anchoring points for FasL on the DNA origami, average distance is annotated at the dotted line. Panels were partially adapted and reprinted with permission from [160], copyright 2025 John Wiley & Sons.

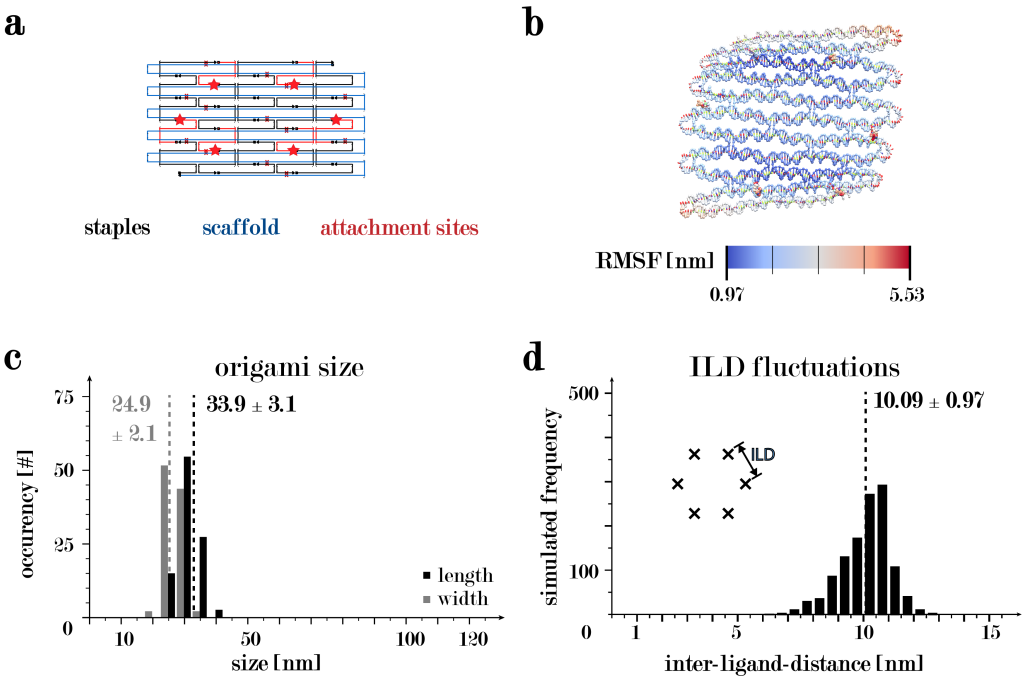

Figure B.22: Structure and *in silico* Analysis of the mini DNA Origami

(**a**) Scaffold and staple layout of the mini DNA origami. The scaffold strand is shown in blue, staples strands are shown in black, and the connection sites for FasL are indicated by red stars. (**b**) Averaged structure from oxDNA simulations with RMSF color-coded from blue to red. (**c**) Size distribution of the DNA origami extracted from TEM micrographs. Length is shown in black, and width is shown in grey, and average values are annotated at the respective dotted lines. (**d**) ILD distribution of the anchoring points for FasL on the DNA origami, average distance is annotated at the dotted line. Panels were partially adapted and reprinted with permission from [160], copyright 2025 John Wiley & Sons.

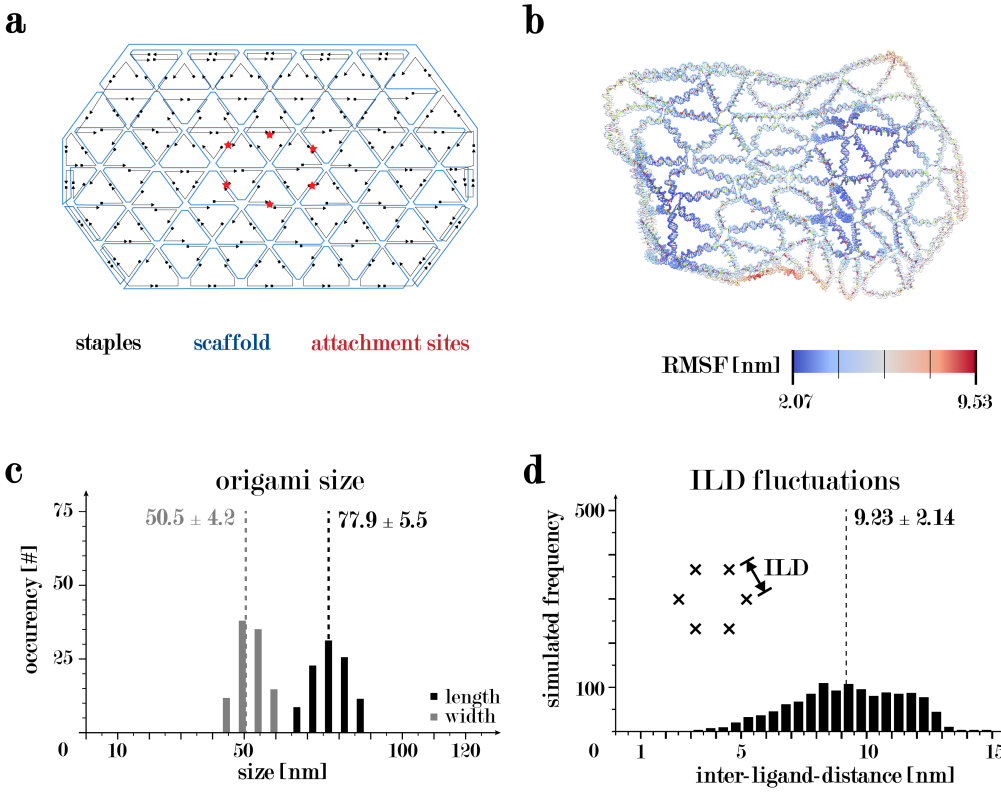

Figure B.23: Structure and *in silico* Analysis of the wf DNA Origami

(**a**) Scaffold and staple layout of the wf DNA origami. The scaffold strand is shown in blue, staples strands are shown in black, and the connection sites for FasL are indicated by red stars. (**b**) Averaged structure from oxDNA simulations with RMSF color-coded from blue to red. (**c**) Size distribution of the DNA origami extracted from TEM micrographs. Length is shown in black, and width is shown in grey, and average values are annotated at the respective dotted lines. (**d**) ILD distribution of the anchoring points for FasL on the DNA origami, average distance is annotated at the dotted line. Panels were partially adapted and reprinted with permission from [160], copyright 2025 John Wiley & Sons.

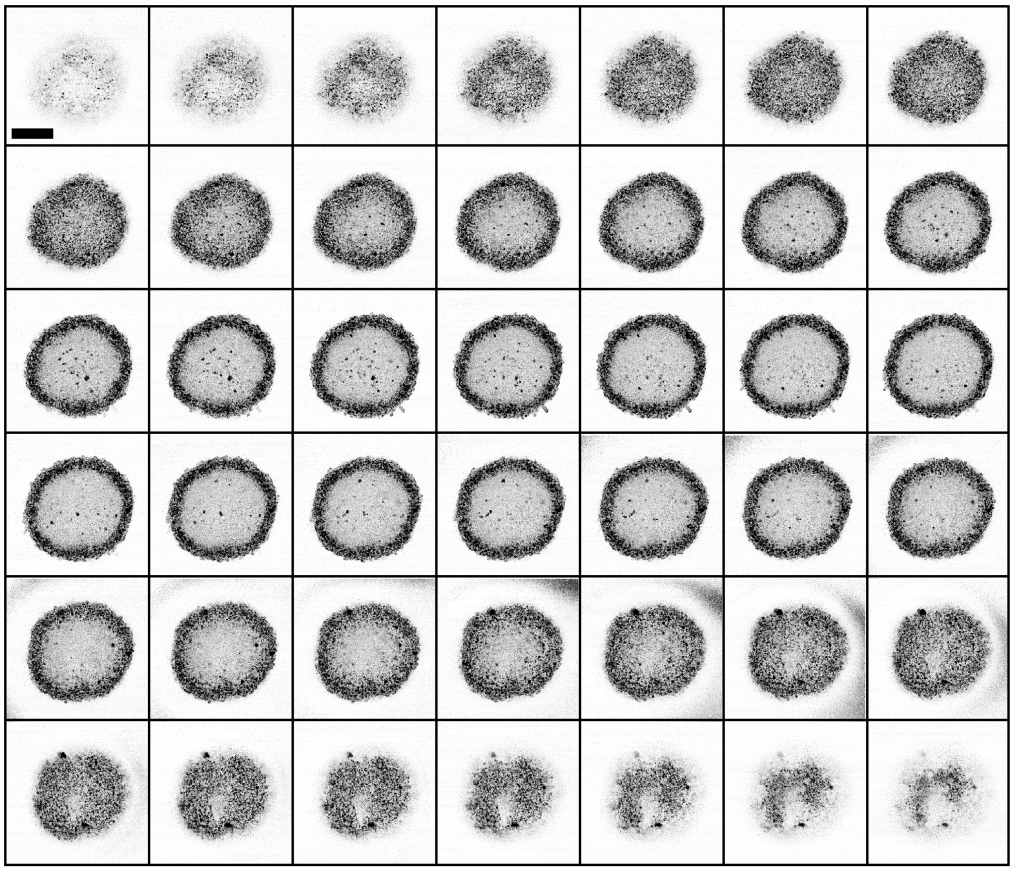

Figure B.24: Montage of Slices at Different Z Heights Through a Spheroid

An exemplary montage of z slices through the spheroid. The slices are equidistant from one another starting with the lowest point on the top left. Only the signal of FISH is shown. The scale bar is 200 μm and holds for all images, slice distance is approximately 4 μm.

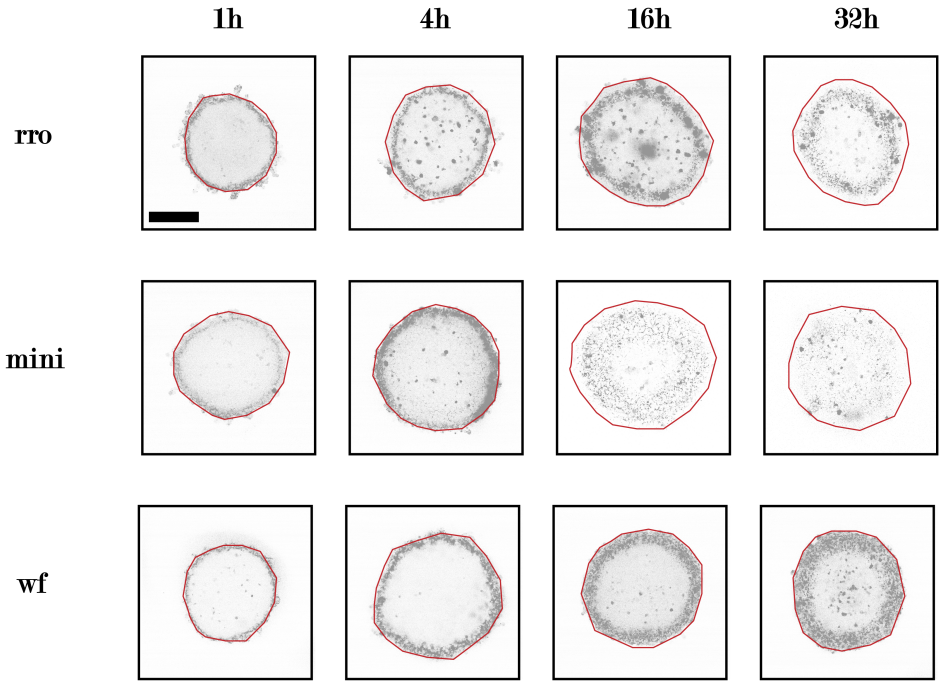

Figure B.25: Penetration of DNA Origami Through Spheroids

Exemplary images of the penetration patterns for different DNA origami structures at different penetration times. Only the signal of the FISH hairpins is shown. The actual size of the spheroids was extracted from the GFP channel and is lined out with a red line in the images. The scale bar is 200 μm and holds for all images. Panels were partially adapted and reprinted with permission from [160], copyright 2025 John Wiley & Sons.

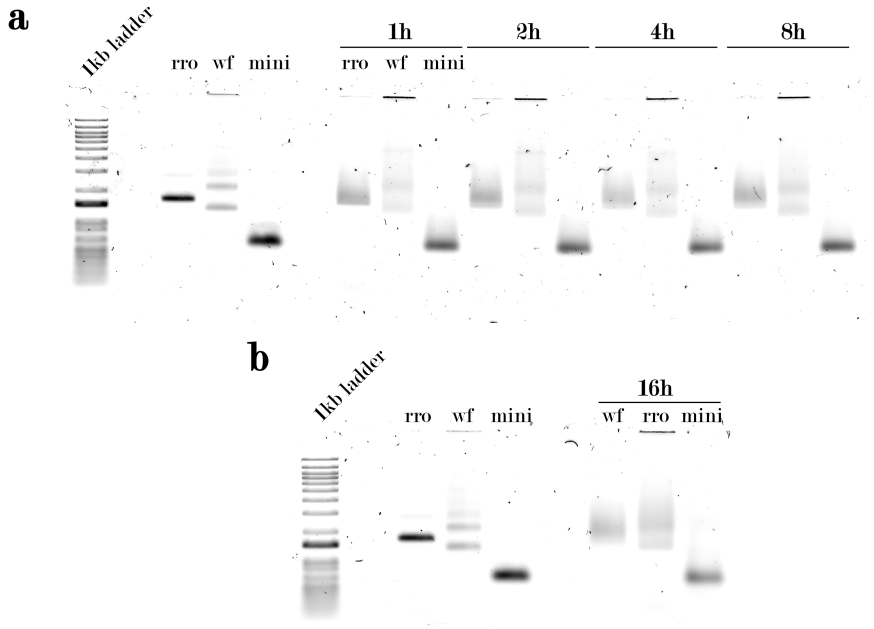

Figure B.26: DNA Origami Stability in Cell Medium

AGE analysis of the three DNA origami used for penetration and apoptosis studies. The DNA origami were incubated for different times in cell medium and 37 °C. In (**a**) the DNA origami were incubated 1, 2, 4, and 8 h, and in (**b**) for 16 h. Panels were partially adapted and reprinted with permission from [160], copyright 2025 John Wiley & Sons.

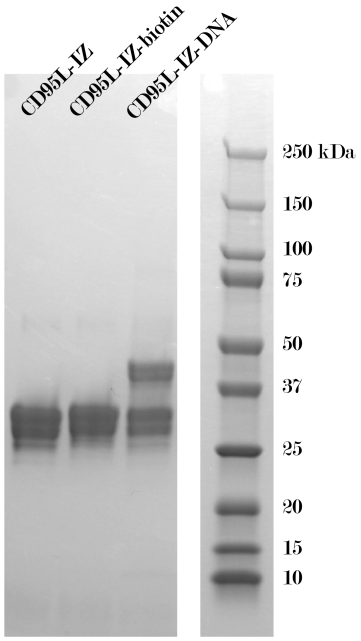

Figure B.27: PAGE Analysis of the Modified FasL

The denaturing PAGE gel shows the FasL monomer as a double band at approximately 30 kDa. The modification with biotin slightly shifts the bands to a higher position, indicating a larger molecular weight of the construct. The modification with DNA leads to two additional bands, slightly larger than 40 kDa, indicating successful labeling with the approximately 14 kDa sized DNA strand. Panels were partially adapted and reprinted with permission from [159], copyright 2025 Springer Nature Ltd.

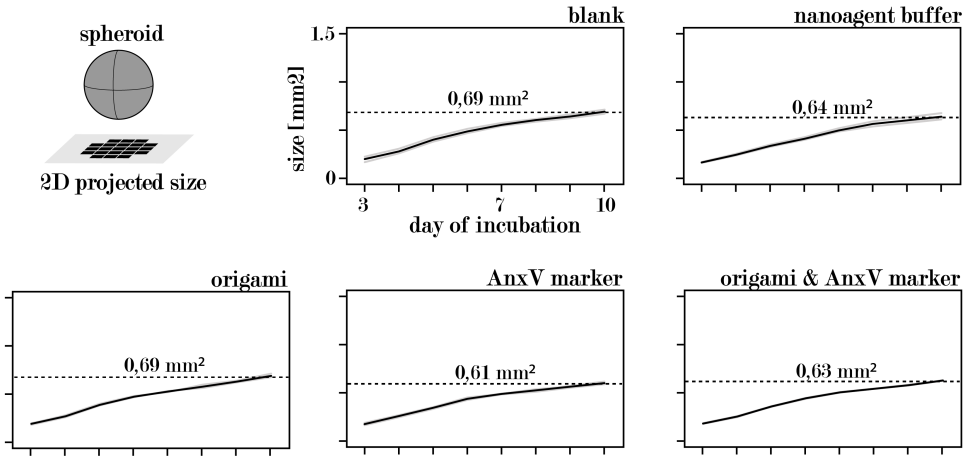

Figure B.28: Spheroid Control Experiments

Spheroid development in control experiments. The projected size of the spheroids is shown in the ordinate, over the incubation days on the abscissa. The behavior of spheroids with no further additions was not different from the behavior of spheroids with high amounts of origami buffer, origami, AnxV marker, or origami in combination with AnxV buffer. Panels were partially adapted and reprinted with permission from [160], copyright 2025 John Wiley & Sons.

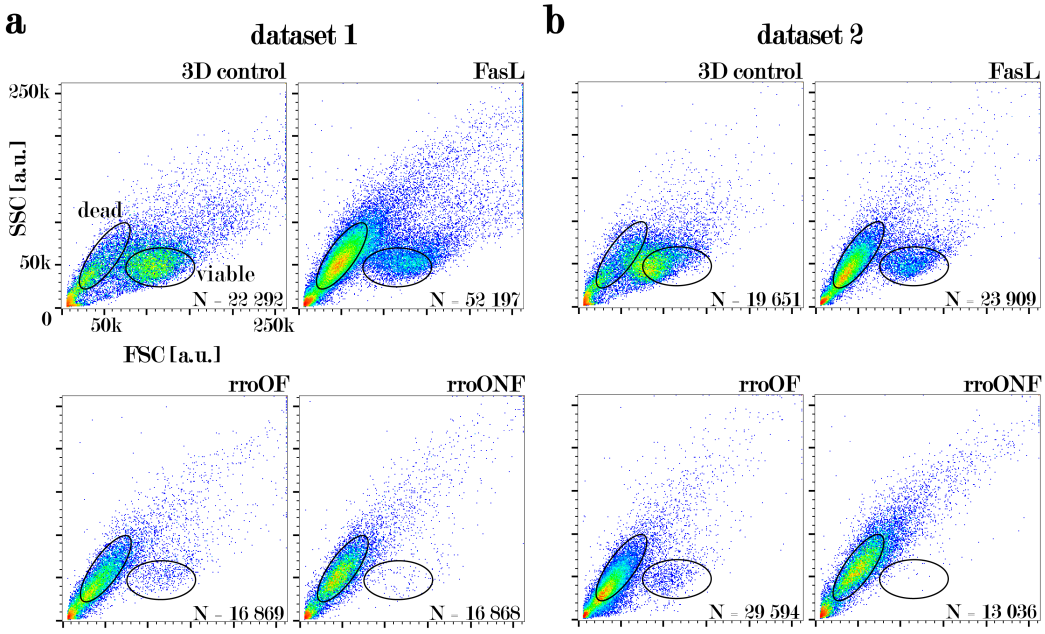

Figure B.29: FACS Data on Spheroid Fate

(**a**) and (**b**) show two different datasets on spheroid fate after incubation for 7 days with the respective nanoagent. The amount of FasL added was 300 fmol, and for the nanoagents 50 fmol. The gates for viable and dead cells are shown in each graph, as well as the respective amount of events counted. Panels were partially adapted and reprinted with permission from [160], copyright 2025 John Wiley & Sons.

Bibliography

[1] Carlos Mariscal. Stanford Encyclopedia of Philosophy, Life. `https://plato.stanford.edu/entries/life/#DefiLifeAntiDarw`. Accessed: 24th of September 2024.

[2] Bruce Alberts, Alexander Johnson, Julian Lewis, Martin Raff, Keith Roberts, Peter Walter . *Molecular Biology of the Cell, 4th edition.* Garland Science , 2002 .

[3] Daniel A.Fletcher, R. Dyche Mullins. Cell mechanics and the cytoskeleton . *Nature*, 463:485–492, 2010.

[4] Susan Standring, Neel Anand, Rolfe Birch, Patricia Collins, Alan R. Crossman, Michael Gleeson, Girish Jawaheer, Ariana L. Smith, Jonathan D. Spratt, Mark D. Stringer, R. Shane Tubbs, Richard Tunstall, Alan J. Wein, Caroline B. Wigley . *Gray's Anatomy - The Anatomical Basis of Clinical Practice.* Elsevier , 2015 .

[5] Francisco A. Bonilla, Hans C. Oettgen . Adaptive Immunity . *Journal of Allergy and Clinical Immunology* , 125 (2), S2:S33–S40, 2010.

[6] Bryan Briney, Anne Inderbitzin, Collin Joyce, Dennis R. Burton . Commonality despite exceptional diversity in the baseline human antibody repertoire . *Nature*, 566:393–397, 2019.

[7] Charles A. Janeway, Jr. and Ruslan Medzhitov . Innate Immune Recognition . *Annual Review of Immunology* , 20:197–216, 2002.

[8] Natalie K. Wolf, Djem U. Kissiov David H. Raulet . Roles of natural killer cells in immunity to cancer, and applications to immunotherapy . *Nature Reviews Immunology* , 23:90–105, 2022.

[9] Adam D. Kennedy, Frank R. DeLeo . Neutrophil apoptosis and the resolution of infection . *Immunologic Research* , 43 (1-3):25–61, 2009.

[10] Ed Palmer . Negative selection — clearing out the bad apples from the T-cell repertoire . *Nature Reviews Immnology* , 3:383–391, 2003.

[11] David Nemazee . Mechanisms of central tolerance for B cells . *Nature Reviews Immnology* , 17:281–294, 2017.

[12] Michael D Jacobson, Miguel Weil, Martin C Raff . Programmed Cell Death in Animal Development . *Cell* , 88 (3):347–354, 1997.

[13] Mark S. D'Arcy . Cell death: a review of the major forms of apoptosis, necrosis and autophagy . *Cell Biology International* , 43 (6):582–592, 2019.

[14] G. Häcker . The morphology of apoptosis . *Cell and Tissure Research* , 301 (1)):5–17, 2000.

[15] M.K. Collins, G.R. Perkins, G. Rodriguez-Tarduchy, M.A. Nieto, A. López-Rivas . Growth factors as survival factors: regulation of apoptosis . *Bioessays* , 16 (2):133–138, 1994.

[16] S.M. Frisch, H. Francis . Disruption of epithelial cell-matrix interactions induces apoptosis . *Journal of Cell Biology* , 124 (4):619–626, 1994.

[17] Kate McArthur, Lachlan W. Whitehead, John M. Heddleston, Lucy Li, Benjamin S. Padman, Viola Oorschot, Niall D. Geoghegan, Stephane Chappaz, Sophia Davidson, Hui San Chin, Rachael M. Lane, Marija Dramicanin, Tahnee L. Saunders, Canny Sugiana, Romina Lessene, Laura D. Osellame, Teng-Leong Chew, Grant Dewson, Michael Lazarou, Georg Ramm, Guillaume Lessene, Michael T. Ryan, Kelly L. Rogers, Mark F. van Delft, Benjamin T. Kile. BAK/BAX macropores facilitate mitochondrial herniation and mtDNA efflux during apoptosis . *Science*, 359 (6378):eaao6047, 2018.

[18] Honglin Li, Hong Zhu, Chi-jie Xu, Junying Yuan. Cleavage of BID by Caspase 8 Mediates the Mitochondrial Damage in the Fas Pathway of Apoptosis . *Cell*, 94 (4):491–501, 1998.

[19] Salvador E. Luria, Max Delbrück. Mutations of bacteria from virus sensitivity to virus resistance . *Genetics*, 28 (6):491–511, 1943.

[20] Oswald T. Avery, Colin M. MacLeod, Maclyn McCarty. Studies on the chemical nature of the substance inducing transformation of pneumococcal types. Induction of transformation by a desoxyribonucleic acid

fraction isolated from pneumococcus type III . *Journal of Experimental Medicine*, 79 (2):137–158, 1944.

[21] Alfred D. Hershey, Martha Chase. Independent functions of viral protein and nucleic acid in growth of bacteriophage. *The Journal of General Physiology*, 36 (1):39–56, 1952.

[22] Francis Crick James D. Watson. Molecular Structure of Nucleic Acids: A Structure for Deoxyribose Nucleic Acid . *Nature* , 171:737–738, 1953.

[23] Francis Crick. On Protein Synthesis . *Symposia of the Society for Experimental Biology* , 12:138–163, 1958.

[24] Denatured DNA as a Direct Template for in vitro Protein Synthesis . B.J. McCarthy, J.J. Holland . *PNAS*, 53 (4):880–886, 1965.

[25] David Baltimore, Hans J. Eggers, Richard M. Franklin, Igor Tamm . Poliovirus-Induced RNA Polymerase and the Effects of Virus-Specific Inhibitors on its Production . *PNAS*, 49 (6):843–849, 1963.

[26] H. M. Temin, S. Mizutami. RNA-dependent DNA polymerase in virions of Rous sarcoma virus. . *Nature*, 226:1211–1213, 1970.

[27] Bernard J. Poiesz, Francis W. Ruscetti, Adi F. Gazdar, Paul A. Bunn, John D. Minna, Robert C. Gallo. Detection and isolation of type C retrovirus particles from fresh and cultured lymphocytes of a patient with cutaneous T-cell lymphoma . *PNAS*, 77 (12):7415–7419, 1980.

[28] Xindan Wang, Paula Montero Llopis, David Z. Rudner . Organization and segregation of bacterial chromosomes . *Nature Reviews Genetics*, 14:191–203, 2013.

[29] Remus T. Dame, Fatema-Zahra M. Rashid, David C. Grainger . Chromosome organization in bacteria: mechanistic insights into genome structure and function . *Nature Reviews Genetics*, 21:227–242, 2019.

[30] Tomas Lindahl . Instability and decay of the primary structure of DNA . *Nature*, 362:709–715, 1993.

[31] Johan SantaLucia Jr. . A unified view of polymer, dumbbell, and oligonucleotide DNA nearest-neighbor thermodynamics . *PNAS*, 95 (4):1460–1465, 1998.

[32] John SantaLucia Jr., Donald Hicks . The Thermodynamics of DNA Structural Motifs . *Annu. Rev. Biophys. Biomol. Struct.*, 33:415–440, 2004.

[33] International Human Genome Sequenceing Consortium. Initial sequencing and analysis of the human genome . *Nature*, 409:860–921, 2001.

[34] Yunhao Wang et al. Nanopore sequencing technology, bioinformatics and applications . *Nature Biotechnology*, 39:1348–1365, 2024.

[35] Yaniv Erlich, Dina Zielinski. DNA Fountain enables a robust and efficient storage architecture . *Science*, 355 (6328):950–954, 2017.

[36] Jean-François Gout, W. Kelley Thomas, Zachary Smith, Kazufusa Okamoto, Michael Lynch . Large-scale detection of in vivo transcription errors . *PNAS*, 110 (46):18584–18589, 2013.

[37] Mansour Boutabout, Marcelle Wilhelm, François-Xavier Wilhelm . DNA synthesis fidelity by the reverse transcriptase of the yeast retrotransposon Ty1 . *Nucleic Acid Research*, 29 (11):2217–2222, 2001.

[38] Robert E. Johnson, M.Todd Washington, Satya Prakash, Louise Prakash . Fidelity of human DNA polymerase . *Journal of Biological Chemistry*, 275 (11):7447–7450, 2000.

[39] G.I. Lang, A.W. Murray . Estimating the Per-Base-Pair Mutation Rate in the Yeast Saccharomyces cerevisiae . *Genetics*, 178 (1):67–82, 2008.

[40] T.M. Albertson, B.D. Preston . DNA Replication Fidelity: Proofreading in Trans . *Current Biology*, 16 (6):209–211, 2006.

[41] Richard W. Hamming . Error detecting and error correcting codes . *Bell Syst. Techn. J.*, 29:147–160, 1950.

[42] P.R. Langer-Safer, M. Levine, D.C. Ward.

[43] Nadrian Seeman. Nucleic acid junctions and lattices . *Journal of Theoretical Biology*, 99 (2):237–247, 1982.

[44] Robin Holliday . A mechanism for gene conversion in fungi . *Genetics Research*, 5 (2):282–304, 1964.

[45] Kallenbach et al. Fourth Rank Immobile Nucleic Acid Junctions . *Journal of Biomolecular Structure and Dynamics*, 1 (1):159–168, 1983.

[46] Xing Wang, Nadrian C. Seeman. Assembly and characterization of 8-arm and 12-arm DNA branched junctions . *JACS*, 129 (26):8169–8176, 2007.

[47] Junghuei Chen, Nadrian C. Seeman. Synthesis from DNA of a molecule with the connectivity of a cube . *Nature*, 350 (6319):631–633, 1991.

[48] Chengde Mao, Weiqiong Sun, Nadrian C. Seeman . Assembly of Borromean rings from DNA . *Nature*, 386:137–138, 1997.

[49] Erik Winfree et al. Design and self-assembly of two-dimensional DNA crystals . *Nature*, 394:539–544, 1998.

[50] Nadrian C. Seeman . DNA in a Material World . *Nature*, 421:427–431, 2003.

[51] Bernard Yurke, Andrew J. Turberfield, Allen P. Mills Jr, Friedrich C. Simmel, Jennifer L. Neumann . A DNA-fuelled molecular machine made of DNA . *Nature*, 406:605–608, 2000.

[52] Robert M. Dirks, Niles A. Pierce .

[53] Shawn M. Douglas, Ido Bachelet, and George M. Church. A Logic-Gated Nanorobot for Targeted Transport of Molecular Payloads . *Science*, 335 (6070):831–834, 2012.

[54] William B. Sherman, Nadrian C. Seeman. A Precisely Controlled DNA Biped Walking Device . *Nano Letters*, 4 (7):1203–1207, 2004.

[55] Martin Jinek, Krzysztof Chylinski, Ines Fonfara, Michael Hauer, Jennifer A. Doudna , Emmanuelle Charpentier . A Programmable Dual-RNA–Guided DNA Endonuclease in Adaptive Bacterial Immunity . *Science*, 337 (6096):816–821, 2012.

[56] Niranjan Srinivas, Thomas E Ouldridge, Petr Sulc, Joseph M Schaeffer, Bernard Yurke, Ard A Louis, Jonathan P K Doye, Erik Winfree . On the biophysics and kinetics of toehold-mediated DNA strand displacement . *Nucleic Acids Research*, 41 (22):10641–10658, 2013.

[57] Paul Rothemund. Folding DNA to create nanoscale shapes and patterns . *Nature*, 440:297–302, 2006.

[58] William M. Shih, Joel D. Quispe, Gerald F. Joyce . A 1.7-kilobase single-stranded DNA that folds into a nanoscale octahedron . *Nature*, 427:618–621, 2004.

[59] Shawn M. Douglas, Hendrik Dietz, Tim Liedl, Björn Högberg, Franziska Graf, William M. Shih . Self-assembly of DNA into nanoscale three-dimensional shapes . *Nature*, 459:414–418, 2009.

[60] Hendrik Dietz, Shawn M Douglas, William M Shih . Folding DNA into twisted and curved nanoscale shapes . *Science*, 325 (5941):725–730, 2009.

[61] Erik Benson, Abdulmelik Mohammed, Johan Gardell, Sergej Masich, Eugen Czeizler, Pekka Orponen, Björn Högberg . DNA rendering of polyhedral meshes at the nanoscale . *Nature*, 523:441–444, 2015.

[62] Yonggang Ke, Shawn M. Douglas, Minghui Liu, Jaswinder Sharma, Anchi Cheng, Albert Leung, Yan Liu, William M. Shih, Hao Yan . Multilayer DNA Origami Packed on a Square Lattice . *JACS*, 131 (43):15903–15908, 2009.

[63] Yonggang Ke, Niels V. Voigt, Kurt V. Gothelf, William M. Shih. Multilayer DNA Origami Packed on Hexagonal and Hybrid Lattices . *JACS*, 134 (3):1770–1774, 2012.

[64] Shawn M. Douglas, Adam H. Marblestone, Surat Teerapittayanon, Alejandro Vazquez, George M. Church, William M. Shih . Rapid prototyping of 3D DNA-origami shapes with caDNAno . *Nucleic Acids Research*, 13 (1):5001–5006, 2009.

[65] Yonggang Ke, Gaëtan Bellot, Niels V. Voigt, Elena Fradkovabc, William M. Shih . Two design strategies for enhancement of multilayer–DNA-origami folding: underwinding for specific intercalator rescue and staple-break positioning . *Chemical Science*, 8:2587–2597, 2012.

[66] Michael Matthies, Nayan P. Agarwal, Erik Poppleton, Foram M. Joshi, Petr Šulc, Thorsten L. Schmidt .

[67] Johann Moritz Weck . Messenger RNA Secondary Structure Determination on Molecular Level. Master's thesis, LMU Munich , 2020.

[68] J. S. Bois B. R. Wolfe M. B. Pierce A. R. Khan R. M. Dirks N. A. Pierce J. N. Zadeh, C. D. Steenberg.

[69] Mark E. Fornace ,Jining Huang ,Cody T. Newman ,Nicholas J. Porubsky ,Marshall B. Pierce ,Niles A. Pierce. NUPACK: Analysis and Design of Nucleic Acid Structures, Devices, and Systems. uploaded: November 11 2022 to ChemRxiv, DOI: https://doi.org/10.26434/chemrxiv-2022-xv98l .

[70] James C. Phillips, David J. Hardy, Julio D. C. Maia, John E. Stone, João V. Ribeiro, Rafael C. Bernardi, Ronak Buch, Giacomo Fiorin, Jérôme Hénin, Wei Jiang, Ryan McGreevy, Marcelo C. R. Melo, Brian K. Radak, Robert D. Skeel, Abhishek Singharoy, Yi Wang, Benoît Roux, Aleksei Aksimentiev, Zaida Luthey-Schulten, Laxmikant V. Kalé Klaus Schulte , Christophe Chipot, Emad Tajkhorshid . Scalable molecular dynamics on CPU and GPU architectures with NAMD . *Journal of Computational Chemistry*, 153:044130, 2020.

[71] Christopher Maffeo, Aleksei Aksimentiev . MrDNA: a multi-resolution model for predicting the structure and dynamics of DNA systems . *Nucleic Acids Research*, 48 (9):5135–5146s, 2020.

[72] Petr Šulc, Flavio Romano, Thomas E. Ouldridge, Lorenzo Rovigatti, Jonathan P. K. Doye, Ard A. Louis . Sequence-dependent thermodynamics of a coarse-grained DNA model. *Journal of Chemical Physics*, 137 : 135101 , 2012.

[73] Erik Poppleton, Roger Romero, Aatmik Mallya, Lorenzo Rovigatti, Petr Šulc . OxDNA.org: a public webserver for coarse-grained simulations of DNA and RNA nanostructures . *Nucleic Acids Research* , 49 (W1) : W491–W498 , 2021.

[74] DN Kim, F Kilchherr, H Dietz, M Bathe. Quantitative prediction of 3D solution shape and flexibility of nucleic acid nanostructures. *Nucleic Acids Research*, 40 (7): 2862–2868 , 2012.

[75] Jae Young Lee, Jae Gyung Lee, Giseok Yun, Chanseok Lee, Young-Joo Kim, Kyung Soo Kim, Tae Hwi Kim, Do-Nyun Kim. Rapid Computational Analysis of DNA Origami Assemblies at Near-Atomic Resolution. *ACS Nano*, 15 (1): 1002–1015 , 2021.

[76] Chien Truong-Quoc, Jae Young Lee, Kyung Soo Kim, Do-Nyun Kim . Prediction of DNA origami shape using graph neural network. *Nature Materials* , 23 : 984–992 , 2024.

[77] Sung Yong Park, Abigail K. R. Lytton-Jean, Byeongdu Lee, Steven Weigand, George C. Schatz, Chad A. Mirkin . DNA-programmable nanoparticle crystallization . *Nature*, 451:553–556, 2008.

[78] Dmytro Nykypanchuk, Mathew M. Maye, Daniel van der Lelie Oleg Gang . DNA-guided crystallization of colloidal nanoparticles . *Nature*, 451:549–552, 2008.

[79] Anton Kuzyk, Robert Schreiber, Zhiyuan Fan, Günther Pardatscher, Eva-Maria Roller, Alexander Högele, Friedrich C. Simmel, Alexander O. Govorov, Tim Liedl. DNA-based self-assembly of chiral plasmonic nanostructures with tailored optical response. *Nature*, 483:311–314, 2012.

[80] G. P. Acuna , F. M. Möller, P. Holzmeister, S. Beater, B. Lalkens, and P. Tinnefeld. Fluorescence Enhancement at Docking Sites of DNA-Directed Self-Assembled Nanoantennas. *Science*, 338 (6106):506–510, 2012.

[81] Ralf Jungmann, Christian Steinhauer, Max Scheible, Anton Kuzyk, Philip Tinnefeld, Friedrich C. Simmel. Single-Molecule Kinetics and Super-Resolution Microscopy by Fluorescence Imaging of Transient Binding on DNA Origami. *Nano Letters*, 10 (11):4756–4761, 2010.

[82] Wendy Xueyi Wang, Travis R. Douglas, Haiwang Zhang, Afrin Bhattacharya, Meghan Rothenbroker, Wentian Tang, Yu Sun, Zhengping Jia, Julien Muffat, Yun Li, Leo Y. T. Chou . Universal, label-free, single-molecule visualization of DNA origami nanodevices across biological samples using origamiFISH . *Nature Nanotechnology*, 19:58–69, 2023.

[83] Lulu Qian, Erik Winfree, Jehoshua Bruck . Neural network computation with DNA strand displacement cascades . *Nature*, 475:368–372, 2011.

[84] Elisa Franco, Eike Friedrichs, Jongmin Kim, Ralf Jungmann, Richard Murray, Erik Winfree, Friedrich C. Simmel . Timing molecular motion and production with a synthetic transcriptional clock . *PNAS*, 108 (40):784–793, 2011.

[85] Alexander A. Green, Pamela A. Silver, James J. Collins, Peng Yin . Toehold Switches: De-Novo-Designed Regulators of Gene Expression . *Cell*, 159 (4):925–939, 2014.

[86] Joerg Schnitzbauer, Maximilian T Strauss, Thomas Schlichthaerle, Florian Schueder, Ralf Jungmann. Super-resolution microscopy with DNA-PAINT. *Nature Protocols*, 12:1198–1228, 2017.

[87] Philipp C. Nickels, Bettina Wünsch, Phil Holzmeister, Wooli Bae, Luisa M. Kneer, Dina Grohmann, Philip Tinnefeld , Tim Liedl. Molecular force spectroscopy with a DNA origami–based nanoscopic force clamp. *Science*, 354 (6310):305–307, 2016.

[88] Martin Langecker, Vera Arnaut, Thomas G. Martin, Jonathan List, Stephan Renner, Michael Mayer, Hendrik Dietz , Friedrich C. Simmel . Synthetic Lipid Membrane Channels Formed by Designed DNA Nanostructures . *Science*, 338 (6109):932–936, 2012.

[89] Ofer I. Wilner, Yossi Weizmann, Ron Gill, Oleg Lioubashevski, Ronit Freeman, Itamar Willner . Enzyme cascades activated on topologically programmed DNA scaffolds . *Nature Nanotechnology*, 19:1521–1531, 2024.

[90] Rémi Veneziano, Tyson J. Moyer, Matthew B. Stone, Eike-Christian Wamhoff, Benjamin J. Read, Sayak Mukherjee, Tyson R. Shepherd, Jayajit Das, William R. Schief, Darrell J. Irvine, Mark Bathe . Role of nanoscale antigen organization on B-cell activation probed using DNA origami . *Nature Nanotechnology*, 15:716–723, 2020.

[91] Jonas J. Funke, Philip Ketterer, Corinna Lieleg, Sarah Schunter, Philipp Korber, Hendrik Dietz. Uncovering the forces between nucleosomes using DNA origami . *Science Advances*, 2 (11):e1600974, 2016.

[92] D. Maurel J. Elezgaray F. Morvan J. J. Vasseur E. Margeat R. B. Quast J. Lai Kee-Him N. Saint C. Benistant A. Nord F. Pedaci G. Bellot A. Mills, N. Aissaoui. A modular spring-loaded actuator for mechanical activation of membrane proteins. *Nature Communications*, 13:3182, 2022.

[93] Minhwan Chung, Kun Zhou, John T. Powell, Chenxiang Lin, Martin A. Schwartz. DNA-Based Molecular Clamp for Probing Protein Interactions and Structure under Force. *ACS Nano*, 18 (40):27590–27596, 2024.

[94] Anton Kuzyk, Yangyang Yang, Xiaoyang Duan, Simon Stoll, Alexander O. Govorov, Hiroshi Sugiyama, Masayuki Endo, Na Liu . A light-

driven three-dimensional plasmonic nanosystem that translates molecular motion into reversible chiroptical function. *Nature Communications*, 7:10591, 2016.

[95] Deepak Karna, Morgan Stilgenbauer, Sagun Jonchhe, Kazuya Ankai, Ibuki Kawamata, Yunxi Cui, Yao-Rong Zheng, Yuki Suzuki, Hanbin Mao . Chemo-Mechanical Modulation of Cell Motions Using DNA Nanosprings . *Bioconjugate Chemistry*, 32 (2):311–317, 2021.

[96] Thomas Gerling, Klaus F. Wagenbauer, Andrea M. Neuner, and Hendrik Dietz . Dynamic DNA devices and assemblies formed by shape-complementary, non–base pairing 3D components . *Science*, 347 (6229):1446–1452, 2015.

[97] Seham Helmi, Christoph Ziegler, Dominik J. Kauert, and Ralf Seidel . Shape-Controlled Synthesis of Gold Nanostructures Using DNA Origami Molds . *Nano Letters*, 14:6693–6698, 2014.

[98] Wei Sun, Etienne Boulais, Yera Hakobyan, Wei Li Wang, Amy Guan, Mark Bathe, Peng Yin . Casting inorganic structures with DNA molds . *Science*, 346 (6210):717–725, 2014.

[99] Jakob Bach Knudsen, Lei Liu, Anne Louise Bank Kodal, Mikael Madsen, Qiang Li, Jie Song, Johannes B. Woehrstein, Shelley F. J. Wickham, Maximilian T. Strauss, Florian Schueder, Jesper Vinther, Abhichart Krissanaprasit, Daniel Gudnason, Anton Allen Abbotsford Smith, Ryosuke Ogaki, Alexander N. Zelikin, Flemming Besenbacher, Victoria Birkedal, Peng Yin, William M. Shih, Ralf Jungmann, Mingdong Dong, Kurt V. Gothelf . Routing of individual polymers in designed patterns . *Nature Nanotechnology*, 10:892–898, 2015.

[100] Yang Yang, Jing Wang, Hideki Shigematsu, Weiming Xu, William M. Shih, James E. Rothman, Chenxiang Lin . Self-assembly of size-controlled liposomes on DNA nanotemplates . *Nature Chemistry*, 8:476–483, 2016.

[101] Iris Seitz, Sharon Saarinen, Esa-Pekka Kumpula, Donna McNeale, Eduardo Anaya-Plaza, Vili Lampinen, Vesa P. Hytönen, Frank Sainsbury, Jeroen J. L. M. Cornelissen, Veikko Linko, Juha T. Huiskonen, Mauri A. Kostiainen . DNA-origami-directed virus capsid polymorphism . *Nature Nanotechnology*, 18:1205–1212, 2023.

[102] Thomas G. W. Edwardson, Kai Lin Lau, Danny Bousmail, Christopher J. Serpell, Hanadi F. Sleiman . Transfer of molecular recognition

information from DNA nanostructures to gold nanoparticles . *Nature Chemistry*, 8:162–170, 2016.

[103] Henri G. Franquelim, Alena Khmelinskaia, Jean-Philippe Sobczak, Hendrik Dietz, Petra Schwille . Membrane sculpting by curved DNA origami scaffolds . *Nature Communications*, 9:811, 2018.

[104] Yuki Suzuki, Masayuki Endo, Hiroshi Sugiyama . Lipid-bilayer-assisted two-dimensional self-assembly of DNA origami nanostructures . *Nature Communications*, 6:8052, 2015.

[105] Beatrice Ramm, Andriy Goychuk, Alena Khmelinskaia, Philipp Blumhardt, Hiromune Eto, Kristina A. Ganzinger, Erwin Frey, Petra Schwille . A diffusiophoretic mechanism for ATP-driven transport without motor proteins . *Nature Physics*, 17:850–858, 2021.

[106] George M. Church, Yuan Gao, Sriram Kosuri. Next-Generation Digital InformationStorage in DNA . *Science*, 337 (6102):1628, 2012.

[107] Cheng Zhang, Ranfeng Wu, Fajia Sun, Yisheng Lin, Yuan Liang, Jiongjiong Teng, Na Liu, Qi Ouyang, Long Qian, Hao Yan . Parallel molecular data storage by printing epigenetic bits on DNA . *Nature*, 634:824–832, 2024.

[108] J. Huang, A. Jaekel, J. van den Boom, D. Podlesainski, M. Elnaggar, A. Heuer-Jungemann, M. Kaiser, H. Meyer, B. Saccà . A modular DNA origami nanocompartment for engineering a cell-free, protein unfolding and degradation pathway . *Nature Nanotechnology*, 34:249–254, 2009.

[109] N. D. Derr, B. S. Goodman, R. Jungmann, A. E. Leschziner, W. M. Shih, S. L. Reck-Peterson . Tug-of-War in Motor Protein Ensembles Revealed with a Programmable DNA Origami Scaffold . *Science*, 338 (6107):662–665, 2012.

[110] Alan Shaw, Vanessa Lundin, Ekaterina Petrova, Ferenc Fördős, Erik Benson, Abdullah Al-Amin, Anna Herland, Andries Blokzijl, Björn Högberg Ana I Teixeira . Spatial Control of Membrane Receptor Function Using Ligand Nanocalipers . *Nature Methods*, 11:841–846, 2014.

[111] Alan Shaw, Ian T. Hoffecker, Ioanna Smyrlaki, Joao Rosa, Algirdas Grevys, Diane Bratlie, Inger Sandlie, Terje Einar Michaelsen, Jan Terje

Andersen, Björn Högberg . Binding to nanopatterned antigens is dominated by the spatial tolerance of antibodies . *Nature Nanotechnology*, 14:184–190, 2019.

[112] Eike-Christian Wamhoff, Larance Ronsard, Jared Feldman, Grant A. Knappe, Blake M. Hauser, Anna Romanov, James Brett Case, Shilpa Sanapala, Evan C. Lam, Kerri J. St. Denis, Julie Boucau, Amy K. Barczak, Alejandro B. Balazs, Michael S. Diamond, Aaron G. Schmidt, Daniel Lingwood, Mark Bathe . Enhancing antibody responses by multivalent antigen display on thymus-independent DNA origami scaffolds . *Nature Communications*, 15:795, 2024.

[113] Joschka Hellmeier, Rene Platzer, Alexandra Eklund, Thomas Schlichthaerle, Gerhard J Schuetz, Ralf Jungmann, Johannes B Huppa, Eva Sevcsik . DNA origami demonstrate the unique stimulatory power of single pMHCs as T-cell antigens . *Biophysical Journal*, 120 (3) 1:330A, 2021.

[114] JM Weck, A Heuer-Jungemann. Fully addressable designer superstructures assembled from one single modular DNA origami. *Nature Communications*, 16:1556, 2025.

[115] Leibniz Institute, DSMZ, Escherichia Phage M13 (Inovirus M13). `https://www.dsmz.de/collection/catalogue/details/culture/DSM-13976`. accessed September 25, 2024.

[116] Bryan Wei, Mingjie Dai, Peng Yin . Complex shapes self-assembled from single-stranded DNA tiles . *Nature*, 485:623–626, 2014.

[117] Yonggang Ke, Luvena L. Ong, William M. Shih, Peng Yin . Three-Dimensional Structures Self-Assembled from DNA Bricks . *Science*, 338 (6111):1177–1183, 2012.

[118] Luvena L. Ong, Nikita Hanikel, Omar K. Yaghi, Casey Grun, Maximilian T. Strauss, Patrick Bron, Josephine Lai-Kee-Him, Florian Schueder, Bei Wang, Pengfei Wang, Jocelyn Y. Kishi, Cameron Myhrvold, Allen Zhu, Ralf Jungmann, Gaetan Bellot, Yonggang Ke, Peng Yin . Programmable self-assembly of three-dimensional nanostructures from 10,000 unique components . *Nature*, 552:72–77, 2017.

[119] Randall K. Saiki, Stephen Scharf, Fred Faloona, Kary B. Mullis, Glenn T. Horn, Henry A. Erlich, and Norman Arnheim . Enzymatic Amplification of -Globin Genomic Sequences and Restriction Site Analysis for Diagnosis of Sickle Cell Anemia . *Science*, 230 (4732):1350–1354, 1985.

[120] Russell Higuchi, Barbara Krummell, Randall K. Saiki . A general method of in vitro preparation and specific mutagenesis of DNA fragments: study of protein and DNA interactions . *Nucleic Acid Research*, 16 (15):7351–7367, 1988.

[121] Steffan N. Ho, Henry D. Hunt, Robert M. Horton, Jeffrey K. Pullen, Larry R. Pease . Site-directed mutagenesis by overlap extension using the polymerase chain reaction . *Gene*, 77 (1):51–59, 1989.

[122] Elisabeth Pound, Jeffrey R. Ashton, Héctor A. Becerril, Adam T. Woolley . Polymerase Chain Reaction Based Scaffold Preparation for the Production of Thin, Branched DNA Origami Nanostructures of Arbitrary Sizes . *Nano Letters*, 9 (12):4302–4305, 2009.

[123] Honglu Zhang , Jie Chao, Dun Pan , Huajie Liu , Qing Huang, Chunhai Fan . Folding super-sized DNA origami with scaffold strands from long-range PCR . *Chemical Communications*, 48:6405–6407, 2012.

[124] L Dente, G Cesareni, R Cortese . pEMBL: a new family of single stranded plasmids . *Nucleic Acids Research*, 11 (6):1645–1655, 1983.

[125] J. Messing . New M13 vectors for cloning . *Methods Enzymology*, 1983.

[126] Parsa M Nafisi, Tural Aksel, Shawn M Douglas . Construction of a novel phagemid to produce custom DNA origami scaffolds . *Synthetic Biology*, 3 (1):ysy015, 2018.

[127] Xiaoxing Chen, Qian Wang, Jin Peng, Qipeng Long, Hanyang Yu, Zhe Li . Self-Assembly of Large DNA Origami with Custom-Designed Scaffolds . *ACS Applied Materials Interfaces*, 10 (29):24344–24348, 2018.

[128] Floris A. S. Engelhardt, Florian Praetorius, Christian H. Wachauf, Gereon Brüggenthies, Fabian Kohler, Benjamin Kick, Karoline L. Kadletz, Phuong Nhi Pham, Karl L. Behler, Thomas Gerling, Hendrik Dietz . Custom-Size, Functional, and Durable DNA Origami with Design-Specific Scaffolds . *ACS Nano*, 13 (5):5015–5027, 2019.

[129] Konlin Shen, Jake J Flood, Zhihuizi Zhang, Alvin Ha, Brian R Shy, John E Dueber, Shawn M Douglas . Engineering an Escherichia coli strain for production of long single-stranded DNA . *Nucleic Acid Research*, 52 (7):4098–4107, 2024.

[130] Alexandria N. Marchi, Ishtiaq Saaem, Briana N. Vogen, Stanley Brown, Thomas H. LaBean . Toward Larger DNA Origami . *Nano Letters*, 14 (10):5740–5747, 2014.

[131] F.A.S. Engelhardt . *De novo Scaffold Strand Sequences to Expand the Construction Space of DNA Origami*. PhD thesis, TUM, 2019.

[132] Thomas Tigges, Thomas Heuser, Rahul Tiwari, Andreas Walther . 3D DNA Origami Cuboids as Monodisperse Patchy Nanoparticles for Switchable Hierarchical Self-Assembly . *Nano Letters*, 16 (12):7870–7874, 2016.

[133] Paul W. K. Rothemund, Axel Ekani-Nkodo, Nick Papadakis, Ashish Kumar, Deborah Kuchnir Fygenson, Erik Winfree . Design and Characterization of Programmable DNA Nanotubes . *JACS*, 126 (50):16344–16352, 2004.

[134] Yi Chen Tong Wang Ruojie Sha Pamela E. Constantinou Stephan L. Ginell Chengde Mao Nadrian C. Seeman Jianping Zheng, Jens J. Birktoft. From molecular to macroscopic via the rational design of a self-assembled 3D DNA crystal. *Nature*, 461:74–77, 2009.

[135] Ralf Jungmann, Max Scheible, Anton Kuzyk, G unther Pardatscher, Carlos E Castro, Friedrich C Simmel . DNA origami-based nanoribbons: assembly,length distribution, and twist . *Nanotechnology*, 22:275301, 2011.

[136] Yihao Zhou, Jinyi Dong, Chao Zhou, Qiangbin Wang . Finite Assembly of Three-Dimensional DNA Hierarchical Nanoarchitectures through Orthogonal and Directional Bonding . *Angewandte Chemie Int. Ed.*, 61 (13):e202116416, 2022.

[137] Zhao Zhao, Yan Liu, Hao Yan . Organizing DNA Origami Tiles into Larger Structures Using Preformed Scaffold Frames . *Nano Letters*, 11:2997–3002, 2011.

[138] Lifeng Zhou, Alexander E. Marras, Chao-Min Huang, Carlos E. Castro, and Hai-Jun Su . Paper Origami-Inspired Design and Actuation of DNA Nanomachines with Complex Motions . *Small*, 14:1802580, 2018.

[139] Shelley F. J. Wickham, Alexander Auer, Jianghong Min, Nandhini Ponnuswamy, Johannes B. Woehrstein, Florian Schueder, Maximilian T. Strauss, Jörg Schnitzbauer, Bhavik Nathwani, Zhao Zhao, Steven D. Perrault, Jaeseung Hahn, Seungwoo Lee, Maartje M. Bastings, Sarah

W. Helmig, Anne Louise Kodal, Peng Yin, Ralf Jungmann, William M. Shih . Complex multicomponent patterns rendered on a 3D DNA-barrel pegboard . *Nature Communications*, 11:5768, 2020.

[140] Myoungseok Kim, Chanseok Lee, Kyounghwa Jeon, Jae Young Lee, Young-Joo Kim, Jae Gyung Lee, Hyunsu Kim, Maenghyo Cho, Do-Nyun Kim . Harnessing a paper-folding mechanism for reconfigurable DNA origami . *Nature*, 619:78–86, 2023.

[141] Minh Tri Luu, Jonathan F. Berengut, Jiahe Li, Jing-Bing Chen, Jasleen Kaur Daljit Singh, Kanako Coffi Dit Glieze, Matthew Turner, Karuna Skipper, Sreelakshmi Meppat, Hannah Fowler, William Close Jonathan P. K. Doye, Ali Abbas, and Shelley F. J. Wickham . Reconfigurable nanomaterials folded from multicomponent chains of DNA origami voxels . *Science Robotics*, 9:eadp2309, 2024.

[142] Marlene Scheffold Mai P. Tran Ulrike Mersdorf Kerstin Göpfrich Kevin Jahnke, Maja Illig. DNA Origami Signaling Units Transduce Chemical and Mechanical Signals in Synthetic Cells. *Advanced Functional Materials*, 34 (20):2301176, 2023.

[143] Ivan Grishchuk Barbara Saccà Lena J. Stenke, Melanie Weiß. Coupling DNA Origami Filament Growth to an Autocatalytic Production of Fuel. *Advanced Materials Interfaces*, page 2400674, 2024.

[144] Juan Jin, Emily G. Baker, Christopher W. Wood, Jonathan Bath, Derek N. Woolfson, Andrew J. Turberfield . Peptide Assembly Directed and Quantified Using Megadalton DNA Nanostructures . *ACS Nano*, 13 (9):9927–9935, 2019.

[145] Alex Buchberger, Chad R. Simmons, Nour Eddine Fahmi, Ronit Freeman, Nicholas Stephanopoulos . Hierarchical Assembly of Nucleic Acid/Coiled-Coil Peptide Nanostructures . *JACS*, 142 (§):1406–1416, 2020.

[146] Willi R. Berg, Dr. Jonathan F. Berengut, Changzhuang Bai, Dr. Laura Wimberger, Prof. Lawrence K. Lee, Dr. Felix J. Rizzuto . Light-Activated Assembly of DNA Origami into Dissipative Fibrils . *Angewandte Chemie, Int. Ed.*, 62 (51):e202314458, 2023.

[147] Arivazhagan Rajendran, Masayuki Endo, Yousuke Katsuda, Kumi Hidaka, Hiroshi Sugiyama . Programmed Two-Dimensional Self-Assembly of Multiple DNA Origami Jigsaw Pieces . *ACS Nano*, 5 (1):665–671, 2012.

[148] Klaus F. Wagenbauer, Christian Sigl, Hendrik Dietz . Gigadalton-scale shape-programmable DNA assemblies . *Nature*, 552:78–83, 2017.

[149] Christian Sigl, Elena M. Willner, Wouter Engelen, Jessica A. Kretzmann, Ken Sachenbacher, Anna Liedl, Fenna Kolbe, Florian Wilsch, S. Ali Aghvami, Ulrike Protzer, Michael F. Hagan, Seth Fraden, Hendrik Dietz . Programmable icosahedral shell system for virus trapping . *Nature Materials*, 20:1281–1289, 2021.

[150] Jingjing Ye, Olha Aftenieva, Türkan Bayrak, Archa Jain, Tobias A. F. König, Artur Erbe, Ralf Seidel . Complex Metal Nanostructures with Programmable Shapes from Simple DNA Building Blocks . *Advanced Materials*, 33 (29):2100381, 2021.

[151] Yang C. Zeng, Olivia J. Young, Christopher M. Wintersinger, Frances M. Anastassacos, James I. MacDonald, Giorgia Isinelli, Maxence O. Dellacherie, Miguel Sobral, Haiqing Bai, Amanda R. Graveline, Andyna Vernet, Melinda Sanchez, Kathleen Mulligan, Youngjin Choi, Thomas C. Ferrante, Derin B. Keskin, Geoffrey G. Fell, Donna Neuberg, Catherine J. Wu, David J. Mooney, Ick Chan Kwon, Ju Hee Ryu, William M. Shih . Fine tuning of CpG spatial distribution with DNA origami for improved cancer vaccination . *Nature Nanotechnology*, 19:1055–1065, 2024.

[152] Zeyu Song, Yihao Zhou, Jinyi Dong, Qiangbin Wang . DNA Origami Guided Helical Assembly of Gold Nanorods with Tailored Optical Chirality . *Applied Optical Materials*, 2024.

[153] Stefan Fischer, Caroline Hartl, Kilian Frank, Joachim O. Rädler, Tim Liedl, Bert Nickel . Shape and Interhelical Spacing of DNA Origami Nanostructures Studied by Small-Angle X-ray Scattering . *Nano Letters*, 16 (7):4282–4287, 2016.

[154] D.Y. Zhang, E. Winfree . Control of DNA Strand Displacement Kinetics Using Toehold Exchange . *JACS*, 131 (47):17303–17314, 2009.

[155] Friedrich C. Simmel, Bernard Yurke, Hari R. Singh . Principles and Applications of Nucleic Acid Strand Displacement Reactions . *Chemical Reviews*, 119 (10):6326–6369, 2019.

[156] C. Rivetti, M. Guthold, C. Bustamante . Scanning force microscopy of DNA deposited onto mica: equilibration versus kinetic trapping studied by statistical polymer chain analysis . *Journal of Molecular Biology*, 264:919–932, 1996.

[157] Christopher M. Wintersinger, Dionis Minev, Anastasia Ershova, Hiroshi M. Sasaki, Gokul Gowri, Jonathan F. Berengut, F. Eduardo Corea-Dilbert, Peng Yin, William M. Shih . Multi-micron crisscross structures grown from DNA-origami slats . *Nature Nanotechnology*, 18 (420):https://doi.org/10.1038/s41565–022–01283–1, 2023.

[158] Ricarda M. L. Berger, Johann M. Weck, Simon M. Kempe, Oliver Hill, Tim Liedl, Joachim O. Rädler, Cornelia Monzel, Amelie Heuer-Jungemann. Nanoscale FasL Organization on DNA Origami to Decipher Apoptosis Signal Activation in Cells. *Small*, 17, 2101678, 2021.

[159] Xiaoyue Shang, Nina Bartels, Johann Moritz Weck, Sabine Suppmann, Jérôme Basquin, Gajen Thaventhiran, Amelie Heuer-Jungemann Cornelia Monzel. High yield purification of an isoleucine zipper-modified CD95 ligand for efficient cell apoptosis initiation and with biotin or DNA-oligomer binding domain to probe ligand functionalization effects. *BMC Biotechnology*, 25:64, 2025.

[160] Johann M. Weck, Riya Nair, Merve-Z. Kesici, Xiaoyue Shang, Svetozar Gavrilović, Cornelia Monzel, Amelie Heuer-Jungemann. Effects of DNA Origami-Based Nanoagent Design on Apoptosis Induction in a Large 3D Cancer Spheroid Model. *Small*, 21 (24):2502490, 2025.

[161] G. Berke . The CTL's Kiss of Death . *Cell*, 81 (1):9–12, 1995.

[162] Ashutosh Tripathi, Vytas A Bankaitis . Molecular Docking: From Lock and Key to Combination Lock . *J. Mol. Med. Clin. Appl.*, 2 (1):doi: https://doi.org/10.16966/2575–0305.106, 2018.

[163] H. Wajant . Principles of antibody-mediated TNF receptor activation . *Cell Death and Differentiation*, 22:1727–1741, 2015.

[164] M.J. Eck, S.R. Sprang . The Structure of Tumor Necrosis Factor alpha at 2.6 A Resolution . *Journal of Biological Chemistry*, 264 (29):17595–17605, 1989.

[165] Juthathip Mongkolsapaya, Jonathan M. Grimes, Nan Chen, Xiao-Ning Xu, David I. Stuart, E.Yvonne Jones, Gavin R. Screaton . Structure of the TRAIL–DR5 complex reveals mechanisms conferring specificity in apoptotic initiation . *Nature Structural and Molecular Biology*, 6:1048–1053, 1999.

[166] James H. Naismith, Tracey Q. Devine, Barbara J. Brandhuber, Stephen R. Sprang . Crystallographic Evidence for Dimerization of

Unliganded Tumor Necrosis Factor Receptor . *Journal of Biological Chemistry*, 270 (22):13303–13307, 1995.

[167] Linlin Zhao, Qingshan Fu, Liqiang Pan, Alessandro Piai, James J. Chou . The Diversity and Similarity of Transmembrane Trimerization of TNF Receptors . *Front. Cell Dev. Biol.*, pages 569684–569684, 2020.

[168] Fiona L. Scott, Boguslaw Stec, Cristina Pop, Małgorzata K. Dobaczewska, JeongEun J. Lee, Edward Monosov, Howard Robinson, Guy S. Salvesen, Robert Schwarzenbacher, Stefan J. Riedl . The Fas–FADD death domain complex structure unravels signalling by receptor clustering . *Nature*, 457:1019–1022, 2008.

[169] E.S. Vanamee, D.L. Faustmann . Structural principles of tumor necrosis factor superfamily signaling . *Science Signalling*, 11 (511):doi: 10.1126/scisignal.aao4910, 2018.

[170] J. D. Graves, J. J. Kordich, T.-H. Huang, J. Piasecki, T. L. Bush, T. Sullivan, I. N. Foltz, W. Chang, H. Douangpanya, T. Dang, J. W. O'Neill, R. Mallari, X. Zhao, D. G. Branstetter, J. M. Rossi, A. M. Long, X. Huang, P. M. Holland . Apo2L/TRAIL and the death receptor 5 agonist antibody AMG 655 cooperate to promote receptor clustering and antitumor activity . *Cancer Cell*, 26:177–189, 2014.

[171] E.S. Vanamee, G. Lippner, D.L. Faustmann . Signal Amplification in Highly Ordered Networks Is Driven by Geometry . *Cells*, 11 (2):DOI: 10.3390/cells11020272, 2022.

[172] Stefanie Freitag, Isolde Le Trong, Ashutosh Chilkoti, Lisa A Klumb, Patrick S. Stayton, Ronald E Stenkamp . A monovalent streptavidin with a single femtomolar biotin binding site . *Journal of Molecular Biology*, 279 (1):211–221, 1998.

[173] Susanne Kleber, Ignacio Sancho-Martinez, Benedict Wiestler, Alexandra Beisel, Christian Gieffers, Oliver Hill, Meinolf Thiemann, Wolf Mueller, Jaromir Sykora, Andreas Kuhn, Nina Schreglmann, Elisabeth Letellier, Cecilia Zuliani, Stefan Klussmann, Marcin Teodorczyk, Hermann-Josef Gröne, Tom M. Ganten, Holger Sültmann, Jochen Tüttenberg, Andreas von Deimling, Ana Martin-Villalba . Yes and PI3K Bind CD95 to Signal Invasion of Glioblastoma . *Cancer Cell*, 13 (3):235–248, 2008.

[174] Steffen M. Sedlak, Leonard C. Schendel, Marcelo C. R. Melo, Diana A. Pippig, Zaida Luthey-Schulten, Hermann E. Gaub, Rafael C. Bernardi

. Direction Matters: Monovalent Streptavidin/Biotin Complex under Load . *Nano Letters*, 19 (6):3415–3421, 2018.

[175] Yang Wang, Igor Baars, Ferenc Fördös, Björn Högber . Clustering of Death Receptor for Apoptosis Using Nanoscale Patterns of Peptides . *ACS Nano*, 15 (6):9614–9626, 2021.

[176] Giuseppe Lamanna, Cristian R. Smulski, Neila Chekkat, Karine Estieu-Gionnet, Gilles Guichard, Sylvie Fournel, Alberto Bianco . Multimerization of an Apoptogenic TRAIL-Mimicking Peptide by Using Adamantane-Based Dendrons† . *Chemistry*, 19 (5):1762–1768, 2012.

[177] Yang Wang, Igor Baars, Ieva Berzina, Iris Rocamonde-Lago, Boxuan Shen, Yunshi Yang, Marco Lolaico, Janine Waldvogel, Ioanna Smyrlaki, Keying Zhu, Robert A. Harris, Björn Högberg . A DNA robotic switch with regulated autonomous display of cytotoxic ligand nanopatterns . *Nature Nanotech*, 19:1366–1374, 2024.

[178] Nina Bartels, Nicolaas TM van der Voort, Oleg Opanasyuk, Suren Felekyan, Annemarie Greife, Xiaoyue Shang, Arthur Bister, Constanze Wiek, Claus AM Seidel, Cornelia Monzel . Advanced multiparametric image spectroscopy and super-resolution microscopy reveal a minimal model of CD95 signal initiation . *Science Advances*, 10 (30):eadn3238, 2023.

[179] Joseph P. Kolb, Thomas H. Oguin III, Andrew Oberst, Jennifer Martinez . Programmed Cell Death and Inflammation: Winter Is Coming . *Trends in Immunology*, 38 (10):705–718, 2017.

[180] Gülce S. Gülcüler Balta, Cornelia Monzel, Susanne Kleber, Joel Beaudouin, Emre Balta, Thomas Kaindl, Si Chen, Liang Gao, Meinolf Thiemann, Christian R. Wirtz, Yvonne Samstag, Motomu Tanaka, Ana Martin-Villalba . 3D Cellular Architecture Modulates Tyrosine Kinase Activity, Thereby Switching CD95-Mediated Apoptosis to Survival . *Cell Reports*, 29 (8):2295–2306, 2019.

[181] Mauro Cataldi, Chiara Vigliotti, Teresa Mosca, MariaRosaria Cammarota, Domenico Capone . Emerging Role of the Spleen in the Pharmacokinetics of Monoclonal Antibodies, Nanoparticles and Exosomes . *Int. J. Mol. Sci*, 18 (6):1249, 2017.

[182] Bujie Du, Mengxiao Yu, Jie Zheng . Transport and interactions of nanoparticles in the kidneys . *Nature Reviews Materials*, 3:358–374, 2018.

[183] Yuxuan Ma, Zhangwei Lu, Bin Jia, Ye Shi, Jun Dong, Shuoxing Jiang, Zhe Li . DNA Origami as a Nanomedicine for Targeted Rheumatoid Arthritis Therapy through Reactive Oxygen Species and Nitric Oxide Scavenging . *ACS Nano*, 16 (8):12520–12531, 2022.

[184] Yang Wang, Erik Benson, Ferenc Fördős, Marco Lolaico, Igor Baars, Trixy Fang, Ana I. Teixeira, Björn Högberg . DNA Origami Penetration in Cell Spheroid Tissue Models is Enhanced by Wireframe Design . *Advanced Materials*, 33 (29):2008457, 2021.

[185] Torsten Strunz, Krisztina Oroszlan, Rolf Schäfer, and Hans-Joachim Güntherodt. Dynamic force spectroscopy of single DNA molecules. *PNAS*, 96 (20):11277–11282, 1999.

[186] Taoran Tian, Tao Zhang, Sirong Shi, Yang Gao, Xiaoxiao Cai, Yunfeng Lin . A dynamic DNA tetrahedron framework for active targeting . *Nature Protocols*, 18:1028–1055, 2023.

[187] Yue Hu, Zhou Chen, He Zhang, Mingkai Li, Zheng Hou, Xiaoxing Luo, Xiaoyan Xue . Development of DNA tetrahedron-based drug delivery system . *Drug Delivery*, 224 (1):1295–1301, 2017.

[188] Jianqin Yan, Xiaohui Zhan, Zhuangzhuang Zhang, Keqi Chen, Maolong Wang, Yong Sun, Bin He, Yan Liang . Tetrahedral DNA nanostructures for effective treatment of cancer: advances and prospects . *Journal of Nanobiotechnology*, 19:412, 2021.

[189] Yu Ouyang, Pu Zhang, Itamar Willner . DNA Tetrahedra as Functional Nanostructures: From Basic Principles to Applications . *Angewandte Chemie Int. Ed.*, 63 (41):e202411118, 2024.

[190] Joseph Sambrook, Davin W Russell. *Molecular CLoning - A Laboratory Manual, third edition.* Cold Spring harbor Laboratory Press, Cold Spring Harbor, New York, 2001.

[191] JA Hewitt. Miniphage - A Class of Satellite Phage to M13. *The journal of General Virology*, 17, 2101678, 1975.

[192] Johannes Schindelin, Ignacio Arganda-Carreras, Erwin Frise, Verena Kaynig, Mark Longair, Tobias Pietzsch, Stephan Preibisch, Curtis Rueden, Stephan Saalfeld, Benjamin Schmid, Jean-Yves Tinevez, Daniel James White, Volker Hartenstein, Kevin Eliceiri, Pavel Tomancak, Albert Cardona . Fiji: an open-source platform for biological-image analysis . *Nature Methods*, 9:676–682, 2012.

[193] B.V. Enustun, J. Turkevich . Coagulation of Colloidal Gold . *JACS*, 85 (21):3317–+, 1963.

[194] M. Dobretsov, G. Petkau, A. Hayar, E. Petkau . Clock Scan Protocol for Image Analysis: ImageJ Plugins . *Jove-J Vis Exp*, page e55819, 2017.

[195] A. Shaw, E. Benson, B. Hoegberg . Purification of functionalized DNA origami nanostructures. . *ACS Nano*, 9:4968–4975, 2015.

[196] Oliver Henrich, Yair Augusto Gutiérrez Fosado, Tine Curk, Thomas E. Ouldridge . Coarse-grained simulation of DNA using LAMMPS : An implementation of the oxDNA model and its applications . *The European Physical Journal E*, 41:57, 2018.

[197] Jonathan P. K. Doye, Hannah Fowler, Domen Prešern, Joakim Bohlin, Lorenzo Rovigatti, Flavio Romano, Petr Šulc, Chak Kui Wong, Ard A. Louis, John S. Schreck, Megan C. Engel, Michael Matthies, Erik Benson, Erik Poppleton, Benedict E. K. Snodin . The oxDNA Coarse-Grained Model as a Tool to Simulate DNA Origami . *Methods Mol. Bio.*, 2639:93–112, 2023.

Scientific Contributions

A list of **publications** contributed to during the dissertation:

[**I**] Ricarda M. L. Berger, **Johann M. Weck**, Simon M. Kempe, Oliver Hill, Tim Liedl, Joachim O. Rädler, Cornelia Monzel, Amelie Heuer-Jungemann, *Nanoscale FasL Organization on DNA Origami to Decipher Apoptosis Signal Activation in Cells*, Small, 17 (26), 2101678, 2021

[**II**] Svetozar Gavrilović, Gereon Andreas Brüggenthies, **Johann Moritz Weck**, Amelie Heuer-Jungemann, Petra Schwille, *Protein-Assisted Large-Scale Assembly and Differential Patterning of DNA Origami Lattices*, Small, 20 (24), 2309680, 2024

[**III**] **Johann M. Weck**, Amelie Heuer-Jungemann, *Fully Addressable, Designer Superstructures Assembled from a Single Modular DNA Origami*, Nature Communications, 16, 1556, 2025

[**IV**] Xiaoyue Shang, Nina Bartels, **Johann Moritz Weck**, Sabine Suppmann, Jérôme Basquin, Amelie Heuer-Jungemann, Cornelia Monzel. *High yield purification of an isoleucine zipper-modified CD95 ligand for efficient cell apoptosis initiation and with biotin or DNA-oligomer binding domain to probe ligand functionalization effects.* BMC Biotechnology, 25, 64, 2025

[**V**] **Johann M. Weck**, Riya Nair, Merve-Z. Kesici, Xiaoyue Shang, Cornelia Monzel, Amelie Heuer-Jungemann. *Effects of DNA Origami-Based Nanoagent Design on Apoptosis Induction in a Large 3D Cancer Spheroid Model.* Small, 21 (24), 2502490, 2025

A list of **conference contributions**:

2021: participant at the FNANO21 (online)

2021: co-organizer of the SFB1032 Blockseminar 2021

2022: oral presentation at the SFB1032 Workshop

2022: poster presentation at the Max Bergmann Symposium

2022: co-organizer of the SFB1032 Blockseminar 2022

2023: oral presentation at the DFG SKM

2023: poster presentation at the DNA29

2024: poster presentation at the FNANO24

2024: co-organizer of the SFB1032 Blockseminar 2024

2024: oral and poster presentation at the DNA nanotechnology

2024: oral presentation at the SFB1032 workshop

2024: oral presentation at the FDN24

Acknowledgements

First and foremost, I thank Amelie Heuer-Jungemann for more than just the opportunity to earn my doctorate. I want to thank her for her generosity, which allowed me to visit several conferences during my doctorate, for her openness toward new ideas, and for her patience with unruly students.

I also want to thank Ralf Jungmann, for being a mentor to me and spending his time and energy supporting my quirky ideas.

I want to thank the *Deoxy* postdocs for fanning my enthusiasm for science and welcoming me so cordially to the field.

Further, I want to thank my fellow (PhD) students in the group and at the institute: Lea Wassermann for some magical first weeks in the PhD, Anna Baptist for many scientific lunches, and Manar Elnagar for not burning down the institute. Thanks to all the students I supervised; you made me a better scientist, too. I want to thank Jakob Reber for great conversations about anything and everything, Sebastian Grün for his stoicism and many after-work beers, and Alex Anastasakis for lifting me up. I also want to thank all other collaboration partners for the big and small projects and for each bit of success we achieved!

I want to thank my dear fellows, some of whom I have known since the very first semester: Francis Schuknecht, Peter Kulosik, and Max Rinnagel, just to name a few. I want to thank my always meddling D&D friends, it is an absolute pleasure to be your DM. I want to thank the IMPRS book club group, for many great evenings and exposing me to new books and fresh ideas. I further thank the SFB1032, of which I had the honor of being the representative since 2021. Thanks also to everyone who participated in the *DNA node*; Arthur Ermatov for co-organizing, thanks to all the speakers, and everyone who joined!

For a great conference in Japan, great evenings, and conversations on and around science, I want to thank Durham Smith, Thomas Mayer, and the Stanford crew. And for a great conference in Snowbird, I want to thank everyone I met inside and outside of the Yakuzzi.

I want to thank everyone whose names did not make it on this short list; be assured, I thought of you, too.

Lastly, and most importantly, I want to thank my dear parents, without whom I would not be here.